

*FLUORESCENCE CORRELATION SPECTROSCOPY STUDIES*

FLUORESCENCE CORRELATION SPECTROSCOPY STUDIES  
CHARACTERIZING  
DIFFUSION  
AND  
PHOTOPHYSICAL PROPERTIES  
OF PROTEINS

By

DANIEL BANKS, B.SC., M.A.

A Thesis

Submitted to the School of Graduate Studies

in Partial Fulfillment of the Requirements

for the Degree

Doctor of Philosophy

McMaster University

© Copyright by Daniel Banks, December 2007

Doctor of Philosophy (2007)

McMaster University

(Physics & Astronomy)

Hamilton, Ontario

TITLE: Fluorescence Correlation Spectroscopy Studies Characterizing Diffusion  
and Photophysical Properties of Proteins

AUTHOR: Daniel Banks, B.Sc. (Bob Jones University), M.A. (Calvary Baptist  
Theological Seminary)

SUPERVISOR: Dr. Cécile Fradin

NUMBER OF PAGES: vi, 154

## Abstract

The primary focus of the research presented here is the characterization of diffusion using Fluorescence Correlation Spectroscopy (FCS). To understand the nature of the anomalous diffusion observed in living systems, we characterized diffusion in complex *in vitro* systems including the diffusion of proteins, random-coil polymers, or dyes in crowded random-coil polymer solutions and the diffusion of polymer beads in agarose gels. Anomalous diffusion is defined where the mean-square-displacement follows a power law in time,  $\langle r^2(t) \rangle \propto t^\alpha$ , with  $\alpha \neq 1$ . We observed that diffusion of proteins in dextran solutions is subdiffusive ( $\alpha < 1$ ) where  $\alpha$  decreases with increasing dextran concentration and molecular weight until it reaches a limit value of  $\alpha \approx 3/4$ . Because subdiffusion implies a length-scale dependent diffusion coefficient, observations were performed at multiple length-scales (0.2 – 1.5  $\mu\text{m}$ ) which allow two complementary methods of determining  $\alpha$  from the power law relationship between the length-scale and the diffusion time and from the width of the decay of correlation data at each length-scale. We report the first direct observations of subdiffusion using these two methods. For example, for the diffusion of polymer beads in 1.4% agarose gels, the value of  $\alpha$  obtained from correlation decays increases from 0.82 to 0.97 as the observation volume is increased, while the diffusion power law yields  $\alpha = 0.92$ . The results are explained as a cross-over effect between two diffusive behaviors, and the significance of such cross-over behavior for live cells observations is discussed. The second focus of this thesis is the characterization of the temperature dependence of fluorescent protein blinking and the application of that dependence as a molecular thermometer. We demonstrate applications of this thermometer in microliter samples, including the calibration of sample temperature when using a temperature-controlled water immersion objective and to measure the sample's spatial temperature gradient.

## **Dedication & Acknowledgements**

To Oscar O'Dell, born at my departure,  
Ever may you live well, borne by your parent's nurture.

I thank Cécile Fradin for her extensive guidance and support during the five years of research and development which culminated in this thesis. Without her, none of this would have been accomplished. May she and her husband Duncan enjoy the many opportunities to cherish Oscar, their first bundle of joy.

I thank the current and former members of the experimental biophysics group led by Cécile Fradin for a warm team atmosphere in which to work. I thank especially Felix Wong and Asmahan Abu-Arish with whom I have had the privilege of collaborating and sharing much of student life.

I thank the Natural Sciences and Engineering Research Council of Canada for providing generous student support which eased my task. I thank the taxpayers to whom final credit for the support of this research is due.

Most of all, I thank my parents, John and Carrie, whose love and confidence in me has never waned.

## Table of Contents

<b>1. Introduction</b>	1
<b>1.1 Theory of Diffusion</b>	3
1.1.1 Fick's Law, the Continuity Equation, and the Diffusion Equation	4
1.1.2 The Stokes-Einstein Equation	7
1.1.3 Random Walks	9
1.1.4 Non-Brownian Motion	11
<b>1.2 Diffusion in Biological Systems</b>	16
1.2.1 The Role and Importance of Diffusion in Biological Systems	17
1.2.2 Observations of Diffusion in Live Cells	19
1.2.3 Complex <i>In Vitro</i> Systems as a Model for Cellular Diffusion	23
<b>1.3 Fluorescence and Photophysics</b>	25
1.3.1 Quantum Mechanical Basis of Fluorescence	26
1.3.2 Photophysics of Intersystem Crossing (Triplet-Singlet Transitions)	28
1.3.3 Photophysics of Photobleaching	29
1.3.4 Fluorescent Proteins and Photophysics of Fluorescent Proteins	31
<b>1.4 Fluorescence Correlation Spectroscopy and Other Fluorescence Experimental Methods</b>	34
1.4.1 Fluorescence Correlation Spectroscopy Theory	35
<i>Definition of the Autocorrelation Function for Fluorescence Signals</i>	36
<i>Interpreting the Correlation Amplitude and Effective Observation Volume</i>	37
<i>Correlation Function for Normal Diffusion</i>	39
<i>Correlation Function for Two-State Photophysical Kinetics</i>	41
<i>Correlation Function for Normal Diffusion and Two-State Photophysical Kinetics</i>	42
<i>Multi-Component Models</i>	44
<i>Anomalous Diffusion Model</i>	46
1.4.2 Fluorescence Correlation Spectroscopy Experimental Description	48
1.4.3 Other Experimental Methods Used to Study Diffusion <i>in Vivo</i>	51
<i>Fluorescence Recovery After Photobleaching (FRAP)</i>	51
<i>Single Particle Tracking (SPT)</i>	53

<b>2. Summary of Research</b>	54
<b>2.1 Summary of Contributions to FCS Experimental Development</b>	55
2.1.1 Description of the <i>FROG 3D</i> LabVIEW program	56
2.1.2 Description of the Development of VLS-FCS	63
<b>2.2 Summary of Manuscripts</b>	67
2.2.1 Summary of <i>Anomalous Diffusion of Proteins Due to Molecular Crowding</i>	67
2.2.2 Summary of <i>Diffusion Power Laws in Polymer Solutions and Gels Observed Using Variable Length Scale Fluorescence Correlation Spectroscopy</i>	71
2.2.3 Summary of <i>A Molecular Thermometer Based on Fluorescent Protein Blinking</i>	75
<b>2.3 Summary of Additional Research</b>	78
2.3.1 Application of VLS-FCS to the Diffusion of Polymers in Organic Solvents	78
2.3.2 Applications of the Molecular Thermometer Based on EGFP Blinking	87
<b>3. References</b>	91
<b>4. Manuscripts</b>	105
<b>4.1 <i>Anomalous Diffusion of Proteins Due to Molecular Crowding</i></b>	105
<b>4.2 <i>Diffusion Power Laws in Polymer Solutions and Gels Observed Using Variable Length Scale Fluorescence Correlation Spectroscopy</i></b>	118
<b>4.3 <i>A Molecular Thermometer based on Fluorescent Protein Blinking</i></b>	142
4.3.1 Table of Contents Graphic	142
4.3.2 Abstract	143
4.3.3 <i>JACS</i> Article	144
4.3.4 Supplementary Data	147

## 1. Introduction

The characterization of diffusion in complex media is of great interest to biophysics and is the primary focus of the research presented in this thesis. The study of diffusion in complex *in vitro* systems is used in order to shed light on biological processes involving diffusion *in vivo* and experimental characterization of diffusion of tracers in cells is often performed to probe the local cellular environment. This thesis presents studies characterizing diffusion with interest in the phenomenon of anomalous, or length-scale dependent, diffusion of proteins and other polymers. The second focus of this thesis is the characterization of the temperature dependence of fluorescent protein blinking and the application of that dependence as a means to measure local temperature in small samples where conventional methods cannot be used. In both cases, the research was conducted experimentally through Fluorescence Correlation Spectroscopy (FCS), a widely used technique in biophysics and biochemistry that relies on the measurement of small fluctuations away from the thermodynamic equilibrium. The studies presented in this thesis, although carried out in order to explain phenomena of interest in biophysics, are also relevant to other fields: the diffusion studies are of interest to polymer scientists and the application of photophysical blinking is expected to be useful in microfluidics.

This introductory section (§1) seeks to provide sufficient theoretical and experimental background material so that the summary of research (§2) and the manuscripts (§4) may be understood by biophysicists who may not be familiar with FCS, diffusion, or photophysical properties of fluorescent proteins. First, there is a background discussion of diffusion. A description of basic diffusion theory is provided as background for understanding the nature of a class of phenomena called anomalous diffusion (§1.1). This part includes a derivation of Fick's law which leads to the diffusion equation (§1.1.1) followed by a discussion of the Stokes-Einstein equation (§1.1.2). Then a brief discussion of a simple random walk model shows the equivalence of discrete random walks and continuous diffusion (§1.1.3). Finally, the anomalous diffusion is presented to model complex behaviors where Brownian theory is insufficient (§1.1.4).

Second, the theory is followed by a description of the importance of diffusion for the study of biological systems (§1.2). A brief discussion of the role and importance of diffusion in biological systems is presented (§1.2.1). A brief literature review of the application of diffusion as a probe of cellular environments (§1.2.2) is followed by a summary of complex diffusion behaviors that have actually been observed in live cells (§1.2.3). The observations of complex diffusion in live cells will thus demonstrate a need for studies of diffusion in complex *in vitro* systems to understand diffusion in live cells (§1.2.4).

Since Fluorescence Correlation Spectroscopy (FCS) and the experimental methods used to observe diffusion in live cells are based on the principle of fluorescence, the third introductory section describes the basic properties of fluorescence and the photophysics of fluorescent proteins which are widely used as *in vivo* tags to proteins of interest (§1.3).

Specifically, the basic concept of fluorescence as a quantum mechanical phenomenon is described (§1.3.1), followed by complications and limitations to observing fluorescence fluctuations such as non-fluorescent triplet states (§1.3.2) and photobleaching (§1.3.3). Having discussed fluorescence in general terms, then there is a more specific description of the properties of green fluorescent protein and various blinking phenomenon observed in fluorescent proteins (§1.3.4).

Finally, the last introductory section will describe FCS and the other fluorescence based methods which are used by biophysicists to observe diffusion via fluorescence (§1.4). Fluorescence Correlation Spectroscopy is given the most attention with detailed descriptions of the theory of FCS (§1.4.1) and of the FCS experimental apparatus used in the research presented in this thesis (§1.4.2). Only brief descriptions of the other methods which are used to observe diffusion will be given, including Fluorescence Recovery After Photobleaching and Particle Tracking (§1.4.3) with particular attention to their strengths and limitations compared to FCS.

## 1.1. Theory of Diffusion

In 1822, Joseph Fourier introduced the heat conduction equation (1), and soon afterwards in 1827, Robert Brown discovered the phenomena now called “Brownian motion” when he observed random movements of pollen grains under a microscope (2, 3). Fourier’s work lead to the diffusion equation derived by A. Fick 1855 (4), while C. Weiner in 1863 gave an explanation for the Brownian motion based on the kinetic theory which was supported by experiments by Gouy. A decade later, Boltzmann published his transport equation in 1872 to describe collision processes which provided the basis for the atomistic random walk approach to Brownian motion. Finally in 1905, Albert Einstein unified the previous theories, and showed how observation of random walks can be used to connect microscopic dynamics of atoms colliding with larger particles and macroscopic observables like the diffusion coefficient and Avogadro’s number (5).

This section gives some of the basic theoretical background describing diffusion. We start by deriving Fick’s Law and the diffusion equation and show how this leads to the mean-square-displacement of particles growing proportionally to time, which is a characteristic of Brownian motion (§1.1.1). Second, we derive the Stokes-Einstein equation to demonstrate how the diffusion coefficient is related to the hydrodynamic radius, absolute temperature, viscosity, and Boltzmann’s constant (§1.1.2). Further, we consider a simple random walk to show how random walk models leads to the same time-dependence of the mean-square-displacement is achieved as is found using Fick’s law and the diffusion equation (§1.1.3). Finally, we discuss more complex systems where non-Brownian motion is observed and we discuss several models of diffusion which led to a particular type of non-Brownian motion called anomalous diffusion (§1.1.4).

### 1.1.1. Fick's Law, the Continuity Equation, and the Diffusion Equation

Fick's Law states that the number flux of particles is proportional to the spatial concentration gradient, where the proportionality constant is the negative of the diffusion coefficient. To derive Fick's law, suppose there is a non-uniform concentration distribution,  $C(x)$  in the direction  $x$ , and a series of planes equally spaced by a distance  $l$  perpendicular to  $x$ , as in Figure 1.1.1-A (see reference (6)).

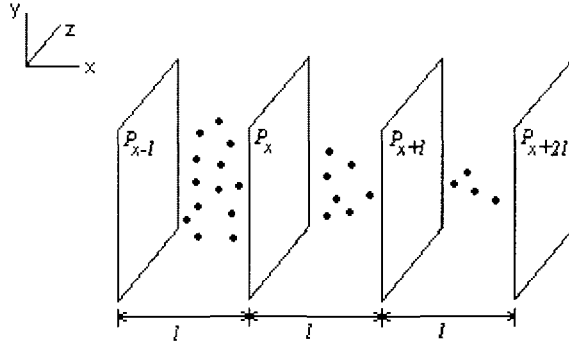


Figure (1.1.1-A). Illustration of a non-uniform concentration distribution,  $C(x)$  in the direction  $x$ , and a series of equally spaced planes,  $P_{x-l}, P_x, P_{x+l}, P_{x+2l}$ , by a distance  $l$  perpendicular to  $x$ .

The ideal gas theory of statistical physics specifies that the mean contribution of the translational kinetic energy of a single particle which is free to move in the  $x$  direction is given by  $mv_x^2/2 = kT/2$ , where  $m$  is the particle's mass,  $k$  is the Boltzmann constant and  $T$  is the absolute temperature. Therefore between collisions, each particle has a root-mean-square average velocity of  $v_x = \pm\sqrt{kT/m}$  along the  $x$ -axis. However, each particle will collide with other particles and scatter, erasing the memory of the particle's previous direction and therefore the average velocity  $\langle v_x \rangle = 0$ . The average distance between collisions is called the mean free path,  $l$ , and we let the average time between collisions be  $\Delta t$ . If we denote the number of particles between planes  $P_x$  and  $P_{x+l}$  as  $N_{x,x+l}$ , then the net number of particles crossing plane  $P_x$  in time  $\Delta t$ , denoted  $N_x(t)$  is:

$$N_x(t) = \frac{1}{2}(N_{x-l,x} - N_{x,x+l}). \quad (1.1.1-1)$$

For particles diffusing in liquid media, the mean free path is very small due to the presence of a high density of solvent molecules. Therefore if we let the distance between planes become very small we consider the continuous limit where we may replace  $l$  with  $dx$  to denote an infinitesimal spatial increment. Further, we denote where  $N(x,t)$  as the number of particles between  $x$  and  $x - dx$  at time  $t$ , and by analogy with Equation 1.1.1-1, we write the net number of particles crossing a plane located between  $x$  and  $x - dx$  during the time interval  $\Delta t$ :

$$\frac{1}{2}(N(x-dx) - N(x)) = -\frac{1}{2}l \frac{d}{dx} N(x). \quad (1.1.1-2)$$

If we denote  $A$  as the area of the plane, then the number flux,  $j(x)$ , of particles across the plane is then:

$$j(x) = \frac{-\frac{1}{2}l \frac{d}{dx} N(x)}{\Delta t \cdot A}. \quad (1.1.1-3)$$

Since the concentration of particles,  $C(x)$ , is the number of particles divided by the volume, then  $N(x) = A \cdot l \cdot C(x)$ , and the flux becomes:

$$j(x) = -\frac{1}{2}l^2 / \Delta t \frac{d}{dx} C(x). \quad (1.1.1-4)$$

Defining the diffusion coefficient,  $D$ , as  $\frac{1}{2}l^2 / \Delta t$ , then we have Fick's Law for one dimension:

$$j(x) = -D \frac{d}{dx} C(x). \quad (1.1.1-5)$$

Using similar arguments for 3-D diffusion, Fick's Law may be written thus:

$$\vec{j} = -D \nabla C(\vec{r}, t). \quad (1.1.1-6)$$

Fick's Law as given in Equation 1.1.1-6 is valid for isotropic media in which the structure and diffusion properties at  $\vec{r}$  are the same in all directions. But where the medium is more complex, Fick's law may fail to describe diffusion in the system (7).

We can derive the continuity equation independently from Fick's law by simply considering the development of the system shown in Figure 1.1.1-A over time, that is, the change in  $N(x)$  over an infinitesimal time step  $dt$ . If we assume that the only phenomenon contributing to the change in the number,  $N(x,t)$ , of particles over time located between two arbitrary planes in space located at  $x$  and  $x + dx$ , is the flux,  $j(x,t)$ , of particles through planes located at  $x$  and  $x + dx$ , then:

$$\frac{\partial}{\partial t} N(x,t) = A \cdot (j(x,t) - j(x+dx,t)). \quad (1.1.1-7)$$

$$\frac{\partial}{\partial t} N(x,t) = - \frac{(j(x+dx,t) - j(x,t))}{l}. \quad (1.1.1-8)$$

Then we arrive at the continuity equation for one dimension:

$$\frac{\partial}{\partial t} C(x,t) = - \frac{\partial}{\partial x} j(x,t). \quad (1.1.1-9)$$

Using similar arguments for 3-D diffusion, one may write the continuity equation thus:

$$\frac{\partial}{\partial t} C(\vec{r}, t) = -\nabla \cdot \vec{j}(\vec{r}, t). \quad (1.1.1-10)$$

The continuity equation given in Equation 1.1.1-10 states that the change in particle concentration at a given time is equal in magnitude to the gradient of the particle flux. In other words, the change in number of particles at a given volume is attributed only to particles diffusing to and from that volume, or matter is conserved in this system. Therefore the continuity equation is general not just for isotropic media but for any system where particles do not undergo conversion to energy or to another particle species. Therefore if there is a change in number of species due to chemical reactions, the continuity equation does not apply and the change in  $C(\vec{r}, t)$  over time will also depend on the reaction rates and concentrations of the reactants and products.

Substituting Fick's law (Equation 1.1.1-6) into the continuity equation (Equation 1.1.1-10) yields the diffusion equation:

$$\frac{\partial C(\bar{r}, t)}{\partial t} = D\nabla^2 C(\bar{r}, t). \quad (1.1.1-11)$$

Consider the non-equilibrium situation where  $N$  particles are at the origin at time  $t = 0$ , then the diffusion equation describes how the system will relax to equilibrium over time. The initial condition is  $\lim_{t \rightarrow 0} C(\bar{r}, t) = N\delta(\bar{r})$  and the boundary condition is  $\lim_{\bar{r} \rightarrow \infty} C(\bar{r}, t) = 0$ .

The solution to the diffusion equation is:

$$C(\bar{r}, t) = \frac{N}{(4\pi Dt)^{3/2}} e^{-\frac{\bar{r}^2}{4Dt}}. \quad (1.1.1-12)$$

$C(\bar{r}, t) / N$  represents the probability to find a particle at position  $\bar{r}$  at time  $t$ . Therefore, the mean-square-displacement of a particle may be calculated thus:

$$\begin{aligned} \langle r^2(t) \rangle &= \int r^2 \frac{1}{(4\pi Dt)^{3/2}} e^{-\frac{\bar{r}^2}{4Dt}} dV \\ &= \frac{1}{(4\pi Dt)^{3/2}} 4\pi \cdot \int_0^\infty r^2 e^{-\frac{r^2}{4Dt}} \cdot r^2 dr = 6Dt \end{aligned} \quad (1.1.1-13)$$

For  $d$ -dimensions, the mean-square-displacement can be generalized, thus:

$$\langle r^2(t) \rangle = 2dDt. \quad (1.1.1-14)$$

The mean-square-displacement is proportional to time, the characteristic of normal diffusion, or Brownian motion.

### 1.1.2 The Stokes-Einstein Equation

The Stokes-Einstein equation relates the macroscopic quantities such as the diffusion coefficient of a particle and solvent viscosity to microscopic quantities such as the hydrodynamic radius of that particle and Boltzmann's constant. We present here a simple justification of this relationship using arguments presented in (6), followed by an outline of Einstein's more rigorous derivation (5). Consider again a sphere having an initial velocity of  $v_{x0} = \pm\sqrt{kT/m}$  due to its kinetic energy and a zero average velocity,  $\langle v_{x0} \rangle = 0$ , as discussed in the derivation of Fick's law (§1.1.1). Now consider that the sphere moves in a stationary continuous viscous medium where it may scatter off particles in the medium and assume that the scattering occurs at an average time interval  $\Delta t$ . The distance traveled between each collision may be written:

$$\Delta x = v_{x0} \Delta t - \frac{1}{2} \frac{f}{m} \Delta t^2 . \quad (1.1.2-1)$$

Here  $f$  is the average force of friction that acts on the sphere between collisions due its contact with the continuous viscous medium. Noting that  $\langle v_{x0} \rangle = 0$ , the magnitude of the average change in position between collisions is:

$$\langle |\Delta x| \rangle = \frac{1}{2} \frac{f}{m} \Delta t^2 . \quad (1.1.2-2)$$

Now we can define the *drift velocity*,  $v_d$ :

$$v_d \equiv \frac{\langle |\Delta x| \rangle}{\Delta t} = \frac{f}{2m} \Delta t = \frac{f}{\zeta} . \quad (1.1.2-3)$$

Here we have also defined the *viscous friction coefficient*,  $\zeta \equiv 2m / \Delta t$ . Since the relative speed of the sphere and the medium determines the force of friction, the magnitude of this frictional force is equal to the force exerted by a flowing viscous medium with velocity  $v_d$  on a stationary sphere suspended in the medium. Stokes demonstrated that the force of viscous friction of a sphere of radius,  $R$ , in a steady state flow of velocity  $v$  of a viscous medium with viscosity  $\eta$  flowing around the sphere is equal to (8, 9):

$$f = 6\pi\eta Rv . \quad (1.1.2-4)$$

From Equation 1.1.2-3 we can write the viscous friction coefficient for such a sphere as:

$$\zeta = 6\pi\eta R . \quad (1.1.2-5)$$

Now we note our definition of the diffusion coefficient used previously in the derivation of Fick's law (Equation 1.1.1-5 for 1 dimension):  $D \equiv \frac{1}{2} l^2 / \Delta t$ . Note also that  $\langle |\Delta x| \rangle$  is not the same as  $l$ , since  $l$  was defined as  $l = v_{x0} \cdot \Delta t$ . Multiplying the diffusion coefficient with the viscous friction coefficient results in a relation independent of the mean free path or the time interval (6):

$$\zeta \cdot D = \frac{2m}{\Delta t} \cdot \frac{l^2}{2\Delta t} = \left( \frac{l}{\Delta t} \right)^2 m = \langle v_{x0}^2 \rangle \cdot m = kT . \quad (1.1.2-6)$$

Now using Equation 1.1.2-5 we arrive at the Stokes-Einstein equation for the diffusion coefficient published by Einstein in 1905 (5):

$$D = \frac{kT}{6\pi\eta R}. \quad (1.1.2-7)$$

Einstein arrived at this expression through more rigorous thermodynamic considerations, thus (5): Because Brownian motion is an entropic effect at thermodynamic equilibrium, there is no change in free energy due to a small displacement,  $\delta x$ , that is,  $\delta E - T\delta S = 0$ , where  $\delta E$  is the work done on suspended spheres by the medium during the displacement through a constant force of friction  $f$  and  $\delta S$  is the corresponding change in entropy of the system. If we consider the liquid medium to be bounded by planes at  $x = 0$  and  $l$ , with unit area of cross-section perpendicular to the x-axis, then we may write the change in energy of the system thus:

$$\delta E = - \int_0^l (Cf\delta x) dx = Cf. \quad (1.1.2-8)$$

Here the  $C$  is the concentration of spheres between  $x = 0$  and  $l$ , and we sum the work done on each particle due to its displacement,  $\delta x$ . Then change in entropy may be calculated thus:

$$\delta S = k \int_0^l \left( C \frac{\partial}{\partial x} \delta x \right) dx = -k \int_0^l \left( \frac{\partial C}{\partial x} \delta x \right) dx = -k \frac{\partial C}{\partial x}. \quad (1.1.2-9)$$

Now using the condition for equilibrium,  $\delta E - T\delta S = 0$  we have:

$$-Cf + kT \frac{\partial C}{\partial x} = 0. \quad (1.1.2-10)$$

Equation 1.1.2-10 demonstrates that two processes counterbalance to produce the equilibrium: movement under the force of friction (first term), and diffusion due to thermal motion (second term). As noted above, the drift velocity equals  $f/\zeta$ , and therefore the flux of particles passing a unit area per unit of time may be written:

$$j(x) = \frac{Cf}{\zeta} = -D \frac{\partial C}{\partial x}. \quad (1.1.2-11)$$

Here we have used Fick's law (Equation 1.1.1-6), and now Equation 1.1.2-11 may be combined with Equation 1.1.2-10 which yields:

$$kT = D\zeta. \quad (1.1.2-12)$$

Equation 1.1.2-12 was obtained previously as Equation 1.1.2-6, and using the definition of the viscous friction coefficient for a sphere in a uniform medium, we arrive again at the Stokes-Einstein equation (Equation 1.1.2-7) which relates a particle's diffusion coefficient to its hydrodynamic radius,  $R$ . By monitoring the random walks of colloid particles, one can use the Stokes-Einstein equation to measure Boltzmann's constant (and hence Avogadro's number) and confirm that the macroscopic motion observed is in fact due to the discontinuous, or atomistic, nature of matter (5). This theoretical prediction of Einstein was one of his contributions to theoretical physics which earned him a Nobel Prize in 1921 (his prize was awarded primarily due to his explanation of the photoelectric effect), and Jean Baptiste Perrin carried out corresponding experimental observations of random walks to estimate Avogadro's number which contributed to his own Nobel Prize in 1926.

### 1.1.3 Random Walks

Having discussed basic diffusion theory in continuous media, a basic random walk model is presented here which will demonstrate equivalence between diffusion theory and random walk models (for more extensive discussions of diffusion and random walks see (10, 11)). The principle of random walks is to allow a particle to take random steps subject to various restrictions. Although one cannot predict the path of an individual particle, by averaging over many possible paths, one may calculate quantities such as the mean-square-displacement and the diffusion coefficient. The simplest 1-D random walk is one in which a particle takes  $n$  steps each of length  $l$  over a time interval  $\Delta t$ . Thus each step adds  $\pm l$  to the position. The average displacement over many paths is always 0, since for every path where the displacement  $x$  at the  $n$ th step is  $x_n$ , there is a symmetric path where  $x = -x_n$ , thus  $\langle x_n \rangle = 0$ . But the mean-square-displacement is not trivial. It is calculated thus, where  $k_n = \pm 1$ :

$$\langle x_n^2 \rangle = \langle (x_{n-1} + k_n l)^2 \rangle = \langle x_{n-1}^2 \rangle + 2\langle k_n x_{n-1} \rangle l + l^2. \quad (1.1.3-1)$$

Since for every possible value of  $x_{n-1}$  there exists an equal number of paths where  $k_n = +1$  or  $-1$ , then  $\langle k_n x_{n-1} \rangle = 0$ , and:

$$\langle x_n^2 \rangle = \langle x_{n-1}^2 \rangle + l^2. \quad (1.1.3-2)$$

Therefore each step adds  $l^2$  to the mean-square-displacement. By induction,

$$\langle x_n^2 \rangle = n l^2. \quad (1.1.3-3)$$

To convert this expression into a function of time, we let  $t = n \Delta t$ .

$$\langle x_n^2(t) \rangle = \frac{l^2}{\Delta t} t = 2Dt. \quad (1.1.3-4)$$

In a manner similar to the derivation of Fick's Law (Equation 1.1.1-6) given previously, we have defined the diffusion coefficient as  $D = \frac{1}{2} l^2 / \Delta t$ , although we have not proved here in which sense these definitions may be considered identical. For three dimensions, where each step consists of one step of  $\pm l$  in each dimension, then

$$\langle \bar{r}_n^2(t) \rangle = \langle x_n^2(t) \rangle + \langle y_n^2(t) \rangle + \langle z_n^2(t) \rangle = 6Dt. \quad (1.1.3-5)$$

The mean-square-displacement of a discrete random walk obeys the same law as a mean-square-displacement of particles in a continuous media governed by the diffusion equation (see Equations 1.1.1-13 and 14), demonstrating that the discrete random walk formulation is equivalent to the diffusion theory as outlined in §1.1.1. This provides a basis for simple modeling of diffusion in continuous media through Monte Carlo simulations of random walks (12-21). In these simulations, particles on a lattice move to neighboring lattice points according to the rules and geometrical limitations established for the system and the random number drawn for each particle at each step. The simulation tracks the paths of a statistically significant number of particles in order to calculate quantities such as the mean-square-displacement. In this manner, one may

avoid complex numerical calculations of diffusion in more complicated systems where it may be difficult to set up and solve the appropriate equations to describe the diffusion.

#### 1.1.4. Non-Brownian Motion

Non-Brownian motion concerns cases where the mean-square-displacement is not simply proportional to time. A simple case is a trapped particle which cannot diffuse outside an accessible volume. The mean-square-displacement of the particle approaches a limit value, that is, the radius of gyration of the accessible volume after the particle has had sufficient time to explore this accessible volume (22). Various other factors may cause the diffusion to deviate from Brownian behavior. One common form of non-Brownian behavior is anomalous diffusion. Anomalous diffusion is defined by the power law dependence of the mean-square-displacement on time, thus:

$$\langle r^2(t) \rangle = \Gamma t^\alpha . \quad (1.1.4-1)$$

Here  $\Gamma$  is called the transport coefficient. When the diffusion is anomalous, it is possible to define an apparent diffusion coefficient that is time-dependent, thus:

$$D(t) = \frac{\Gamma}{2n} t^{\alpha-1} . \quad (1.1.4-2)$$

Here  $n$  is the number of spatial dimensions of the system. Normal diffusion is recovered where  $\alpha$  is equal to 1. Where  $\alpha < 1$ , the motion is called subdiffusive, and the motion is called superdiffusive where  $\alpha > 1$ . Superdiffusion characterizes enhanced motion where the apparent diffusion coefficient increases with time. A special type of superdiffusion, called ballistic motion, occurs in a uniform flow where  $\alpha = 2$ . With a combination of ballistic behavior and Brownian motion,  $2 > \alpha > 1$  can occur. Such superdiffusion has been observed for tracer particles in two-dimensional flows in a rapidly rotating tank where the flow consists of a chain of vortices sandwiched between two azimuthal jets (23-26) where such superdiffusive motion is characterized by infrequent long jumps such that the mean-squared step size is infinite. Such random walks are called Lévy flights (27). In contrast, subdiffusion characterizes restricted motion where the apparent diffusion coefficient decreases with time. Subdiffusion has been described theoretically in fractal systems below the percolation threshold where tracers' motions are limited by obstacles over an infinite range of length scales (28-30), and has been observed in complex systems where motion is restricted, many of which will be discussed here. In this thesis, discussion of anomalous diffusion concerns subdiffusion where  $\alpha < 1$ , unless otherwise stated.

In the previous section, we discussed the case of a simple random walk that leads to motion equivalent to the Brownian motion resulting from Fick's law and the diffusion equation. In contrast, the Continuous Time Random Walk model (CTRW) leads to anomalous diffusion. In the CTRW model, the tracers move randomly as in the simple random walk described above (§1.1.3), but the time between steps,  $\Delta t$ , is not uniform. Instead, if a particle follows a random walk on a regular lattice where the waiting-times have a distribution,  $P(\Delta t)$ , with long-time tails such as,  $P(\Delta t) = \alpha / (1 + \Delta t)^{1+\alpha}$  or  $P(\Delta t) = \Delta t^{-1-\alpha}$ , the mean-square-displacement follows a power law in time at large times  $\langle r^2(t) \rangle \propto t^\alpha$  (31-34). In this manner, the CTRW model gives anomalous diffusion by

invoking temporal complications in contrast to Lévy flights which give anomalous diffusion by invoking spatial complications by having a distribution of step sizes. The CTRW model can be used to simulate diffusion on a lattice of fixed binding sites where the distribution of waiting times accounts for a wide range of binding strengths in the lattice. This approach could be useful for modeling cellular environments where a broad distribution of interactions may exist in a network of obstacles. In fact, it may be useful to allow for both the spatial and time domains to be disordered, for example by modeling a CTRW on a fractal lattice. Examples of systems that are disordered in both time and space include transient flows through porous rocks, and percolation systems where the strengths of interactions are randomly distributed (34).

A similar approach to modeling anomalous diffusion is to require the motion to be characterized by a special class of stochastic (i.e. involving or containing random variables) processes called fractional Brownian motion (fBm). fBm approaches allow for the motion at each time step to be not completely random as Brownian motion is. Brownian motion is a category of Markov processes where sufficiently distant samples of these processes are independent, or in other words, the system has no memory, or the memory is short-lived compared to the time-scale of interest. fBm's have a memory such that the process's dependence on its distant history is not negligible. A fractional Brownian motion is a process whose signal, denoted  $F(t)$ , that has the following three properties (35-37): 1) the time-lag correlation of the process,

$G(\tau) = \langle (F(t) \cdot F(t + \tau))^2 \rangle / \langle F(t) \rangle^2 - 1$ , decays asymptotically from a constant amplitude as  $G(\tau) \propto \text{Const.} - \tau^\alpha$ ; 2) the variance  $v(t) = \langle (F(t) - F(t + \tau))^2 \rangle$  scales as  $\tau^\alpha$ ; and 3) the fractal dimension of  $F(t)$ ,  $d_f$ , is  $d_f = 2 - \alpha/2$ , which refers to the self-similarity of the signal itself at different time-scales.

fBm's exist in a wide range of phenomenon. Business cycles can be modeled as an fBm since cycles exist of all orders of magnitude (36). H. E. Hurst studied water flows in rivers, including the Nile, and described its statistical properties (38) that led to the study of fBm's and their applications to design of water systems (references in (36)). Other systems having the above three characteristics have been observed in physical systems such as conductance fluctuations of quantum samples in solid-state physics (39-42), and recently Weiss *et al.* searched for these characteristic in the fluorescence signal of diffusing membrane proteins in the Golgi apparatus with some success and suggested that the fBm be attributed to binding (37). In some cases, fBm models have been used to simulate experimental observations of anomalous diffusion in cellular systems, where the precise underlying physical cause of the anomalous diffusion is uncertain, in order to gain insights into how such data should be modeled (15, 37).

Whereas CTRW models consider random walks with a singular distribution of waiting times, and fBm approaches result from considerations of properties of stochastic processes, fractional dynamics approaches consider solutions to deterministic equations

which are then related to how stochastic processes evolve. Theories for fractional dynamics approaches have recently been developed including generalized diffusion theory with non-integer order calculus, i.e. fractional calculus, for the purpose of describing transport dynamics in complex systems where anomalous diffusion appears (43, 44). Whereas the diffusion equation (Equation 1.1.1-11) contains a second-order derivative in space and a first-order derivative in time, the generalized space-time fractional diffusion equation allows the derivative in time to be of order 0 to 1, and the derivative in space to be of order 0 to 2. Such a generalized diffusion equation can be derived from generalized Fick's laws where particle flux is also governed by a fractional derivatives (44). Such a model allows for a non-local relationship in space and time between particle flux and the concentration and leads to various forms of anomalous diffusion (subdiffusion, Lévy flights) depending on the order of the derivatives used.

Having discussed three theoretical approaches for modeling anomalous diffusion which may be considered in abstraction without knowledge of an underlying physical process, we will also discuss two physical models for anomalous diffusion which are biologically relevant: obstruction and binding. For obstructed diffusion, tracers are hindered by the physical presence of obstacles. Where obstacle concentrations are below the percolation threshold, anomalous diffusion is observed over short distances or times, with a cross-over to normal diffusion at large distances or times. As the concentration increases, the anomalous effect becomes stronger over longer distances, while at the percolation threshold the cross-over time becomes infinite (13). Percolation clusters have no characteristic length scale and diffusion in such systems is anomalous at large times. Anomalous diffusion due to this type of obstructed diffusion results in strongly anomalous behavior ( $\alpha = 0.697$  to 1 for 2-D diffusion, and 0.526 to 1 for 3-D diffusion (28, 30) (see Figure 1.1.4-A).

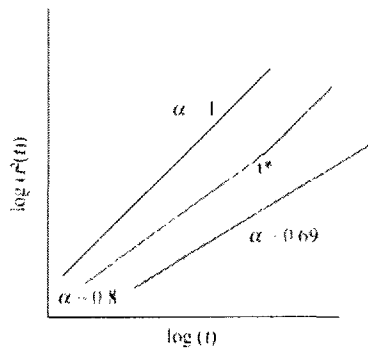


Figure 1.1.4-A. Diagram of mean-square-displacements of particles obstructed by obstacles described in the text: (left to right) Zero obstacle concentration ( $C = 0$ ) gives  $\alpha = 1$ , higher concentration ( $0 < C < C_p$ ) shows anomalous diffusion (e.g.  $\alpha = 0.8$ ) at short time and then crosses-over to normal diffusion at  $t^*$ , and at the percolation limit ( $C = C_p$ ) the diffusion as anomalous at all times ( $\alpha = 0.697$ , for 2-D diffusion). Compare results from simulations in 2-D diffusion with obstacles in reference (13).

A second biologically relevant example of a physical system which produces anomalous diffusion is media where particles can bind to moving or fixed obstacles. Binding models are similar to obstructed diffusion models except that the tracers may stick to the obstacles. When tracers tend to bind to the obstacles, anomalous diffusion may also be observed, depending on the conditions such as concentration, type of binding, and whether the system is at thermal equilibrium (15). It is possible for diffusion to be anomalous at all times given a suitable infinite hierarchy of binding sites, and for finite hierarchies diffusion is anomalous at short times and normal at long times (16). In this case “hierarchy of binding sites” refers to the distribution of the number of traps with the trap depth. Deep traps are present but less common such that long times are required for the system to reach equilibrium, and until the system reaches equilibrium, anomalous diffusion will be observed. This model is of particular interest to biological systems, where particles diffusing in search of a target binding site may encounter a distribution of binding sites with varying similarity to the target, which may result in the anomalous diffusion over the time or length scale of a typical experiment (16).

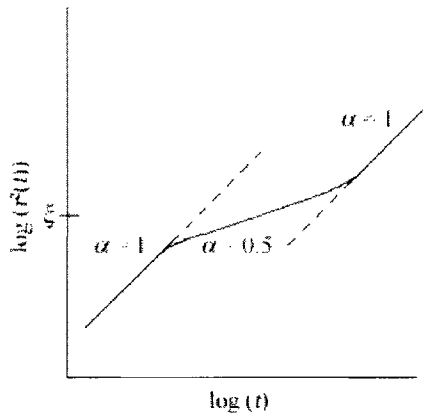


Figure 1.1.4-B. Diagram of mean-square-displacements of particles exhibiting extended cross-over behavior between two regimes where  $\xi$  is the characteristic length-scale of the system.

In most real physical systems, diffusion may be anomalous over a range of length scales associated with the complicating phenomena such as the size of obstacles or passageways. The obstructed diffusion model illustrates the importance of the observation length scale for physical systems where there is a characteristic length scale,  $\xi$ . For particles having an initial distribution localized away from the obstacles, diffusion will be normal for short times, i.e., for  $\langle r^2(t) \rangle \ll \xi^2$ ,  $\langle r^2(t) \rangle = 6D_1t$ . After the particles have had plenty of time to encounter many obstacles, the diffusion is normal again but is slower, and may be modeled as an isotropic media with higher effective viscosity, i.e., for  $\langle r^2(t) \rangle \gg \xi^2$ ,  $\langle r^2(t) \rangle = 6D_2t$ , where  $D_2 < D_1$ . In order to bridge these two

behaviors, there will be a crossover regime where  $\langle r^2(t) \rangle \approx \xi^2$  and  $\langle r^2(t) \rangle \propto t^\alpha$  where  $\alpha < 1$  (see Figure 1.1.4-B). If the initial distribution is random, some of the particles will already be in contact with the obstacles at  $t = 0$ , and therefore the short-time scale regime where diffusion is normal might not be seen. Instead, simulations with tracers and obstacles of the same shape with initial random distribution show that the diffusion is initially anomalous until later time-scales where it becomes normal again (13). On the other hand, simulations in gels show all three regimes, depending on the gel properties and tracer size (22). Experimental systems such as gels, polymer networks and colloidal systems have also been shown to have anomalous regimes with cross-over to normal diffusion at larger times (45-49).

## 1.2. Diffusion in Biological Systems

The nature of diffusion of proteins and other macromolecules in live cells is of great interest to biophysics, and the studies of diffusion presented in this thesis contribute to our knowledge of diffusion in such complex systems. First in this introductory section is a brief discussion of the role and importance of diffusion in cells where the case of diffusion-limited reactions is considered to highlight the importance of intracellular diffusion (§1.2.1). But not only is diffusion of interest by itself, it is also frequently used as a probe to understand the nature of living systems. Therefore we also discuss several examples of insights into living systems which diffusion has brought as well as current efforts to characterize the diffusion itself, with particular attention to reports of anomalous diffusion (§1.2.2). Finally, since the approach taken in this thesis, namely, to study the diffusion in complex *in vitro* systems in order to shed light on corresponding phenomena *in vivo*, has been used by other research groups recently, this section closes by discussing examples of these other experimental studies which demonstrate the need for a more complete understanding of diffusion in complex systems such as are found in cellular environments (§1.2.3).

### 1.2.1 The Role and Importance of Diffusion in Biological Systems

Although some proteins such as kinesin are motor proteins which specialize in actively transporting cargo along intracellular highways composed of microtubules, diffusion is the predominant form of intracellular transport. This fact is not surprising, considering that diffusion is an entropic effect which costs no energy, in contrast to active transport which consumes chemical energy stored in molecules such as ATP which compose a cell's energy currency (6). When a protein must search the entire volume of a cell to find its target, diffusion will be slower than active transport, but in such a case, a cell's small size ensures that a protein can do so in a reasonable amount of time. For example, a protein with a diffusion coefficient,  $D$  equal to  $10 \mu\text{m}^2/\text{s}$  in a cell  $10 \mu\text{m}$  in diameter will on average explore the cell in a time  $t \approx 1.7 \text{ s}$ , i.e.,  $\sqrt{\langle r^2(t) \rangle} = \sqrt{6Dt} \approx 10 \mu\text{m}$ . Once a protein is synthesized, it may rely on diffusion to reach another location in the cell in order to perform its function, and therefore many processes rely on proteins which undergo diffusion (e.g. gene expression, see (50)). Further, it has been shown that diffusion may play a more significant regulatory role in various cellular functions, including functions as important as signal transduction (51, 52), self-assembly of supramolecular structures (53), gene transcription (54), kinetics of reaction (55), embryogenesis (56), or regulation of cell polarization (57).

All of these functions involve diffusion of chemically reacting components, and therefore these systems will be limited by the rate of diffusion. Thus understanding the diffusion of reactants in various cellular environments is a prerequisite to understanding diffusion-limited reactions. A general model for these systems is a set of coupled differential equations with contributions from diffusion and reaction terms. For example a simple two-state reaction with diffusion is described thus:

$$\frac{\partial}{\partial t} C_1(\bar{r}, t) = D_1 \nabla^2 C_1(\bar{r}, t) - k_2 C_1(\bar{r}, t) + k_1 C_2(\bar{r}, t) \quad (1.2.1-1)$$

$$\frac{\partial}{\partial t} C_2(\bar{r}, t) = D_2 \nabla^2 C_2(\bar{r}, t) - k_1 C_2(\bar{r}, t) + k_2 C_1(\bar{r}, t). \quad (1.2.1-2)$$

Here  $\frac{\partial}{\partial t} C_i(\bar{r}, t)$  is the rate of change of the concentration of the  $i$ th species at position  $\bar{r}$  and  $k_1$  and  $k_2$  are rates of conversion to states 1 and 2 respectively, and  $D_1$  and  $D_2$  are the diffusion coefficients. In many cases of reacting systems, it is often convenient to use a mean-field approach in which spatial fluctuations in concentration due to the diffusion are deemed to be negligible. In such cases Smoluchowski's mass action laws are used, and the diffusion terms are dropped while replacing the real rates of conversion with effective reaction rates (58). These mass action laws are based on several assumptions which break down in complex cellular environments, particularly that diffusion rates are constant over all length scales, an assumption underlying Fick's law. For proper analysis of such systems, it is necessary to know the nature of the diffusion. For example, the classical Michaelis–Menten formalism for enzyme reactions does not apply if the diffusion is anomalous, and one simulation study shows that reactions rates can actually

increase due to a decreased probability of reactants escaping each other after collisions (59). A second simulation study shows that the resulting kinetics are dependent on the time scale in a fractal manner and the substrate and the product can segregate spatially, leading to a hypothesis that anomalous diffusion contributes to self-organization in cellular membranes (55). Patterns which spontaneously arise out of systems with diffusing reactants, called Turing patterns, have been studied in detail (60-62). Recently, a theoretical study has demonstrated through numerical calculations that subdiffusion of reactants at low concentrations, i.e., where the effect of number fluctuations cannot be neglected, can produce Turing patterns, and thus suggests that subdiffusion plays a role in cellular phenomena such as cell division and formation of membrane domains such as rafts while the patterns may change over the various stages in the cell's life cycle (61).

### 1.2.2 Observations of Diffusion in Live Cells

As discussed above, diffusion of proteins and other biomacromolecules is important to the functioning of many processes in cells and is therefore worthy of attention. But not only is it of interest by itself, it is also frequently used as a probe to understand the nature of living systems (15, 19, 20, 37, 50, 63-80). Studies which observe protein diffusion in living cells do not separate investigation into the diffusion itself from investigation into the local environment of those proteins. Some studies achieve some separation of these inquiries by observing diffusion in complex *in vitro* systems of known composition and these will be discussed in the next section (§1.2.3). Here in this section we discuss several examples of insights into living systems which diffusion has brought, often through the observation of non-Brownian behavior. This is followed by a discussion of current efforts to characterize the diffusion itself, with particular attention to reports of anomalous diffusion.

First, diffusion yields information about the size and oligomeric state of tracers. According to the Stokes-Einstein equation (Equation 1.1.2-7), diffusion coefficients in water are inversely proportional to the hydrodynamic radius of the tracer. Although the interpretation of the diffusion coefficient to determine the size of cellular particles in a more complex environment is more difficult, current research into the size-dependence of the diffusion of objects embedded in membranes seeks to make these measurements more precise (81). Second, the mean-square-displacement data as a function of time can also be used to calculate linear viscoelastic properties including viscous and elastic shear moduli over a wide frequency range (82). This approach has been applied to determine these characteristics in HeLa, THLE, and HepG2 cells by measuring the anomalous diffusion of gold particles in the nucleus and cytoplasm for which values of  $\alpha$  in the range 0.5-0.7 were found (68).

An exhaustive discussion of the studies of diffusion in cellular environments and the insights contributed by these studies is not possible in the space of this thesis. Instead, a selection of interesting examples is discussed, including a study in which the characteristics of the diffusion were in fact a surprise to the researchers and led to a quite specific insight into the nature of the system. First, we note that characterization of diffusion in membranes is a common tool to probe membrane organization (15, 19, 20, 71-80). For example, Wawrezynieck *et al.* studied the diffusion of lipids in monophasic Giant Unilamellar Vesicles and in the plasma membranes of COS-7 cells (77-79). These studies emphasized the importance of the diffusion law, that is, the dependence of the mean-square-displacement on time, which may have a non-zero intercept as illustrated in Figure 1.2.2-A. More precisely, they looked at the dependence of the characteristic diffusion time,  $\tau_D$ , on the square of the radius of the FCS observation volume,  $w_0^2$  and showed that in these systems  $\tau_D$  may have a non-zero intercept (see §1.4.1, FCS Theory, for the meaning of  $\tau_D$  and  $w_0^2$ ). The time-intercept indicates non-Brownian behavior (compare with Equation 1.1.1-13 which has no intercept). According to the simulations in these studies, diffusion among isolated microdomains results in a positive time-

intercept, and diffusion hindered by a meshwork results in a negative time-intercept (79). In this manner, consideration of the diffusion laws of multiple tracers including lipids, transmembrane proteins, and anchored proteins were characterized to show that both lipid-dependent microdomains and cytoskeleton-mediated meshwork contribute to the compartmentalization of the membrane (77).

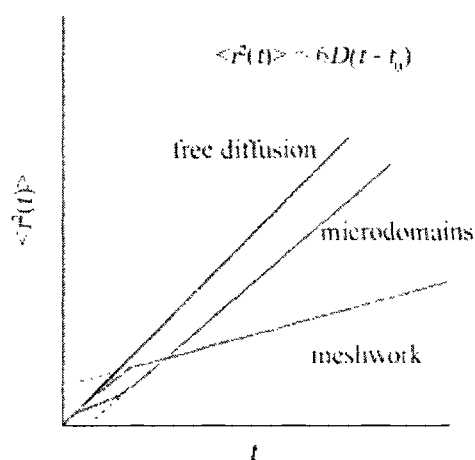


Figure 1.2.2-A. Diagram of the mean-square-displacement as a function of time for free diffusion ( $t_0 = 0$ ), diffusion in microdomains ( $t_0 > 0$ ), and diffusion in a meshwork ( $t_0 < 0$ ). Compare reference (79).

Diffusion of macromolecules outside membranes in cytoplasmic or nucleoplasmic environments has also been studied (37, 50, 63, 65, 67-70). In one study where neuron dendrites were loaded with one species of labeled dextrans, it came as a surprise that the FCS analysis suggested that the labeled species had subdivided in two with greatly different diffusion coefficients (69). Further investigation led to the further development of confined diffusion models for FCS to include the case of anisotropic diffusion. It was found that anisotropic diffusion in the dendrites due to the intradendritic microtubular network could explain this anomaly. Specifically, the orientation of the microtubules parallel to the axis of the dendrite likely causes the anisotropic diffusion, as the network should obstruct transverse diffusion while allowing freer movement for longitudinal diffusion (69).

As an example of insights obtained through the study of diffusion in cytoplasmic environments, Single Particle Tracking experiments have recently shown the diffusion of messenger RNA molecules inside live *E. coli* to be subdiffusive (50). Because the anomalous exponent  $\alpha$  changes little when the cytoskeleton is disrupted, this study suggests that macromolecular crowding plays the major role in anomalous diffusion rather than entanglement in the cytoskeletal network, and proposes that the need for reevaluating diffusion-limited intracellular kinetics may be greater than previously expected. In fact, anomalous diffusion of transcription factors may explain how

transcription factors which are expressed close to the target site may find their targets faster than is predicted based on simple diffusion models (50).

As an example of insights gained through study of diffusion of subcellular organelles, a Single Particle Tracking study of the mobility of Cajal bodies (CBs) characterize the diffusion to determine whether the mobility is active or passive, and to detect interactions between CBs and their local environment (67). CBs are subnuclear organelles located amongst the chromatin in the nucleus in order to assist with various operations on the DNA such as splicing and transcription. This study found that the diffusion of a majority of CBs was limited by some form of a constraint or tether, produced by some factor that is closely associated with the chromatin, and that the CBs associated and dissociated from the tether. In these cases, the diffusion was anomalous at short time scales and normal at longer time scales. The insights gleaned from study of the diffusion of CB's suggested that a function of the CB is to aid assembly and delivery of large macromolecular complexes to active transcription sites.

Now having discussed several examples of insights into living systems which observation of non-Brownian diffusion behavior has brought, we focus on the nature of the diffusion itself and current efforts to characterize it in specific cases. Studies of diffusion of macromolecules *in vivo* frequently show diffusion data which is not easy to explain. Mobility studies in live cells report widely disparate data: the diffusion coefficients of macromolecules in cells are found to lie anywhere between 0 and 80% of their value in aqueous solution (65, 83-90) reflecting the fact that the observed reduction in mobility depends on many variables. A tracer's mobility depends not only on which cell type (89), or on which cell (85), but on which position inside the cell (65) is selected for the study. The relative mobility of a tracer in a cell compared to an aqueous solution has been shown to decrease with increasing size of the diffusing particles (70, 84, 87). The propensity of a protein to interact with other cytoplasmic macromolecules will also affect the mobility (91). Also, results may depend on the technique used (89). In one of the few Single Particle Tracking studies where tracer proteins were tracked in the nucleoplasm and cytoplasm, the mean-square-displacement could not be observed over multiple orders of magnitude of time, but apparent diffusion coefficients could be determined at the observation time-scale. The results showed that the distribution of diffusion coefficients was too broad to correspond to a simple viscous fluid (18), suggesting that some form of non-Brownian diffusion was present.

Some of the complexity of the diffusion behavior in live cells and modeling it properly comes from geometrical constraints which may be unknown to the observer. For example, the presence of a membrane which constrains the diffusion will alter the behavior of the diffusion. The case where confining membranes, which are fixed in shape, bound the volume has been described such that if the geometry of the bounding membranes are known, the FCS diffusion times can be interpreted correctly (92). For the case where a soft fluctuating membrane is present in or near the observation volume, it has been shown through an *in vitro* study that FCS data may appear anomalous but the

diffusion time is misinterpreted by the usual model for anomalous diffusion (93). Monte Carlo simulations of diffusion measured by FRAP experiments where the geometrical constraints resembled specific organelle structures (a long closed cylinder containing fixed obstacles for a mitochondria, and a network of interconnected cylinders for an endoplasmic reticulum) show that the apparent diffusion coefficients do depend on the specific geometry, and the diffusion may appear anomalous due to the geometry (17).

Geometrical considerations are not enough to explain all the observations in live cells. The existence of anomalous diffusion in these systems where the diffusion coefficient is length scale-dependent due to a wide-range of physical obstruction, may explain some of the disparate data. Indeed, there have been several reports of anomalous diffusion of proteins (or complexes of proteins) observed unambiguously in membranes through particle tracking methods: lipoprotein receptor in human skin fibroblasts,  $\alpha = 0.2 - 0.9$  (94, 95), IgE receptor Fc $\epsilon$ RI in rat basophilic leukemia cells (96), gold-labeled Thy-1 in fibroblasts,  $\alpha = 0.42 - 0.58$  (97), neural cell adhesion molecules (NCAM-180) in 3T3 cells,  $\alpha = 0.51$  and  $\alpha = 0.29$  (98), and the class I major histocompatibility complex in HeLa cells,  $\alpha = 0.49$  (99). Single particle tracking has the advantage of observing the mean-square-displacement directly without a model-dependence. Studies using Fluorescence Recovery After Photobleaching (FRAP) (66) and Fluorescence Correlation Spectroscopy (FCS) (73, 100) have also reported anomalous diffusion of proteins in membranes in live cells.

For 3-D diffusion in the cytoplasmic environments such as the cytoplasm, nucleoplasm, and subcellular organelles, diffusion is faster and much more difficult to characterize through particle tracking methods, but however a few such studies have been done using particle tracking (50, 101), FCS (63, 65, 68), FRAP (102), and pulse-field gradient spin-echo 1H NMR (103). Some of these studies (50, 63, 65, 68, 101) report anomalous diffusion and suggest that macro-molecular crowding is a significant factor in the anomalous diffusion observed: lipid granules in SV80 cell cytoplasm,  $\alpha \approx 0.75$  (101), mRNA molecules in *E. coli* cytoplasm  $\alpha \approx 0.7$  (50), labeled dextrans,  $\alpha = 0.59 - 0.84$ , and FITC-labeled IgG antibody  $\alpha \approx 0.55$  in the cytoplasm of HeLa cells in interphase (63), EGFP,  $\alpha = 0.7 - 1$ , and EGFP-b-galactosidase fusion protein,  $\alpha = 0.63 - 1$ , in the cytoplasm and nucleus in AT-1 and COS-7 cells (65), fluorescently tagged gold beads in the cytoplasm and nucleus of HeLa, THLE, and HepG2 cells,  $\alpha = 0.48 - 0.69$ , depending on osmotic pressure. To test whether crowding by the macromolecules in environments such as the cytoplasm and nucleus contributes to complex diffusion behavior, one group used *in vivo* FRAP measurements to measure the diffusion of green fluorescent protein in *E. coli* and to directly study the effect of the volume fraction of macromolecules by adjusting the osmotic pressure of the buffer (102). While this study did not allow for the possibility of anomalous diffusion in its data analysis, the authors concluded that simple diffusion models are not sufficient to explain either the diffusion coefficients measured or the dispersion in the measurements taken in different cells, but they were not able to distinguish between possible causes such as binding, crowding or confinement.

### 1.2.3 Complex *In Vitro* Systems as a Model for Cellular Diffusion

Given the complexity and highly heterogeneous composition of cellular environments, it is advisable to isolate causes for various diffusive behaviors by studying controlled *in vitro* systems. The effects of various factors, such as macromolecular crowding, binding, trapping in polymer networks, or the composition of membrane domains, can then be studied separately and compared to *in vivo* studies to shed light on the corresponding phenomena in live cells. One focus of the research in this thesis is to understand diffusion in controlled *in vitro* systems, such as the diffusion of proteins in polymer solutions or of beads in agarose gels. Therefore in this section, a brief discussion of diffusion in model membranes, polymer networks and crowded solutions which aid our understanding of cellular diffusion is presented.

One focus of current research is to characterize the diffusion of lipids, proteins and protein complexes in membranes to understand the structural composition of and transport processes in membranes. Biomembranes are complex environments with transmembrane proteins, receptor complexes, lipid rafts and domains. Therefore they are often replaced by simpler systems for *in vitro* study such as two-phase artificial membranes as well as for simulations (12, 15, 19, 20, 55, 72, 73, 75, 76, 104-107). Observations of transport in the membranes of live cells show different types of motion including normal diffusion, anomalous diffusion, directed flow with diffusion, and corralled motion. How to relate these observations to various models for membrane structure is not well understood (75, 105). But we do know that the type of motion depends on the geometry of the system and obstacles such as coexisting domains. Hac *et al.* point out that with coexisting fluid and gel domains in an artificial membrane, the diffusion will be dependent on whether the concentration of gel domains (which can be considered obstacles in some cases) has reached the percolation threshold, and since the size and shape of the domains fluctuate, the time-scale of the diffusion will also fluctuate (19). This may explain in part the wide range of time-scales for diffusion reported in the literature in such systems. It has been suggested that experimental observations where the fluorescence recovery after photobleaching due to diffusion in the liquid phase is slow or incomplete (71, 76, 108) may be explained by percolating gel domains (108). Indeed, a Monte Carlo simulation study where membranes were modeled as self-similar percolating clusters has successfully showed that the anomalous diffusion which results from obstruction is consistent with this hypothesis (15).

The study of diffusion in polymer networks *in vitro* has been shown to be quite relevant to corresponding networks *in vivo*. The cytoskeleton is largely composed of networks of filamentous actin (*F*-actin) and microtubules. Particle tracking of beads attached to microtubules shows that at short times the motion of the point under observation follows a subdiffusive power law where the mean-square-displacement of the filament scales as  $t^{3/4}$  before reaching a limit determined by the finite length of the filament, a result which matches the theoretical description (109). Likewise, it was shown both experimentally in *F*-actin networks, and in theory, that the mean-square-displacement of beads also scales

as  $t^{3/4}$  when the beads are not attached to the filaments but are appropriately sized to be caged by the network such that the diffusion of the beads are dominated by the thermal motions of the filaments (47). The same observation was made in a recent study of the diffusion of microspheres in collagen, in which an average value of  $\alpha = 0.78$  was recently reported (110). Measurements showing that force is required to twist beads in cytoplasmic networks suggest that strong coupling of the beads to the filaments is a realistic hypothesis for comparison to cellular observations, see for example (111). These *in vitro* observations are helpful in explaining the anomalous diffusion of beads observed by particle tracking in cytoskeletons *in vivo* (101). In this case, there is superdiffusion at short times,  $\langle r^2(t) \rangle \sim t^\alpha$ , where  $\alpha \approx 3/2$ . The superdiffusion is explained by the effect of motor proteins. At longer times, the motion is subdiffusive where  $0.5 < \alpha < 1$ , which is explained by the coupling to the thermal motions of the filaments.

As discussed previously (§1.2.2), some *in vivo* studies suggest that macromolecular crowding plays a significant role in anomalous diffusion observed in cell cytoplasm (50, 63, 65, 68, 101, 103), while others show that it is not the exclusive cause (102). In order to understand the contribution of macromolecular crowding to *in vivo* diffusion, many studies have used crowded *in vitro* solutions as models for nucleoplasmic and cytoplasmic environments (103, 112-117). Of these, DNA solutions are compared to the nucleoplasmic environment (115, 116), while sol-gels (113), dextran solutions (113), Ficoll-70 solutions (114) and cell extracts are compared to the cytoplasm (117). Most *in vitro* studies confirm that macromolecular crowding is a crucial factor in determining a particle's mobility, but few such studies have investigated the possibility that the diffusion coefficient of proteins in crowded solutions may be length-scale dependent, that is, whether the diffusion of proteins may be anomalous only due to crowding in solution. Therefore research presented in this thesis includes two papers which first have sought to determine whether the anomalous diffusion model applies to the diffusion of proteins in crowded dextran solutions observed by FCS (§2.2.1), and then to observation it directly by modifying conventional FCS to achieve varying observation length scales (§2.2.2). As is discussed in the summaries of this research and in the manuscripts, we successfully reproduce anomalous diffusion reported in various cellular systems which demonstrates that macromolecular crowding is indeed a significant factor in contributing to the anomalous diffusion observed in the cell cytoplasm and nucleus. Further, we demonstrate that we can observe the length-scale dependence of the correlation data which cannot be explained by normal diffusion. We suggest that a cross-over interpretation of the length-scale dependence of the diffusion is possible, and this explanation may be applied to some of the observations of anomalous diffusion *in vivo* where the cross-over regime could be quite broad.

### **1.3. Fluorescence and Photophysics**

Fluorescence combined with modern technologies for the manipulation of light and precise time and space resolution for collection of fluorescence has provided many useful techniques for the study of biological systems (118-120) including Fluorescence Correlation Spectroscopy (FCS) (121-125), Fluorescence Intensity Distribution Analysis (126-128), Fluorescence Recovery After Photobleaching (129-131), Fluorescence Lifetime Imaging Microscopy (121, 122, 132), Fluorescence Microscopy (133-138), Fluorescence Resonance Energy Transfer Imaging Microscopy (132, 139), Single Particle Tracking (129, 140, 141), and Single Molecule High Resolution Imaging Microscopy with Photobleaching (142). Fluorescence experimental methods are widely used by biochemists and biophysicists to study a wide range of biological phenomena, from small-scale processes such as the rates of conformational changes of single RNA molecules (143) to whole-cell distributions of the locations of protein complexes (144). Fluorescence methods are well established (FCS was developed in the 1970's) while improvements and variations on existing methods are still being published (79, 145-151). Fluorescence methods have the advantage of allowing the separation of the fluorescence signal from the excitation leading to very high signal-to-noise ratios, making single molecule studies possible. Modern technological developments in optics including improved laser sources, fluorescence probes, and automation of processes such as confocal imaging in commercial instruments have made fluorescence methods a mature technology such that these techniques can now be used by biologists and biochemists even without advanced knowledge of the physics and technology involved. Significantly, the discovery and development of fluorescent proteins which can be expressed by cells without greatly perturbing the system has greatly increased the ease and appeal of performing fluorescence-based experiments on live cells. Due to the fundamental importance to the understanding of fluorescence methods, a brief description of fluorescence is presented here with particular attention to aspects relevant to FCS.

### 1.3.1 Quantum Mechanical Basis of Fluorescence

Fluorescence is defined as “the emission of photons by atoms or molecules whose electrons are transiently stimulated to a higher excitation state by radiant energy from an outside source” (152). When a large molecule is labeled with a dye or naturally contains a chemical subunit that fluoresces, the chemical moiety responsible for the fluorescence is called the fluorophore (152).

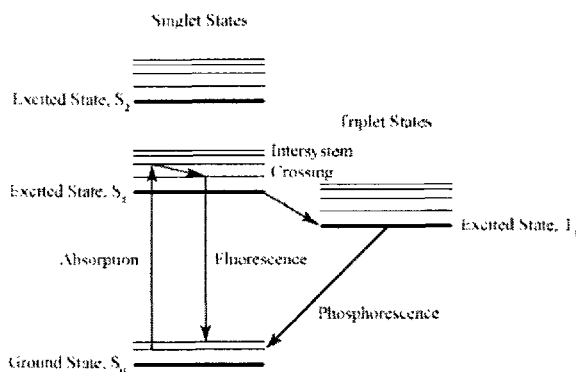


Figure 1.3.1-A. A Jablonski diagram illustrating the energy levels of a fluorophore in order of increasing energy from bottom to top. The arrows indicate transitions between energy states.

The concept of fluorescence may be illustrated using a Jablonski diagram which shows energy levels and sublevels of a fluorophore in order of increasing energy from bottom to top (see Figure 1.3.1-A). The arrows indicate possible transitions between energy states of an electron in the fluorophore. The fluorescence cycle involves the absorption of an excitation photon and emission of a lower energy fluorescence photon. For example in a typical fluorophore, an electron in the ground state,  $S_0$ , absorbs a photon that excites it to the first excited state,  $S_1$ . More precisely, the ground state and excited state  $S_1$  may consist of several states closer in energy. Some energy of the electron in the excited state can be converted into other forms (for example, vibrational modes of the fluorophore), while leaving the electron in the first excited state, but in a lower sub-level. Then finally the electron relaxes back to a sublevel in the ground state, emitting a fluorescence photon of lower energy than the absorption photon. Since fluorescence is a function of the interaction of light with matter via discrete energy levels, fluorescence is clearly a quantum mechanical phenomenon.

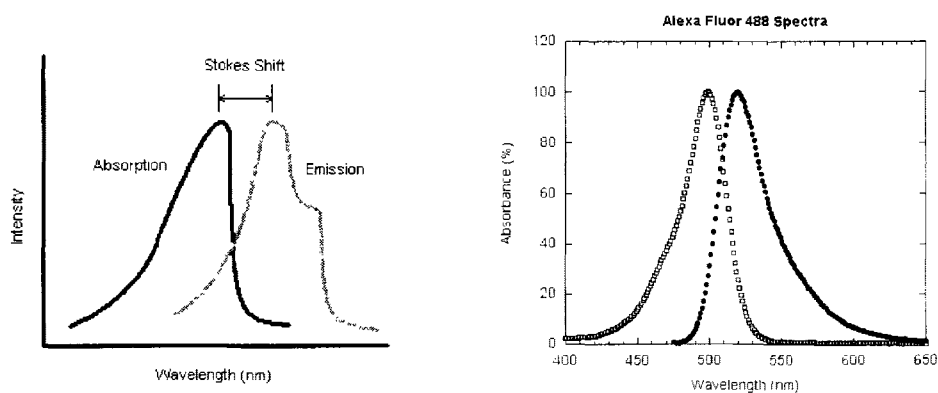


Figure 1.3.1-B. *Left panel:* Schematic of typical absorption (*black*) and emission (*gray*) spectra of a fluorescent dye showing the Stokes shift between the absorption peak and the emission peak. *Right panel:* Absorption (*open symbols*) and emission (*closed symbols*) spectra of Alexa Fluor 488 goat anti–mouse IgG antibody in pH 8.0 buffer. The data are provided by Invitrogen <http://probes.invitrogen.com/servlets/spectra?fileid=11001ph8> and are normalized to show the spectral similarity.

The difference in energy corresponds to a difference in wavelength, since the energy of a photon is  $E = hc / \lambda$ , where  $h$  is Planck’s constant,  $c$  is the speed of light in a vacuum, and  $\lambda$  is the wavelength of the photon. The difference in wavelength between the excitation photon and the fluorescence photon is called the “Stokes shift,” named after the Irish physicist George G. Stokes. The Stokes shift may range from a few nanometers to several hundred. A typical dye such as fluorescein has a Stokes shift of about 20 nm which is sufficient for modern dichroic mirrors and band-pass filters to easily distinguish emission photons from excitation photons.

If there were a single pathway for excitation and fluorescence emission where the energy levels were entirely discrete, we would expect there to be a single fluorescence wavelength for a single absorption wavelength. Instead, there is a spectrum of absorption and a spectrum of emission for every fluorophore (see Figure 1.3.1-B). The excitation-emission cycle is not a single pathway due to the existence of many energy sub-levels due, for example, to the existence of small differences between vibration states of the fluorophore. Each energy sub-level will vary in lifetime, and before the electron returns to the ground state, some energy may be converted from vibrational energy to forms other than radiation. These factors result in a range of fluorescence emission around a peak value. The Stokes shift is then determined by the difference between the peak absorption wavelength and the peak emission wavelength.

### 1.3.2. Photophysics of Intersystem Crossing (“Triplet-Singlet” Transitions)

In addition to fluorescence decay, there are other decay pathways including internal conversion, where the energy is released as heat instead of a photon, and intersystem crossing, where a transition (forbidden by first-order quantum selection rules) occurs from a singlet excited state to a triplet excited state (see Figure 1.3.1-A). The triplet state is long-lived (often  $\sim 1-10 \mu\text{s}$ ) compared to typical fluorescence lifetimes (often  $\sim 1-10 \text{ ns}$ ). Any photons emitted in the decay from the triplet state are typically lower in energy than the fluorescence photons and eliminated through the use of emission filters. Therefore the triplet state typically appears completely dark to the experimentalist. Once the photon returns to the ground state, the molecule can begin the fluorescence cycle anew, and therefore fluorescent molecules which were “off” while in the triplet state will again be “on” for a period of time before returning to the triplet state. This cycle results in “triplet state blinking” where the excited fluorophore does not give a constant fluorescent signal, but flickers instead.

For many imaging applications, the flickering is too fast to have a significant effect on the experiment. To an experimentalist using Fluorescence Correlation Spectroscopy (FCS), this blinking of fluorophores due to intersystem crossing is both an observable phenomena sometimes of interest and a complication sometimes of annoyance. Under typical FCS conditions, fluorescent dyes often have 5-30% or more of the fluorophores in the illumination volume in the “off” state at any given time, while the fluorophore cycles between the on and off states with an average time of a few microseconds. The effect of triplet state blinking is frequently observed by FCS as a major component of the correlation data on the microsecond time scale (see §1.4 for FCS theory and experimental description), which makes it difficult to observe phenomena which create correlations at the same time scale. On the other hand, FCS is an excellent tool to study the kinetics of intersystem crossing itself under various conditions (153, 154). Since the process is entirely reversible, the triplet-singlet transition may be modeled as a simple two-state unimolecular isomerization reaction (see FCS theory, §1.4.1, Equation 1.4.1-35). The kinetics of intersystem crossing are sensitive to the local environment of the molecule and to the photon flux of excitation light. Factors that contribute to the chemical environment such as solvent polarity, viscosity, and presence of quenching agents (oxygen, potassium iodide), which are known to influence the kinetics of fluorescence overall, also have effects on the kinetics of singlet-triplet transitions (154).

### 1.3.3. Photophysics of Photobleaching

Photobleaching is a process whereby fluorophores lose their ability to fluoresce. It affects all known fluorophores with the possible exception of quantum dots. Photobleaching is a complex process that does not follow a unified mechanism and it is not entirely understood (146, 155-159). A common photobleaching pathway involves first a transition to the first triplet state which is much more reactive than the singlet ground state, and much more likely to react than the singlet excited state because the singlet excited state is very short-lived. Molecular oxygen,  $O_2$ , is a common reactive agent that may react with a fluorophore in the excited triplet state, thereby destroying its ability to fluoresce and creating a free radical singlet oxygen molecule that can further damage molecules in the sample. In contrast to the foregoing and as an example of the complicated behavior of photobleaching, it has been reported that the triplet state is not a major factor in the photobleaching observed when using two-photon excitation where the fluorophore is excited by two photons, rather than one, each having half of the excitation energy (158). Further, studies on rhodamine dye (Rh6G) suggest that for excitation laser intensities commonly used ( $>1 \text{ kW/cm}^2$ ), models which allow for photobleaching from higher excited state populations are required to explain the observations (157, 159).

Fluorescence methods rely on collected high numbers of fluorescence photons from a sample. But the longer one illuminates a fluorophore endeavoring to increase the collected fluorescence photons, the more chance that it will photobleach. Similarly, one cannot have an arbitrarily high excitation intensity due to photobleaching. Both the excitation intensity and how long fluorophores are illuminated are key parameters. Slowly diffusing particles will absorb more photons than faster particles during one passage through the observation volume. Therefore photobleaching becomes a more severe problem as the speed of the tracer decreases or if the tracer is immobilized. The effects of photobleaching on an experiment are also determined by the number of particles in the sample. In a small volume such as a cell where the number of copies of a tracer may be quite limited, photobleaching often places stringent limits on the observations which may be conducted from a single cell. Further, even when the observation volume is a part of an open bath of fluorophores, photobleaching is often a serious problem. For particle tracking methods, photobleaching of the fluorophore limits the length of time each particle can be tracked. In FCS, the diffusion coefficient is measured from the amount of time particles spend in the observation volume. Because a tracer is no longer detected when it photobleaches, a bleached tracer appears to have left the observation volume, thus creating an apparent reduction in the time spent in the volume and causing the diffusion coefficient to be overestimated.

Often the best means of preventing photobleaching is to reduce the excitation intensity to low levels where photobleaching is infrequent, but this is done at the cost of lowering the fluorescence signal itself. Some other methods to prevent photobleaching involve replacement of oxygen with nitrogen or oxygen scavengers (158) or fast scanning of the

excitation beam (in the case of techniques that use a focus laser such as confocal microscopy and FCS) (146).

### 1.3.4. Fluorescent Proteins and Photophysics of Fluorescent Proteins

Fluorescent proteins are biological sources of fluorescence. Fluorescent proteins are of great interest to biochemists and biophysicists because cells can be manipulated to express them as a tag on a protein of interest without any need for traumatic approaches such as microinjection of foreign molecules (160, 161). The most commonly used fluorescent protein, green fluorescent protein (GFP), was discovered in 1962 when it was extracted from bioluminescent cells from the jellyfish *Aequorea victoria* and was first functionally expressed in bacteria in 1994 (161). The x-ray diffraction crystal structure was published in 1996 (162) and is shown in Figure 1.3.4-A.

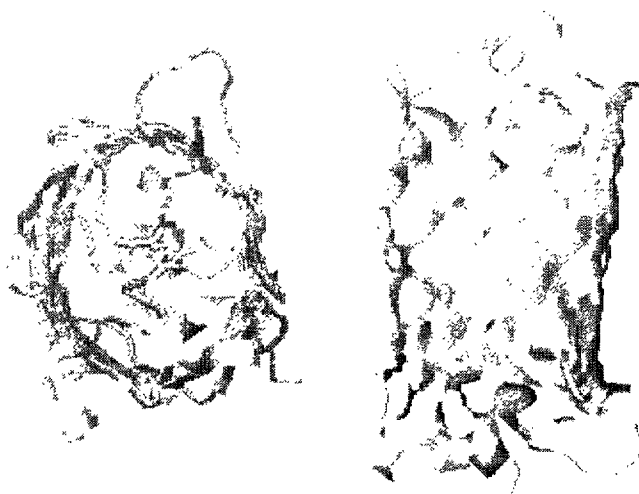


Figure 1.3.4-A. End-on (*left*) and side-on (*right*) views of a cartoon ribbon diagram of the structure of green fluorescent protein (Protein Data Bank Entry 1GFL).

GFP contains a fluorophore composed of a few amino acids in a central  $\alpha$ -helix which is surrounded by a cylindrical  $\beta$ -sheet structure. The  $\beta$ -sheet acts as a protective shield around the fluorophore which is located in the central  $\alpha$ -helix within angstroms of the center of the cylinder. The fluorophore is formed by three amino acids (Ser-Tyr-Gly) which are post-translationally modified to a fluorescent 4-(*p*-hydroxybenzylidene)-imidazolidin-5-one structure (161). The protective outer layer is a likely cause for GFP's resistance to quenching by molecular oxygen. Many variations of GFP, including enhanced green fluorescent protein (the most commonly used variant) have been derived by modifying amino acids in the vicinity of the fluorophore or on the outer surface of the protein which alter the absorption and emission spectra, quantum yield of fluorescence, photostability, time to maturation, dimerization properties and many other properties (163). Attempts to vary GFP have not resulted in a red fluorescent protein suitable for use as a protein-tag, however, several monomeric red fluorescent proteins have been developed from a red fluorescent protein (DsRed) cloned from *Discosoma* coral which existed only in tetrameric form in nature (164, 165). These proteins have a variety of emission colors to suit one's taste, as illustrated by their fruity names: honeydew, banana,

orange, tomato, tangerine, strawberry, and cherry. Many other fluorescent proteins derived from a variety of different organisms are currently being investigated, and are likely to add to the selection of fluorophores for genetic encoding in the near future.

Fluorescent proteins are known to have photophysical properties that few other commonly used fluorophores have. For example, FCS measurements on wild-type Green Fluorescent Protein (wtGFP) show the existence of five photophysical effects (166) due to rotational diffusion, conformational fluctuations, triplet state kinetics, and two photoinduced isomerization reactions. The probability of a fluorophore to absorb an excitation photon and emit fluorescence depends on the orientation of its electric dipole moment with respect to the optical axis and polarization of the excitation beam (specifically, the absorption is minimized when the dipole is parallel to the optical axis) (166). Therefore the specific brightness of the fluorophore changes over time as the fluorophore rotates. For small molecules such as fluorescein dye, the rate of rotational diffusion is too fast for changes in specific brightness to be observable through typical fluorescence experimental methods, including FCS. Similarly, the change in specific brightness is not observable for many larger molecules labeled with dyes because of the relative orientation of multiple labeling or the ability of the label to fluctuate in orientation independently of the rest of the molecule. But since the change in specific brightness of the fluorophore of GFP is observable on a 20 ns time-scale, we can deduce that the fluorophore is fixed in orientation with respect to the rest of the molecule (166).

The photoinduced isomerization effects observed in wtGFP are consistent with a photo-induced transition from a fluorescent state to a non-fluorescent state and a photo-induced back-transition to the fluorescent state similar to that reported for cyanine dyes (167). A *cis-trans* isomerization is a 180° rotation about a double bond where two chemical moieties are aligned adjacent (*cis*) or opposite (*trans*) to each other (168). In the case of cyanine, the *trans* state is much more fluorescent than *cis* state, giving rise to fluorescent blinking of the fluorophore in a manner similar to the blinking effect of intersystem crossing (singlet-triplet transitions, §1.3.2). But while cyanine dyes exhibit only one such isomerization process, wtGFP apparently has two such processes which contribute to fluorescent blinking. Including the above mentioned conformational fluctuations, the nature of which is unknown, wtGFP has then four such blinking processes in total, only one of which is common to most fluorophores, that is, intersystem crossing. These blinking processes occur in the microsecond to low-millisecond time ranges (166).

The most commonly used fluorescent protein is enhanced green fluorescent protein (EGFP). It contains several performance enhancing mutations which make it brighter and more photostable than wtGFP. EGFP has been observed to have three blinking states (169). In addition to the triplet state observable at high excitation intensities, EGFP exhibits a pH-dependent blinking term and a pH-independent blinking term. The characteristic decay time of the pH-dependent term decreases from 300  $\mu$ s to 45  $\mu$ s from pH 7 to pH 5, while the fraction of molecules in the nonfluorescent state may reach as high as 80% at pH 5. The pH-dependent correlation is attributed to a reversible

protonation-deprotonation reaction with protons in the buffer. EGFP's absorption peak at approximately 490 nm is greatly reduced by lowering the pH due to the high fraction of protonated EGFP molecules with altered energy levels. This protonation-deprotonation reaction is also sensitive to temperature. This sensitivity is most apparent at pH 5 and is reflected in changes in the relaxation time and amplitude of the corresponding correlation term. This sensitivity is the basis for the molecular thermometer proposed in this thesis (§2.2.3, §2.3.2). The pH-independent term was reported at 340  $\mu\text{s}$  with a fraction of 13% nonfluorescent molecules. The mechanism for this term is unknown, but may be associated with a similar protonation process with an internal proton rather than one from the buffer.

Other unusual behaviors have been reported in other variations of GFP and fluorescent protein not related to GFP. First, the yellow fluorescent protein (YFP) shows a protonation-deprotonation interaction with the protons in the buffer similar to EGFP, but also exhibits a photo-induced blinking process whose characteristic time varies from  $\sim 10 - 100 \mu\text{s}$ , according to one FCS study which suggested that the blinking is due to a reversible transition between two molecular states which are only coupled through the excited state of the fluorophore (170). Second, other GFP-variants proteins have been designed to optimize the sensitivity of the fluorescent blinking due to the protonation-deprotonation reaction on the pH of the buffer, thereby acting as pH sensors. For this purpose, Ecliptic GFP and Ratiometric GFP show a greater pH sensitivity and suitability at physiological pH than EGFP (171). Third, there is also a class of fluorescent proteins including a number of GFP-variants which are photoactivatable (172), that is, they can be "turned on" by illumination with violet or ultraviolet light, resulting in a change in photophysical properties that greatly increases fluorescence (70-fold for PA-mRFP1). One such mechanism for the photoactivation is due to structural changes in the fluorophore where the chromophore transitions from a nonfluorescent *trans*-state to a fluorescent stable *cis*-state (172).

In conclusion, fluorescent proteins often exhibit photophysical behaviors which are less frequently seen in common dyes used for fluorescent experimental methods including FCS. Since these photophysical behaviors are often sensitive to various effects such as pH and temperature, observing the corresponding correlations via FCS is a useful probe of the local environment of the protein. On the other hand, when these proteins are used as *in vivo* protein tags to study other phenomena, the extra blinking behaviors represent extra complications which must be modeled correctly to interpret the FCS data. Such behaviors also represent complications for other techniques such as quantitative imaging where fluorescence brightness is altered by excitation intensity-dependent or pH-dependent blinking. A redeeming factor for the value of these proteins for *in vivo* FCS studies is that the analysis is eased by the fact that much of the photophysics of fluorescent proteins reported in the literature is on timescales much faster than the diffusion of protein in cellular media.

#### **1.4. Fluorescence Correlation Spectroscopy and Other Fluorescence Experimental Methods**

The studies presented in this thesis used Fluorescence Correlation Spectroscopy (FCS) to investigate diffusion and photophysical phenomena. Therefore detailed background material concerning this method is presented here, both theoretical (§1.4.1) and experimental (§1.4.2). The studies of diffusion are aimed at understanding diffusive phenomena that occur in cells in order to provide insights into related biological functions. Many studies of diffusion in cellular or model systems have been discussed previously (§1.3) to provide context for this thesis. Many of those experiments employed Particle Tracking methods or Fluorescence Recovery After Photobleaching to observe diffusion. Each of those methods have advantages and limitations on their ability to contribute to understanding diffusion in the cellular environment. Therefore, a brief description of each of those methods has been included here as well, with attention to those advantages and limitations (§1.4.3).

### 1.4.1. Fluorescence Correlation Spectroscopy Theory

Fluorescence Correlation Spectroscopy (FCS) is an experimental method based on temporal analysis of fluctuations in a fluorescence signal. FCS was invented by Douglas Magde, Elliot Elson, and Watt W. Webb in the early 1970's to study chemical reaction rates and translational diffusion coefficients (173-175). In theory, FCS can be used to observe the kinetics of any phenomenon that creates characteristic fluctuations about equilibrium in a measurable fluorescence signal. FCS can determine reaction rates not just when the reaction changes fluorescence intensity, but also when the diffusion coefficients of the fluorescent reactant and product are significantly different (176). Perhaps the most common usage of FCS is to characterize translational diffusion (37, 69, 73, 79, 92, 124, 129, 147, 149, 177-184). FCS is also used to observe concentration (185), rotational diffusion (186), active transport (187, 188), rates of conformational changes (143, 189-191), and various photophysical phenomena such as intersystem crossing between singlet and triplet states (153, 154), electron transfer quenching (192), light-induced blinking (170), photoisomerization (166, 167), and photobleaching (156).

The crux of FCS is to determine the time-lag correlation of fluorescence signals both experimentally and theoretically. The correlation of one signal with itself is called the autocorrelation, while the correlation between two signals is called a crosscorrelation. Experimentally, the time-lag correlation of the fluorescence signal is calculated using a correlator card which is a hardware component specialized to perform the calculation quickly using large amounts of fluorescence data. Correlator technology is sufficiently advanced that the average experimentalist may perform FCS without knowledge of the technical details of how the correlator card calculates the correlation data, although there are some pitfalls to avoid. For example, when measuring oscillatory signals with a multi-tau correlator, the oscillation in the correlation data will appear damped at large lag times (193).

However, the theoretical basis of FCS is of great significance to the experimentalist. The correlation data may be useless until it is fit to an appropriate model. Even in the simple case of a single species of fluorescent dye diffusing in the sample, the form of the correct model depends on the geometry of the observation volume and the presence of correlated photophysics of the dye. The most common form of FCS uses a confocal microscope resulting in a 3-D Gaussian observation volume. Other geometries occur with variations of FCS such as the dual observation volume method (194), multi-photon excitation methods (100, 118, 124), or Total Internal Reflection Fluorescence Microscopy (195-198). The model has to be adjusted whenever there are additional complications such as whether the diffusion has multiple interacting or non-interacting components, or has non-Brownian behavior; whether the correlation of interest is a cross-correlation between different fluorescence signals; or whether there are experimentally-induced correlations due, for example, to a scanning excitation beam.

*Definition of the Autocorrelation Function for Fluorescence Signals*

To denote the fluctuations in a quantity  $x$  about its average value  $\langle x \rangle$ , we used the symbol  $\delta$  where  $\delta x = x - \langle x \rangle$ . The autocorrelation function,  $G(\tau)$ , is defined in terms of the fluorescence fluctuations, thus:

$$G(\tau) \equiv \frac{\langle \delta F(t) \delta F(t + \tau) \rangle}{\langle F \rangle^2}. \quad (1.4.1-1)$$

$F(t)$  is the fluorescence signal at time  $t$ ,  $\delta F(t)$  is the fluctuation in  $F(t)$  at time  $t$ , and the angle brackets  $\langle \rangle$  may denote either a time average or a thermodynamic average for ergodic samples. Both ergodicity and stationarity, in the context of FCS imply that the autocorrelation function should converge to a stable form with a long enough collection time, and that form does not depend on the time at which the measurement is recorded. Thus, to simplify the expression some authors set  $t = 0$  and write the definition thus:

$$G(\tau) = \frac{\langle \delta F(\tau) \delta F(0) \rangle}{\langle F \rangle^2}. \quad (1.4.1-2)$$

Using the relationship  $F(t) = \langle F \rangle + \delta F(t)$ , and noting that  $\langle \delta F \rangle = 0$ , one may also express the correlation function in terms of  $F(t)$ :

$$G(\tau) = \frac{\langle F(t) F(t + \tau) \rangle}{\langle F \rangle^2} - 1. \quad (1.4.1-3)$$

An alternative correlation function may be defined thus:

$$G(\tau) = \frac{\langle F(t) F(t + \tau) \rangle}{\langle F \rangle^2}. \quad (1.4.1-4)$$

Equation 1.4.1-1 is the correlation in the fluctuations of the fluorescence signal, in contrast to Equation 1.4.1-4, which is the correlation in the fluorescence signal itself. These functions differ only by the fact that the correlation in the fluorescence fluctuations decays to 0 as  $t$  approaches infinity, while the correlation in the fluorescence signal approaches 1 instead. In this thesis, Equation 1.4.1-1 will be used as the definition of the correlation function rather than Equation 1.4.1-4.

For typical FCS conditions,  $F(t)$  is determined by  $C(\bar{r}, t)$ , the number density, i.e. concentration, of the particles at time  $t$  and at position  $\bar{r}$  relative to the center of the observation volume, by the spatial excitation intensity profile,  $I(\bar{r})$ , the spatial extent of the sample, and the spatial extent over which fluorescence is measured, as well as factors affecting the specific brightness of the fluorophore such as absorption cross-section at the excitation wavelength, quantum efficiency of the fluorophore, and fluorescence collection efficiency of the experimental apparatus. This thesis will only discuss the case with samples much larger than the extent of the optical transfer function,  $S(\bar{r})$ , which describes

the spatial collection efficiency of the confocal optics through the objective and pinhole. In summary, we may write:

$$F(t) = \sum_{i=1}^n \int Q_i(t) \cdot C_i(\bar{r}, t) \cdot I(\bar{r}) \cdot S(\bar{r}) dV. \quad (1.4.1-5)$$

where there are  $n$  fluorescent species,  $Q_i(t)$  is the proportionality constant which accounts for the specific brightness of the  $i$ th species, and  $C_i(\bar{r}, t)$  is the number density for the  $i$ th species. The function  $w(\bar{r})$  accounts for the excitation profile  $I(\bar{r})$  and the optical transfer function  $S(\bar{r})$  and is defined as

$$w(\bar{r}) \equiv I(\bar{r})S(\bar{r})/I_0, \quad (1.4.1-6)$$

where  $I_0$  is the peak excitation intensity. Fluctuations may arise from changes in brightness and concentration over time, but usually the excitation geometry is constant over a measurement, that is,  $w(\bar{r})$  and  $I_0$  are constant. Thus:

$$\delta F(t) = I_0 \sum_{i=1}^n \int w(\bar{r}) \delta(Q_i(t) \cdot C_i(\bar{r}, t)) dV. \quad (1.4.1-7)$$

The correlation function may now be expanded thus:

$$G(\tau) = \frac{\sum_{j=1}^n \sum_{i=1}^n \iint w(\bar{r}') w(\bar{r}) \langle \delta(Q_i(t) \cdot C_i(\bar{r}, t)) \delta(Q_j(t+\tau) \cdot C_j(\bar{r}, t+\tau)) \rangle dV dV'}{\left( \sum_{i=1}^n \int w(\bar{r}) \langle Q_i(t) \cdot C_i(\bar{r}, t) \rangle dV \right)^2}. \quad (1.4.1-8)$$

We note that  $\delta(Q_i(t) \cdot C_i(\bar{r}, t)) \equiv Q_i(t) \cdot \delta C_i(\bar{r}, t) + \delta Q_i(t) \cdot C_i(\bar{r}, t)$ , where second-order fluctuations are neglected. This approximation is valid if  $\delta Q_i(t) \delta C_i(\bar{r}, t) \rightarrow 0$ , that is, where the fluctuations are small and  $\delta Q_i(t)$  is not correlated with  $\delta C_i(\bar{r}, t)$ , which is usually the case. For the case of a single species of constant brightness, we may simplify further:

$$G(\tau) = \frac{\iint w(\bar{r}') w(\bar{r}) \langle \delta C(\bar{r}, t) \delta C(\bar{r}', t+\tau) \rangle dV dV'}{\langle C \rangle^2 \left( \int w(\bar{r}) dV \right)^2}. \quad (1.4.1-9)$$

#### *Interpreting the Correlation Amplitude and Effective Observation Volume*

The average number  $\langle N \rangle$  of particles in the observation volume over the period of measurement is expected to conform to Poisson statistics, in which case the variance of  $N$  equals the average of  $N$ . For the case where only one species exists in the sample, the amplitude of the correlation function  $G(0)$  is interpreted thus:

$$G(0) = \frac{\langle \delta F(t)^2 \rangle}{\langle F \rangle^2} = \frac{\langle F^2 \rangle - \langle F \rangle^2}{\langle F \rangle^2} = \frac{\langle N^2 \rangle - \langle N \rangle^2}{\langle N \rangle^2} = \frac{1}{\langle N \rangle}. \quad (1.4.1-10)$$

Since  $G(0)$  is determined by the average number of particles in the observation volume, and  $G(\tau)$  is expressed in terms of concentration, we can obtain an expression for the size

of an effective observation volume,  $V_{eff} = \langle C \rangle / \langle N \rangle$ . To do so, we note that the correlation in the position of two particles infinitely distant is zero at any time. Then  $\lim_{\bar{r}-\bar{r}' \rightarrow \infty} \langle \delta C(\bar{r}, 0) \delta C(\bar{r}', \tau) \rangle = 0$  and since the spatial correlation length of a particle must be very small and Poisson statistics specify that the mean-square fluctuation of  $C$  in a unit of volume is  $\langle C \rangle$  (see (174)), then  $\lim_{t \rightarrow 0} \langle \delta C(\bar{r}, 0) \delta C(\bar{r}', 0) \rangle = \langle C \rangle \delta(\bar{r} - \bar{r}')$ :

$$G(0) = \frac{1}{\langle N \rangle} = \frac{\iint w(\bar{r}') w(\bar{r}) \langle C \rangle \delta(\bar{r} - \bar{r}') dV dV'}{\langle C \rangle^2 \left( \int w(\bar{r}) dV \right)^2} = \frac{1}{\langle C \rangle} \frac{\int w^2(\bar{r}) dV}{\left( \int w(\bar{r}) dV \right)^2}. \quad (1.4.1-11)$$

Then:

$$V_{eff} = \frac{\left( \int w(\bar{r}) dV \right)^2}{\int w^2(\bar{r}) dV}. \quad (1.4.1-12)$$

For confocal geometry, the radial excitation intensity profile for the fundamental laser mode is a 2-D Gaussian, while the confocal pinhole filters out emission signals originating out of the focal plane. In this case,  $w(\bar{r})$  may be well approximated by an overall 3-D Gaussian function (177, 199):

$$w(\bar{r}) \approx e^{-\frac{2x^2+y^2}{r_0^2}} e^{-\frac{2z^2}{z_0^2}}. \quad (1.4.1-13)$$

The 3-D Gaussian geometry for the observation volume implies that the highest probability for detecting fluorescence is for particles at the origin. Under typical conditions,  $r_0 < z_0$  and thus the probability of detection decays with distance from the origin faster in the radial direction than the axial direction. Using this expression for  $w(\bar{r})$ , we may calculate  $V_{eff}$  using equation (1.4.1-12):

$$V_{eff} = r_0^2 \pi^{\frac{3}{2}} z_0. \quad (1.4.1-14)$$

To interpret the effective volume, consider the case where the 3-D Gaussian profile is replaced with an ellipsoidal step function where the fluorescence excitation and the probability of fluorescence detection does not vary within the volume, while no fluorescence is detected outside the volume. More precisely:

$$w_{ellipsoid}(\bar{r}) = \begin{cases} 1 & x, y \leq (3/4)^{1/3} \pi^{1/6} r_0, z \leq (3/4)^{1/3} \pi^{1/6} z_0 \\ 0 & \text{otherwise} \end{cases}. \quad (1.4.1-15)$$

The volume of this ellipsoid, which is symmetric about the  $z$ -axis, is:

$$\begin{aligned} Volume &= \frac{4}{3} \pi \cdot radius^2 \cdot halfheight \\ &= \frac{4}{3} \pi \cdot \left( (3/4)^{1/3} \pi^{1/6} r_0 \right)^2 \cdot \left( (3/4)^{1/3} \pi^{1/6} z_0 \right) = r_0^2 \pi^{\frac{3}{2}} z_0 \end{aligned}. \quad (1.4.1-16)$$

Note that this value for the volume is equal to the volume that is calculated by inserting  $w_{ellipsoid}(\bar{r})$  into Equation (1.4.1-12) and to the value of  $V_{eff}$  for the 3-D Gaussian profile (Equation 1.4.1-14). Thus for purposes such as calculating the concentration from the

amplitude of the correlation function, it may be convenient to think of the observation volume as an effective ellipsoid rather than a 3-D Gaussian, where the ellipsoid dimensions are slightly larger (a factor of  $(3/4)^{1/3} \pi^{1/6} \approx 1.10$ ) than the characteristic dimensions of the 3-D Gaussian,  $r_0$  and  $z_0$ .

#### *Correlation Function for Normal Diffusion*

To derive the correlation function for normal diffusion in a confocal volume (199), the simplest case is to consider one species of constant brightness using Equation 1.4.1-9. But first we must obtain an expression for the quantity  $\langle \delta C(\vec{r}, t) \delta C(\vec{r}', t + \tau) \rangle$  using diffusion theory. In section §1.2.1, Fick's Law and the Continuity Equation were derived, leading to the diffusion equation:

$$\frac{\partial C(\vec{r}, t)}{\partial t} = D \nabla^2 C(\vec{r}, t). \quad (1.4.1-17)$$

If all particles start at the origin at  $t = 0$ , and the system is allowed to relax toward equilibrium in the absence of any physical barriers, the initial condition is  $C(\vec{r}, 0) = \langle C \rangle \delta(\vec{r})$  and the boundary condition is  $\lim_{\vec{r} \rightarrow \infty} C(\vec{r}, t) = 0$ , and the corresponding solution is:

$$C(\vec{r}, t) = \frac{\langle C \rangle}{(4\pi Dt)^{3/2}} e^{-\vec{r}^2 / 4Dt}. \quad (1.4.1-18)$$

Using the definition of the concentration fluctuation,  $\delta C(\vec{r}, t) = C(\vec{r}, t) - \langle C \rangle$ , it is straightforward to show that the fluctuations in concentration  $\delta C(\vec{r}, t)$  also satisfy the diffusion equation:

$$\frac{\partial}{\partial t} \delta C(\vec{r}, t) = D \nabla_{\vec{r}}^2 \delta C(\vec{r}, t). \quad (1.4.1-19)$$

The diffusion equation is also satisfied if we write the fluctuations in concentration in terms of the lag time,  $\tau$ :

$$\frac{\partial}{\partial \tau} \delta C(\vec{r}, \tau) = D \nabla_{\vec{r}}^2 \delta C(\vec{r}, \tau). \quad (1.4.1-20)$$

After multiplying Equation 1.4.1-22 by  $\delta C(\vec{r}', 0)$ , taking the ensemble average, one has:

$$\frac{\partial}{\partial \tau} \langle \delta C(\vec{r}, \tau) \delta C(\vec{r}', 0) \rangle = D \nabla_{\vec{r}}^2 \langle \delta C(\vec{r}, \tau) \delta C(\vec{r}', 0) \rangle. \quad (1.4.1-21)$$

For ergodic samples,  $\langle \delta C(\vec{r}, \tau) \delta C(\vec{r}', 0) \rangle = \langle \delta C(\vec{r}, t) \delta C(\vec{r}', t + \tau) \rangle$ , and therefore:

$$\frac{\partial}{\partial \tau} \langle \delta C(\vec{r}, t) \delta C(\vec{r}', t + \tau) \rangle = D \nabla_{\vec{r}}^2 \langle \delta C(\vec{r}, t) \delta C(\vec{r}', t + \tau) \rangle. \quad (1.4.1-22)$$

Therefore the correlation in concentration fluctuations,  $\langle \delta C(\vec{r}, t) \delta C(\vec{r}', t + \tau) \rangle$ , satisfies the diffusion equation (for a similar approach see (195)). The correlation in concentration fluctuations may also be called the propagator of the diffusion, since it is proportional to the probability that a particle at  $\vec{r}$  at time  $t$  will be at  $\vec{r}'$  at time  $t + \tau$  later where the

proportionality constant is  $\langle C \rangle$ . The boundary conditions discussed earlier (see 1.4.1-11) are  $\lim_{\bar{r}-\bar{r}' \rightarrow \infty} \langle \delta C(\bar{r}, 0) \delta C(\bar{r}', \tau) \rangle = 0$ , and  $\lim_{t \rightarrow 0} \langle \delta C(\bar{r}, 0) \delta C(\bar{r}', 0) \rangle = \langle C \rangle \delta(\bar{r} - \bar{r}')$ . Then the propagator of the diffusion may be written as the solution to the diffusion equation, thus:

$$\langle \delta C(\bar{r}, t) \delta C(\bar{r}', t + \tau) \rangle = \frac{\langle C \rangle}{(4\pi D \tau)^{3/2}} e^{-\frac{(\bar{r}-\bar{r}')^2}{4D\tau}}. \quad (1.4.1-23)$$

Now inserting Equations 1.4.1-13 and 1.4.1-23 into Equation 1.4.1-9, we have a series of Gaussian integrals which may be solved analytically.

$$\begin{aligned} G(\tau) &= \frac{\iint w(\bar{r}') w(\bar{r}) \langle \delta C(\bar{r}, t) \delta C(\bar{r}, t + \tau) \rangle dV dV'}{\langle C \rangle^2 \left( \int w(\bar{r}) dV \right)^2} \\ &= \frac{\iint e^{-2\frac{x'^2+y'^2}{r_0^2}} e^{-2\frac{z'^2}{z_0^2}} e^{-2\frac{x^2+y^2}{r_0^2}} e^{-2\frac{z^2}{z_0^2}} \langle C \rangle e^{-\frac{(\bar{r}-\bar{r}')^2}{4D\tau}} dV dV'}{\langle C \rangle^2 \left( \int e^{-2\frac{x^2+y^2}{r_0^2}} e^{-2\frac{z^2}{z_0^2}} dV \right)^2}. \quad (1.4.1-24) \end{aligned}$$

After introducing the conventional definition of the characteristic diffusion time  $\tau_D$  and the aspect ratio  $S$ , where

$$\tau_D \equiv \frac{r_0^2}{4D}, \text{ and } S = \frac{z_0}{r_0}, \quad (1.4.1-25)$$

and making use of our expression for the effective volume in Equation 1.4.1-14 we arrive at the final expression for the autocorrelation function for 3-D diffusion in a confocal volume first reported in 1976 (199),

$$\begin{aligned} G(\tau) &= \frac{1}{\langle C \rangle} \frac{1}{r_0^2 \pi^3 z_0} \left( 1 + \frac{\tau}{\tau_D} \right)^{-1} \left( 1 + \frac{1}{S^2} \frac{\tau}{\tau_D} \right)^{-\frac{1}{2}} \\ G(\tau) &= \frac{1}{\langle N \rangle} \left( 1 + \frac{\tau}{\tau_D} \right)^{-1} \left( 1 + \frac{1}{S^2} \frac{\tau}{\tau_D} \right)^{-\frac{1}{2}}. \quad (1.4.1-26) \end{aligned}$$

There is a special case if  $S \gg 1$ , where the observation volume may be compared to a cylinder of infinite height where only the radial movement of the fluorescent species contributes to the fluorescence fluctuations:

$$G(\tau) = \frac{1}{\langle N \rangle} \left( 1 + \frac{\tau}{\tau_D} \right)^{-1}. \quad (1.4.1-27)$$

Equation 1.4.1-27 is identical to that for particles constrained to two-dimensional motion the plane  $z = 0$ .

### Correlation Function for Two-State Photophysical Kinetics

The simplest case of photophysics is a two-state system in a reversible reaction where one state is fluorescent and the second is completely dark. The dynamics of intersystem crossing (the singlet energy states and triplet energy states are the separate “systems”) have been described in detail as a three-state model, the singlet ground state, the first singlet excited state, and the first triplet excited state (154), but by recognizing that the singlet-singlet transitions are much faster than singlet-triplet transitions, the analysis is greatly simplified by assuming an effective two-state system. Following (143), consider particles undergoing the following reversible reaction:  $N_1 \leftrightarrow N_2$  where  $k_1$  and  $k_2$  are rates of conversion to states 1 and 2 respectively. The system is described by  $N_1(t) + N_2(t) = N$  where  $N$  is the total number of particles and by a pair of differential equations:

$$\frac{d}{dt} \begin{pmatrix} N_1(t) \\ N_2(t) \end{pmatrix} = \begin{pmatrix} -k_1 & k_2 \\ k_1 & -k_2 \end{pmatrix} \begin{pmatrix} N_1(t) \\ N_2(t) \end{pmatrix}. \quad (1.4.1-28)$$

The solutions to these equations both have the form:

$$N_m(t) = (N_m(0) - \langle N_m \rangle) e^{-t/\tau_r} + \langle N_m \rangle. \quad (1.4.1-29)$$

Here the long-time average value of the number of particles in state  $m$ ,  $\langle N_m \rangle$ , is independent of initial conditions at  $t = 0$ , and  $\tau_r$  is the characteristic relaxation time for the system:

$$\langle N_m \rangle = \frac{k_m}{k_1 + k_2} N, \text{ and } \tau_r = \frac{1}{k_1 + k_2}. \quad (1.4.1-30)$$

The probability for a single particle to be in a state  $m$  at any time is  $P(m) = \langle N_m \rangle / N$ . To calculate the normalized probability that a single particle in state  $m$  at time  $t$  will be in state  $n$  at a later time  $t + \tau$ , we allow all the particles to be in state  $m$  at time  $t$ , that is,  $N_m(t) = N$ , and divide the number in state  $n$  at a later time  $t + \tau$ ,  $N_n(t + \tau)$ , by  $N_m(t)$  in order to get the fraction of particles which changed states.

$$N_n(t + \tau) = (N_n(t) - \langle N_n \rangle) e^{-\tau/\tau_r} + \langle N_n \rangle. \quad (1.4.1-31)$$

$$P(m, t; n, t + \tau) = (\delta_{mn} - \langle N_n \rangle / N) e^{-\tau/\tau_r} + \langle N_n \rangle / N. \quad (1.4.1-32)$$

In the case of  $N$  fixed particles in the effective observation volume where the fluorescence signal depends only on the state that the molecule is in, Equation 1.4.1-3 may be expanded thus:

$$G(\tau) = \frac{\langle F(t)F(t + \tau) \rangle}{\langle F \rangle^2} - 1 = \frac{\sum_{m=1}^2 \sum_{n=1}^2 N Q_m Q_n P(m) P(m, t; n, t + \tau)}{\left( \sum_{m=1}^2 Q_m \langle N_m \rangle \right)^2} - 1. \quad (1.4.1-33)$$

Here  $Q_m$  is the specific brightness of a particle in the state  $m$ . The form for the correlation function due to two-state blinking may be evaluated to show:

$$G(\tau) = \frac{1}{N} \frac{(Q_1 - Q_2)^2 (1-T) T}{(Q_1(1-T) + Q_2 T)^2} e^{-\tau/\tau_T}. \quad (1.4.1-34)$$

$T$  is the probability of finding the particle in state 2,  $T = k_2 / (k_1 + k_2)$ . But where state 2 is completely dark, i.e. the triplet state, and state 1 is fluorescent, i.e. the singlet state, Equation 1.4.1-34 may be simplified by setting  $Q_2 = 0$ :

$$G(\tau) = \frac{1}{N} \frac{T}{1-T} e^{-\tau/\tau_T}. \quad (1.4.1-35)$$

Here  $T$  is the average fraction of particles in the triplet state, and  $\tau_T$  is the characteristic relaxation time of the two-state system.

#### *Correlation Function for Normal Diffusion and Two-State Photophysical Kinetics*

A very common case for simple FCS experiments involves particles that exhibit two-state photophysical kinetics such as singlet-triplet transitions diffusing in three dimensions. In such a case, the rate of change in the space-time concentration function of the fluorescent species,  $C_1(\vec{r}, t)$ , is determined not just by diffusion, but also by the reversible reaction between the two states:  $N_1 \leftrightarrow N_2$  where  $k_1$  and  $k_2$  are the rates of conversion to states 1 and 2 respectively. Therefore the diffusion terms from 1.4.1-17 and the reaction terms from Equation 1.4.1-28, and combined to give the following coupled differential equations:

$$\frac{d}{dt} C_1(\vec{r}, t) = D \nabla^2 C_1(\vec{r}, t) - k_2 C_1(\vec{r}, t) + k_1 C_2(\vec{r}, t). \quad (1.4.1-36)$$

$$\frac{d}{dt} C_2(\vec{r}, t) = D \nabla^2 C_2(\vec{r}, t) - k_1 C_2(\vec{r}, t) + k_2 C_1(\vec{r}, t). \quad (1.4.1-37)$$

In the manner that Equation 1.4.1-17 was rewritten as 1.4.1-22 in terms of the concentration correlation, these coupled differential equations may also be rewritten in terms of the concentration correlations,  $\phi_{ij}(\vec{r} - \vec{r}', \tau) = \langle \delta C_i(\vec{r}, t) \delta C_j(\vec{r}', t + \tau) \rangle$ :

$$\frac{d}{d\tau} \phi_{11} = D \nabla_{\vec{r}}^2 \phi_{11} - k_2 \phi_{11} + k_1 \phi_{21}. \quad (1.4.1-38)$$

$$\frac{d}{d\tau} \phi_{22} = D \nabla_{\vec{r}}^2 \phi_{22} - k_1 \phi_{22} + k_2 \phi_{12}. \quad (1.4.1-39)$$

$$\frac{d}{d\tau} \phi_{12} = D \nabla_{\vec{r}}^2 \phi_{12} - k_2 \phi_{12} + k_1 \phi_{22}. \quad (1.4.1-40)$$

$$\frac{d}{d\tau} \phi_{21} = D \nabla_{\vec{r}}^2 \phi_{21} - k_1 \phi_{21} + k_2 \phi_{11}. \quad (1.4.1-41)$$

The boundary conditions due to Poisson statistics are  $\lim_{t \rightarrow 0} \phi_{ii} = \langle C_i \rangle \delta(\vec{r} - \vec{r}')$  and since two different particles cannot occupy the same space at the same time,  $\lim_{t \rightarrow 0} \phi_{ij} = 0$  for  $i \neq j$ . Further, we note that  $\lim_{\vec{r} - \vec{r}' \rightarrow \infty} \phi_{ij} = 0$  since there can be no correlation between the positions of two randomly moving particles which are infinitely far apart. By first taking

the Laplace transforms with respect to position ( $\bar{r} \rightarrow \bar{q}$ ) and Fourier transforms with respect to time ( $t \rightarrow \omega$ ), the equations may be decoupled and after performing the inverse transforms the exact results are (compare (174, 195)):

$$\phi_{11} = \langle C_1 \rangle \left( 1 - T + T e^{-\tau/\tau_r} \right) \left( \frac{1}{4\pi D \tau} \right)^{3/2} e^{-\frac{(\bar{r}-\bar{r}')^2}{4D\tau}}. \quad (1.4.1-42)$$

$$\phi_{22} = \langle C_2 \rangle \left( T + (1-T) e^{-\tau/\tau_r} \right) \left( \frac{1}{4\pi D \tau} \right)^{3/2} e^{-\frac{(\bar{r}-\bar{r}')^2}{4D\tau}}. \quad (1.4.1-43)$$

$$\phi_{12} = \phi_{21} = \langle C_1 \rangle T \left( 1 - e^{-\tau/\tau_r} \right) \left( \frac{1}{4\pi D \tau} \right)^{3/2} e^{-\frac{(\bar{r}-\bar{r}')^2}{4D\tau}}. \quad (1.4.1-44)$$

Here  $T$  and  $\tau_r$  are defined as described above for the case of two-state photophysical kinetics without diffusion (see Equations 1.4.1-30 and 1.4.1-34). To obtain the correlation function, we now rewrite Equation 1.4.1-8 in terms of the concentration correlations  $\phi_{ij}$ :

$$G(\tau) = \frac{\langle \delta F(t) \delta F(t+\tau) \rangle}{\langle F \rangle^2} = \frac{\int \int w(\bar{r}') w(\bar{r}) \sum_{j=1}^2 \sum_{i=1}^2 Q_i Q_j \phi_{ij} dV dV'}{\left( \int w(\bar{r}) dV \right)^2 \left( \sum_{i=1}^2 \langle C_i \rangle \right)^2}. \quad (1.4.1-45)$$

Now inserting the solutions for  $\phi_{ij}$ , we note that the integrals over space for all four terms are identical apart from a prefactor which results in the expression for the 3-D diffusion correlation, and after simplifying we arrive at:

$$G(\tau) = \frac{1}{\langle N \rangle} \left( 1 + \frac{\tau}{\tau_D} \right)^{-1} \left( 1 + \frac{1}{S^2} \frac{\tau}{\tau_D} \right)^{-\frac{1}{2}} \left( 1 + \frac{(Q_1 - Q_2)^2 (1-T) T}{(Q_1(1-T) + Q_2 T)^2} e^{-\tau/\tau_r} \right). \quad (1.4.1-46)$$

Note that  $N$  here is the total number of particles including both states. Equation 1.4.1-48 is exact. In many cases, the diffusion time-scale is much slower than the photophysics, that is,  $\tau_D \gg \tau_r$ , and the terms may be decoupled and the correlation is simply a sum of the diffusion and photophysical contributions (compare for example the correlation function used in (182)):

$$G(\tau) = \frac{1}{\langle N \rangle} \cdot \left( 1 + \frac{\tau}{\tau_D} \right)^{-1} \left( 1 + \frac{1}{S^2} \frac{\tau}{\tau_D} \right)^{-\frac{1}{2}} + \frac{1}{\langle N \rangle} \cdot \frac{(Q_1 - Q_2)^2 (1-T) T}{(Q_1(1-T) + Q_2 T)^2} e^{-\tau/\tau_r}. \quad (1.4.1-47)$$

For triplet state kinetics where  $Q_2 = 0$ , the correlation function may be simplified into its usual form for 3-D diffusion in a confocal volume with the presence of a single ‘‘on-off’’ blinking term:

$$G(\tau) = \frac{1}{\langle N \rangle} \left( 1 + \frac{\tau}{\tau_D} \right)^{-1} \left( 1 + \frac{1}{S^2} \frac{\tau}{\tau_D} \right)^{-\frac{1}{2}} \left( 1 + \frac{T}{(1-T)} e^{-\tau/\tau_r} \right). \quad (1.4.1-48)$$

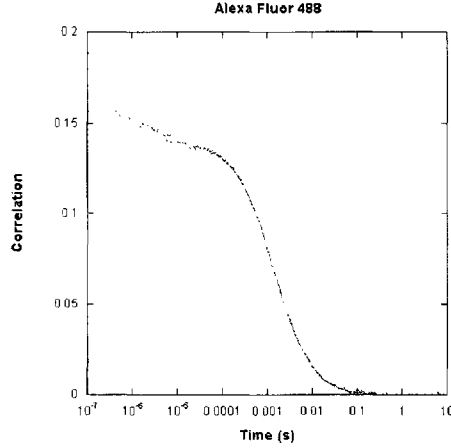


Figure 1.4.1-A. Experimental correlation data of Alexa Fluor 488 dye diffusing in buffer solution with a visible triplet state term, observed with a large observation volume ( $w_0 = 950$  nm) to show a clear separation of the diffusion and triplet terms. The solid line is a fit to Equation 1.4.1-48:  $N = 6.38$ ,  $\tau_D = 1.4$  ms,  $S = 5.5$ ,  $T = 0.11$ , and  $\tau_T = 3.7$   $\mu$ s.

In this case, the amplitude  $G(0)$  is no longer the inverse of the average number of particles in the volume,  $N$ :

$$G(0) = 1/\langle N \rangle (1 - T). \quad (1.4.1-49)$$

The correlation amplitude is instead the inverse of the average number of particles in the volume which are also in the fluorescent singlet state. Some FCS studies use an alternative form of Equation 1.4.1-48 with a different normalization convention:

$$G(\tau) = \frac{1}{\langle N \rangle} \left( 1 + \frac{\tau}{\tau_D} \right)^{-1} \left( 1 + \frac{1}{S^2} \frac{\tau}{\tau_D} \right)^{-1/2} (1 - T + T e^{-\tau/\tau_T}). \quad (1.4.1-50)$$

Here  $G(0) = 1/\langle N \rangle$  where  $\langle N \rangle$  is the average number of particles in the volume which are in the “on,” or singlet, state, rather than the total number of particles in the volume.

#### *Multi-Component Models*

For more general cases where there are  $n$  non-interacting species of particles with constant brightness  $Q_i$  and diffusion times,  $\tau_{D,i}$ ’s, then by definition the fluctuations in spatial concentration of species  $i$  and  $j$  are not correlated, and the corresponding propagator is zero, that is,  $\langle \delta C_i(\vec{r}, t) \delta C_j(\vec{r}, t + \tau) \rangle = 0$ . Therefore the cross-correlation terms,  $i \neq j$ , in Equation 1.4.1-8 vanish and thus it may be simplified (200, 201):

$$G(\tau) = \frac{\sum_{i=1}^n Q_i^2 \int \int w(\bar{r}') w(\bar{r}) \langle \delta C_i(\bar{r}, t) \delta C_i(\bar{r}, t + \tau) \rangle dV dV'}{\left( \sum_{i=1}^n Q_i \langle C_i \rangle \right)^2 \left( \int w(\bar{r}) dV \right)^2} = \frac{\sum_{i=1}^n Q_i^2 \langle N_i \rangle g_{D,i}(\tau)}{\left( \sum_{i=1}^n Q_i \langle N_i \rangle \right)^2}. \quad (1.4.1-51)$$

Here  $g_{D,i}(\tau)$  is the diffusion term of the correlation function corresponding to Equation 1.4.1-26 for the  $i$ th species, that is,

$$g_{D,i}(\tau) = \left( 1 + \frac{\tau}{\tau_{D,i}} \right)^{-1} \left( 1 + \frac{1}{S^2} \frac{\tau}{\tau_{D,i}} \right)^{-1/2}. \quad (1.4.1-52)$$

A simple case for Equation 1.4.1-51 is a single fluorescent species which divides into multiple diffusing and non-interacting subspecies having equal specific brightness. Such a case could be achieved where a mobile macromolecule is labeled covalently with one dye molecule while free dye molecules of the same type diffuse in the same solution. Then Equation 1.4.1-51 applies where  $n = 2$ :

$$G(\tau) = \frac{1}{N} \left[ F \left( 1 + \frac{\tau}{\tau_{D,1}} \right)^{-1} \left( 1 + \frac{1}{S^2} \frac{\tau}{\tau_{D,1}} \right)^{-1/2} + (1-F) \left( 1 + \frac{\tau}{\tau_{D,2}} \right)^{-1} \left( 1 + \frac{1}{S^2} \frac{\tau}{\tau_{D,2}} \right)^{-1/2} \right]. \quad (1.4.1-53)$$

Here  $F$  is the fraction of particles with diffusion time  $\tau_{D,1}$  and  $N$  is the total number of particles including both components. Where the triplet state of each component is also observable, Equation 1.4.1-51 may be generalized thus:

$$G(\tau) = \frac{\sum_{i=1}^n Q_i^2 \langle N_i \rangle g_{D,i}(\tau) \cdot g'_{T,i}(\tau)}{\left( \sum_{i=1}^n Q_i \langle N_i \rangle \right)^2}. \quad (1.4.1-54)$$

Here  $g'_{T,i}(\tau)$  is the triplet state term of the correlation function corresponding to Equation 1.4.1-48 for the  $i$ th species, that is,

$$g'_{T,i}(\tau) = \left( 1 + \frac{T_i}{(1-T_i)} e^{-\tau/\tau_{T,i}} \right). \quad (1.4.1-55)$$

Here  $g'_{T,i}(\tau)$  is not the same as the correlation function given by Equation 1.4.1-35 which was derived for the case of triplet-state kinetics only, because it reflects the coupling between the detection of diffusion and the triplet-state kinetics. Indeed,  $g'_{T,i}(\tau)$  cannot be a true correlation function of the fluctuations when isolated because it decays to 1 at long times rather than to 0. However, in the case where  $\tau_D \gg \tau_T$ , the terms may be decoupled and Equation 1.4.1-54 may be rewritten thus:

$$G(\tau) = \frac{\sum_{i=1}^n Q_i^2 \langle N_i \rangle \cdot (g_{D,i}(\tau) + g_{T,i}(\tau))}{\left( \sum_{i=1}^n Q_i \langle N_i \rangle \right)^2}. \quad (1.4.1-56)$$

Here the triplet state correlation function for the  $i$ th species is (see Equation 1.4.1-35):

$$g_{T,i}(\tau) = \frac{T_i}{(1-T_i)} e^{-\tau/\tau_{T,i}}. \quad (1.4.1-57)$$

For the simple case where a single fluorescent species which divides into two diffusing and non-interacting subspecies with equal the brightness where the triplet state kinetics are identical between the subspecies, then Equation 1.4.1-54 becomes:

$$G(\tau) = \frac{1}{N} \left( 1 + \frac{T}{(1-T)} e^{-\tau/\tau_T} \right) \times \left( F \left( 1 + \frac{\tau}{\tau_{D,1}} \right)^{-1} \left( 1 + \frac{1}{S^2} \frac{\tau}{\tau_{D,1}} \right)^{-\frac{1}{2}} + (1-F) \left( 1 + \frac{\tau}{\tau_{D,2}} \right)^{-1} \left( 1 + \frac{1}{S^2} \frac{\tau}{\tau_{D,2}} \right)^{-\frac{1}{2}} \right). \quad (1.4.1-58)$$

As in Equation 1.4.1-53,  $F$  is the fraction of particles in the first component with diffusion time  $\tau_{D,1}$  and  $N$  is the total number of particles including both components.

Equation 1.4.1-58 is the correlation function for the two-component diffusion model used in the papers in this thesis for comparison with the anomalous diffusion model.

#### *Anomalous Diffusion Model*

For cases where Fick's Law does not apply, diffusion may be non-Brownian, as discussed in §1.1.4. To model anomalous diffusion via FCS, it is common to allow the propagator of the diffusion to take the following form which accounts for one subclass of non-Brownian anomalous diffusion (73):

$$\langle \delta C(\bar{r}, t) \delta C(\bar{r}', t + \tau) \rangle = \frac{\langle C \rangle}{(\pi l^2 \tau^\alpha)^{3/2}} e^{-\frac{(\bar{r}-\bar{r}')^2}{4D\tau^\alpha}}. \quad (1.4.1-59)$$

The definition of the diffusion time is then modified thus:

$$\tau_D^\alpha \equiv \frac{r_0^2}{4D}. \quad (1.4.1-60)$$

This definition allows the autocorrelation functions derived for normal diffusion to be easily adapted to anomalous diffusion by replacing  $\tau/\tau_D$  with  $(\tau/\tau_D)^\alpha$  throughout the derivations. Therefore for anomalous 3-D diffusion with the presence of triplet state kinetics, Equation 1.4.1-48 becomes (73):

$$G(\tau) = \frac{1}{\langle N \rangle} \left( 1 + \left( \frac{\tau}{\tau_D} \right)^\alpha \right)^{-1} \left( 1 + \frac{1}{S^2} \left( \frac{\tau}{\tau_D} \right)^\alpha \right)^{-\frac{1}{2}} \left( 1 + \frac{T}{(1-T)} e^{-\tau/\tau_T} \right). \quad (1.4.1-61)$$

This simple analytical equation represents the result from using one of several possible propagators leading to anomalous diffusion, and hence is not necessarily an exact solution for all cases of anomalous transport. The propagator used here (Equation 1.4.1-59) is unphysical as the apparent diffusion coefficient is singular at  $t = 0$ . Use of the fractional Fokker-Planck equation is required to derive the correct expression (43). However, numerical calculations show that this simple analytical equation (Equation 1.4.1-61) is a very good approximation of the correlation function which results from the more complex solution to the fractional Fokker-Planck equation (63). Importantly, the asymptotic behavior of the autocorrelation function depends only on the probability of a particle to return to the origin, which is independent of the anomalous diffusion model used (43). Equation 1.4.1-61 was commonly used throughout the research reported in this thesis to fit correlation data to determine the presence of anomalous diffusion in various systems.

### 1.4.2. Fluorescence Correlation Spectroscopy Experimental Description

An FCS experimental apparatus must perform three functions: excitation illumination, collection of emitted fluorescence, and calculation of the correlation data. In its standard setup based on a confocal microscope, the means to excite the observation volume sample is typically a collimated laser beam focused through a microscope objective lens. The objective lens then performs a double function by also collecting emitted fluorescence, while a fluorescence filter cube distinguishes the fluorescence emission wavelength from the excitation wavelength and a confocal pinhole spatially filters out the out-of-focus fluorescence. The detected fluorescence signal is processed by specialized hardware in order to efficiently calculate the time-lag correlation of the fluorescence signal. A diagram of our FCS apparatus is shown in Figure 1.4.2-A.

#### *Excitation Illumination*

In our FCS apparatus, a set of lenses expands and collimates the beam after the laser source so that the beam fills the back aperture of the objective. A set of linear polarizers (or a continuously variable neutral density filter, see §2.1.2) controls the laser power illuminating the sample. The shutters, which are located immediately before and after the microscope, may be used to stop the illumination of the sample or detection from the sample respectively. The filter cube, composed of the dichroic mirror and both the excitation and emission filters, is located in the body of the microscope. The narrow band pass excitation filter transmits light with wavelengths within a small range around the excitation wavelength. The dichroic mirror directs the excitation beam into the back aperture of the objective which excites fluorescence in the sample. For typical experiments reported in this thesis, we used a 488-nm argon ion laser attenuated to obtain a radiant exposure at the focus in the range of 1–10 kW/cm<sup>2</sup>.

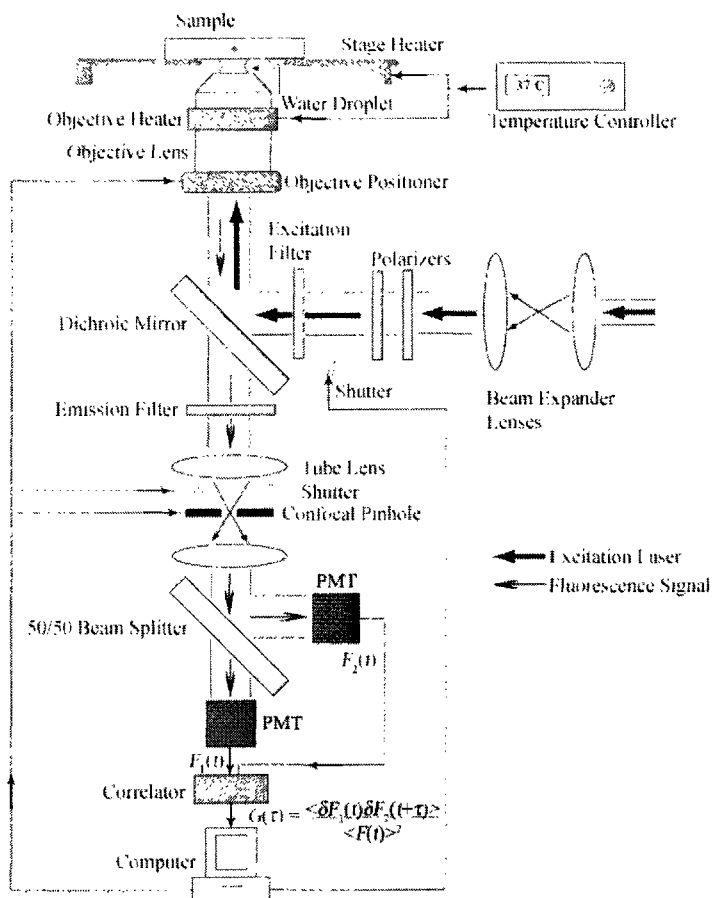


Figure 1.4.2-A. A diagram of our FCS apparatus.

### Fluorescence Collection

Some of the fluorescence originating from the diffraction-limited focal spot is collected by the objective. For typical experiments, we used a 60x 1.20 N.A. water immersion objective, but for samples in organic solvents a 100x 1.3 N.A. oil immersion objective was used due to the higher index of refraction of the solvent. The fluorescence signal then passes through both the dichroic mirror and emission filter which select according to wavelength. The confocal pinhole then spatially filters out-of-focus fluorescence resulting in an observation volume which is well approximated by a 3-D Gaussian profile. The remaining fluorescence signal is then divided in half by a beam splitter and each half is collected by a photomultiplier tube (PMT) and the arrival of each photon is indicated by an electrical pulse that is sent to the correlator card.

*Correlation Calculation*

The signal detected by the photomultiplier tubes is fed into a multi-tau correlator that computes the correlation for time lags on a logarithmic time scale from 8 ns until the length of the experiment. The correlator calculates the cross-correlation between the two halves of the fluorescence signal and outputs the correlation data and average photon counts to the computer for subsequent modeling. As an alternative, the autocorrelation function for the whole signal detected by only one PMT may be calculated instead, but the resulting correlation data will exhibit an extra correlation due to a phenomenon called shot noise. Shot noise is a quantum mechanical effect that causes a PMT to have a high probability of detecting an echo shortly after detecting a photon, with the result that the electrical output signal from the detector is a Poisson transform of the photon input signal at the detector (202, 203). When autocorrelation data is calculated rather than cross-correlations, we observe an extremely large correlation that occurs in a characteristic time range of 40 – 75 ns with residual effects up to 250 ns or longer. This correlation occurs even without a sample present and is attributed to this shot noise. Therefore the effects of the shot noise are eliminated by taking a crosscorrelation between two detectors since there is no correlation between the photon detected by one detector and the echo in the second detector. Otherwise, the crosscorrelation between two detectors and the autocorrelation of the signal in one detector are identical.

*FCS Calibration and statistical accuracy*

Equation 1.4.1-48 is the fit equation used to model typical FCS data taken from a dye diffusing in solution. The characteristic diffusion time  $\tau_D$  obtained as a fit parameter is related to the diffusion coefficient through its definition:

$$\tau_D \equiv \frac{r_0^2}{4D}$$

Thus, to obtain the diffusion coefficient from  $\tau_D$ , the value of the observation volume radius  $r_0$  must be known. By first observing the diffusion time  $\tau_D$  of a dye with known diffusion coefficient, such as Rhodamine 6G for which  $D = 280 \mu\text{m}^2/\text{s}$ , one can fix the value of  $r_0$  to be used for further measurements of other samples for which the diffusion coefficient may be otherwise unknown.

Calibration with a standard dye also serves another purpose, that is, to confirm to the experimentalist that FCS is functioning at optimal performance. Correlation data taken for calibration should fit very well to the theoretical equation which confirms that the optical components are correctly aligned to produce the 3-D Gaussian profile at the sample. Further, one may calculate the photon counts collected per molecule from the average fluorescence signal collected divided by the value of  $N$  obtained as a fit parameter. The brightness per molecule serves as a quality-control parameter. The lower the brightness, the longer fluorescence data must be taken to obtain reliable correlation data (193). It is well known to FCS experimentalists that the brightness per molecule is much more important in determining the statistical accuracy of the experiment than the total fluorescence signal (204).

### 1.4.3. Other Experimental Methods Used to Study Diffusion *in Vivo*

#### *Fluorescence Recovery after Photobleaching (FRAP)*

Generally speaking, the difference between FRAP and FCS is that while FCS observes fluctuations about equilibrium, FRAP takes the system away from equilibrium and observes it relax back to equilibrium. In both methods, the fluorescence signal is recorded as a function of time. But in FRAP, a portion of the sample is quickly photobleached and the recovery of the fluorescence in the photobleached area over time is analyzed. In its simplest version, an experimental FRAP apparatus is very similar to an FCS apparatus. The FRAP apparatus does not need the correlator card but does require an efficient means of photobleaching. This can be accomplished using the same laser as is used for excitation provided that the irradiation power can be quickly adjusted between normal and photobleaching levels, for example by using acousto-optic modulators.

Figure 1.4.3-A illustrates a typical FRAP data set, where the total fluorescence signal drops to zero and slowly recovers. When FRAP is performed in cells where there is a limited number of copies of the tracer of interest, the fluorescence will not return to pre-bleach levels, but if all the particles are mobile within a cellular compartment containing the bleach spot, the fluorescence intensity of the bleached spot will become indistinguishable from that of the rest of the compartment. If the fluorescence remains lower than the rest of the compartment, then some of the particles may be immobile on the time-scale of the experiment. In fact, the sensitivity to immobile fluorescent particles is a chief advantage of FRAP over FCS, since in FCS any immobile particles in the observation volume will simply contribute to the background until photobleaching and are therefore not detected.

A second advantage of FRAP is its ability to easily change the length-scale of observation by photobleaching areas of different sizes. But often it is necessary to photobleach areas larger than the diffraction limit in order to take the system far enough from equilibrium to obtain a statistically significant amount of data. The larger scales required may also be a disadvantage where the diffusive phenomena of interest occur around or below the diffraction limit.

Furthermore, the geometry of the beam usually limits FRAP to the study of 2-D diffusion in membranes due to the difficulty in controlling the photobleaching in the sample along the optical axis. Reducing out-of-plane photobleaching to observe 3-D diffusion with FRAP requires modifications such as Total Internal Reflection FRAP or multi-photon FRAP (64).

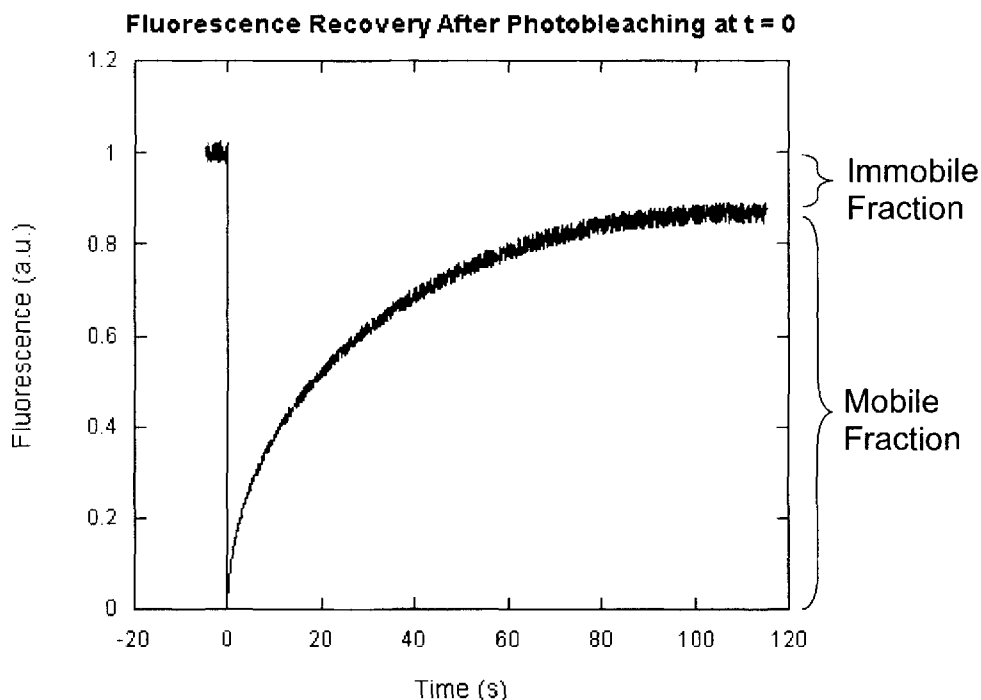


Figure 1.4.3-A Illustration of the form of FRAP data for a case where full fluorescence recovery is not achieved. Such data may be obtained for slowly diffusing tracers such as receptor complexes in a cell membrane (66).

Like FCS, the results of a FRAP experiment are model-dependent, and one must make assumptions about the geometry and nature of the diffusion in the sample in the model. For example, if the bleach spot is circular and of uniform intensity, then the recovery curve follows:

$$F(t) = e^{-z} \cdot (I_0(z) + I_1(z)). \quad (1.4.3-1)$$

Here  $z = 2\tau_D / t$ , and  $\tau_D = r_0^2 / 4D$  is the characteristic diffusion time, and  $I_0(z)$  and  $I_1(z)$  are modified Bessel functions. If the diffusion is anomalous, then the same equation applies, except that the diffusion coefficient is no longer constant, but is instead a function of time  $D(t) = \Gamma t^{\alpha-1}$ . FRAP is commonly used to measure lateral diffusion of proteins and larger complexes in cell membranes. Until Single Particle Tracking experiments in such systems showed the diffusion to be anomalous, FRAP data was often interpreted as free Brownian motion of only a subpopulation of molecules (the so-called mobile fraction) in presence of an immobile subpopulation. At that time, FRAP models for anomalous diffusion were applied which demonstrated that the lack of recovery due to

the so-called immobile fraction may be in fact be due to anomalous diffusion instead (15, 33, 66, 205).

### *Single Particle Tracking*

Single Particle Tracking (SPT) is a method based on tracing the random paths of many individual particles to characterize the motion of the particles (45, 80, 99, 206-209). In diffusion studies, the direct observation of the mean-square-displacement is this method's main advantage over model-dependent methods such as FCS and FRAP. SPT is performed by labeling the particle of interest with a fluorescent molecule or gold particle followed by recording consecutive images of samples and subsequent analysis of each particle's position in successive images. In SPT, illumination by a light source such as a mercury lamp (not a laser in contrast to FCS) gives a fluorescence image over the entire field of view rather than just a diffraction-limited spot.

In order to chart the path of each particle in successive images, the position of the particle in each image is precisely determined with precision below the diffraction limit. To obtain this precision, the intensity distribution of each fluorescence spot over several pixels is analyzed by fitting to an appropriate model of the point spread function such as a 2-D Gaussian function. Experimental conditions will typically be chosen to make crossing of particle paths infrequent and obtain relative ease of identifying particles in successive images. Algorithms used to analyze the images will often take into account the probability distribution of the change in the particle's position and intensity between images and allow for fitting with multiple overlapping point-spread functions when particles appear close together in an image.

The paths of the particles are typically analyzed in two ways in an SPT experiment. The first is to examine the relationship between the mean-square displacement and time, called mobility analysis. This analysis can often distinguish between Brownian motion, anomalous diffusion, particle flow, and motion within a limited domain, provided that there is a single behavior. The second method of analysis is to examine the probability distribution of the displacement for all particles as a function of the time interval which will also yield values of the diffusion coefficient and anomalous exponent. The probability histograms provide a way to resolve multiple behaviors in the sample, but at the cost of introducing model-dependence into the analysis (99, 206, 207).

Disadvantages of SPT relate to technical limitations concerning the speed and resolution of the data collection. SPT in systems of biological interest are usually limited to 2-D diffusion of protein complexes in membranes due to their slow motion and the difficulty in tracking particles in three dimensions (99, 206-208). In systems where the motion is 3-D, often only the 2-D projection of the motion is tracked and analyzed, and each particle can be tracked only as long as it stays in the focus which significantly reduces the statistical accuracy in determining the mean-square-displacement (45, 140). A further limitation is the low concentrations of particles which must be used in order that the paths of particles do not frequently cross within a diffraction-limited area.

## 2. Summary of Research

This chapter summarizes my research as presented in two published papers and one manuscript prepared for publication as well as related aspects of my research which have not been prepared for publication. As the title of this thesis indicates, a common theme for all of this research is the use of FCS methods to study biologically-relevant phenomena, including diffusion behavior in complex media and photophysical properties of fluorescent proteins. Therefore, I begin with my contributions to the development of our home-built FCS apparatus (§2.1). A major contribution to this apparatus is a software program serving as an interface between several hardware components and the user. The program performs several functions which significantly increase the efficiency of the FCS measurements performed by myself and others in the group (§2.1.1). A brief description of my development our apparatus to include the capability of Variable Length Scale Fluorescence Correlation Spectroscopy (VLS-FCS) is also included here (§2.1.2).

Having described the prerequisite experimental development, I summarize the published papers and manuscripts and specify my contributions to each (§2.2.1-2.2.3). *Anomalous Diffusion of Proteins Due to Molecular Crowding* describes our observations of protein diffusion in crowded media at a fixed observation length scale, demonstrating the usefulness of the anomalous diffusion model in this system. *Diffusion Power Laws in Polymer Solutions and Gels Observed Using Variable Length Scale Fluorescence Correlation Spectroscopy* takes the next step by observing the length-scale dependence of diffusion in not just the protein system described in the previous paper, but also in a system of beads diffusing in agarose gels. When studying the behavior of photophysical correlations rather than the diffusion term, a potential application for EGFP as a thermometer based on its blinking rate was realized experimentally and the results are reported in *A Molecular Thermometer based on Fluorescent Protein Blinking*.

Following the summaries of the above named manuscripts, I summarize additional research related to the preceding work. First, I describe an additional application of VLS-FCS to study the diffusion of polymers in organic solvents and I report on the insights which this method contributed to our understanding of the system (§2.3.1). Then I report the first applications of EGFP as a thermometer which allowed us to ensure that FCS samples could be held at precisely 37°C using only an objective heater, an important feature for studies in live cells, and to determine the temperature is spatially uniform across the sample (§2.3.2).

## **2.1 Summary of My Contributions to Our Home-built FCS Apparatus**

When I joined Cecile Fradin's research group as a graduate student, no correlation data from samples other than shot noise had been observed using our work-in-progress FCS set-up. I made various improvements to the alignment of optical components through manual means before I was able to regularly obtain collected specific brightness values of about 20 kHz per molecule from standard dyes such as fluorescein illuminated with 20  $\mu\text{W}$  at 488 nm. The various components that were adjusted in the process included spatial filters, alignment mirrors, polarizers, the objective, the confocal pinhole, the photo-multiplier tubes, and even the correlator card. After sufficiently high-quality data could be achieved regularly, I wrote a software program to automate or control several functions of the experimental setup and to ease the process of data analysis. More adjustments to the optical components were required to add the functionality of VLS-FCS. This software and adjustments for VLS-FCS are described below.

### 2.1.1. Description of the *FROG 3D* LabVIEW program

LabVIEW 8.0 is a programming system designed for ease of interfacing hardware to a computer controller. The interface of the programming mode itself appeals to the intuition of one familiar with electronics. LabVIEW requires the programmer to design a “front panel” which is analogous to the front panel of an electronics unit, and a “block diagram” which is analogous to a circuit diagram of the unit’s hard-wired logic. In this manner, the “code” written in LabVIEW is a reproduction of the logic in diagram form rather than lines of text. Examples from *FROG 3D* of the front panel and block diagram are shown in Figures 2.1.1-A,B,C.

The first functionality of my *FROG 3D* program<sup>1</sup> was to automatically align the position of the confocal pinhole. To perform alignment, *FROG 3D* controls the motors which control the radial position of the confocal pinhole along the optical axis, while reading the signal output from the correlator card. Starting from an initial guess based on the experience of manual alignments, the program moves the pinhole in 0.2 mm increments while recording the average photon counts in the detectors as reported by the correlator card at each position. The pinhole finds the maximal signal position along the two radial axes and then searches further around the maximal signal position at smaller increments of 0.04 mm and then finally at increments of 0.008 mm. In this manner, the optimal radial position for the confocal pinhole is found. To provide visual confirmation of the success of the routine to find the optimal position, the signal detected vs. 2-D position is plotted on a 3-D plot which usually results in a Gaussian-like profile as shown in Figure 2.1.1-B. An unclear peak may alert the user to an alignment failure.

Later, the ability to search for an optimal position along the optical axis, the “z-axis,” was added, but as the signal is less sensitive along the z-position, alignment precision of 0.5 mm is usually sufficient, and this functionality is usually only required when significant changes to the optical setup are made. For the case where two wavelengths of fluorescence are being detected at once, the program has an optional two-color mode which allows the user to align the pinhole by taking the mid-point between the two optimal maximal signal positions corresponding to each channel.

---

<sup>1</sup> The name of the program comes from my assembly programming professor’s pedagogical habit of always naming objects of a specific type by similar names for ease of recognition by students. He usually named the programs used in lectures with names such as “frog” or “log.” Thus, I began saving the work-in-progress program as “frog” and the name stuck, as it seemed somewhat appropriate due to the way the pinhole hops around during alignment. The designation 3D was added to the name when I developed the functionality to move the pinhole along the optical axis as well as the radial axes.

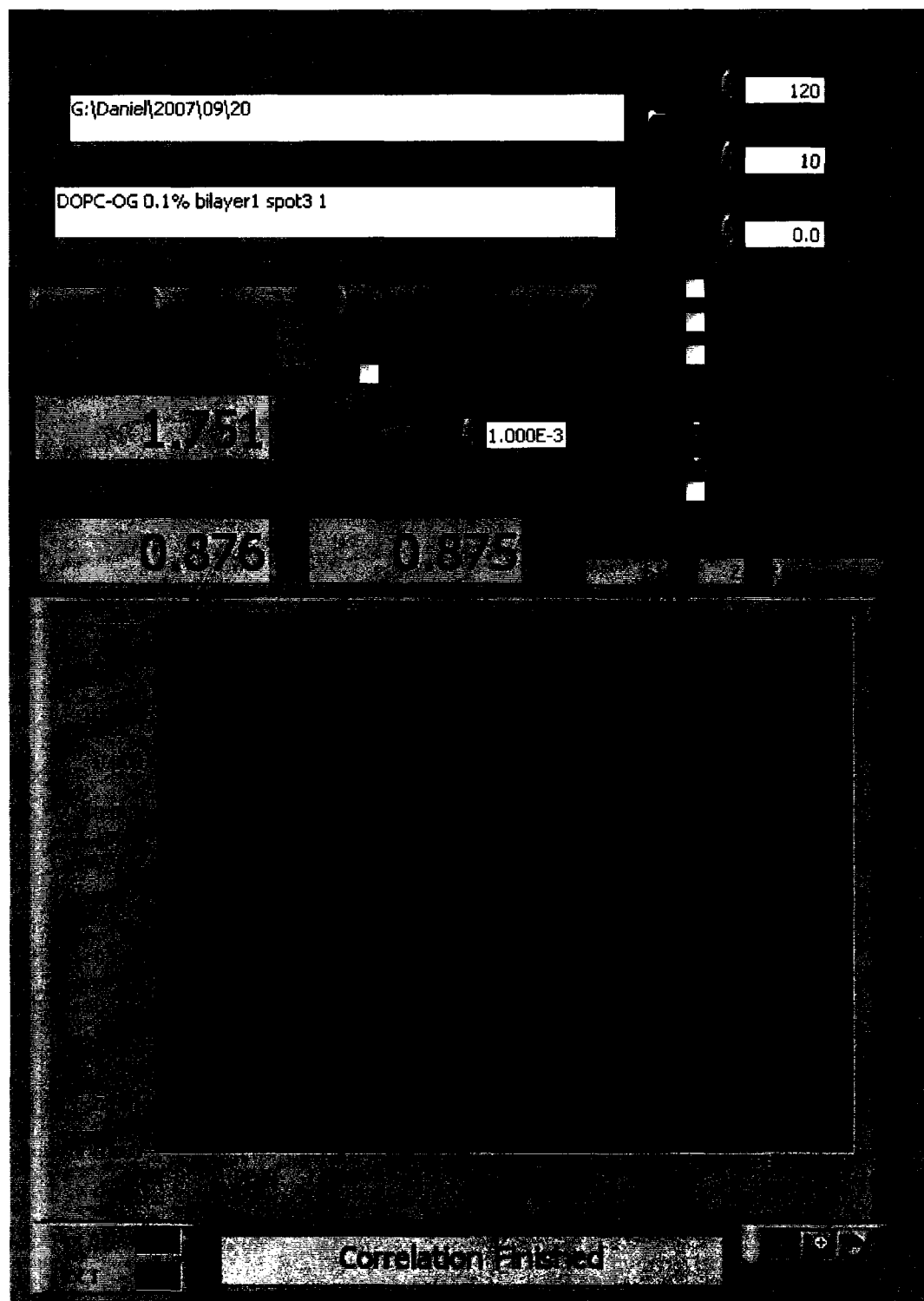


Figure 2.1.1-A. The right side of the front panel of *FROG 3D*.

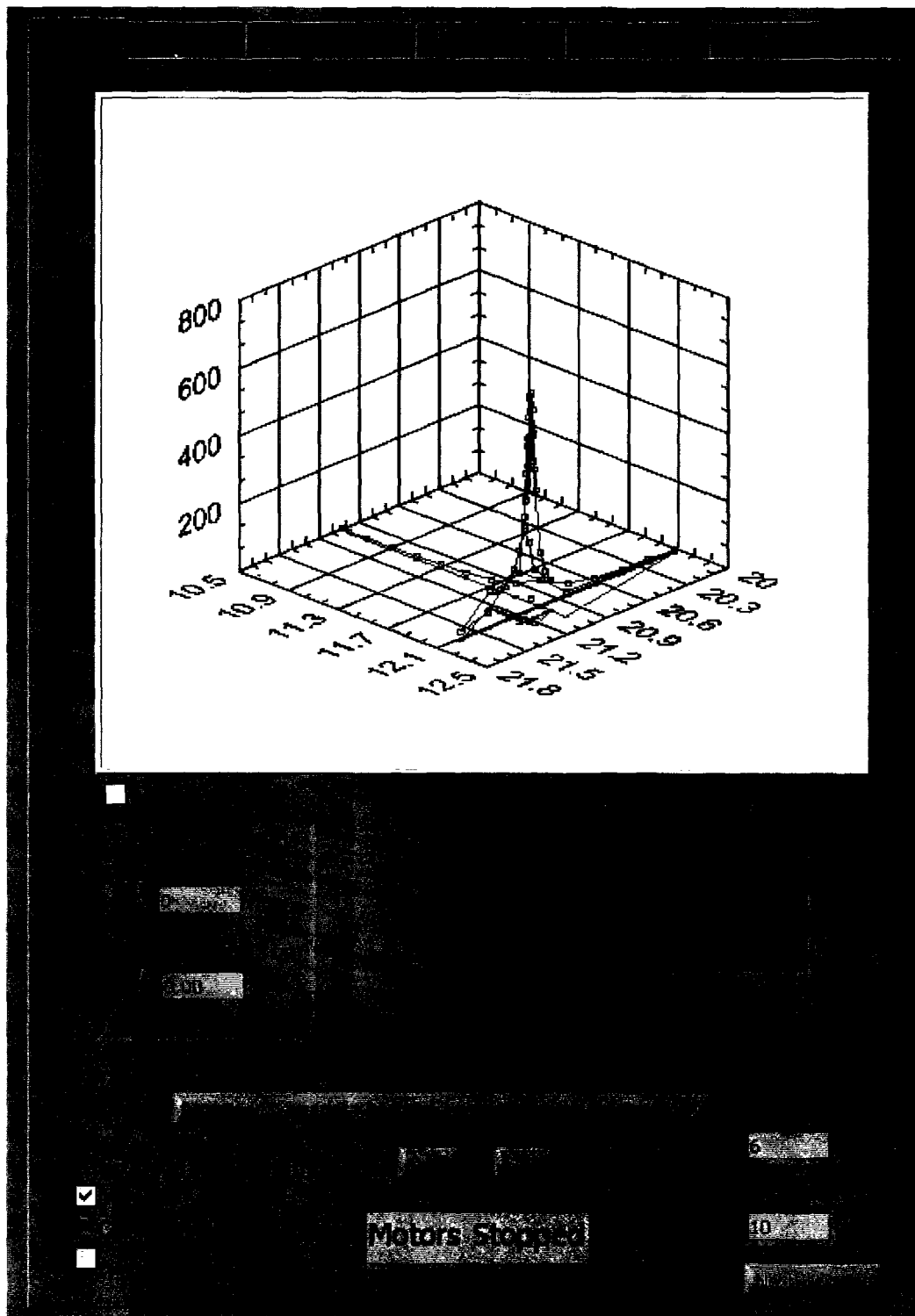


Figure 2.1.1-B. The left side of the front panel of *FROG 3D*.

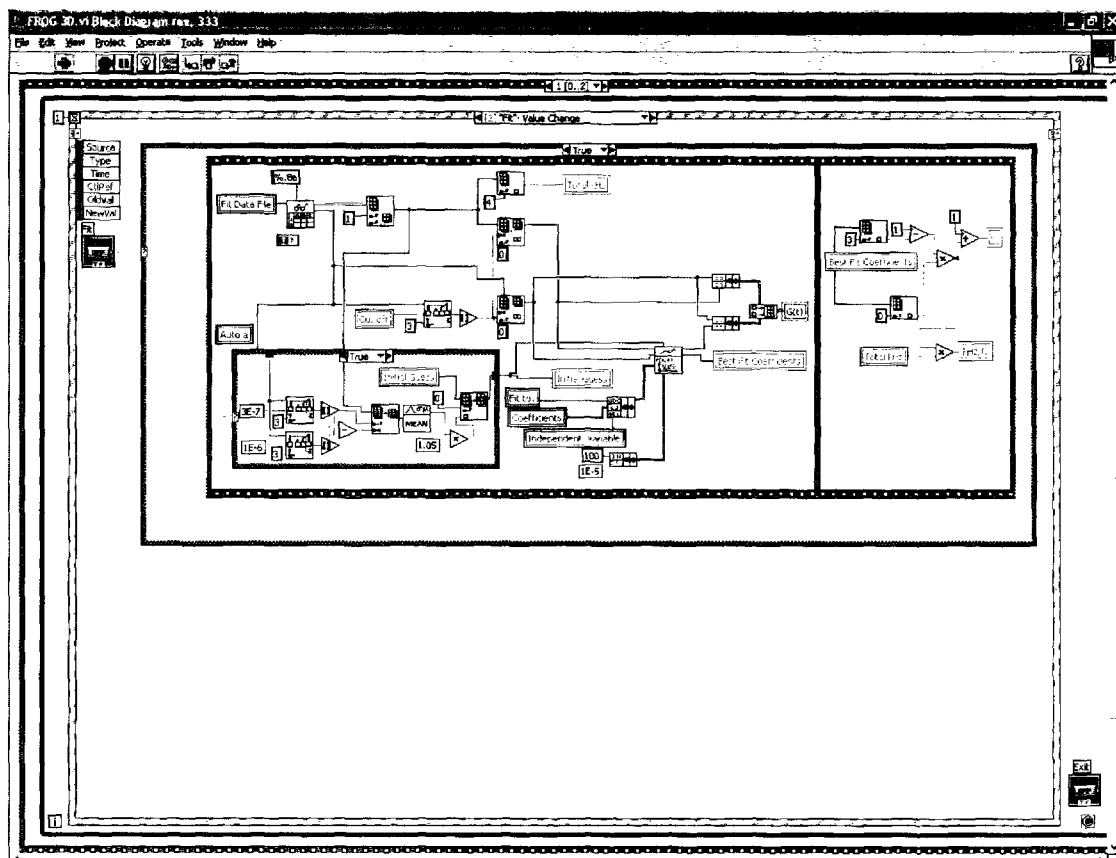


Figure 2.1.1-C. A section of the block diagram of *FROG 3D* illustrating the analogy of the hard-wired logic of a circuit diagram.

The second function of *FROG 3D* is to record and save the correlation data as instructed by the user who chooses how long to record and how many data sets to be taken consecutively. This functionality allows the user to set the experiment to take data for, say, 20-30 minutes at a time while the user leaves the “dark room” to restore his emotional well-being in another room or to eat lunch. While recording, it displays the correlation data and photon counts as the data so that the user gets immediate feedback concerning the success and quality of the measurement. These plots are updated every 750 ms and the resolution of the photon count history data is 67 ms. After recording the data, the correlation data and photon counts at 67ms resolution are saved in separate files. The program also contains an option to allow the user to record the photon count at higher resolutions where bin times less than 1  $\mu$ s are possible, though this can result in very large data files. In principle, one can calculate photon counting histograms with the photon count data as an alternative to the correlation data to measure specific brightness, but this capability was not included in *FROG 3D*.

Third, a simple fitting routine allows the user to obtain an immediate estimate of the brightness per molecule and quality of the fit (the red line in Figure 2.1.1-A is the fit to the data in blue). This allows the user to observe the shape of the correlation decay and the quality of the signal compared to reference samples. Distortion in either the shape or brightness value may alert the user to problems with the optical alignment or sample.

Fourth, the program allows the user to control the position of the objective along the z-axis via a piezo-electric objective-positioner and the x- or y-position of the sample using a piezo-electric stage controller (see Figure 1.4.2-A). Unfortunately, due to the limitations of the hardware controller, only 2 of the 3 axes can be controlled at once. The third axis must be adjusted manually.

The fifth function is to control two optical shutters, one immediately before the microscope, and one immediately after it (see Figure 1.4.2-A). As a safety mechanism, the program will automatically close the shutters if either of the two photomultiplier detectors receives an average photon count above 1 MHz over a 750 ms interval in order to prevent damage to the detectors. The user can also control the shutters manually from the computer and insert a delay between opening the shutters and recording the correlation.

Sixth, the program creates script files for each correlation data file created to be used later with KaleidaGraph software to automate some of the data analysis process. It allows the user to automate a fit to the data provided that the user selects the appropriate fit equation to be used in advance of recording the data. The script files contains the path with the name of the files containing the correlation data photon count histories, and it contains the selected fit options including the range of data to be fit and the values of fit parameters to be used as either initial guesses or as fixed values. When the script file is executed within KaleidaGraph, the script instructs KaleidaGraph to do the following: (1) open the correlation data file, (2) calculate an appropriate initial guess for the correlation amplitude based on the values between 0.5 and 1  $\mu$ s, (3) calculate an initial guess for the diffusion time based on the time range at which the correlation data reaches 40-60% of the initial guess for the amplitude, (4) mask the data below a value set by the user (for example, ignoring the correlation data for lag times less than  $<1 \mu$ s is often useful due to high scatter in the data or due to the presence of shot noise if the only one detector is used, see section §1.4.2), (5) set the values of the aspect ratio  $S$  or triplet state time  $\tau_T$  to be used as initial guesses or fixed values in the fit, (6) open a pre-existing KaleidaGraph plot that acts as a template according to which KaleidaGraph will plot and fit the correlation data, (7) save the correlation plot, (8) open corresponding file containing the photon count history, (9) plot the photon count history according to another template plot, and (10) save the plot of the photon count history. *FROG 3D* also contains script files which can be run immediately after refreshing the correlation plot showing the fit to export the curve fit parameters with errors into the operating system clipboard to be pasted into Microsoft Excel for further analysis.

Although this functionality greatly increased the speed of my data analysis, it suffered from the following limitations: (1) only one data file at a time could be processed, (2) the script file was useless if the path or file name of the data was changed, (3) if the user selected the wrong fit before taking the data or if the user wished to fit with more than one fit, additional fits still had to be applied manually, and (4) this process was not found to be friendly to other users. Eventually, I solved many of these limitations by writing a separate LabVIEW program that is more user-friendly and able to write the script files upon demand rather than solely at the time the data is taken. The new program (“WriteScirptFile4.vi”) facilitates successful fitting of multiple data files at once and compiles the results from all the fits in a convenient format both in a single file and in the operating system clipboard and is shown in Figure 2.1.1-D.

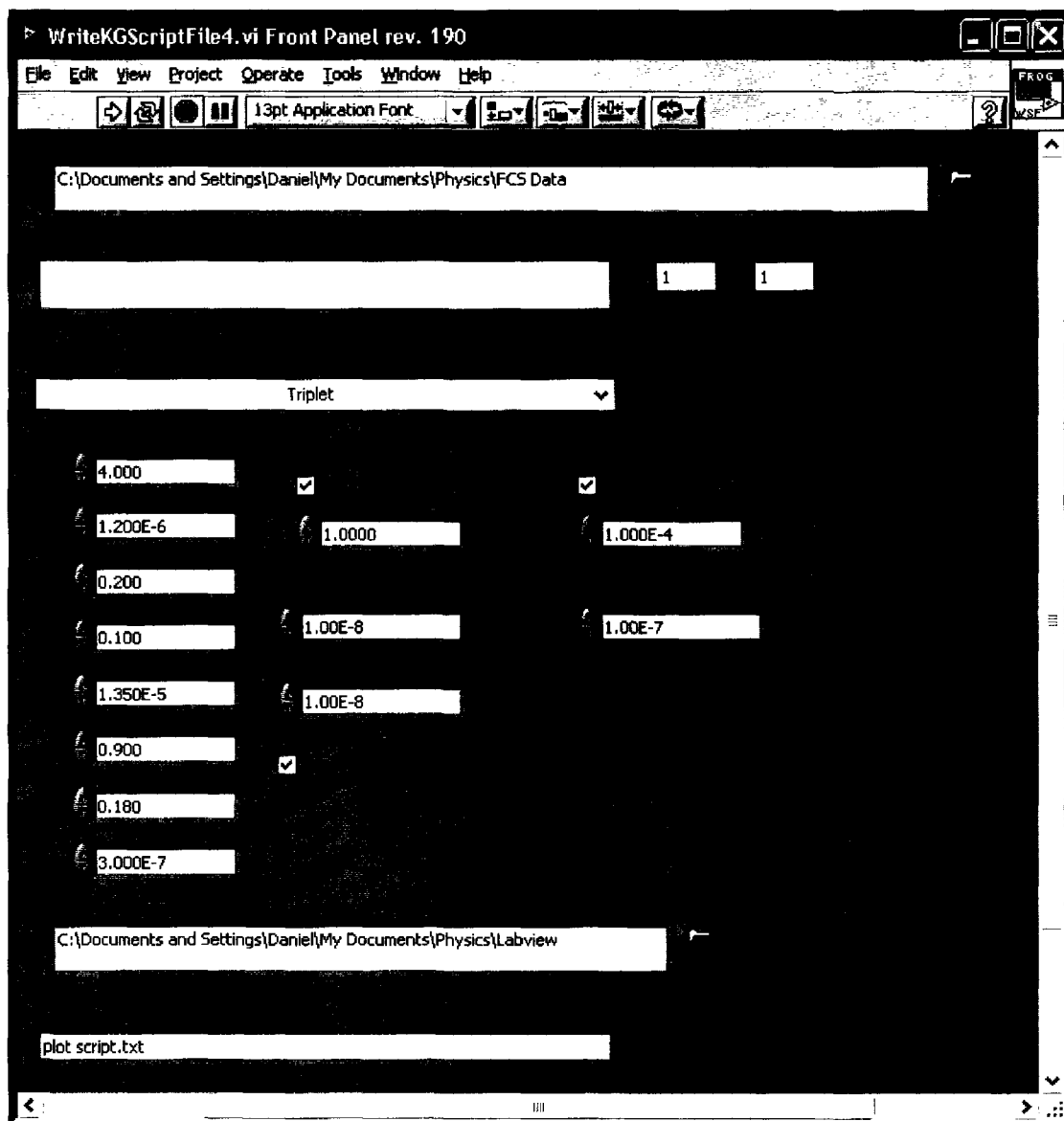


Figure 2.1.1-D. Front Panel of WriteScriptFile4.vi.

### 2.1.2. Description of the development of the VLS-FCS capability

Variable Length Scale Fluorescence Correlation Spectroscopy (VLS-FCS) is a recently published variation of FCS in which one varies the size of the observation volume in order to study the length scale dependence of the diffusion (77-79, 147, 182, 210). In conventional FCS, an excitation laser fills the back aperture of the objective to obtain a diffraction-limited excitation volume, thereby determining diffusion coefficients at a fixed observation length-scale. In VLS-FCS, the width of the beam illuminating the back aperture of the objective is incrementally reduced which effectively sacrifices the full resolving power of the objective to create wider excitation volumes. The resulting fit parameters are then analyzed as a function of the observation length-scale. To optimize the specific brightness and the range of accessible length scales, a confocal pinhole must also be selected to match the observation volume radius at each observation volume size. This change in the observation volume is illustrated in Figure 2.1.2-A.

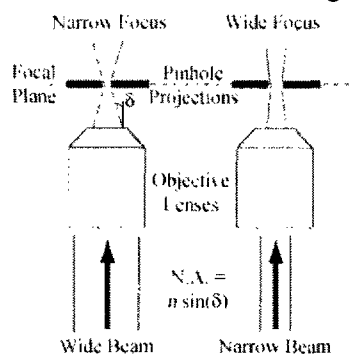


Figure 2.1.2-A. Diagram of the change in excitation spot size at the focal plane due to filling or under-filling the back aperture of the objective lens. The dashed line indicates the focal plane, and the dark bands are projections of the confocal pinhole into the focal plane. The numerical aperture of the lens (N.A.) is equal to  $n \sin(\delta)$ , where  $\delta$  is the angle indicated in the diagram (the half-angle of the cone of light accepted by the objective lens), and  $n$  is the index of refraction.

To adjust our home-built setup to perform VLS-FCS, I added two components to the optical excitation path: a continuously variable metallic neutral density filter in place of the polarizers, and a calibrated iris diaphragm. The iris diaphragm was added after the spatial filter to control the width of the beam reaching the back aperture of the objective (see Figure 2.1.2-B). Due to the spatial gradient of transmission of the filter, it was placed immediately after the laser where the beam is the smallest in order to minimize distortion in the otherwise Gaussian beam profile. The disadvantage of the polarizers as a means to adjust intensity compared to neutral density filters is that the polarizers also slightly change the angle of the beam path. This slight change can greatly distort the observation volume when the diameter of the iris aperture further down the optical path is small, especially when the peak of the 2-D Gaussian beam does not pass through the aperture. With VLS-FCS, it is advantageous to adjust the laser power before the iris for each different observation volume in order to achieve equal laser power after the iris (i.e.,

at the sample). Since the continuously variable neutral density filter does not alter the beam path, it is a great advantage to VLS-FCS experiments.

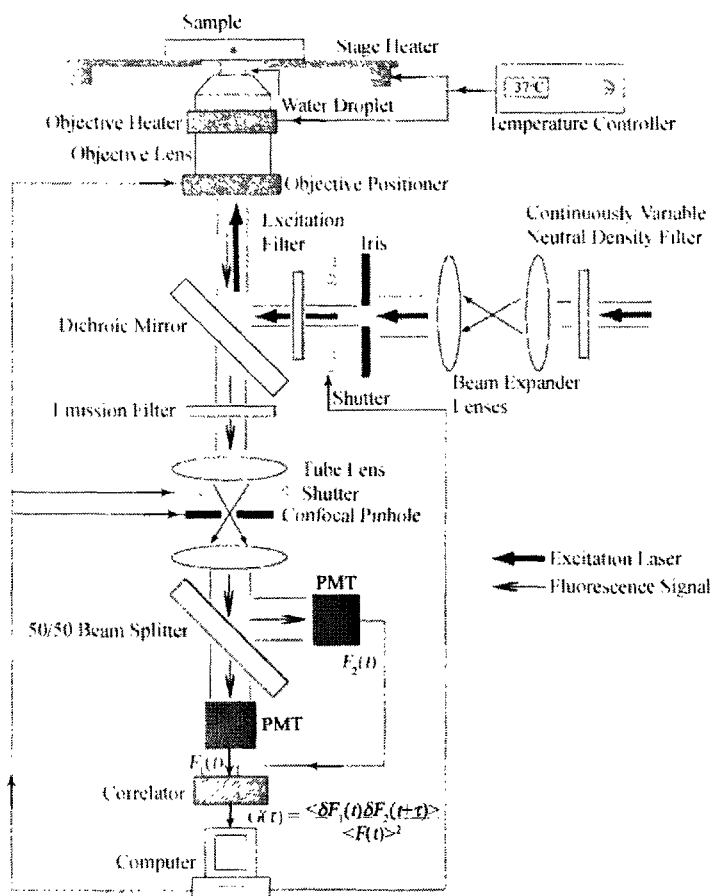


Figure 2.1.2-B. A diagram of the FCS apparatus adjusted for VLS-FCS. Compared to Figure 1.4.2-A, the polarizers have been removed, and a continuously variable neutral density filter and an iris diaphragm have been added along the excitation beam path.

In addition to the added components, a set of pinholes with various diameters were acquired so that the optimal pinhole size could be used for each iris diaphragm diameter. I performed FCS measurements on standard dyes and fluorescent proteins with various combinations of confocal pinholes and iris diameters to determine by trial and error convenient combinations to achieve strong specific brightness values with observation volume radii spaced appropriately on a log scale. As noted earlier (§1.4.2), the specific brightness is a crucial parameter determining the statistical significance of the FCS data. The final result was a choice of pinholes with diameters of 50, 75, 100, 150, 200, and 300

$\mu\text{m}$ , corresponding to iris diameters of 12, 4, 2.5, 1.25, 0.9 and 0.5 mm respectively, resulting in observation volume radii from about  $r_0 = 200$  nm to  $r_0 = 1.5$   $\mu\text{m}$  using the 60x 1.20 N.A. water immersion objective. These combinations were then used for all VLS-FCS experiments reported in §4.2, and were also found to be satisfactory for observations taken in toluene using a 100x 1.3 N.A. oil immersion objective, as reported in §2.3.1.

To determine the appropriate laser power to use to avoid photobleaching for each sample that we used with VLS-FCS, systematic measurements were taken of the brightness per molecule and diffusion times as a function of laser intensities at both smaller and larger values of  $r_0$ . See for example, Figures 2.1.2-C, D. For Alexa Fluor 488 at the diffraction-limited volume,  $r_0 = 210$ nm, the specific brightness rises to saturation at 100 kHz per particle at approximately 300  $\mu\text{W}$ . In contrast, fluorescein reaches saturation at only 50  $\mu\text{W}$  after which the brightness decreases. At a larger volume,  $r_0 = 750$ nm, saturation is not reached at these laser powers because the laser intensity is reduced by an order of magnitude due to the larger beam radius. The inset to Figure 2.1.2-C shows the same specific brightness data as a function of laser intensity.

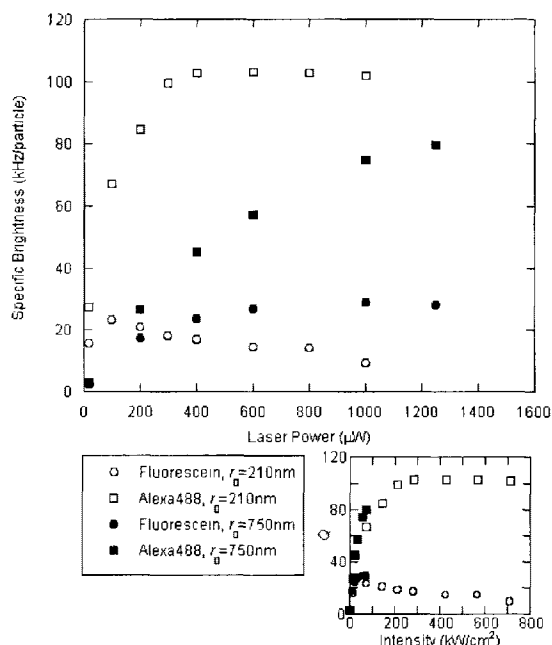


Figure 2.1.2-C. Specific brightness (kHz/particle) of fluorescein (*circles*) and Alexa Fluor 488 (*squares*) as a function of excitation power and intensity (*inset*) at  $r_0 = 210$  nm and 750 nm.

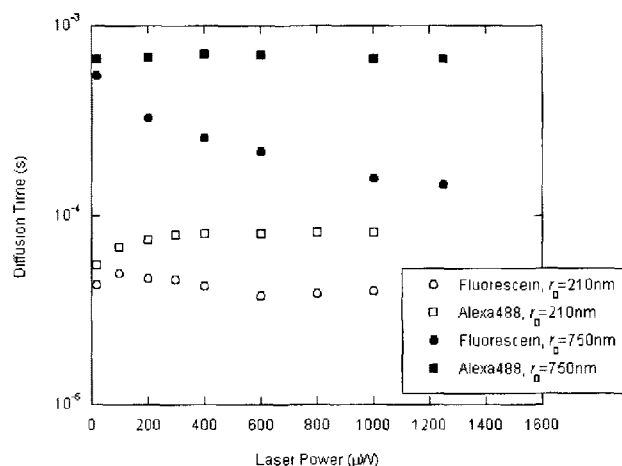


Figure 2.1.2-D. Diffusion times (s) of fluorescein (*circles*) and Alexa Fluor 488 (*squares*) as a function of excitation power and intensity (*inset*) at  $r_0 = 210$  nm and 750 nm.

Figure 2.1.2-D shows the diffusion time,  $\tau_D$ , as a function of laser power. For Alexa Fluor 488 at the diffraction-limited volume,  $r_0 = 210$  nm, the diffusion time rises due to optical saturation occurring not just at the optical axis, but over the entire observation volume. When such saturation occurs, the brightness of the dyes are no longer spatially dependent, and therefore the 3-D Gaussian profile is significantly distorted, resulting in an apparently larger observation volume with correspondingly larger diffusion times (211). At the larger volume,  $r_0 = 750$  nm, the diffusion time does not increase because the corresponding intensities are lower (see Figure 2.1.2-C inset), nor does it show a decrease due to photobleaching.

Fluorescein, on the other hand, appears to be much more susceptible to photobleaching. Photobleaching reduces the average amount of time each particle spends fluorescing in the volume, and therefore the apparent diffusion time decreases. The data suggest that the laser power is the relevant parameter in determining the presence of photobleaching rather than the laser intensity. A simple scaling argument suggests the correctness of this observation: When the excitation power is held constant, the photon flux,  $\Phi$ , scales as the inverse square of the observation volume radius,  $\Phi \propto r_0^{-2}$ . If the diffusion time of the fluorophore scales as the square of the observation volume radius,  $\tau_D \propto r_0^2$ , then the number of photons absorbed by the fluorophore during a passage through the volume scales as  $\Phi \tau_D$  and should not depend on  $r_0$ . Therefore, the laser power was held constant at each observation volume rather than the laser intensity, and when using fluorescein for calibration, we found that a constant laser power at 20  $\mu$ W for all values of  $r_0$  is a good rule of thumb to avoid photobleaching and saturation while retaining sufficient signal.

## 2.2 Summary of Manuscripts

### 2.2.1 Summary of *Anomalous Diffusion of Proteins Due to Molecular Crowding*

#### *Introduction*

In the introductory sections, I have described the biological importance of diffusion and reviewed experimental studies concerning the nature of diffusion in complex media such as the cellular environment (§1.2). The research reported in *Anomalous Diffusion of Proteins Due to Molecular Crowding* seeks to determine experimentally whether the anomalous diffusion of proteins reported in the cytoplasm can be reproduced *in vitro* by molecular crowding alone. The system chosen to imitate the cytoplasmic crowding by macromolecules was a buffer solution of highly concentrated random-coil polymers or globular proteins. Streptavidin labeled with Alex Fluor 488 dye was the fluorescent protein whose diffusion was characterized by FCS.

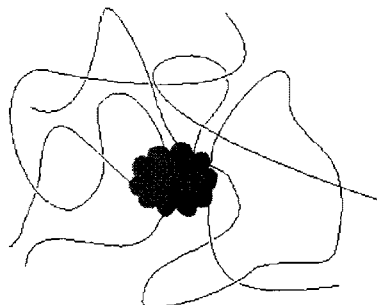


Figure 2.2.1-A. Cartoon illustration of overlapping random coil polymers in solution transiently trapping a globular macromolecule and thus hindering its diffusion.

#### *Results*

The correlation data corresponding to the diffusion of streptavidin in this system showed a noticeable deviation from Brownian diffusion behavior. Figure 2.2.1-B shows this deviation, where the correlation decay for the simple diffusion model decays over a shorter time range, that is, the simple diffusion model falls below the data at long times and above at shorter times.

Due to the model-dependent nature of FCS, we introduce two methods of distinguishing anomalous diffusion from two-component diffusion in our system. First, we look at the long time scaling of the correlation decay, since at long lag times, the correlation function for normal diffusion scales as  $\sim t^{-3/2}$ , while for anomalous diffusion it scales as  $t^{-3\alpha/2}$ . Second, we use a Maximum Entropy Method for FCS (MEMFCS) analysis which fits the correlation data assuming a quasi-continuous distribution of average diffusion times. For correlation data which is truly two-component in nature, the MEMFCS algorithm should produce two distinct narrow distributions, whereas for anomalous diffusion, it should

produce one broad distribution. Use of these methods confirmed that the anomalous diffusion model was preferred for our data.

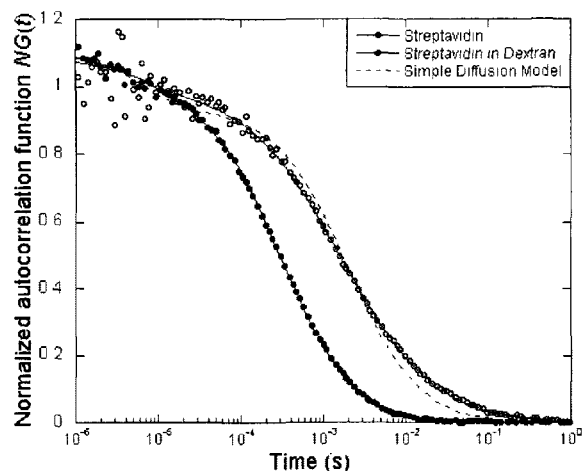


Figure 2.2.1-B. Normalized autocorrelation functions for streptavidin diffusing in Phosphate Buffered Saline (PBS) with and without dextran obstacles (200 g/l of 276.5 kDa dextran). The fit of these autocorrelation functions using the anomalous diffusion model gives  $\alpha = 0.99 \pm 0.01$  for no obstacles, and  $\alpha = 0.76 \pm 0.01$  with obstacles (solid lines). The failure of the fit with the simple diffusion model for the case with obstacles is also shown (dashed line).

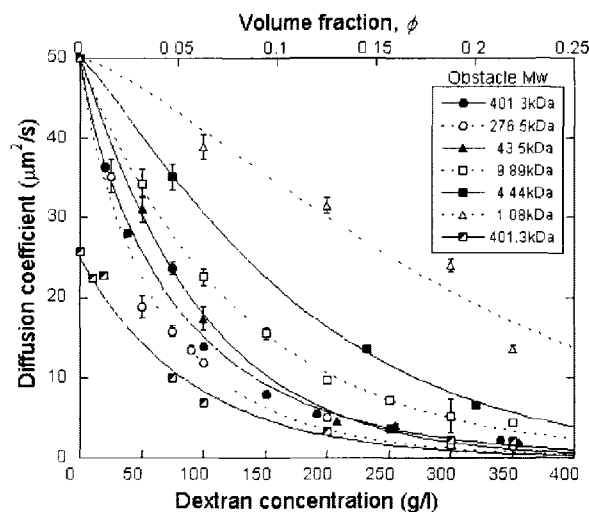


Figure 2.2.1-C. Apparent diffusion coefficient,  $D$ , associated with the diffusion of streptavidin as a function of dextran concentration for dextrans of having the average molecular weights (Mw) indicated (open and solid symbols). Also shown is  $D$  for a 282 kDa dextran diffusing in a solution crowded by a 401.3 kDa dextran (half-solid symbols). Lines represent stretched exponential fits as explained in the text (see manuscript).

Using the anomalous diffusion model, we found that the apparent diffusion coefficient (defined in Equation 1.1.4-2) decreases roughly exponentially with increasing dextran concentration as was expected (see Figure 2.2.1-C). The central result of this study was that the anomalous diffusion exponent was observed to decrease exponentially toward a limit value of  $\alpha \approx 3/4$  at high concentrations of high molecular weight dextran approaching 400 g/l (see Figure 2.2.1-D). Further, we observed that the diffusion of proteins in dextran solutions is anomalous even at low obstacle concentration. The anomalous diffusion exponent  $\alpha$  decreases continuously with increasing obstacle concentration and molecular weight, but was not observed to depend on buffer ionic strength nor to depend strongly on solution temperature. In this paper, a hypothesis is discussed that the limit value of  $\alpha \approx 3/4$  corresponds to a coupling between the motions of the tracer proteins and the segments of the dextran chains.

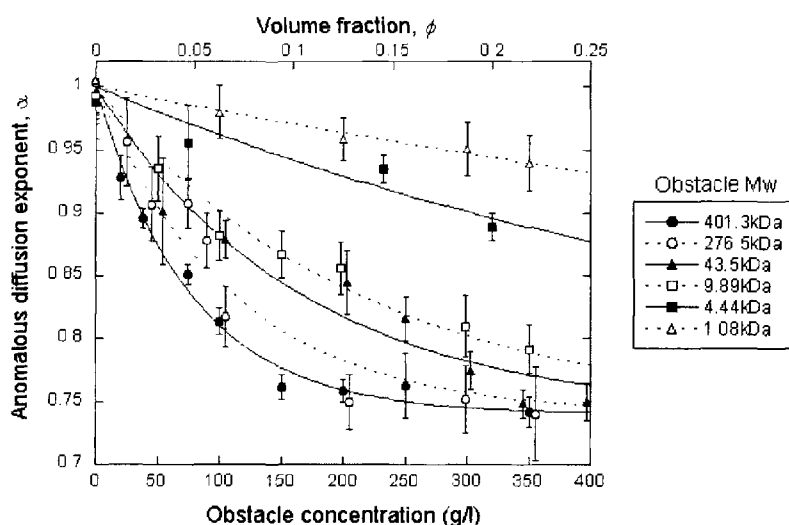


Figure 2.2.1-D. Anomalous diffusion exponent associated with the diffusion of streptavidin as a function of obstacle concentration for dextrans of having the average molecular weights (Mw) indicated. Lines are fits to the data using with  $\alpha = \alpha_l + (1 - \alpha_l)\exp(-\phi/\phi_0)$  where  $\alpha_l = 0.74$ . Where necessary, some of the data points have been slightly shifted horizontally for clarity of the plots.

We also tested for similar effects using EGFP, fluorescently labeled dextran, and fluorescein. The diffusion of the EGFP was anomalous to a similar degree as the streptavidin, while the diffusion of the dextran and fluorescein were both normal. Similar, although less pronounced, subdiffusive behavior is also observed for the diffusion of streptavidin in concentrated globular protein solutions.

### Conclusion

The successful reproduction of the anomalous diffusion reported in various cellular systems indicates that macromolecular crowding may indeed be a significant factor in

contributing to the anomalous diffusion observed in the cell cytoplasm and nucleus, and argues for the correctness of the anomalous diffusion model over the two-component model for analysis of data taken *in vivo*. Our study has been used to discuss the crowded nature of bacterial cytoplasm in a recent single particle tracking study of mRNA in *E. coli*, which suggests that the macromolecular concentration in the bacterial cytoplasm is above the threshold volume fraction,  $\phi_0$ , where the value of  $\alpha$  is stable (50). Our initiative in using the MEMFCS algorithm to distinguish between two-component diffusion and anomalous diffusion has now been followed by at least one other study which investigated diffusion in sol-gels (113).

**2.2.2 Summary of Diffusion Power Laws in Polymer Solutions and Gels Observed Using Variable Length Scale Fluorescence Correlation Spectroscopy**

*Introduction*

The previous paper, *Anomalous Diffusion of Proteins Due to Molecular Crowding*, showed the success of anomalous diffusion theory in modeling the FCS data taken at a fixed length scale for the system studied. Since the anomalous diffusion model predicts that the apparent diffusion coefficient is length-scale dependent, then a crucial test of this model is to alter the length scale of observation to determine whether the predicted dependence is correct. The recent development of Variable Length Scale Fluorescence Correlation Spectroscopy (VLS-FCS) to study the length-scale dependence of diffusion (77-79, 147, 182, 210) suggested a suitable means to perform this test.

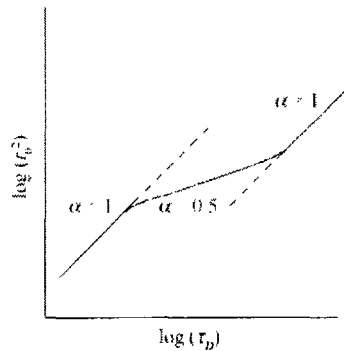


Figure 2.2.2-A. Illustration of the diffusion power law, that is, the scaling law  $r_0^2 \propto \tau_D^\alpha$ , for the case where a region of power law behavior occurs in between two regions of normal diffusion.

A key concept in this paper is the diffusion power law, illustrated in Figure 2.2.2-A. For anomalous diffusion the mean-squared-displacement scales as a power law in time,  $\langle r^2(t) \rangle \propto t^\alpha$ . In FCS, the observation volume radius,  $r_0$ , is the observation length scale, and the characteristic diffusion time,  $\tau_D$ , is the corresponding observation time-scale. Therefore when  $r_0$  is varied in VLS-FCS, one should expect to observe the relationship  $r_0^2 \propto \tau_D^\alpha$ , which we call the diffusion power law (as distinct from the diffusion law defined by Wawrezynieck *et. al.* (78, 79) where  $\tau_D = r_0^2 / 4D + \tau_0$  and where non-Brownian behavior is indicated by  $\tau_0 \neq 0$ ). The wide range of  $r_0$  allows one to obtain the anomalous exponent  $\alpha$  by directly observing the diffusion power law, denoted  $\alpha_{DL}$ , in addition to observing  $\alpha$  obtained from the correlation data fit at each  $r_0$ , denoted  $\alpha_p$ . The modification of our FCS setup to achieve VLS-FCS with a range of change in observation volume radius  $r_0$  of nearly a factor of 10 is described in §2.1.2 and a brief description is also included in the manuscript. We applied this method to the study of

systems where anomalous diffusion has been reported previously, including our streptavidin-dextran system.

*Results*

For the diffusion of polymer beads in 1.4% agarose gels, the value of  $\alpha_p$  increases from 0.82 to 0.97 as the observation volume is increased, and the diffusion power law yields a corresponding value of  $\alpha_{DL} = 0.92$ . This result is important because it demonstrates agreement between the complementary methods and directly verifies a length-scale dependence of diffusion in this system, namely, a 35% drop in the apparent diffusion coefficient over an order of magnitude difference in  $r_0$ . For streptavidin diffusion in dextran solutions, the diffusion power law shows no observable length-scale dependence over this range, that is,  $\alpha_{DL} = 1$ . Yet,  $\alpha_p$  increases from  $\sim 0.82$  to  $\sim 1.02$  as the observation volume is increased in a manner similar to the beads in agarose. Observations similar to the protein-dextran system are reproduced in the bead-agarose system by reducing the concentration of the agarose to 0.5%.

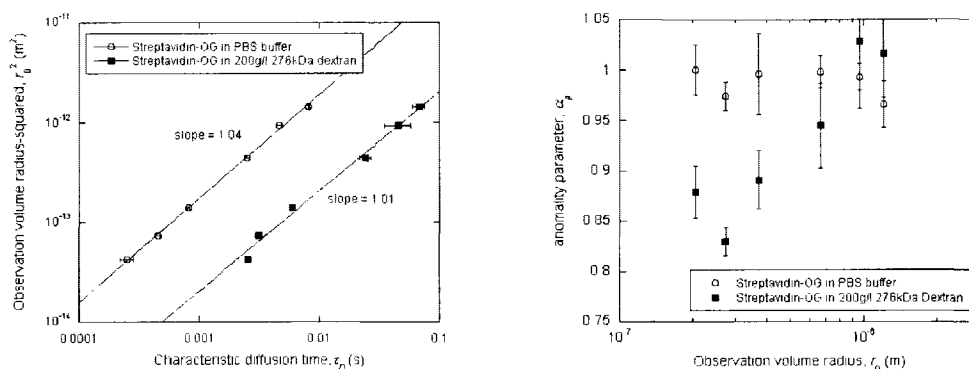


Figure 2.2.2-B. Left Panel: Diffusion laws for Streptavidin-OregonGreen in PBS buffer (*circles*) and with 200 g/l 276 kDa dextran (*squares*). The slope gives the value of the anomalous exponent for the diffusion power law,  $\alpha_{DL}$ . Right Panel: The values of the anomalous exponent determined by direct fit of the correlation data at each observation volume,  $\alpha_p$ .

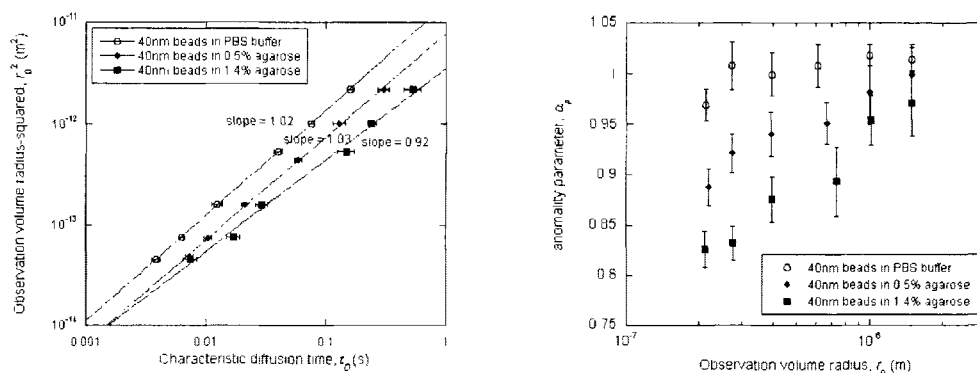


Figure 2.2.2-C. Left Panel: Diffusion laws for 40 nm Orange beads in PBS buffer (*circles*) and with 0.5% agarose (*diamonds*) and 1.5% agarose (*squares*). The slope gives the value of the anomalous exponent for the diffusion power law,  $\alpha_{DL}$ . Right Panel: The values of the anomalous exponent determined by direct fit of the correlation data at each observation volume,  $\alpha_p$ .

### Discussion

The manuscript argues that the results are consistent with a cross-over model of two diffusion behaviors each dominating at a different length scale. Further, it is argued that the two-component model, which is independent of length-scale, is insufficient to account for the observations. Numerical calculations are reported as illustrations of cross-over behavior. The calculations were based on a recently published stick and diffuse model which gives an analytical correlation function. The calculations show that in a cross-over regime, the numerical values of  $\alpha_{DL}$  and  $\alpha_p$  are not in general identical, nor will their minima occur at the same value of  $r_0$ .

### Conclusion

In the systems studied here, we confirmed that there is a length-scale dependence of the correlation data which cannot be explained by normal diffusion. A cross-over interpretation of the length-scale dependence of the diffusion is possible, and this may be important to explain some of the observations of anomalous diffusion *in vivo* where the cross-over regime could be quite broad. We have achieved nearly an order of magnitude difference in  $r_0$  to allow us to successfully observe the diffusion power law directly. Thus, VLS-FCS has been demonstrated to be an important tool for the study of anomalous diffusion in systems that are accessible to FCS.

### Summary of Contributions and Acknowledgements

Robert Peters acquired approximately half of the correlation data with respect to streptavidin diffusing in PBS with and without dextran obstacles and the data where the extra correlation term was studied for streptavidin labeled with fluorescein and Alexa488 (this data was mentioned in the manuscript but not discussed here) and assisted me in fitting the correlation data to various models. The development of the VLS-FCS set up,

the data acquisition and analysis of remaining streptavidin data and all of the agarose systems, and the numerical modeling of the modified stick and diffuse model for illustration purposes were my own work.

### 2.2.3 Summary of A Molecular Thermometer based on Fluorescent Protein Blinking

#### Introduction

The previous manuscripts focused on the diffusion term of the correlation function to gain insight into the system of interest. Here we demonstrate a practical use for one of the photophysical correlation terms of EGFP observed with FCS. By analyzing its rate of blinking as a function of temperature at low pH, we should that we could use the rate of blinking to determine the temperature where the temperature is not controlled. Thus we are able to use EGFP as a molecular thermometer for precise characterization of physicochemical parameters in very small fluid volumes.

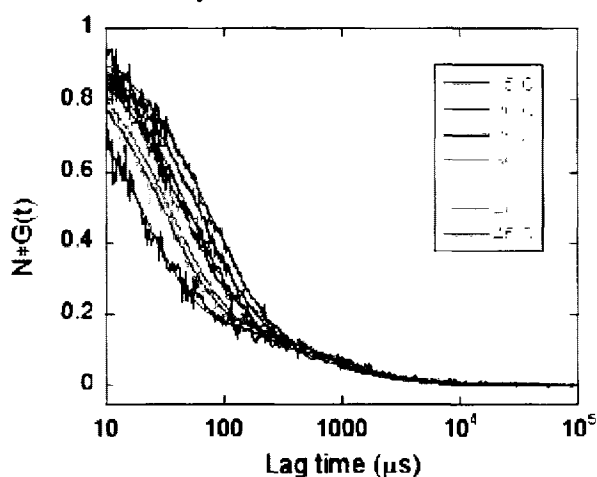


Figure 2.2.3-A. Autocorrelation data obtained for EGFP in CP buffer (pH = 5) at different temperatures. Each curve corresponds to a 60s measurement. Correlation functions have been normalized to allow a better comparison between the different curves. Lines are fit of the data using Equation 1.4.1-48. The correlation corresponding to protein blinking is visible around 50-100  $\mu\text{s}$ , and shows a very clear temperature dependence.

#### Results

Simple expressions were derived to relate the characteristic blinking relaxation time and the amplitude of the correlation blinking term to the activation energies of protonation and deprotonation and to the corresponding frequency factors (Equations 2.2.3-1,2). These thermodynamic parameters were obtained at different pH's and laser excitation powers and reported in the supplementary data.

$$1/\tau_B = 10^{-\text{pH}} A_p e^{-E_p/RT} + A_d e^{-E_d/RT} \quad (2.2.3-1)$$

$$B/(1-B) = 10^{-\text{pH}} (A_p / A_d) e^{-(E_p - E_d)/RT} \quad (2.2.3-2)$$

Here  $E_p$  and  $E_d$  are the activation energies, and  $A_p$  and  $A_d$ , are the frequency factors at different pH.  $B$  is the average fraction of fluorophores found in the protonated state, and  $\tau_B$  is the characteristic relaxation time associated with protonation.

The application of this thermometer reported here is the measurement of laser-heating effects in thin liquid samples. As expected, we observed a linear dependence between the temperature increase at the laser focus and both the laser power and the sample extinction coefficient, as shown in Figure 2.2.3-B. In addition, we were able to measure the laser induced temperature increase at the glass to liquid interface, which is a value difficult to predict and hard to access experimentally. Indeed, far from the glass surface, the theoretical model shown in Figure 2.2.3-C predicts the temperature increase we measured, but close to the surface, it fails due to the difficulty of accurately taking boundary conditions into account. Our method on the other hand allows an accurate temperature measurement at the cover slip.

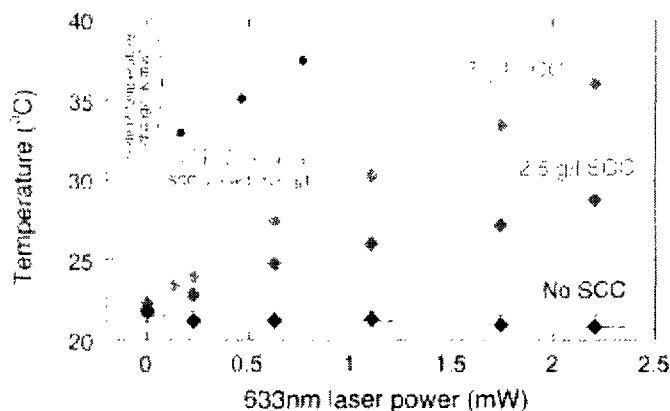


Figure 2.2.3-B. Increase in temperature at the focus of a 633nm laser beam for solutions containing different concentrations of SCC. Lines represent linear fit of the data.

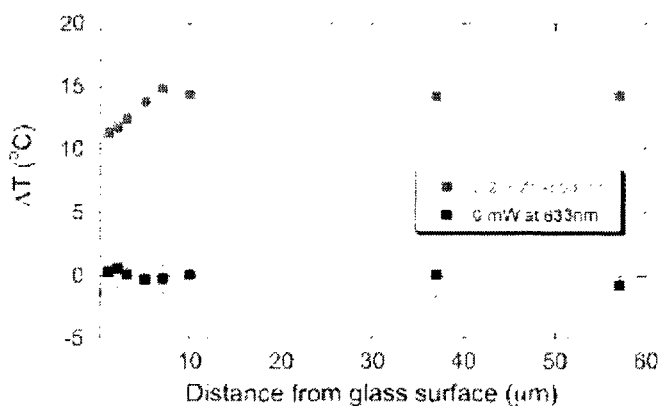


Figure 2.2.3-C. Temperature change at the laser focus in a 5g/l SCC solution as a function of the distance between the laser focus and the glass cover slip, in the presence and in the absence of 633nm laser excitation. Solid lines are theoretical predictions from Reference (212) calculated using  $\epsilon = 35 \text{ cm}^{-1}$  and  $K = 5.86 \text{ W K}^{-1} \text{ cm}^{-1}$ .

*Conclusion*

We have successfully demonstrated a molecular thermometer using EGFP blinking. This thermometer provides an absolute temperature measurement. The use of GFP derivatives as molecular thermometers should have direct applications for microfluidics such as studying surface effects in microfluidic chips. Further, single-cell calorimetry applications are possible through genetic encoding of the protein. This work was recently highlighted in *Nature* (213).

*Summary of Contributions and Acknowledgements*

Initial temperature calibration experiments at pH 5.0 were conducted by both Felix H. C Wong and me. Felix H. C. Wong conducted the remaining experiments and data analysis reported in the paper and supplementary data. I derived Equations 2.2.3-1 and 2.2.3-2 assuming that the reaction rates follow the Arrhenius law. The derivation given in the supplementary data includes modifications by Cécile Fradin to include the case where there are small concentration fluctuations away from equilibrium. Asmahan Abu-Arish contributed through unpublished studies of fluorescent protein blinking characteristics which provided intellectual background for the material presented, including verifying the temperature dependence at pH 5.0 (Haupts *et al.* (169) only reported it at pH 6.5) and comparative measurements in Phosphate Buffered Saline.

## 2.3 Summary of Additional Research

### 2.3.1. Application of VLS-FCS to the diffusion of polymers in organic solvents

#### *Introduction*

In previous sections, I described our development of our own VLS-FCS setup and its application to dextran solutions and Agarose gel as reported in *Diffusion Power Laws in Polymer Solutions and Gels Observed Using Variable Length Scale Fluorescence Correlation Spectroscopy*. An additional application of this method has been made to characterize the correlation data obtained from the diffusion of a dye and a labeled polymer in organic solutions. In this section, I will summarize these observations which further demonstrate the usefulness of VLS-FCS to obtain insight into diffusion in complex systems.

This research was part of a collaborative effort to observe for the first time the slowing diffusion coefficient of growing polymers during a polymerization reaction. The particular polymerization method of interest is called Atom Transfer Radical Polymerization (ATRP). ATRP is of extensive current interest because it results in low levels of polydispersity and gives a high degree of control over the final molecular weight of the product of the synthesis reaction. However, the dynamics of ATRP are not fully understood. In this system, the rate of the reaction is affected by the diffusion, and characterization of the diffusion *in situ* may allow fundamental theories (214) regarding polymerization kinetics to be tested and allows for a more profound understanding of ATRP.

In an *in situ* observation of such an ATRP reaction via FCS, the diffusion time of the labeled initiator is expected to show an increase over time as the polymer grows due to increasing hydrodynamic radius of the tracer, increasing viscosity of the medium, and increasing steric hindrances due to the polymer network, which could also cause the diffusion to progress from normal to anomalous as the reaction proceeds. Since there are multiple factors contributing to the resulting diffusion time, precise interpretation of the *in situ* data will require the use of control systems.

The ATRP reaction chosen for study consists of methyl methacrylate (MMA) in toluene solution where a small fraction of the polymer initiators have been labeled with a dye so that its diffusion can be observed by FCS. The initiator is the chemical subunit to which the MMA molecules are added in sequence to form a polymer chain during ATRP. Thus, polymerization starting from initiators with a single dye-label results in only one dye-label per molecule of poly-(methyl methacrylate) (pMMA). Note that HYC6Br denotes the labeled initiator for the ATRP reaction derived from the dye hostasol (see Appendix A to this section for structure and fluorescence properties), and HYC6-pMMA-Br denotes the labeled polymer which results from the reaction.

*FCS Results*

In anticipation of observations of the ATRP reaction *in situ*, initial FCS measurements were conducted directly on the product of the ATRP reaction, that is, a toluene solution containing 26 wt% pMMA and 2.5 nM 10 kDa HYC6-pMMA-Br, as well as catalysts left over from the reaction since no purification was performed. The diffusion coefficient was approximately  $D \approx 8 \mu\text{m}^2/\text{s}$ , which is equal to the diffusion coefficient we measured for streptavidin under equal concentrations of 10 kDa dextran, as reported in §4.1. The fluorescence correlation data was well fit by an anomalous diffusion model with  $\alpha = 0.6 - 0.7$ , suggesting further inquiry should be conducted using VLS-FCS to determine whether the diffusion is length-scale dependent as predicted by the anomalous diffusion model.

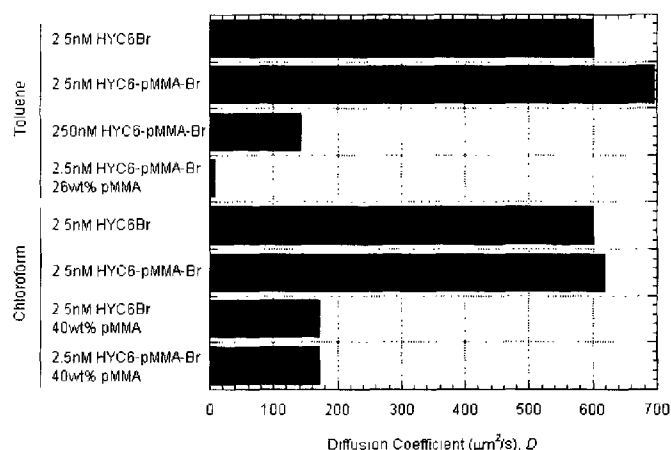


Figure 2.3.1-A. Apparent diffusion coefficients,  $D$ , for the samples specified in either toluene or chloroform, as discussed in the text.

Diffusion in other control systems were characterized, with surprising results. The diffusion of the labeled initiator, 2.5 nM HYC6Br, in toluene alone, that is, without any pMMA as a crowding agent, ( $D \approx 600 \mu\text{m}^2/\text{s}$ )<sup>2</sup> was in fact slightly slower than the diffusion observed for the labeled polymer, 2.5 nM 10 kDa HYC6-pMMA-Br, under the same conditions ( $D \approx 696 \mu\text{m}^2/\text{s}$ )m even though the polymer's molecular weight is approximately 20 times larger than that of the initiator. Although the Stokes-Einstein Equation (Equation 1.1.2-7),  $D = kT/(6\pi\eta R)$ , predicts that the smaller molecules should diffuse faster than larger ones, the diffusion of HYC6Br-pMMA was observed to be 16%

<sup>2</sup> The values of diffusion coefficients in organic solvents reported in this section are only approximate as we do not have access to a dye for calibration with a well-known diffusion coefficient in these solvents. An estimate of  $D \approx 600 \mu\text{m}^2/\text{s}$  was obtained by comparing diffusion times obtained from fluorescein in water and HY6Br in toluene with air, water, and oil immersion objectives. All other values of  $D$  are based on the measurements of diffusion times relative to HY6Br in toluene. Similarly, the diffusion coefficient of HYC6Br is estimated to be  $\approx 600 \mu\text{m}^2/\text{s}$ , but there is a difference in the diffusion times observed which may be due to the difference in the index of refraction of the solvent.

faster than HYC6Br (see Figure 2.3.1-A). Indeed, with a viscosity,  $\eta$ , of 0.0059 poise for toluene, the hydrodynamic radius  $R$ , for the initiator is estimated to be 0.6 nm using the Stokes-Einstein equation, and the hydrodynamic radius for the polymer is approximately 0.5 nm, much less than one should expect. Strikingly, the diffusion process observed from the correlation data in the case of HYC6-pMMA-Br slows by a factor of 5 when the concentration of labeled polymer was increased 100 times to 250 nM ( $D \approx 144 \mu\text{m}^2/\text{s}$ ), with a corresponding hydrodynamic radius of approximately 2.5 nm which is much more consistent with the size that should be expected for a 10 kDa random coil polymer (compare for example §4.1 where we report that 10 kDa dextran has a radius of gyration of approximately 2.6 nm). One hypothesis which may explain these observations is that the dye is not as tightly bound to the polymer as was previously supposed, but the dye is instead dissociating from the polymer in a concentration-dependent manner.

Further interesting observations were made when the solvent was changed to chloroform rather than toluene. When dissolved in chloroform with 40 wt% pMMA as crowding agents, the apparently anomalous diffusion behavior was reduced to normal diffusion with a diffusion coefficient of  $D \approx 171 \mu\text{m}^2/\text{s}$ . Further, both 10 kDa HYC6-pMMA-Br and HYC6Br in chloroform without crowding agents were observed to have nearly identical diffusion coefficients,  $D \approx 616 \mu\text{m}^2/\text{s}$ , and  $D \approx 600 \mu\text{m}^2/\text{s}$  respectively. While the apparent diffusion coefficient of the polymer, which was  $696 \mu\text{m}^2/\text{s}$  in toluene, shifted towards an expected range of values, this result is still surprising given the larger molecular weight of the polymer (for example, 50-175  $\mu\text{m}^2/\text{s}$  would be reasonable).

#### *VLS-FCS Results*

The FCS observations at fixed length-scale in this system exhibit counter-intuitive diffusion coefficients, and in addition, the measurements taken in a crowded system (labeled polymer in 26wt% pMMA in toluene) are well fit to an anomalous diffusion model, suggesting that the diffusion may be length-scale dependent and suitable for investigation with VLS-FCS. Therefore, observations were conducted on samples consisting of 2.5nM 10kDa HYC6-pMMA-Br dissolved in toluene solutions containing 20, 30, and 40 wt% of pMMA. For the higher concentrations of pMMA (30 and 40 wt%), the anomalous diffusion model fails to describe the shape of the correlation data. Instead, the data was well fit by a two-component diffusion model, Equation 1.4.1-58 (see Figure 2.3.1-C).

Thus the two-component model was applied to the data obtained at all observation volumes, and the scaling of the characteristic diffusion times,  $\tau_{D1}$  and  $\tau_{D2}$ , with the observation volume radius,  $w_0$ , was determined individually. The diffusion laws of both components are shown in Figures (2.3.1-B, D) with corresponding diffusion coefficients and anomalous exponents derived from the diffusion law.

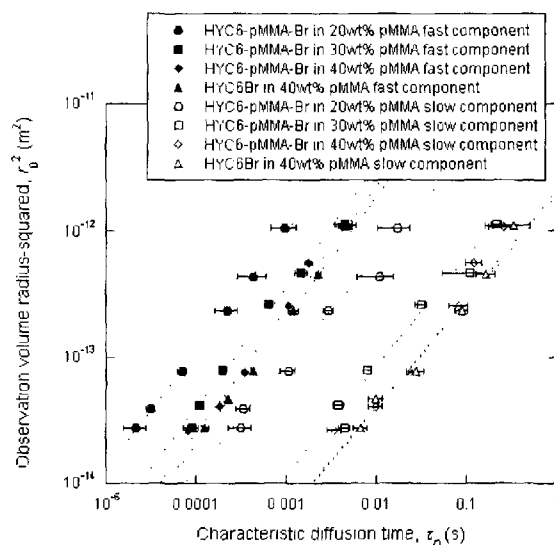


Figure 2.3.1-B. Diffusion laws (observation volume radius-squared vs. the characteristic diffusion time) in toluene solutions observed by VLS-FCS for each component of the diffusion: 2.5nM 10kDa HYC6-pMMA-Br with 20, 30, and 40 wt% pMMA, and 2.5nM HYC6Br with 40 wt% pMMA.

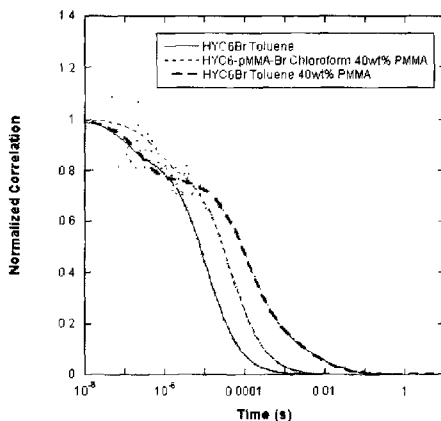


Figure 2.3.1-C. Correlation data of HYC6Br and HYC6-pMMA-Br diffusing in the indicated solution. The fits for HYC6Br in toluene (without pMMA) and HYC6-pMMA-Br in chloroform with 40wt% pMMA show the normal diffusion model (*thin lines*, Equation 1.4.1-48), while HYC6Br in toluene with 40wt% pMMA is fit to the two component model (*thick line*, Equation 1.4.1-58). Apart from the triplet state term in the microsecond time scale exhibited in all three cases, HYC6Br in toluene with 40wt% pMMA exhibits two correlation decays attributed to diffusion with characteristic times 120  $\mu$ s and 6 ms.

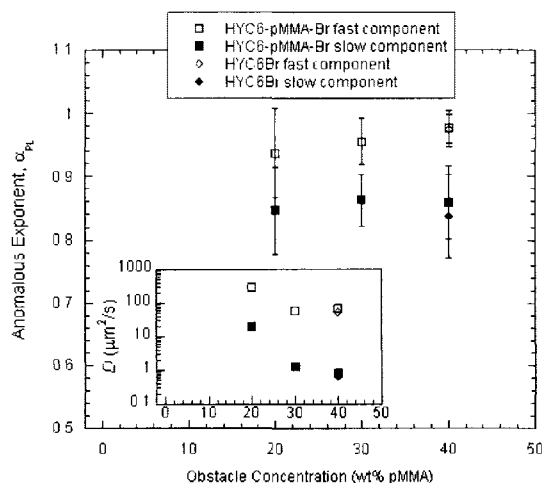


Figure 2.3.1-D. Anomalous exponents,  $\alpha_{PL}$ , equal to the slopes of the diffusion power laws shown in Figure 2.3.1-B for each component of the diffusion. The *inset* shows the apparent diffusion coefficients calculated from the intercept of the corresponding power laws. The values from the graph are given in Table 2.3.1B-A in Appendix B to this section.

The VLS-FCS observations demonstrate that both components of the correlation which are fit with the two-component diffusion model are indeed diffusive in nature, since the slopes of the diffusion power laws,  $\alpha_{PL}$ , are close to 1, whereas correlations due to photophysical effects should show corresponding values close to 0. It should also be noted that the ratio of the amplitudes for the fast component of the diffusion correlation to the slower component remained constant ( $\approx 4:1$ ), which is also consistent with two-component diffusion. Note that for two subspecies of equal specific brightness, the ratio of the amplitudes of the components is interpreted as the ratio of the number of particles composing each subspecies. Furthermore, the fast component of each corresponds to normal Brownian motion because the diffusion power law is 1 within error. For the slower components, the diffusion power law is consistently about 0.85, although the errors are larger. This confirms that the slower diffusion component is indeed length-scale dependent with the diffusion coefficient decreasing at larger observation length scales and therefore the slower component of the diffusion is anomalous.

The origin of these two separate diffusing components to the system is not immediately clear. To elucidate the nature of diffusion of this system, a control sample consisting of 2.5nM HYC6Br in toluene with 40wt% of pMMA was also observed by VLS-FCS (See Figures 2.3.1-B, D). The diffusion of the labeled initiator, HYC6Br, behaves qualitatively in the same manner as the polymerized product, HYC6-pMMA-Br, that is, two-components are observed, one fast-Brownian component and one anomalous-slow component. The unexpectedly fast motion of the polymer discussed above is again seen here: both diffusing components of HYC6Br are 25% slower than those of HYC6-

pMMA-Br (Figure 2.3.1-D). The ratio of the amplitudes for the fast component to the slower component (5.4:1) is also similar to that observed for the diffusion of the polymer in crowded solution.

These results demonstrate that the nature of the observed diffusion components of this system is not well understood. The hypothesis that the dye dissociates from the HYC6-pMMA-Br in a concentration-dependent manner seems to explain much of the unusual behavior observed here. In that case, we may also suppose that the chloroform is a better solvent for this dye which causes the dye to dissociate more efficiently from the polymer, which results in only one fast component corresponding to the motion of the dye alone even at 40 wt% of pMMA. In contrast, it is known that molecular crowding can significantly alter thermodynamic parameters and reaction rate constants, which may explain the two components observed in toluene: the fast component is dye alone, while the slow component is the fraction of polymer to which the dye is associated. It is even possible that the dye-initiator, HYC6Br, associates to the unlabeled pMMA giving rise to the two components observed in the 40 wt% pMMA sample. However, this hypothesis is in need of further testing, and it is uncertain why the dye would dissociate given that the dye was expected to be bound covalently to the pMMA.

#### *Conclusion*

Initial observations have been made toward an *in situ* FCS study to characterize diffusion of polymers in organic solvents during the polymerization reaction where the diffusion time is expected to show an increase over time. FCS observations on control samples demonstrate this system to have unexpected properties. VLS-FCS has been used to characterize polymer diffusion at high polymer concentrations. Specifically, both the initiator and the polymer in toluene with high concentrations of pMMA have been observed to have two diffusing components, where the fast component is Brownian while the slow component is length-scale dependent.

#### *Summary of Contribution & Acknowledgments*

Santiago Faucher synthesized the samples used for this study via ATRP with the assistance of Georg Witek in some cases. I performed the FCS and VLS-FCS measurements and subsequent data analysis. I thank Santiago Faucher for stimulating discussions concerning the possible nature of this system.

## Appendix A to 2.3.1: Properties of Hostasol and HYC6Br

Hostasol is a brightly fluorescent yellow dye commercially available through Clariant (HY-3G, Hostasol Yellow 3G™). It is based on the benzothioxanthene ring structure as shown in Figure 2.3.1A-A.

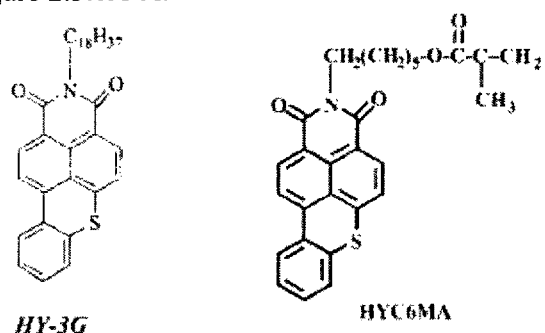


Figure 2.3.1A-A. Structure of Hostasol (HY-3G) and a methacrylate derivate (HYC6MA) reported in (215).

The molecule HYC6Br was synthesized to combine the fluorescent dye with a chemical moiety to serve as the initiator for the ATRP reaction. The initiator is an alkyl halide. In order to prevent these two moieties from affecting each other's function, a carbon chain is inserted between them. The synthesis of the fluorescent ATRP initiator HYC6Br is based on the work of Tronc *et al.* and Limer *et al.* (216). The expected structure is shown in Figure 2.3.1A-B.

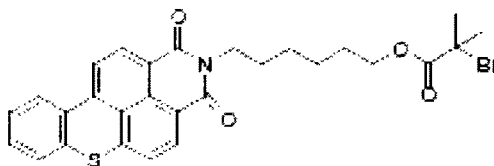


Figure 2.3.1A-B. Expected structure of HYC6Br as synthesized by Santiago Faucher and Georg Witek.

The excitation and emission spectrum of HYC6MA which are typical of hostasol derivatives (215) are shown in Figure 2.3.1A-C. The extinction coefficient,  $\epsilon$ , of HYC6MA is  $4 \times 10^4 \text{ M}^{-1} \text{ cm}^{-1}$  (215). The corresponding properties of HYC6Br are expected to be similar.

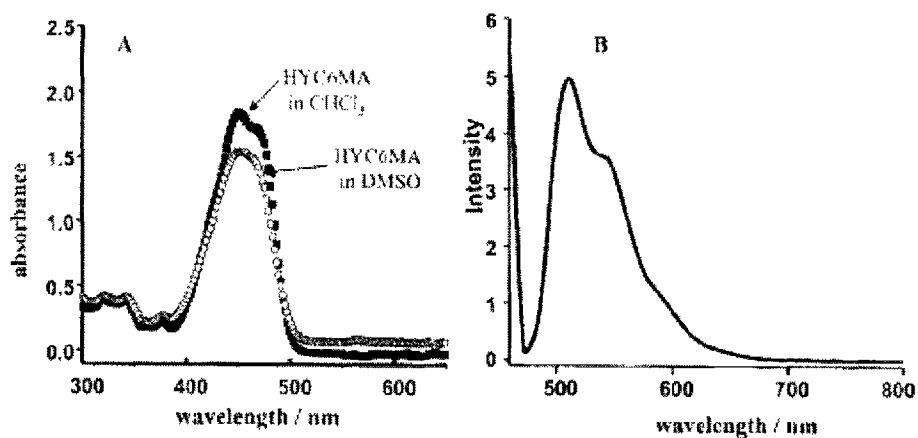


Figure 2.3.1A-C. Absorption (A) and emission spectrum (B) of a methacrylate derivative of hostasol (HYC6MA) as reported in (215) showing an absorption peak at 450 nm and an emission peak at 510 nm.

## Appendix B to 2.3.1:

Table of Results Reported in Figures 2.3.1-A,B,C and in the text.

Tracer	wt% pMMA	Solvent	Term	$D$	$\alpha_{PL}$	$\alpha_{PL}$ error
2.5nM HYC6Br-pMMA	20	Toluene	Fast	297.0	0.937	0.071
2.5nM HYC6Br-pMMA	20	Toluene	Fast	62.7	0.955	0.037
2.5nM HYC6Br-pMMA	40	Toluene	Fast	72.7	0.976	0.023
2.5nM HYC6Br	40	Toluene	Fast	58.0	0.975	0.029
2.5nM HYC6Br-pMMA	20	Toluene	Slow	20.53	0.846	0.069
2.5nM HYC6Br-pMMA	30	Toluene	Slow	1.26	0.862	0.040
2.5nM HYC6Br-pMMA	40	Toluene	Slow	0.83	0.859	0.058
2.5nM HYC6Br	40	Toluene	Slow	0.66	0.837	0.066
2.5nM HYC6Br	0	Toluene	--	600.0	--	--
2.5nM HYC6Br-pMMA	0	Toluene	--	696.0	--	--
<b>250nM HYC6Br-pMMA</b>	0	Toluene	--	143.3	--	--
2.5nM HYC6Br	0	Chloroform	--	600.0	--	--
2.5nM HYC6Br-pMMA	0	Chloroform	--	619.0	--	--
2.5nM HYC6Br	40	Chloroform	--	171.5	--	--
2.5nM HYC6Br-pMMA	40	Chloroform	--	171.2	--	--

Table 2.3.1B-A: Summary of VLS-FCS results for HYC6Br and 10kDa HYC6Br-pMMA in organic solvents. The relative diffusion coefficients ( $\mu\text{m}^2/\text{s}$ ) are based on the diffusion of HYC6Br in the respective solvent.

### 2.3.2 Applications of the molecular thermometer based on EGFP blinking

#### *Introduction*

In previous sections, I described our development of a molecular thermometer using EGFP for use with FCS as reported in *A Molecular Thermometer based on Fluorescent Protein Blinking* (§4.3). Although not reported in the publication, the first use of EGFP as a thermometer was in fact to calibrate the temperature of FCS samples using only an objective heater, and the second was to measure the spatial temperature gradient across the sample to determine the consistency of the sample temperature spatially. The motivation for the second application was simply to determine whether our FCS samples could be regarded as having a uniform temperature. The motivation for the first application was based on technical experimental details: Live human cell measurements should be taken at 37°C to achieve biologically relevant results and yet controlling the precise position of the FCS observation volume is also important. However, our home-built setup did not allow us to fix precisely both the sample temperature and position simultaneously due to the fact that we have one microscope stage which controls the temperature precisely but not the position, and one which controls position precisely, but not temperature. Therefore it was desirable to devise a method to control the sample temperature using only the objective temperature controller, thus taking advantage of the thermal contact between the sample and the water immersion objective. However, the temperature difference at the sample when using only the objective temperature controller was unknown. This problem was easily solved using EGFP blinking as a thermometer.

#### *Results*

All measurements reported in this section were taken on EGFP in CP buffer at pH 5.0. As described previously (§2.2.3), the thermometer was calibrated using both the objective and stage temperature controllers to determine the average relaxation time of EGFP blinking as a function of temperature. Having performed the calibration, the stage temperature controller was then turned off and the relaxation time was again determined as a function of the temperature setting of the objective temperature controller only. The second set of relaxation times could then be converted into actual temperature in the sample using the calibration function, and the result is shown in Figure 2.3.2-A.

At temperatures above room temperature, I observed a small decrease in the sample temperature above the fixed temperature of the objective temperature controller, corresponding to heat dissipation along the objective and the water interface. Similarly the sample temperature is higher than the set temperature at lower temperatures due to absorption of heat from the room. Through interpolation from the polynomial fit shown in Figure 2.3.2-A, I concluded that by heating the objective to 39°C, we obtain a sample temperature of 37°C.

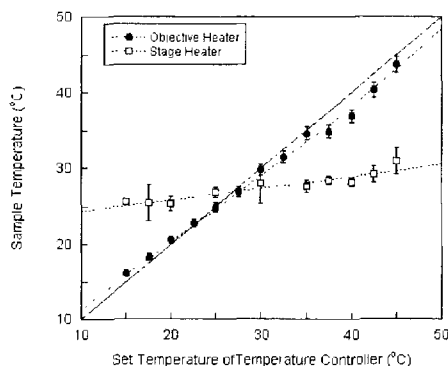


Figure 2.3.2-A. Sample temperature measured with the EGFP thermometer as a function of fixed temperature of the objective (*filled circles*) or of the stage (*empty squares*). As a guide for the eyes, the solid line shows the expected temperature in a case without heat dissipation. The dotted lines are linear or polynomial fits to the data.

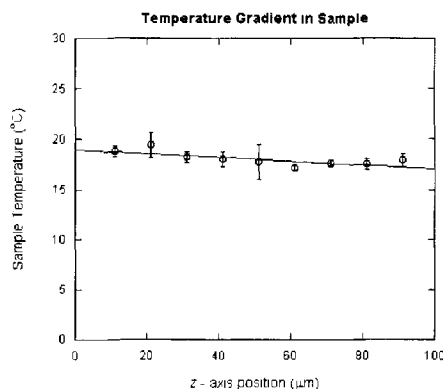


Figure 2.3.2-B. Local sample temperature as a function of position above the bottom cover glass (at  $z = 0$ ) where the objective was held at 15 °C and the microscope stage was held at 45 °C. The fit shows a decrease in temperature of  $0.02 \pm 0.01$  °C/ $\mu\text{m}$ .

The second application of this thermometer was equally straightforward. We attempted to create a temperature gradient in the sample by holding the objective and stage at temperature differences as wide as possible without risking damage to the optics. Therefore the objective temperature was set to 15 °C while the microscope stage was held at 45 °C. By measuring EGFP blinking in the sample as a function of the distance above the cover glass, we observed that this 30 °C difference resulted in an almost negligible temperature gradient ( $-0.02 \pm 0.01$  °C/ $\mu\text{m}$ , see Figure 2.3.2-B). Not only does this experiment tell us that the sample temperature is largely uniform, but that the objective temperature controller is dominant in setting the sample temperature, since the average temperature of the sample is only 18 °C. Indeed, the efficiency of the stage temperature

controller was then observed more directly by observing the sample temperatures when only the stage heater was used (see Figure 2.3.2-A).

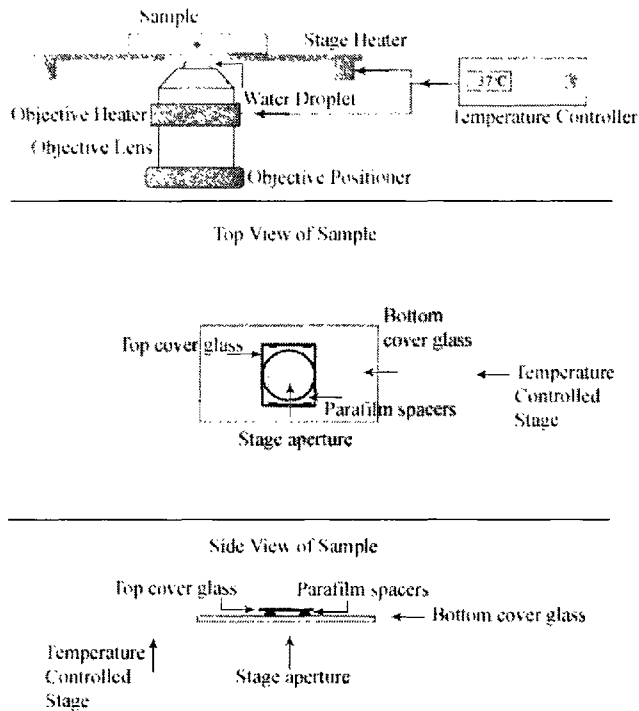


Figure 2.3.2-C. A diagram of the sample showing positions of temperature controllers, objective, and water droplet (*top panel*), a view of the sample from the top (*middle panel*) and side (*bottom panel*) where the  $\leq 10 \mu\text{L}$  sample is located between the parafilm spacers and bounded by cover glass at the top and bottom which are  $150 - 200 \mu\text{m}$  apart.

The difference in efficiency can be understood by considering the geometry of the sample, illustrated in Figure 2.3.2-C. Due to the small size of the sample chamber used, holding about  $10 \mu\text{L}$  or less, the majority of the sample lay above the stage aperture and the water immersion objective rather than above the temperature controlled stage. The bottom cover glass serves as the medium to conduct heat from the stage, which is less effective than the water droplet on the objective lens. Thus, it is not surprising that the stage temperature controller is much less effective in controlling the sample temperature than is the objective temperature controller. Indeed, the slightly negative temperature gradient may be explained by the increased distance from the stage as the position above the glass increases. Further experiments were conducted (data not shown) to observe the temperature gradient under different geometries, such as placing the stage above the sample, but in every case, the sample temperature was largely uniform, a fact attributed to the water droplet on the objective which acts as an efficient temperature bath for the sample.

*Conclusion*

Our molecular thermometer based on fluorescent protein blinking was successfully used to determine a simple way to fix our FCS samples at 37°C for observation of live cells using only the objective heater, and to determine that the sample temperature was quite uniform. In general, this method may be used to determine the real temperatures in the sample and determine the efficiency of various methods to control the temperature of small samples of various geometries including microfluidic devices. These results also emphasize the need to verify the effectiveness of temperature controls which act on the sample indirectly.

*Summary of Contribution & Acknowledgements*

The original application of the EGFP thermometer to determine the 2°C correction to hold the sample at 37°C for biological samples was my work. FCS data acquisition for observation of the temperature spatial gradient in the sample was a joint experiment between Felix Wong and me, and I performed the data analysis. Observations using the stage temperature controller alone and the further attempts to measure the spatial gradient in the sample (mentioned in the text but data not shown) were the work of Felix Wong exclusively.

### 3. References

1. Fourier, J. 1822. *The analytic theory of heat*. Cambridge University Press, Cambridge.
2. Brown, R. 1828. *Phil. Mag.* 4:161.
3. Brown, R. 1828. *Ann. Phys. Chem.* 14:294.
4. Fick, A. 1855. Ueber Diffusion. *Ann. Phys. (Leipzig)* 170:59 - 86.
5. Einstein, A. 1905. *Investigations on the Theory of the Brownian Movement*. *Annalen der Physik* 17:549.
6. Nelson, P. 2003. *Biological Physics: Energy, Information, Life*. Freeman, New York.
7. Crank, J. 1975. *The Mathematics of Diffusion*. Clarendon Press, Oxford.
8. Stokes, G. G. 1845. On the Theories of Internal Friction of the Fluids in Motion. *Transactions of the Cambridge Philosophical Society* 8:287–319.
9. Stokes, G. G. 1851. On the Effect of the Internal Friction of Fluids on the Motion of a Pendulum. *Transactions of the Cambridge Philosophical Society* 9:8–106.
10. Mazo, R. M. 2002. *Brownian Motion: Fluctuations, Dynamics, and Applications*. Oxford University Press, Oxford.
11. Weiss, G. H. 1994. *Aspects and Applications of the Random Walk*. North-Holland, New York.
12. Saxton, M. 1990. Lateral diffusion in a mixture of mobile and immobile particles. A Monte Carlo study. *Biophys. J.* 58:1303-1306.
13. Saxton, M. 1994. Anomalous diffusion due to obstacles: a Monte Carlo study. *Biophys. J.* 66:394-401.
14. Saxton, M. 1996. Anomalous diffusion due to binding: a Monte Carlo study. *Biophys. J.* 70:1250-1262.
15. Saxton, M. J. 2001. Anomalous Subdiffusion in Fluorescence Photobleaching Recovery: A Monte Carlo Study. *Biophys. J.* 81:2226-2240.
16. Saxton, M. J. 2007. A Biological Interpretation of Transient Anomalous Subdiffusion. I. Qualitative Model. *Biophys. J.* 92:1178-1191.
17. Olveczky, B. P., and A. S. Verkman. 1998. Monte Carlo Analysis of Obstructed Diffusion in Three Dimensions: Application to Molecular Diffusion in Organelles. *Biophys. J.* 74:2722-2730.
18. Goulian, M., and S. M. Simon. 2000. Tracking Single Proteins within Cells. *Biophys. J.* 79:2188-2198.
19. Hac, A. E., H. M. Seeger, M. Fidorra, and T. Heimburg. 2005. Diffusion in Two-Component Lipid Membranes--A Fluorescence Correlation Spectroscopy and Monte Carlo Simulation Study. *Biophys. J.* 88:317-333.
20. Nicolau, D. V., Jr., J. F. Hancock, and K. Burrage. 2007. Sources of Anomalous Diffusion on Cell Membranes: A Monte Carlo Study. *Biophys. J.* 92:1975-1987.
21. Dix, J. A., E. F. Y. Hom, and A. S. Verkman. 2006. Fluorescence Correlation Spectroscopy Simulations of Photophysical Phenomena and Molecular Interactions: A Molecular Dynamics/Monte Carlo Approach. *J. Phys. Chem. B* 110:1896-1906.

22. Netz, P. A., and T. Dorfmueller. 1995. Computer simulation studies of anomalous diffusion in gels: Structural properties and probe-size dependence. *The Journal of Chemical Physics* 103:9074-9082.
23. Weeks, E. R., T. H. Solomon, and J. S. Urbach. 1995. Observation of anomalous diffusion and Levy flights. In *Levy flights and Related Phenomena in Physics*. G. M. Zaslavsky, M. S. Shlesinger, and U. Frisch, editors. Springer-Verlag.
24. Solomon, T. H., E. R. Weeks, and H. L. Swinney. 1993. Observations of anomalous diffusion and Levy flights in a 2-dimensional rotating flow. *Phys. Rev. Lett.* 71:3975-3979.
25. Solomon, T. H., E. R. Weeks, and H. L. Swinney. 1994. Chaotic advection in a two-dimensional flow: Levy flights and anomalous diffusion. *Physica D* 76:70-84.
26. Weeks, E. R., and H. L. Swinney. 1998. Random walks and Levy flights observed in fluid flows. In *Nonlinear Science Today*. Springer-Verlag, New York.
27. Shlesinger, M. F. 1983. Weierstrassian Levy flights and self-avoiding random walks. *The Journal of Chemical Physics* 78:416-419.
28. Bouchard, J.-P., and A. Georges. 1990. *Physics Reports* 195:127.
29. Bunde, A., and S. Havlin. 1991. Percolation II. In *Fractals and Disorderd Systems*. Springer-Verlag, Berlin. 96-149.
30. Havlin, S., and D. Ben-Avraham. 1987. *Advances in Physics* 36:695.
31. Scher, H., M. F. Shlesinger, and J. T. Bendler. 1991. Time-scale invariance in transport and relaxation. *Physics Today* 44:26-34.
32. Blumen, A., J. Klafter, B. S. White, and G. Zumofen. 1984. Continuous time random walks on fractals. *Physical Review Letters* 53:1301–1304.
33. Nagle, J. 1992. Long tail kinetics in biophysics? *Biophys. J.* 63:366-370.
34. Blumen, A., J. Klafter, B. S. White, and G. Zumofen. 1984. Continuous-Time Random Walks on Fractals. *Phys. Rev. Lett.* 53:1301 LP - 1304.
35. Feder, J. 1988. *Fractals*. Plenum Press, New York.
36. Mandelbrot, B. B., and J. W. V. Ness. 1968. Fractional Brownian Motions, Fractional Noises and Applications. *SIAM Review* 10:422-437.
37. Weiss, M., H. Hashimoto, and T. Nilsson. 2003. Anomalous Protein Diffusion in Living Cells as Seen by Fluorescence Correlation Spectroscopy. *Biophys. J.* 84:4043-4052.
38. Hurst, H. E., R. P. Black, and Y. M. Sinaika. 1965. *Long Term Storage in Reservoirs. An Experimental Study*. Constable, London.
39. Sachrajda, A. S., R. Ketzmerick, C. Gould, Y. Feng, P. J. Kelly, Delage, and Z. Wasilewski. 1998. Fractal Conductance Fluctuations in a Soft-Wall Stadium and a Sinai Billiard. *Phys. Rev. Lett.* 80:1948-1951.
40. Hufnagel, L., R. Ketzmerick, and M. Weiss. 2001. Conductance fluctuations of generic billiards: Fractal or isolated? *Europhys. Lett.* 54:703-708.
41. Casati, G., I. Guarneri, and G. Maspero. 2000. Fractal Survival Probability Fluctuations. *Phys. Rev. Lett.* 84:63-66.

42. Sachrajda, A. S., and R. Ketzmerick. 1999. Sachrajda and Ketzmerick Reply: Comment on “Fractal Conductance Fluctuations in a Soft-Wall Stadium and a Sinai Billiard”. *Phys. Rev. Lett.* 83:1075.
43. Metzler, R., and J. Klafter. 2000. The random walk's guide to anomalous diffusion: a fractional dynamics approach. *Physics Reports* 339:1-77.
44. Gorenflo, R., F. Mainardi, D. Moretti, G. Pagnini, and P. Paradisi. 2002. Discrete random walk models for space-time fractional diffusion. *Chem. Phys.* 284:521-541.
45. Valentine, M. T., P. D. Kaplan, D. Thota, J. C. Crocker, T. Gisler, R. K. Prud'homme, M. Beck, and D. A. Weitz. 2001. Investigating the microenvironments of inhomogeneous soft materials with multiple particle tracking. *Phys. Rev. E* 64:061506-061509.
46. Wong, I. Y., M. L. Gardel, D. R. Reichman, E. R. Weeks, M. T. Valentine, A. R. Bausch, and D. A. Weitz. 2004. Anomalous Diffusion Probes Microstructure Dynamics of Entangled F-Actin Networks. *Phys. Rev. Lett.* 92:178101-178104.
47. Amblard, F., A. C. Maggs, B. Yurke, A. N. Pargellis, and S. Leibler. 1996. Subdiffusion and anomalous local viscoelasticity in actin networks. *Phys. Rev. Lett.* 77:4470-4473.
48. Weeks, E. R., and D. A. Weitz. 2002. Properties of Cage Rearrangements Observed near the Colloidal Glass Transition. *Phys. Rev. Lett.* 89:095704-095704.
49. Weeks, E. R., and D. A. Weitz. 2002. Subdiffusion and the cage effect studied near the colloidal glass transition. *Chem. Phys.* 284:361-367.
50. Golding, I., and E. C. Cox. 2006. Physical Nature of Bacterial Cytoplasm. *Phys. Rev. Lett.* 96:098102.
51. Pederson, T. 2000. Diffusional protein transport within the nucleus: a message in the medium. *Nature Cell Biol.* 2:E73-E74.
52. Cluzel, P., M. Surette, and S. Leibler. 2000. An ultrasensitive bacterial motor revealed by monitoring signaling proteins in single cells. *Science* 287:1652-1655.
53. Macnab, R. 2000. Action at a distance: bacterial flagellar assembly. *Science* 290:2086-2087.
54. Guthold, M., X. Zhu, C. Rivetti, G. Yang, N. Thomson, S. Kasas, H. Hansma, B. Smith, P. Hansma, and C. Bustamante. 1999. Direct observation of one-dimensional diffusion and transcription by *Escheria coli* RNA polymerase. *Biophys J* 77:2284-2294.
55. Berry, H. 2002. Monte Carlo Simulations of Enzyme Reactions in Two Dimensions: Fractal Kinetics and Spatial Segregation. *Biophys. J.* 83:1891-1901.
56. Crick, F. 1970. Diffusion in embryogenesis. *Nature* 225:420-422.
57. Valdez-Taubas, J., and H. R. B. Pelham. 2003. Slow Diffusion of Proteins in the Yeast Plasma Membrane Allows Polarity to Be Maintained by Endocytic Cycling. *Current Biology* 13:1636-1640.
58. Smoluchowski, M. V. 1917. Versuch einer mathematischen Theorie der Koagulationskinetik kolloider Loesungen. *Z. Phys. Chem.* 92:129-168.

59. Saxton, M. J. 2002. Chemically limited reactions on a percolation cluster. *The Journal of Chemical Physics* 116:203-208.
60. Murray, J. D. 1993. *Mathematical Biology*. Springer, New York.
61. Weiss, M. 2003. Stabilizing Turing patterns with subdiffusion in systems with low particle numbers. *Physical Review E (Statistical, Nonlinear, and Soft Matter Physics)* 68:036213.
62. Turing, A. M. 1952. The chemical basis of morphogenesis. *Philosophical Transactions of the Royal Society of London, Series B* 237:37-72.
63. Weiss, M., M. Elsner, F. Kartberg, and T. Nilsson. 2004. Anomalous Subdiffusion Is a Measure for Cytoplasmic Crowding in Living Cells. *Biophys. J.* 87:3518-3524.
64. Brown, E. B., E. S. Wu, W. Zipfel, and W. W. Webb. 1999. Measurement of Molecular Diffusion in Solution by Multiphoton Fluorescence Photobleaching Recovery. *Biophys. J.* 77:2837-2849.
65. Wachsmuth, M., W. Waldeck, and J. Langowski. 2000. Anomalous diffusion of fluorescent probes inside living cell nuclei investigated by spatially-resolved fluorescence correlation spectroscopy. *J. Mol. Biol.* 298:677-689.
66. Feder, T., I. Brust-Mascher, J. Slattery, B. Baird, and W. Webb. 1996. Constrained diffusion or immobile fraction on cell surfaces: a new interpretation. *Biophys. J.* 70:2767-2773.
67. Platani, M., I. Goldberg, A. I. Lamond, and J. R. Swedlow. 2002. Cajal Body dynamics and association with chromatin are ATP-dependent. *J. Cell Biol.* 158:502-508.
68. Guigas, G., C. Kalla, and M. Weiss. 2007. Probing the Nanoscale Viscoelasticity of Intracellular Fluids in Living Cells. *Biophys. J.* 93:316-323.
69. Gennerich, A., and D. Schild. 2002. Anisotropic Diffusion in Mitral Cell Dendrites Revealed by Fluorescence Correlation Spectroscopy. *Biophys. J.* 83:510-522.
70. Luby-Phelps, K., D. Taylor, and F. Lanni. 1986. Probing the structure of cytoplasm. *J. Cell Biol.* 102:2015-2022.
71. Almeida, P. F. F., and W. L. C. Vaz. 1995. Structure and Dynamics of Membranes. In *Handbook of Biological Physics*. R. Lipowsky, and E. Sackmann, editors.
72. Minton, A. 1989. Lateral diffusion of membrane proteins in protein-rich membranes. A simple hard particle model for concentration dependence of the two-dimensional diffusion coefficient. *Biophys. J.* 55:805-808.
73. Schwille, P., J. Korfach, and W. W. Webb. 1999. Fluorescence correlation spectroscopy with single-molecule sensitivity on cell and model membranes. *Cytometry* 36:176-182.
74. Ohsugi, Y., K. Saito, M. Tamura, and M. Kinjo. 2006. Lateral Mobility of Membrane-Binding Proteins in Living Cells Measured by Total Internal Reflection Fluorescence Correlation Spectroscopy. *Biophys. J.* 91:3456-3464.
75. Saxton, M. J. 1999. Lateral diffusion of lipids and proteins. *Current Topics in Membranes* 48:229–282.

76. Almeida, P. F. F., and W. L. C. Vaz. 1995. Lateral diffusion in membranes. In *Structure and Dynamics of Membranes: From Cells to Vesicles*. R. Lipowski, and E. Sackmann, editors. Elsevier, Amsterdam, The Netherlands. 305–357.
77. Lenne, P.-F., L. Wawrezinieck, F. Conchonaud, O. Wurtz, A. Boned, X.-J. Guo, H. Rigneault, H.-T. He, and D. Marguet. 2006. Dynamic Molecular Confinement in the Plasma Membrane by Microdomains and the Cytoskeleton Meshwork. *The EMBO Journal* 25:3245-3256.
78. Wawrezinieck, L., P.-F. Lenne, D. Marguet, and H. Rigneault. 2004. Fluorescence correlation spectroscopy to determine diffusion laws: application to live cell membranes. In *Biophotonics Micro- and Nano-Imaging*. D. Anselmetti, editor. SPIE. 92-102.
79. Wawrezinieck, L., H. Rigneault, D. Marguet, and P.-F. Lenne. 2005. Fluorescence Correlation Spectroscopy Diffusion Laws to Probe the Submicron Cell Membrane Organization. *Biophys. J.* 89:4029-4042.
80. Ritchie, K., R. Lino, T. Fujiwara, K. Murase, and A. Kusumi. 2003. The fence and picket structure of the plasma membrane of live cells as revealed by single molecule techniques. *Molecular Membrane Biology* 20:13 - 18.
81. Guigas, G., and M. Weiss. 2006. Size-Dependent Diffusion of Membrane Inclusions. *Biophys. J.* 91:2393-2398.
82. Mason, T. G., and D. A. Weitz. 1995. Optical Measurements of Frequency-Dependent Linear Viscoelastic Moduli of Complex Fluids. *Phys. Rev. Lett.* 74:1250 LP - 1253.
83. Dayel, M., E. Hom, and A. Verkman. 1999. Diffusion of green fluorescent protein in the aqueous-phase lumen of endoplasmic reticulum. *Biophys J* 76:2843-2851.
84. Lukacs, G., P. Haggie, O. Seksek, D. Lechardeur, N. Freedman, and A. Verkman. 2000. Size-dependent DNA mobility in cytoplasm and nucleus. *J. Biol. Chem.* 275:1625-1629.
85. Swaminathan, R., C. Hoang, and A. Verkman. 1997. Photobleaching recovery and anisotropy decay of green fluorescent protein GFP-S65T in solution and cells: cytoplasmic viscosity probed by green fluorescent protein translational and rotational diffusion. *Biophys. J.* 72:1900-1907.
86. Mastro, A. M., M. A. Babich, W. D. Taylor, and A. D. Keith. 1984. Diffusion of a small molecule in the cytoplasm of mammalian cells. *Proc Natl Acad Sci U S A* 81:3414-3418.
87. Luby-Phelps, K. 1994. Physical properties of the cytoplasm. *Curr. Op. Cell Biol.* 6:3-9.
88. Seksek, O., J. Biwersi, and A. S. Verkman. 1997. Translational Diffusion of Macromolecule-sized Solutes in Cytoplasm and Nucleus. *J. Cell Biol.* 138:131-142.
89. Verkman, A. 2002. Solute and macromolecule diffusion in cellular aqueous compartments. *Trends Biochem. Sci.* 27:27-33.
90. Wojcieszyn, J. W., R. A. Schlegel, E. S. Wu, and K. A. Jacobson. 1981. Diffusion of injected macromolecules within the cytoplasm of living cells. *Proc Natl Acad Sci U S A* 78:4407-4410.

91. Elowitz, M. B., M. G. Surette, P.-E. Wolf, J. B. Stock, and S. Leibler. 1999. Protein Mobility in the Cytoplasm of *Escherichia coli*. *J. Bacteriol.* 181:197-203.
92. Gennerich, A., and D. Schild. 2000. Fluorescence Correlation Spectroscopy in Small Cytosolic Compartments Depends Critically on the Diffusion Model Used. *Biophys. J.* 79:3294-3306.
93. Fradin, C., A. Abu-Arish, R. Granek, and M. Elbaum. 2003. Fluorescence Correlation Spectroscopy Close to a Fluctuating Membrane. *Biophys. J.* 84:2005-2020.
94. Ghosh, R. N. 1991. Mobility and clustering of individual low density lipoprotein receptor molecules on the surface of human skin fibroblasts. Ph.D. Thesis. Cornell University, Ithaca, NY.
95. Ghosh, R. N., and W. W. Webb. 1994. Automated detection and tracking of individual and clustered cell surface low density lipoprotein receptor molecules. *Biophys. J.* 66:1301-1318.
96. Slattery, J. P. 1995. Lateral mobility of FcεRI on rat basophilic leukemia cells as measured by single particle tracking using a novel bright fluorescent probe. Ph.D. Thesis. Cornell University, Ithaca, NY.
97. Sheets, E. D., G. M. Lee, R. Simson, and K. Jacobson. 1997. Transient Confinement of a Glycosylphosphatidylinositol-Anchored Protein in the Plasma Membrane. *Biochemistry* 36:12449-12458.
98. Simson, R., B. Yang, S. Moore, P. Doherty, F. Walsh, and K. Jacobson. 1998. Structural mosaicism on the submicron scale in the plasma membrane. *Biophys. J.* 74:297-308.
99. Smith, P. R., I. E. G. Morrison, K. M. Wilson, N. Fernandez, and R. J. Cherry. 1999. Anomalous Diffusion of Major Histocompatibility Complex Class I Molecules on HeLa Cells Determined by Single Particle Tracking. *Biophys. J.* 76:3331-3344.
100. Schwille, P., U. Haupts, S. Maiti, and W. W. Webb. 1999. Molecular Dynamics in Living Cells Observed by Fluorescence Correlation Spectroscopy with One- and Two-Photon Excitation. *Biophys. J.* 77:2251-2265.
101. Caspi, A., R. Granek, and M. Elbaum. 2002. Diffusion and directed motion in cellular transport. *Physical Review E (Statistical, Nonlinear, and Soft Matter Physics)* 66:011916.
102. Konopka, M. C., I. A. Shkel, S. Cayley, M. T. Record, and J. C. Weisshaar. 2006. Crowding and Confinement Effects on Protein Diffusion In Vivo. *J. Bacteriol.* 188:6115-6123.
103. Garcia-Perez, A. I., E. A. Lopez-Beltran, P. Kluner, J. Luque, P. Ballesteros, and S. Cerdan. 1999. Molecular Crowding and Viscosity as Determinants of Translational Diffusion of Metabolites in Subcellular Organelles. *Archives of Biochemistry and Biophysics* 362:329-338.
104. Chiantia, S., J. Ries, N. Kahya, and P. Schwille. 2006. Combined AFM and Two-Focus SFCS Study of Raft-Exhibiting Model Membranes. *ChemPhysChem* 7:2409 - 2418.

105. Saxton, M. J., and K. Jacobson. 1997. Single-Particle Tracking: Applications to Membrane Dynamics. *Annu. Rev. Biophys. Biomol. Struct.* 26:373-399.
106. Burgos, P., C. Yuan, M.-L. Viriot, and L. J. Johnston. 2003. Two-Color Near-Field Fluorescence Microscopy Studies of Microdomains ("Rafts") in Model Membranes. *Langmuir* 19:8002-8009.
107. Jin, S., P. M. Haggie, and A. S. Verkman. 2007. Single-Particle Tracking of Membrane Protein Diffusion in a Potential: Simulation, Detection, and Application to Confined Diffusion of CFTR Cl<sup>-</sup> Channels. *Biophys. J.* 93:1079-1088.
108. Almeida, P. F. F., W. L. C. Vaz, and T. E. Thompson. 1992. Lateral diffusion and percolation in two-phase, two-component lipid bilayers: Topology of the solid-phase domains in-plane and across the lipid bilayer. *Biochemistry* 31:7198–7210.
109. Caspi, A., M. Elbaum, R. Granek, A. Lachish, and D. Zbaida. 1998. Semiflexible Polymer Network: A View From Inside. *Phys. Rev. Lett.* 80:1106 LP - 1109.
110. Sisan, D. R., R. Arevalo, C. Graves, R. McAllister, and J. S. Urbach. 2006. Spatially Resolved Fluorescence Correlation Spectroscopy Using a Spinning Disk Confocal Microscope. *Biophys. J.* 91:4241-4252.
111. Moller, W., I. Nemoto, T. Matsuzaki, T. Hofer, and J. Heyder. 2000. Magnetic Phagosome Motion in J774A.1 Macrophages: Influence of Cytoskeletal Drugs. *Biophys. J.* 79:720-730.
112. Zimmerman, S. B., and A. P. Minton. 1993. Macromolecular Crowding: Biochemical, Biophysical, and Physiological Consequences. *Annu. Rev. Biophys. Biomol. Struct.* 22:27-65.
113. Sanabria, H., Y. Kubota, and M. N. Waxham. 2007. Multiple Diffusion Mechanisms Due to Nanostructuring in Crowded Environments. *Biophys. J.* 92:313-322.
114. Dauty, E., and A. S. Verkman. 2004. Molecular crowding reduces to a similar extent the diffusion of small solutes and macromolecules: measurement by fluorescence correlation spectroscopy. *J. Mol. Recognit.* 17:441-447.
115. Dwyer, J. D., and V. A. Bloomfield. 1993. Brownian Dynamics Simulations of Probe and Self-Diffusion in Concentrated Protein and DNA Solutions. *Biophys. J.* 65:1810-1816.
116. Busch, N. A., T. Kim, and V. A. Bloomfield, editors. 2000. Tracer Diffusion of Proteins in DNA Solutions. 2. Green Fluorescent Protein in Crowded DNA Solutions.
117. Zimmerman, S. B., and S. O. Trach. 1991. Estimation of macromolecule concentrations and excluded volume effects for the cytoplasm of *Escherichia coli*. *J. Mol. Biol.* 222:599-620.
118. Diaspro, A., editor. 2001. *Confocal and Two-Photon Microscopy: Foundations, Applications and Advances*. Wiley.
119. Marriott G, P. I. 2003. *Biophotonics. Methods in Enzymology* 360/361.
120. Schutz, G. J., M. Sonnleitner, P. Hinterdorfer, and H. Schindler. 2000. Single molecule microscopy of biomembranes. *Molecular Membrane Biology* 17:17 - 29.

121. Hovius, R., P. Vallotton, T. Wohland, and H. Vogel. 2000. Fluorescence techniques: shedding light on ligand–receptor interactions. *Trends in Pharmacological Sciences* 21:266-273.
122. Yan, Y., and G. Marriott. 2003. Analysis of protein interactions using fluorescence technologies. *Current Opinion in Chemical Biology* 7:635–640.
123. Jameson, D., J. Croney, and P. Moens. 2003. Fluorescence: basic concepts, practical aspects, and some anecdotes. *Methods in Enzymology* 360:1-43.
124. Schwille, P. 2001. Fluorescence Correlation Spectroscopy and Its Potential for Intracellular Applications. *Cell Biochemistry and Biophysics* 34:383-408.
125. Mcoletta, K., and S. Petra. 2006. Fluorescence correlation studies of lipid domains in model membranes. *Molecular membrane biology* 23:29-39.
126. Palo, K., L. Brand, C. Eggeling, S. Jager, P. Kask, and K. Gall. 2002. Fluorescence Intensity and Lifetime Distribution Analysis: Toward Higher Accuracy in Fluorescence Fluctuation Spectroscopy. *Biophys. J.* 83:605-618.
127. Kask, P., K. Palo, D. Ullmann, and K. Gall. 1999. Fluorescence-intensity distribution analysis and its application in biomolecular detection technology. *PNAS* 96:13756–13761.
128. Palo, K., U. Mets, S. Jager, P. Kask, and K. Gall. 2000. Fluorescence Intensity Multiple Distributions Analysis: Concurrent Determination of Diffusion Times and Molecular Brightness. *Biophys. J.* 79:2858-2866.
129. Lippincott-Schwartz, J., E. Snapp, and A. Kenworthy. 2001. Studying Protein Dynamics In Living Cells. *Nature Reviews Molecular Cell Biology* 2:444-456.
130. Sprague, B. L., and J. G. McNally. 2004. FRAP analysis of binding: proper and fitting. *Trends in Cell Biology* 15:84-91.
131. Houtsmuller, A. B., and W. Vermeulen. 2001. Macromolecular dynamics in living cell nuclei revealed by fluorescence redistribution after photobleaching. *Histochem. Cell Biol.* 115:13-21.
132. Wallrabe, H., and A. Periasamy. 2005. Imaging protein molecules using FRET and FLIM microscopy. *Current Opinion in Biotechnology* 16:19-27.
133. Neri, L. M., A. M. Martelli, M. Previati, A. Valmori, and S. Capitani. 1992. From two dimensional (2D) to three dimensional (3D) analysis by confocal microscopy. *Liver* 12:268-279.
134. Petty, H. R. 2007. Fluorescence microscopy: established and emerging methods, experimental strategies, and applications in immunology. *Microsc. Res. Techniq.* 70:687-709.
135. Hoffman, R. M. 2005. Advantages of multi-color fluorescent proteins for whole-body and in vivo cellular imaging. *Journal of Biomedical Optics* 10:41202.
136. Blake, R. A. 2001. Cellular screening assays using fluorescence microscopy. *Current Opinion in Pharmacology* 1:533-539.
137. Paddock, S. W. 2000. Principles and practices of laser scanning confocal microscopy. *Molecular Biotechnology* 16:127-149.
138. Brelje, T. C., M. W. Wessendorf, and R. L. Sorenson. 2002. Multicolor laser scanning confocal immunofluorescence microscopy: practical application and limitations. *Methods in Cell Biology* 70:165-244.

139. Sekar, R. B., and A. Periasamy. 2003. Fluorescence resonance energy transfer (FRET) microscopy imaging of live cell protein localizations. *J. Cell Biol.* 160:629-633.
140. Kubitscheck, U., O. Kuckmann, T. Kues, and R. Peters. 2000. Imaging and Tracking of Single GFP Molecules in Solution. *Biophys. J.* 78:2170-2179.
141. Kues, T., R. Peters, and U. Kubitscheck. 2001. Visualization and Tracking of Single Protein Molecules in the Cell Nucleus. *Biophys. J.* 80:2954-2967.
142. Gordon, M. P., T. Ha, and P. R. Selvin. 2004. Single-molecule high-resolution imaging with photobleaching. *PNAS* 101:6462-6465.
143. Kim, H. D., G. U. Nienhaus, T. Ha, J. W. Orr, J. R. Williamson, and S. Chu. 2002. Mg<sup>2+</sup>-dependent conformational change of RNA studied by fluorescence correlation and FRET on immobilized single molecules. *PNAS* 99:4284-4289.
144. Tanaka, M., M. Nishi, M. Morimoto, T. Sugimoto, and M. Kawata. 2005. Imaging analysis of mineralocorticoid receptor and importins in single living cells by using GFP color variants. *Cell and Tissue Research* 320:447-453.
145. Wu, B., Y. Chen, and J. D. Muller. 2006. Dual-Color Time-Integrated Fluorescence Cumulant Analysis. *Biophys. J.* 91:2687-2698.
146. Satsoura, D., B. Leber, D. W. Andrews, and C. Fradin. 2006. Circumvention of Fluorophore Photobleaching in Fluorescence Fluctuation Experiments: a Beam Scanning Approach. *ChemPhysChem* 8:834 - 848.
147. Masuda, A., K. Ushida, and T. Okamoto. 2006. New fluorescence correlation spectroscopy (FCS) suitable for the observation of anomalous diffusion in polymer solution: Time and space dependences of diffusion coefficients. *Journal of Photochemistry & Photobiology, A: Chemistry* 183:304-308.
148. Kellermayer, M. S. Z., A. Karsai, A. Kengyel, A. Nagy, P. Bianco, T. Huber, A. Kulesar, C. Niedetzky, R. Proksch, and L. Grama. 2006. Spatially and Temporally Synchronized Atomic Force and Total Internal Reflection Fluorescence Microscopy for Imaging and Manipulating Cells and Biomolecules. *Biophys. J.* 91:2665-2677.
149. Humpolickova, J., E. Gielen, A. Benda, V. Fagulova, J. Vercaemmen, M. vandeVen, M. Hof, M. Ameloot, and Y. Engelborghs. 2006. Probing Diffusion Laws within Cellular Membranes by Z-Scan Fluorescence Correlation Spectroscopy. *Biophys. J.* 91:L23-25.
150. Garai, K., M. Muralidhar, and S. Maiti. 2006. Fiber-optic fluorescence correlation spectrometer. *Applied Optics* 45:7538-7542.
151. Fink, M. C., K. V. Adair, M. G. Guenza, and A. H. Marcus. 2006. Translational Diffusion of Fluorescent Proteins by Molecular Fourier Imaging Correlation Spectroscopy. *Biophys. J.* 91:3482-3498.
152. Murphy, D. B. 2001. *Fundamentals of Light Microscopy and Electronic Imaging.* Wiley-Liss, New York.
153. Widengren, J., R. Rigler, and U. Mets. 1994. Triplet-state monitoring by fluorescence correlation spectroscopy. *Journal of Fluorescence* 4:255-258.

154. Widengren, J., U. Mets, and R. Rigler. 1995. Fluorescence Correlation Spectroscopy of Triplet States in Solution: A Theoretical and Experimental Study. *Journal of Physical Chemistry* 99:13368-13379.
155. Patterson, G. H., and D. W. Piston. 2000. Photobleaching in Two-Photon Excitation Microscopy. *Biophys. J.* 78:2159-2162.
156. Widengren, J., and R. Rigler. 1996. Mechanisms of photobleaching investigated by fluorescence correlation spectroscopy. *Bioimaging* 4:149-157.
157. Eggeling, C., J. Widengren, R. Rigler, and C. A. M. Seidel. 1998. Photobleaching of Fluorescent Dyes under Conditions Used for Single-Molecule Detection: Evidence of Two-Step Photolysis. *Anal. Chem.* 70:2651-2659.
158. Dittrich, P. S., and P. Schuille. 2001. Photobleaching and stabilization of fluorophores used for single-molecule analysis with one- and two-photon excitation. *Applied Physics B: Lasers and Optics* 73:829-837.
159. Eggeling, C., A. Volkmer, and C. A. M. Seidel. 2005. Molecular Photobleaching Kinetics of Rhodamine 6G by One- and Two-Photon Induced Confocal Fluorescence Microscopy. *ChemPhysChem* 6:791-804.
160. Giepmans, B. N. G., S. R. Adams, M. H. Ellisman, and R. Y. Tsien. 2006. The Fluorescent Toolbox for Assessing Protein Location and Function. *Science* 312:217-224.
161. Chalfie, M., and S. Kain, editors. 1998. *Green Fluorescent Protein: Properties, Applications, and Protocols*. Wiley, New York.
162. Yang, F., L. G. Moss, and G. N. Phillips. 1996. The molecular structure of green fluorescent protein. *Nat. Biotech.* 14:1246-1251.
163. Tsien, R. Y. 1998. The Green Fluorescent Protein. *Annual Review of Biochemistry* 67:509-544.
164. Campbell, R. E., O. Tour, A. E. Palmer, P. A. Steinbach, G. S. Baird, D. A. Zacharias, and R. Y. Tsien. 2002. A monomeric red fluorescent protein. *PNAS* 99:7877-7882.
165. Shaner, N. C., R. E. Campbell, P. A. Steinbach, B. N. G. Giepmans, A. E. Palmer, and R. Y. Tsien. 2004. Improved monomeric red, orange and yellow fluorescent proteins derived from *Discosoma* sp. red fluorescent protein. *PNAS* 101:14758-14763.
166. Widengren, J., U. Mets, and R. Rigler. 1999. Photodynamic properties of green fluorescent proteins investigated by fluorescence correlation spectroscopy. *Chem. Phys.* 250:171-186.
167. Widengren, J., and P. Schuille. 2000. Characterization of Photoinduced Isomerization and Back-Isomerization of the Cyanine Dye Cy5 by Fluorescence Correlation Spectroscopy. *J. Phys. Chem. A* 104:6416-6428.
168. Dugave, C. 2006. *Cis-trans Isomerization in Biochemistry*. Wiley-VCH, Weinheim, Germany.
169. Haupts, U., S. Maiti, P. Schuille, and W. W. Webb. 1998. Dynamics of fluorescence fluctuations in green fluorescent protein observed by fluorescence correlation spectroscopy. *PNAS* 95:13573-13578.

170. Schwille, P., S. Kummer, A. A. Heikal, W. E. Moerner, and W. W. Webb. 2000. Fluorescence correlation spectroscopy reveals fast optical excitation-driven intramolecular dynamics of yellow fluorescent proteins. *PNAS* 97:151-156.
171. Hess, S. T., A. A. Heikal, and W. W. Webb. 2004. Fluorescence Photoconversion Kinetics in Novel Green Fluorescent Protein pH Sensors (pHluorins). *J. Phys. Chem. B* 108:10138 - 10148.
172. Verkhusha, V. V., and A. Sorkin. 2005. Conversion of the monomeric red fluorescent protein into a photoactivatable probe. *Chem. Biol.* 12:279-285.
173. Magde, D., E. Elson, and W. W. Webb. 1972. Thermodynamic Fluctuations in a Reacting System—Measurement by Fluorescence Correlation Spectroscopy. *Phys. Rev. Lett.* 29:705-708.
174. Elson, E. L., and D. Magde. 1974. Fluorescence correlation spectroscopy. I. Conceptual basis and theory. *Biopolymers* 13:1-27.
175. Magde, D., E. L. Elson, and W. W. Webb. 1974. Fluorescence correlation spectroscopy. II. An experimental realization. *Biopolymers* 13:29-61.
176. Kinjo, M., and R. Rigler. 1995. Ultrasensitive hybridization analysis using fluorescence correlation spectroscopy. *Nucl. Acids Res.* 23:1795-1799.
177. Rigler, R., U. Mets, J. Widengren, and P. Kask. 1993. Fluorescence correlation spectroscopy with high count rate and low background: analysis of translational diffusion. *Eur. Biophys. J.* 22:169-175.
178. Brock, R., M. A. Hink, and T. M. Jovin. 1998. Fluorescence Correlation Microscopy of Cells in the Presence of Autofluorescence. *Biophys. J.* 75:2547-2557.
179. Sengupta, P., K. Garai, J. Balaji, N. Periasamy, and S. Maiti. 2003. Measuring Size Distribution in Highly Heterogeneous Systems with Fluorescence Correlation Spectroscopy. *Biophys. J.* 84:1977-1984.
180. Björling, S., M. Kinjo, Z. Földes-Papp, E. Hagman, P. Thyberg, and R. Rigler. 1998. Fluorescence Correlation Spectroscopy of Enzymatic DNA Polymerization. *Biochemistry* 37:12971-12978.
181. Zettl, H., W. Häfner, A. Böker, H. Schmalz, M. Lanzendörfer, A. H. E. Müller, and G. Krausch. 2004. Fluorescence Correlation Spectroscopy of Single Dye-Labeled Polymers in Organic Solvents. *Macromolecules* 37:1917 -1920.
182. Masuda, A., K. Ushida, and T. Okamoto. 2005. New Fluorescence Correlation Spectroscopy Enabling Direct Observation of Spatiotemporal Dependence of Diffusion Constants as an Evidence of Anomalous Transport in Extracellular Matrices. *Biophys. J.* 88:3584-3591.
183. Labille, J., N. Fatin-Rouge, and J. Buffle. 2007. Local and Average Diffusion of Nanosolutes in Agarose Gel: The Effect of the Gel/Solution Interface Structure. *Langmuir* 23:2083-2090.
184. Yeung, C., M. Shtrahman, and X.-I. Wu. 2007. Stick-and-Diffuse and Caged Diffusion: A Comparison of Two Models of Synaptic Vesicle Dynamics. *Biophys. J.* 92:2271-2280.

185. Eigen, M., and R. Rigler. 1994. Sorting Single Molecules: Application to Diagnostics and Evolutionary Biotechnology 10.1073/pnas.91.13.5740. PNAS 91:5740-5747.
186. Aragón, S. R., and R. Pecora. 1975. Fluorescence correlation spectroscopy and Brownian rotational diffusion. *Biopolymers* 14:119-137.
187. Kohler, R., P. Schwille, W. Webb, and M. Hanson. 2000. Active protein transport through plastid tubules: velocity quantified by fluorescence correlation spectroscopy. *J Cell Sci* 113:3921-3930.
188. Magde, D., W. W. Webb, and E. L. Elson. 1978. Fluorescence correlation spectroscopy. III. Uniform translation and laminar flow. *Biopolymers* 17:1939–1955.
189. Chattopadhyay, K., S. Saffarian, E. L. Elson, and C. Frieden. 2005. Measuring Unfolding of Proteins in the Presence of Denaturant Using Fluorescence Correlation Spectroscopy. *Biophys. J.* 88:1413-1422.
190. Chattopadhyay, K., E. L. Elson, and C. Frieden. 2005. The kinetics of conformational fluctuations in an unfolded protein measured by fluorescence methods 10.1073/pnas.0500127102. PNAS 102:2385-2389.
191. Wallace, M. I., L. Ying, S. Balasubramanian, and D. Klenerman. 2000. FRET Fluctuation Spectroscopy: Exploring the Conformational Dynamics of a DNA Hairpin Loop. *J. Phys. Chem. B* 104:11551-11555.
192. Widengren, J., J. Dapprich, and R. Rigler. 1997. Fast interactions between Rh6G and dGTP in water studied by fluorescence correlation spectroscopy. *Chem. Phys.* 216:417-426.
193. Saffarian, S., and E. L. Elson. 2003. Statistical Analysis of Fluorescence Correlation Spectroscopy: The Standard Deviation and Bias. *Biophys. J.* 84:2030-2042.
194. Dittrich, P. S., and P. Schwille. 2002. Spatial Two-Photon Fluorescence Cross-Correlation Spectroscopy for Controlling Molecular Transport in Microfluidic Structures. *Anal. Chem.* 74:4472-4479.
195. Thompson, N. L., T. P. Burghardt, and D. Axelrod. 1981. Measuring surface dynamics of biomolecules by total internal reflection fluorescence with photobleaching recovery or correlation spectroscopy. *Biophys. J.* 33:435-454.
196. Lieto, A. M., R. C. Cush, and N. L. Thompson. 2003. Ligand-Receptor Kinetics Measured by Total Internal Reflection with Fluorescence Correlation Spectroscopy. *Biophys. J.* 85:3294-3302.
197. Lieto, A. M., and N. L. Thompson. 2004. Total Internal Reflection with Fluorescence Correlation Spectroscopy: Nonfluorescent Competitors. *Biophys. J.* 87:1268-1278.
198. Starr, T. E., and N. L. Thompson. 2001. Total Internal Reflection with Fluorescence Correlation Spectroscopy: Combined Surface Reaction and Solution Diffusion. *Biophys. J.* 80:1575-1584.
199. Aragón, S. R., and R. Pecora. 1976. Fluorescence correlation spectroscopy as a probe of molecular dynamics. *The Journal of Chemical Physics* 64:1791-1803.

200. Schwille, P., and E. Haustein. Fluorescence Correlation Spectroscopy: An Introduction to its Concepts and Applications. In *Biophysics Textbook Online*.
201. Thompson, N. L. 1991. Fluorescence Correlation Spectroscopy. In *Topics in Fluorescence Spectroscopy*. J. Lakowicz, editor. Plenum Press, New York. 338-378.
202. Saleh, B. 1978. *Photoelectron Statistics*. Springer-Verlag, Berlin.
203. Qian, H. 1990. On the statistics of fluorescence correlation spectroscopy. *Biophysical Chemistry* 38:49-57.
204. Koppel, D. E. 1974. Statistical accuracy in fluorescence correlation spectroscopy. *Phys. Rev. A* 10:1938 LP - 1945.
205. Schutz, G. J., H. Schindler, and T. Schmidt. 1997. Single-molecule microscopy on model membranes reveals anomalous diffusion. *Biophys. J.* 73:1073-1080.
206. Anderson, C., G. Georgiou, I. Morrison, G. Stevenson, and R. Cherry. 1992. Tracking of cell surface receptors by fluorescence digital imaging microscopy using a charge-coupled device camera. Low-density lipoprotein and influenza virus receptor mobility at 4 degrees C. *J Cell Sci* 101:415-425.
207. Wilson, K., I. Morrison, P. Smith, N. Fernandez, and R. Cherry. 1996. Single particle tracking of cell-surface HLA-DR molecules using R-phycoerythrin labeled monoclonal antibodies and fluorescence digital imaging. *J Cell Sci* 109:2101-2109.
208. Sheetz, M. P., S. Turney, H. Qian, and E. L. Elson. 1989. Nanometre-level analysis demonstrates that lipid flow does not drive membrane glycoprotein movements. 340:284-288.
209. Martin, D. S., M. B. Forstner, and J. A. Kas. 2002. Apparent Subdiffusion Inherent to Single Particle Tracking. *Biophys. J.* 83:2109-2117.
210. Masuda, A., K. Ushida, and T. Okamoto. 2005. Direct observation of spatiotemporal dependence of anomalous diffusion in inhomogeneous fluid by sampling-volume-controlled fluorescence correlation spectroscopy. *Physical Review E (Statistical, Nonlinear, and Soft Matter Physics)* 72:060101.
211. Ingo Gregor, D. P., Jörg Enderlein,. 2005. Optical Saturation in Fluorescence Correlation Spectroscopy under Continuous-Wave and Pulsed Excitation. *ChemPhysChem* 6:164-170.
212. Saxena, A. M., J. B. Udgaonkar, and G. Krishnamoorthy. 2005. Protein dynamics control proton transfer from bulk solvent to protein interior: A case study with a green fluorescent protein. *Protein Sci* 14:1787-1799.
213. 2007. Research highlights: Chemistry: Blinking Hot. *Nature* 448:842-843.
214. Faucher, S., and S. Zhu. 2006. Feasibility Analysis of Surface Mediation in Supported Atom Transfer Radical Polymerization. *Macromolecules* 39:4690-4695.
215. Tronc, F., M. Li, J. Lu, M. A. Winnik, B. L. Kaul, and J.-C. Graciet. 2003. Fluorescent Polymer Particles by Emulsion and Miniemulsion Polymerization. *Journal of Polymer Science: Part A* 41:766-778.
216. Limer, A. J., A. K. Rullay, V. S. Miguel, C. Peinado, S. Keely, E. Fitzpatrick, S. D. Carrington, D. Brayden, and D. M. Haddleton. 2006. Fluorescently tagged star

polymers by living radical polymerisation for mucoadhesion and bioadhesion.  
Reactive and Functional Polymers 66:51-64.

#### **4. Manuscripts**

##### ***4.1 Anomalous Diffusion of Proteins Due to Molecular Crowding***

Banks, D. S., and C. Fradin. 2005. Anomalous Diffusion of Proteins Due to Molecular Crowding. *Biophys. J.* 89:2960-2971.

## Anomalous Diffusion of Proteins Due to Molecular Crowding

Daniel S. Banks\* and Cécile Fradin\*†

\*Department of Physics and Astronomy, and †Department of Biochemistry and Biomedical Sciences, McMaster University, Hamilton, Ontario, Canada

**ABSTRACT** We have studied the diffusion of tracer proteins in highly concentrated random-coil polymer and globular protein solutions imitating the crowded conditions encountered in cellular environments. Using fluorescence correlation spectroscopy, we measured the anomalous diffusion exponent  $\alpha$  characterizing the dependence of the mean-square displacement of the tracer proteins on time,  $\langle r^2(t) \rangle \sim t^\alpha$ . We observed that the diffusion of proteins in dextran solutions with concentrations up to 400 g/l is subdiffusive ( $\alpha < 1$ ) even at low obstacle concentration. The anomalous diffusion exponent  $\alpha$  decreases continuously with increasing obstacle concentration and molecular weight, but does not depend on buffer ionic strength, and neither does it depend strongly on solution temperature. At very high random-coil polymer concentrations,  $\alpha$  reaches a limit value of  $\alpha_1 \approx 3/4$ , which we take to be the signature of a coupling between the motions of the tracer proteins and the segments of the dextran chains. A similar, although less pronounced, subdiffusive behavior is observed for the diffusion of streptavidin in concentrated globular protein solutions. These observations indicate that protein diffusion in the cell cytoplasm and nucleus should be anomalous as well, with consequences for measurements of solute diffusion coefficients in cells and for the modeling of cellular processes relying on diffusion.

### INTRODUCTION

A detailed understanding of the diffusion of proteins in solutions containing high concentrations of soluble macromolecules is presently lacking. However, such an understanding is needed to correctly model passive intracellular transport, a process likely to regulate important cellular functions such as signal transduction (1,2), self-assembly of supramolecular structures (3), gene transcription (4), kinetics of reaction (5), embryogenesis (6), or regulation of cell polarization (7). This understanding would also be beneficial to several important fields of studies across disciplines. In the fields of physical chemistry of solutions and polymer physics, it would facilitate the resolution of long-standing fundamental questions such as the clarification of the mechanisms that govern the dynamics of single chains in polymer solutions and the determination of the relationship between the macroscopic and microscopic viscosities of these solutions (8–10). In pharmaceutical research, it would permit the improvement of drug delivery systems relying on the slow release of drugs from polymer matrices (11,12).

Molecular crowding affects solute diffusion by increasing the effective viscosity of the medium (13). It is also known to cause depletion interactions, which tend to segregate macromolecules according to their size due to the increase in free volume accessible to the solutes upon segregation (14) and to affect the rates of chemical reactions taking place in solution (13,15). In cells, for example, it is thought to influence not only protein and nucleic acid diffusion, but also molecular recognition (16), protein assembly (17), and protein folding

(9,18). However, despite its crucial importance, diffusion in crowded environments remains a challenge to study and predict. Even in simple model systems such as concentrated polymer solutions none of the many models proposed can fully describe the body of experimental evidence available (8,19). In this article, we investigate the nature of diffusion in crowded globular protein and random-coil polymer solutions that we take as a model system for diffusion in the intracellular environment, and show that protein diffusion strongly deviates from simple diffusion in these systems.

### ANOMALOUS DIFFUSION

The description of the diffusion of a solute in a continuous medium is usually based on Fick's law, which defines the diffusion coefficient,  $D$ , of the solute in the media. Combined with conservation of matter, Fick's law leads to the diffusion equation, whose solution yields the usual expression for the mean-square displacement of a diffusing particle in three dimensions:

$$\langle r^2(t) \rangle = 6Dt, \quad (1)$$

which is characteristic of simple diffusion. The dependence of  $D$  on the diffusing particle's hydrodynamic radius and on the solvent viscosity is captured in the Stokes-Einstein equation. However, whereas Fick's law is an established phenomenological law for diffusion in isotropic fluids, there is no physical reason why it should always apply to more complex systems (20). More generally, in complex media, one might expect the mean-square displacement to obey a power law:

$$\langle r^2(t) \rangle = 6\Gamma t^\alpha, \quad (2)$$

Submitted August 10, 2004, and accepted for publication August 3, 2005.

Address reprint requests to Cécile Fradin, E-mail: fradin@physics.mcmaster.ca.

© 2005 by the Biophysical Society

0006-3495/05/11/2960/12 \$2.00

doi: 10.1529/biophysj.104.051078

where  $\Gamma$  is a constant that does not depend on time. If the exponent  $\alpha$  is different from 1, then the diffusion is said to be anomalous, and if  $\alpha < 1$  it is said to be subdiffusive. The quantity  $\langle r^2 \rangle / 6t$  may still be defined as the apparent diffusion coefficient  $D(t)$ , but it will depend on the timescale, or equivalently on the length scale of the measurements:

$$D(t) = \Gamma t^{\alpha-1}. \quad (3)$$

In fractal media, where there is no characteristic length scale, true anomalous diffusion is expected at all scales (21,22). Many physical systems, however, possess a characteristic length scale  $\xi$ , or a range of characteristic length scales. For example, in crowded solutions  $\xi$  is determined by various parameters such as the size of the solutes and the range of the pair correlation function (23). In general, when  $\langle r^2 \rangle \ll \xi^2$  diffusion should be simple and correspond to diffusion in the fluid without obstacles. When  $\langle r^2 \rangle \gg \xi^2$  diffusion should also be simple but correspond to diffusion in the composite medium. But when  $\langle r^2 \rangle \approx \xi^2$ , diffusion has to be anomalous to bridge these two regimes (24). This simple phenomenological argument does not predict pure anomalous diffusion, but just subdiffusion over an intermediary range of timescales. This type of crossover effect is well illustrated in Monte Carlo simulations of diffusion in the presence of immobile point obstacles (25).

## ANOMALOUS DIFFUSION IN CELLS

Although observations of anomalous protein diffusion in cells have been reported (26–29), in the majority of studies to date, three-dimensional (3-D) cellular diffusion has been assumed to be simple. One reason for this is that, whereas two-dimensional membrane diffusion has been clearly shown to be anomalous (24,30,31), a fact sometimes attributed to corralling effects or to interactions with immobile membrane proteins acting as fixed obstacles, in the cytoplasm or the nucleus the case for anomalous diffusion of proteins is not easy to demonstrate, because diffusing proteins are too fast to be easily followed by single-particle tracking. With other experimental methods such as fluorescence recovery after photobleaching and fluorescence correlation spectroscopy (FCS), many artifacts have to be accounted for before the conclusion can be made that diffusion is anomalous, including: fluorophore blinking (29,32), reversible photobleaching (33), restriction of diffusion by membranes (34,35), and division of the population of tracers in several subspecies with different diffusion coefficients (29). As well, in our experience the aspect ratio of the experimental detection volume must be very accurately determined if one wants to study deviations from simple diffusion with FCS, because using an artificially high value of that parameter may conceal the real anomaly of the diffusion if  $\alpha > 0.9$ . In one of the rare studies that considered anomalous diffusion of proteins inside cells, anomalous exponents in the range 0.7–1

were found, depending on the position within the cell (far from membranes), with smaller exponents consistently found in the nucleus (29). However, the authors showed that the data could be analyzed as well using a two-component model. In another study considering the anomalous diffusion of dextran polymers inside HeLa cells, anomalous exponents ranged from 0.7 to 0.9 (27). However, most of the evidence for 3-D anomalous protein diffusion in cells is in fact indirect.

Groups that have studied diffusion in cells report widely disparate data: the diffusion coefficients of tracer particles in cells are found to lie anywhere between 0 and 80% of their value in aqueous solution (29,33,36–43), reflecting the fact that the observed reduction in mobility depends on many variables. A tracer's mobility depends on which cell type (41), on which cell (33), but also on which position inside the cell (29) is selected for the study. The relative mobility of a tracer in a cell compared to an aqueous solution,  $D_{\text{cell}}/D_{\text{aq}}$ , has been shown to decrease with increasing size of the diffusing particles (37–39), which is an indirect indication that simple diffusion models may not apply and that diffusion might be anomalous. Possible interactions of the tracer particle with its environment also play a role (44). Finally, it seems that results might depend on the technique used (41), another possible indication that analysis of experimental data based on a simple diffusion model is misleading. A timescale-dependent  $D(t)$  may explain some of the disparate data.

In this article, we report our studies as to whether the diffusion of proteins in the presence of molecular crowding due to other solutes is anomalous, a possibility that had not yet been investigated experimentally. We chose to focus on model systems where molecular crowding is provided by controlled concentrations of inert random-coil polymer molecules or globular proteins, thus reproducing the crowded conditions present in cells while reducing the risk of misinterpreting the experimental data. We used FCS to extract the anomalous diffusion exponent  $\alpha$  corresponding to the diffusion of the proteins. The length scale of FCS measurements is set by the 0.5- $\mu\text{m}$  diameter confocal detection volume and is relevant to the length scale of diffusion in the intracellular medium.

## MATERIALS AND METHODS

### Tracer particles and obstacles

Our samples were composed of a small concentration (typically 20 nM) of fluorescent tracer particles diffusing in an aqueous buffer (phosphate buffered saline (PBS)) in which obstacles were dissolved at a concentration up to 400 g/l. We used Dulbecco's PBS without magnesium and calcium: 137 mM NaCl, 15 mM  $\text{Na}_2\text{HPO}_4$ , 2.7 mM KCl, 1.5 mM  $\text{KH}_2\text{PO}_4$ , pH 7.4. The molecules used as obstacles were bovine serum albumin ((BSA) 66 kDa, Bioshop, Burlington, Ontario, Canada), streptavidin (52.8 kDa, Sigma-Aldrich, St Louis, MO), and dextrans (also from Sigma-Aldrich). The peak molecular weight values  $M_p$ , and polydispersity indices ( $M_w/M_n$ ) of the dextrans used, as well as their approximate radii of gyration ( $R_g$ ) and approximate overlap volume fractions ( $\phi^*$ ) in aqueous solution are shown in Table 1. The molecular weight values are reported as given by the supplier, and the values

**TABLE 1** Characteristics of the dextrans used as obstacles

$M_p$ (kDa)	$M_n$ (kDa)	$M_w$ (kDa)	$M_w/M_n$	$R_g$ (nm)	$\phi^*$
1.1	1.0	1.3	1.26	0.82	0.49
4.4	3.3	5.2	1.60	1.7	0.22
9.9	8.1	11.6	1.43	2.6	0.14
43.5	35.6	48.6	1.37	5.8	0.055
276.5	236.3	409.8	1.73	17	0.014
401.3	332.8	667.8	2.01	22	0.009

$M_p$ ,  $M_n$ ,  $M_w$  are the peak value, number average, and weight average of the molecular mass, respectively.  $M_w/M_n$  is the polydispersity index.  $R_g$  is the radius of gyration and  $\phi^*$  is the overlap volume fraction in aqueous solution, approximated as explained in the text.

of  $R_g$  were estimated from the molecular weight data using an experimental relationship from the literature (45). The values of  $\phi^*$  were calculated following an approximate method (Schaefer, 1984) that divides the volume occupied by the monomers of a chain by an approximate expression for the pervaded volume of a chain:  $\phi^* = (M_p \cdot v/N_A) / ((4/3)\pi R_g^3)$ , where  $v = 0.625 \text{ cm}^3/\text{g}$  is the specific volume of dextran (46) and  $N_A$  is Avogadro's number. The fluorescent tracers used in this study were streptavidin labeled with Alexa Fluor 488 (52.8 kDa, Molecular Probes, Eugene, OR), enhanced green fluorescent protein (EGFP) 27 kDa, BD Biosciences Clontech, San Jose, CA), fluorescein, and FITC-dextran (282 kDa, Sigma-Aldrich). All molecules were used without further purification. They were dissolved at high concentrations with stirring as needed. The tracer molecules were selected for their absence of known interaction with the chosen obstacles and, except for the dextran, for their perfect monodispersity. To characterize the size of a tracer, its hydrodynamic radius  $R_H$  can be calculated from its diffusion coefficient using the Stokes-Einstein relation. The diffusion coefficients of EGFP, streptavidin, and FITC-dextran in the aqueous buffer in the absence of obstacles were measured by FCS and their hydrodynamic radii in the absence of obstacles were found to be 3.3, 4.9, and 9.5 nm respectively. The hydrodynamic radius of fluorescein can be estimated to be 0.8 nm from its known diffusion coefficient  $D = 260 \mu\text{m}^2/\text{s}$ . The isoelectric point of streptavidin is  $pI = 6.3$  (47), whereas that of EGFP is  $pI = 5.5$  (48), meaning that in the pH = 7.4 buffer used both proteins are negatively charged. The use of charged proteins reduces the risks of aggregation, which are higher in crowded solutions due to the presence of depletion interactions.

## Fluorescence correlation spectroscopy

FCS is a method relying on the detection and temporal analysis of the fluorescence signal emitted from a small confocal detection volume (49–52). Our homebuilt FCS setup is based on an inverted Nikon Eclipse TE2000-U microscope (Nikon, Tokyo, Japan). Fluorescence is excited by an argon ion laser (Melles Griot, Carlsbad, CA) whose 488-nm wavelength is selected by an excitation filter (HQ480/40 $\times$ , Chroma Technology, Brattleboro, VT). The beam is focused in the sample by a water immersion objective (Plan Apo 60 $\times$ , N.A. 1.20, Nikon). The output power of the laser is attenuated by neutral density filters and polarizers to obtain a radiant exposure at the focus in the range of 1–10 kW/cm<sup>2</sup>. The emitted fluorescence collected by the objective passes through a dichroic mirror (Q505LP, Chroma), is filtered by an emission filter (HQ535/50m, Chroma), and focused through either a 30- or a 75- $\mu\text{m}$ -diameter pinhole (Thorlabs, Newton, NJ) depending on the diameter of the beam entering the objective. The signal is detected by a photomultiplier (H7421, Hamamatsu Photonics, Shimokanzo, Japan) and fed into a multi-tau correlator (Flex01–08 ns, Correlator.com, Bridgewater, NJ) that computes its autocorrelation function. Autocorrelation functions were typically recorded for durations of 2–3 min and the measurements repeated 10–30 times for each sample. Analyses of the measured autocorrelation functions were performed using the software KaleidaGraph (Synergy Software, Reading, PA) that relies on the Levenberg-Marquardt algorithm. The exact dimensions of the confocal detection volume were

evaluated before each experiment by fitting the autocorrelation function obtained from the free diffusion of fluorescein in PBS assuming  $D = 260 \mu\text{m}^2/\text{s}$  (53). Typical values obtained for the  $1/e^2$  half-width of the detection volume were  $w_0 = 220 \text{ nm}$  and  $w_0 = 350 \text{ nm}$  for the two different pinhole sizes used. Most of the measurements were done at room temperature, but when necessary the temperature of the sample was controlled using both an inverted Peltier stage heater (PE100-NI, Linkam Scientific, Surrey, UK) and a custom-made Peltier objective heater (also from Linkam Scientific).

## Analysis of the autocorrelation functions

Autocorrelation functions were analyzed using an expression modified to account for the possibility of anomalous diffusion. In this case, because the mean-square displacement follows a power law,  $\langle r(t)^2 \rangle \sim t^\alpha$ , the expression of the autocorrelation function can be expected to be (54):

$$G(t) = \frac{1/N}{\left(1 + \left(\frac{t}{\tau_D}\right)^\alpha\right) \left(1 + \frac{1}{S^2} \left(\frac{t}{\tau_D}\right)^\alpha\right)^{1/2}} \cdot \left(1 + \frac{T}{1-T} - e^{-t/\tau_T}\right). \quad (4)$$

$S$  is the aspect ratio, height to width, of the ellipsoidal detection volume.  $N$  is the average number of fluorophores and  $\tau_D$  their characteristic residence time in this volume;  $\tau_D$  is related to the apparent diffusion coefficient  $D$  of the fluorophores and to the half-width  $w_0$  of the detection volume:

$$\tau_D = \frac{w_0^2}{4D}. \quad (5)$$

The second term in Eq. 4 accounts for the existence of a nonfluorescent triplet state (55):  $\tau_T$  is the relaxation time of the triplet state, and  $T$  is the average fraction of fluorophores found in the triplet state. The simple analytical equation given in Eq. 4 was derived using one of several possible diffusion equations leading to anomalous diffusion, and hence is not necessarily an exact solution for all cases of anomalous transport. However, it has been shown to be a very good approximation of the more complex solution of a larger class of anomalous diffusion equations (27). Importantly, the asymptotic behavior of the autocorrelation function depends only on the probability of a particle to return to the origin, which is independent of the anomalous diffusion model used (56). Both the triplet state relaxation time,  $\tau_T$ , and the aspect ratio,  $S$ , were fixed in the fitting process for all the samples containing obstacles. The value of these two parameters was determined by fitting autocorrelation functions measured for the diffusion of the tracer in an aqueous solution immediately before performing the experiments in the presence of molecular crowding. In the case of EGFP,  $\tau_T$  is the decay time of the fast protonation process that causes fluorophore blinking, whereas the blinking due to the slow protonation process is not expected to occur at the pH used in this study (32). Indeed, Eq. 4 with  $\alpha = 1$  fits the autocorrelation data well for diffusion of EGFP in PBS without obstacles.

In the case where  $\alpha = 1$ , diffusion is simple and the diffusion coefficient  $D$  calculated from the measured value of  $\tau_D$  using Eq. 5 is a constant, as defined in Eq. 1. On the other hand, when  $\alpha \neq 1$  diffusion is anomalous and the diffusion coefficient  $D$  calculated using Eq. 5 is just an apparent diffusion coefficient, describing diffusion at the length scale  $w_0$  set by the experiment, or equivalently at the timescale  $\tau_D$ . As defined in Eqs. 2 and 3, the apparent diffusion coefficient is:

$$D(\tau_D) = \Gamma \tau_D^{\alpha-1}. \quad (6)$$

Multicomponent models are often used to explain deviations from simple diffusion. The corresponding expression of the diffusion term of the autocorrelation function for such models is:

$$G(\tau) = \sum_{i=1}^n \frac{a_i}{\left(1 + \frac{\tau}{\tau_{Di}}\right) \left(1 + \frac{1}{S^2} \left(\frac{\tau}{\tau_{Di}}\right)\right)^{1/2}}, \quad (7)$$

where  $a_i$  is the contribution of the  $i$ th component to the total amplitude of the autocorrelation function,  $G(0)$ , and  $\tau_{Di}$  is the characteristic residence time of this component. To assess the validity of using an anomalous diffusion model as opposed to a multiple-component model, the autocorrelation functions were analyzed both using a two-component model (Eq. 7 with  $n = 2$ ), where it is assumed that two different fluorescent species are diffusing normally in solution (29), and using a maximum entropy method adapted for FCS (MEMFCS), where it is assumed that a large number of different fluorescent species are diffusing normally in solution (Eq. 7 with  $n = 100$ ), each with a different diffusion coefficient (57,58). We used the MEMFCS algorithm recently made available by Sengupta and colleagues (57) based on the maximum entropy method of Skilling and Bryan (59). Like other fitting algorithms, MEMFCS seeks to minimize the chi-square parameter  $\chi^2$  describing the distribution of the residuals, but MEM algorithms also seek to maximize an entropy-like quantity,  $S = -\sum_i p_i \ln p_i$ , where  $p_i = a_i / \sum_j a_j$  for FCS. Maximizing entropy results in the maximally wide distribution of  $\tau_{Di}$  values that is consistent with the data.

Autocorrelation data showing obvious signs of the passage of large fluorescent aggregates through the detection volume during the measurement, both by erratic deviations from a smooth decay in the 0.1–10-s time range and the presence of spikes in the photon count history recorded by the correlator at a resolution of 67 ms were rejected. In contrast to the discarded measurements showing evidence of aggregation, the measurements retained for analysis were highly reproducible and independent from protein preparation. The occurrence of aggregates varied considerably from one protein batch to the next, implying that aggregation is not an intrinsic property of the system, but suggesting instead that aggregates are formed around impurities. The number of aggregation occurrences became more frequent at very high concentrations of high molecular weight dextrans, and up to two-thirds of the curves had to be rejected. However, ultracentrifugation of our samples up to  $200,000 \times g$  using a Beckman TL-100 Tabletop Ultracentrifuge (Beckman Coulter, Fullerton, CA) greatly reduced the frequency of the aggregation occurrences. But the anomalous diffusion exponent and the diffusion coefficient measured did not change after ultracentrifugation.

## RESULTS

Two different types of diffusion behavior were obtained depending on the presence or absence of obstacles in the buffer, as illustrated by the autocorrelation curves presented in Fig. 1. In samples containing only very low concentrations of solutes, the resultant diffusion cannot be distinguished from simple diffusion. The simple diffusion model for a single species in solution (Eq. 4 with  $\alpha = 1$ ) is very successful in fitting the correlation data for such systems. However, in crowded solutions, this simple equation no longer fits the data. The autocorrelation data show a broadening in the decay at timescales corresponding to diffusion (Fig. 1), indicating a wider distribution of diffusion times of the tracer through the detection volume.

Two models frequently used to model the diffusion of tracers in living cells are the two-component model (Eq. 7 with  $n = 2$ ) and the anomalous diffusion model (Eq. 4), as described in Materials and Methods. For the crowded solution, the fit obtained using the anomalous diffusion model is shown in Fig. 1 *a*, whereas Fig. 1 *b* compares the residuals of the fits for both models, showing that the anomalous diffusion model gives a slightly better match. Another way to distinguish between these two models is to examine

the long-time behavior of the autocorrelation data. Although multi-tau correlators may introduce errors at long times for oscillatory signals (60), the signal considered here is not oscillatory, and thus the long-time behavior of the correlation data should be reliable. At timescales above the characteristic average residence time, the autocorrelation function of multicomponent models scales as  $t^{-3/2}$  (Eq. 7), whereas in the anomalous diffusion model, the autocorrelation function scales as  $t^{-3\alpha/2}$  (Eq. 4). As shown in Fig. 1 *c*, the asymptotic behavior of the autocorrelation function corresponding to the diffusion of streptavidin in the absence of dextran obstacles is identical to that predicted by the simple diffusion model. But when dextran obstacles are present, it clearly deviates from the  $t^{-3/2}$  scaling predicted by multicomponent models. On the contrary, in the latter case, it is well described by the  $t^{-3\alpha/2}$  scaling predicted by the anomalous model. Finally, the fact that the same exponent  $\alpha = 0.76$  describes equally well short-time behavior around  $\tau_D$  and the asymptotic behavior above  $\tau_D$  indicates that the diffusion may be consistently anomalous over a large time range.

We used the MEMFCS fitting algorithm to further test the agreements of the two models with the experimental data, and to validate the use of the anomalous diffusion model to analyze our data. Fig. 2 shows the effective distributions in average residence times calculated using the MEMFCS software that correspond to the autocorrelation data shown in Fig. 1 *a*. Although diffusion in the absence of obstacles yields a narrow distribution, as expected (57), diffusion in the presence of obstacles produces a wide distribution with a distinct tail at long times. Such a distribution is not compatible with a two-component model. Indeed, if we apply the MEMFCS algorithm to simulated autocorrelation data generated using the equation for the two-component model (Eq. 7 with  $n = 2$  where the parameters were obtained by fitting the experimental data shown in Fig. 1), then we find a distribution with two narrow peaks centered around the characteristic residence time of the two species (cf. Fig. 2). The presence of two clearly separated peaks is not due to the use of simulated autocorrelation data. The maximum entropy method has been shown to be able to separate the contributions of two different species in different real two-component samples (58,61). The failure of the two-component model to predict the correct distribution of residence times proves that the complex behavior of the systems under study cannot be reduced to coexistence of two distinct tracer populations.

In contrast, if the MEMFCS algorithm is applied to simulated autocorrelation data generated using the anomalous diffusion model, then we find a wide and asymmetric distribution of residence times nearly identical to the distribution obtained from the experimental data (cf. Fig. 2). The experimental distribution is in good agreement with a subdiffusive behavior of the fluorescent tracer particles, and we found this agreement to hold for all concentrations of obstacles. A wide distribution of diffusion times is expected in the case of anomalous diffusion, as shown by applying the

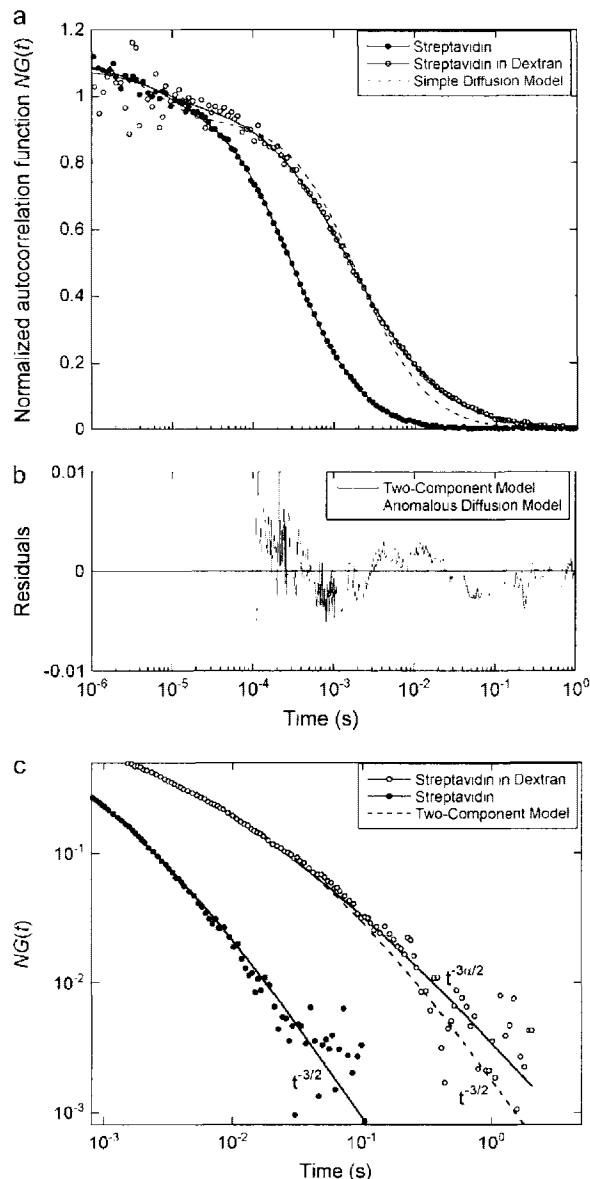


**FIGURE 1** Normalized autocorrelation functions for streptavidin diffusing in PBS buffer with and without dextran obstacles (200 g/l of 276.5 kDa dextran). The fit of these autocorrelation functions using the anomalous diffusion model (Eq. 4) gives  $\alpha = 0.99 \pm 0.01$  for no obstacles, and  $\alpha = 0.76 \pm 0.01$  with obstacles (solid lines). The failure of the fit with the simple diffusion model (Eq. 4 with  $\alpha = 1$ ) for the case with obstacles is also shown (dashed line). The fit with the two-component model (Eq. 7) closely resembles the fit with the anomalous diffusion model and is not shown for clarity of the plot. (b) Residuals of the fits of the autocorrelation function in panel a for the case with dextran obstacles with both the anomalous diffusion model (dots,  $\chi^2 = 0.0024$  for 459 data points from  $t = 0.5 \mu\text{s}$  to 1 s, with three adjustable parameters) and the two-component model (solid line,  $\chi^2 = 0.0028$  for the same data points with four adjustable parameters) are shown for the timescale relevant to diffusion. At shorter timescales, the two models are practically identical and the scatter in the data is large. (c) Asymptotic long-time behavior of the data and fits to the autocorrelation functions shown in panel a. For the case without dextran obstacles, the fit with the anomalous diffusion model shows a  $t^{-3/2}$  scaling (solid line). For the case

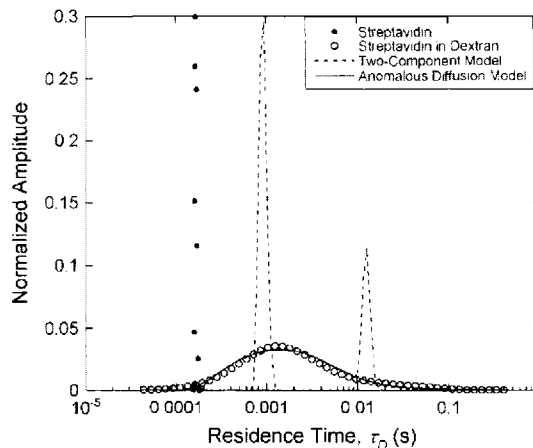


**FIGURE 2** Effective distributions in average residence times calculated with the MEMFCS algorithm for the experimental autocorrelation data shown in Fig. 1 a (symbols), and for two sets of simulated autocorrelation data corresponding to the case of streptavidin diffusing in 200 g/l 276 kDa dextran. The first set was generated using the anomalous diffusion model and the parameters found from the fit of the experimental data ( $\alpha = 0.76$ ,  $\tau_D = 1.6$  ms) and the second set was generated using the two-component model and the parameters found from the fit of the experimental data ( $\tau_{D1} = 0.90$  ms,  $\tau_{D2} = 12$  ms, relative amplitude  $a_2/a_1 = 0.41$ ), as explained in the text. The peak values of the distributions found by the MEMFCS algorithm for the two-component model are 0.94 and 13 ms.

maximum entropy method to simulated fluorescence recovery after photobleaching experiments (53). Also, long-tail kinetics, which will result in an asymmetric distribution of diffusion times, were predicted as a result of anomalous diffusion (62). The MEMFCS analysis does not distinguish between a single component diffusing anomalously and a continuous distribution of components diffusing normally having coincidentally the same distribution of residence times. However, if the diffusion in our samples were not actually anomalous, then the distribution produced by the MEMFCS algorithm from the experimental data could have been incompatible with anomalous diffusion. But because the distributions do agree, even if the diffusion is not in fact anomalous, we can characterize the experimental distribution using only the two parameters  $D(\tau_D)$  and  $\alpha$  extracted from the anomalous diffusion model, which determine the center and the width of the distribution. For the above reasons, we discuss our results using the anomalous diffusion model throughout the rest of this article.

The apparent diffusion coefficient  $D(\tau_D)$  obtained using the anomalous diffusion model for streptavidin in the presence of various concentrations of dextrans of different molecular weight is shown in Fig. 3 a. For streptavidin,  $D(\tau_D)$  is found to decrease with increasing concentration of

with obstacles, the fit with the anomalous diffusion model shows a  $t^{-3\alpha/2}$  scaling (solid line,  $\alpha = 0.76$ ), whereas the fit with the two-component model shows a  $t^{-3/2}$  scaling (dashed line).

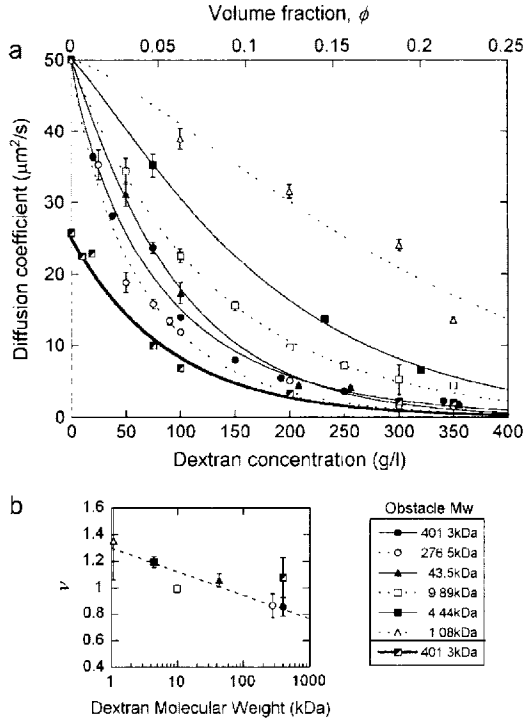


FIGURE 3 (a) Apparent diffusion coefficient,  $D(\tau_D)$ , associated with the diffusion of streptavidin as a function of dextran concentration for dextrans of various average molecular weights (open and solid symbols). Also shown is  $D(\tau_D)$  for a 282 kDa dextran diffusing in a solution crowded by a 401.3 kDa dextran (half-solid symbols). Lines represent stretched exponential fits as explained in the text. Where necessary, some of the data points have been slightly shifted horizontally for clarity of the plot. (b) Value of the exponent  $\nu$  as a function of the molecular weight of the polymers used as obstacle. The dotted line is a guide for the eyes.

dextran as predicted by all models describing the diffusion of spherical tracer particles in the presence of macromolecular crowding (8,13,19) and as previously observed in similar systems (63). Our data in Fig. 3 a can be satisfactorily fitted by a stretched exponential:

$$\frac{D}{D_0} = e^{-\beta\phi^\nu}, \quad (8)$$

where  $D_0$  is the diffusion coefficient of the tracer particle in aqueous solution,  $\phi$  is the polymer volume fraction, and  $\beta$  and  $\nu$  are scaling parameters. Equation 8 corresponds to the prediction made by several models describing the diffusion of globular tracer particles in polymer solutions. All these models rely to some extent on phenomenological arguments, and the physical significance of the coefficients  $\beta$  and  $\nu$  is not well defined (8). Some models predict different constant values for  $\nu$  (64), whereas Phillies' model predicts a dependence on molecular weight (65). In our case we observe no clear trend in  $\beta$  as a function of the polymer molecular weight, and find that  $\nu$  drops from 1.35 to 0.85 as the polymer molecular weight increases (cf. Fig. 3 b).

However, the novel and surprising result of our study is that the diffusion of streptavidin is anomalous in the presence of dextran. The data in Fig. 4 a show two trends with respect to the anomalous exponent. First,  $\alpha$  drops with increasing dextran concentration until it reaches a limit value  $\alpha_1 \approx 0.74$  for the large molecular weight dextrans. In the cases of the smaller dextran obstacles, only the decay regime is observable. Second, the initial decay of the anomalous exponent becomes steeper with increasing molecular weight of the obstacles. The fits indicated in Fig. 4 a have been made assuming an asymptotic exponential decay to a limit value  $\alpha_1$  common for all dextrans:

$$\alpha = \alpha_1 + (1 - \alpha_1)e^{-\phi/\phi_0}, \quad (9)$$

where  $\alpha_1$  was estimated first by fitting the curves in Fig. 3 a for the three highest molecular weight dextrans allowing  $\alpha_1$  to vary. We found  $\alpha_1 = 0.74 \pm 0.02$ . Then all curves were fitted using this limit value. The origin and value of  $\alpha_1$  are discussed below. Fig. 4 b shows the value of  $\phi_0$  as a function of the polymer molecular weight.

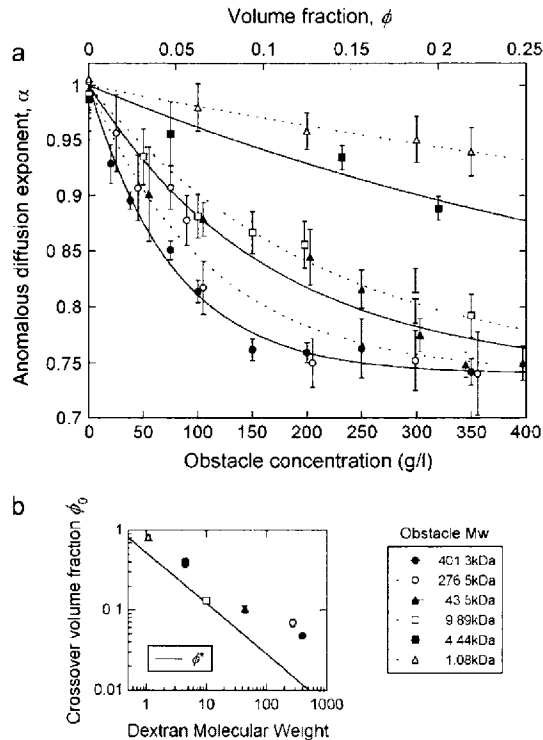


FIGURE 4 (a) Anomalous diffusion exponent associated with the diffusion of streptavidin as a function of obstacle concentration for dextrans of various average molecular weights. Lines are fits to the data using Eq. 10 with  $\alpha_1 = 0.74$ . Where necessary, some of the data points have been slightly shifted horizontally for clarity of the plots. (b) Crossover volume fraction  $\phi_0$  found as a result of the fit shown in panel a for the different dextrans used as obstacles. The solid line shows the overlap volume fraction  $\phi^*$  calculated as explained in Materials and Methods.

To test for an effect of the negative charge of streptavidin on the diffusion, we modified the ionic strength of the buffer solution by increasing the NaCl concentration in our samples to screen the interactions due to the charges on the streptavidin. As shown in Fig. 5, adding up to 1 M NaCl to the PBS buffer has no effect on the anomalous diffusion exponent  $\alpha$ , with or without dextran crowding. Above a 1-M concentration of salt in the sample containing 200 g/l of the 276 kDa dextran, there is an increase in the rate of aggregation as evidenced by spikes in the photon count history and corresponding correlations at long times. This is due to the well-known salting out effect: proteins start aggregating upon screening of their electrostatic charges. As expected, aggregation is enhanced by the presence of the dextran, which induces attractive depletion interactions between the proteins. In the control samples not containing dextran, the presence of aggregates was not detected even at the highest salt concentrations used (5 M). For the samples containing dextran, the error introduced by the presence of aggregates reduces the measured value of  $\alpha$  as shown above 1 M salt. And above 2 M, the aggregations become too frequent to admit a fit of the data with the anomalous diffusion model. We also observed that the apparent diffusion coefficient is independent of ionic strength (data not shown).

We tested for a temperature dependence of the subdiffusive behavior within a biologically relevant range, from 15 to 45°C. The experiment was done for streptavidin diffusing in samples containing either 75 g/l or 200 g/l of the 276 kDa dextran. Results are shown in Fig. 6. Although the apparent diffusion coefficient increases with increasing temperatures as expected from the change in the buffer viscosity, the anomalous exponent  $\alpha$  is remarkably constant in both cases, showing that temperature changes in this temperature window do not strongly affect the anomalous nature of the diffusion.

To assess whether the anomalous behavior would depend on the nature of the tracers used, we repeated this experiment with different tracers. As shown in Fig. 7, the diffusion of the

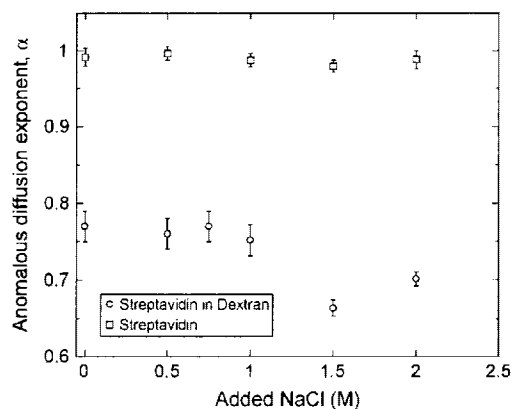


FIGURE 5 Anomalous diffusion exponent corresponding to the diffusion of streptavidin in PBS with and without 200 g/l of 276 kDa dextran, as a function of added NaCl.

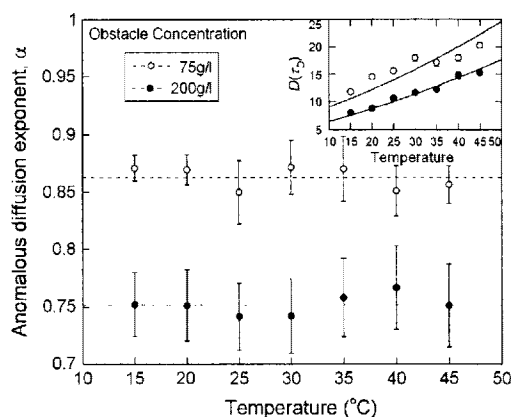


FIGURE 6 Anomalous diffusion exponent  $\alpha$  associated with the diffusion of streptavidin in presence of 75 g/l and 200 g/l of 276 kDa dextran as a function of the temperature. The average values of the anomalous diffusion exponent  $\alpha$  over the considered temperature range are shown:  $\alpha = 0.86 \pm 0.01$  and  $0.75 \pm 0.01$ . The inset shows the corresponding variation of the apparent diffusion coefficient  $D(\tau_D)$  in  $\mu\text{m}^2/\text{s}$ , and the lines are fits assuming that the temperature dependence is only due to the change in the viscosity of water.

other globular protein used as a tracer, EGFP, is anomalous to a degree comparable to that of streptavidin. On the other hand, for fluorescein, the diffusion is normal within experimental errors. For the large dextran tested, the diffusion is also observed to be normal or only slightly anomalous, suggesting that the rules governing the self-diffusion of the polymer obstacles are quite different from those governing the diffusion of the globular tracers.

Finally, to check whether the effect we observe in random-coil polymer solutions is in fact relevant to the diffusion of proteins in the cytoplasm of cells, where molecular crowding

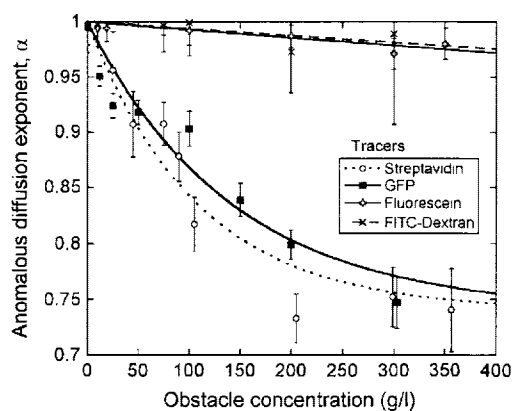


FIGURE 7 Anomalous diffusion exponent as a function of dextran concentration fitted to Eq. 10 for various tracers: EGFP and streptavidin in solutions crowded with the 276.5 kDa dextran, and fluorescein and 282 kDa FITC-dextran in solutions crowded with 401.3 kDa dextrans. Where necessary, some of the data points have been slightly shifted horizontally for clarity of the plots.

is mainly due to high protein concentrations, we used other proteins as obstacles. We investigated the diffusion of streptavidin against very high concentrations of bovine serum albumin, a globular protein of comparable molecular weight, and against high concentrations of unlabeled streptavidin. Results are shown in Fig. 8. At a 350 g/l concentration of BSA, the exponent  $\alpha$  corresponding to the diffusion of streptavidin is  $0.91 \pm 0.02$ . Thus, the subdiffusive behavior is considerably weaker than that observed in the case of the large dextrans, but comparable to that obtained in the case of the smaller dextrans. In the case where streptavidin (not fluorescently labeled) was used as an obstacle, behavior more anomalous than in the case of BSA was observed up to  $\sim 130$  g/l. However, comparison could not be made at higher concentrations due to the lower solubility of streptavidin in PBS. The observation that streptavidin can cause the subdiffusion of labeled streptavidin molecules is nevertheless significant, because it indicates that anomalous diffusion can occur in these systems in the absence of depletion interactions.

## DISCUSSION

Anomalous diffusion has been previously observed and explained in a variety of nonbiological systems (56). Subdiffusion is expected either in the presence of a high concentration of fixed obstacles or in the presence of a distribution of binding sites, as was shown by Monte Carlo simulations of random walks (25,66,67). In fractal systems, the value of  $\alpha$  depends on the type of fractal. For site percolation at the percolation threshold, numerical methods show that  $\alpha = 0.53$  in 3-D (22). Experimentally, subdiffusion has been unambiguously observed in cross-linked polymer networks where the centers-of-mass of the obstacles are fixed (68–71). The variety of anomalous exponents

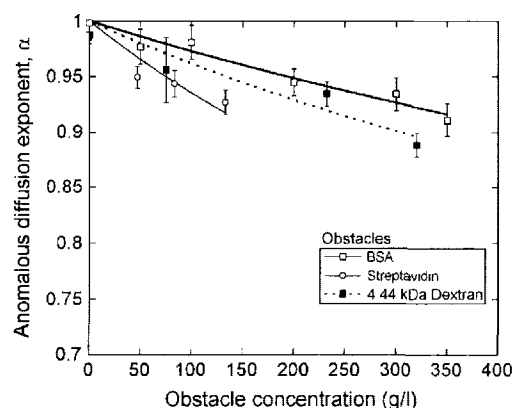


FIGURE 8 Anomalous diffusion exponents associated with the diffusion of streptavidin in solutions crowded with either BSA or nonfluorescent streptavidin for different concentrations of the obstacle proteins fitted to Eq. 10. For comparison, the exponent associated with diffusion in a solution crowded with a 4.44 kDa is also indicated.

measured in these networks were explained by the existence of different effects in addition to the excluded volume effects considered in the simulations: coupling of the tracer motion with the fluctuations of the network filaments (69), trapping (70), and interactions with the obstacles (71).

But in the experiments presented here, the obstacles causing the anomalous diffusion are mobile, and have a mobility comparable to that of the tracer proteins (cf. Fig. 3 for the diffusion of the 282 kDa dextran). This is an unexpected result because for diffusing point obstacles interacting with a point tracer through excluded volume effects, simulations either do not show anomalous diffusion (25), or they show anomalous diffusion only at very short timescales (72). Furthermore, some groups have measured the diffusion of tracers in solutions crowded with mobile random-coiled polymers or globular proteins without observing or reporting this diffusion to be anomalous (73–77). However, our experiments and analysis show very clearly otherwise. One reason for this apparent discrepancy is that subdiffusion does not seem to appear or is very weak, as we show here, for small tracer particles such as fluorescein or for random-coil polymer tracers such as dextran, and most studies to date have been concentrating on the behavior of such tracers (74,76). Other studies have been restricted to low polymer concentrations (77), where the effect is slight and can easily be missed, because it can be incorrectly attributed to the artifacts mentioned in the introduction. In support of our observation that diffusion of tracer particles is anomalous in polymer solutions, it has very recently been shown using scale-dependent FCS measurements that the diffusion of dyes in polymer solutions was slightly anomalous (78). Furthermore, it was reported several times that the measured diffusion coefficients of proteins point to a difference between macroscopic and microscopic viscosities (10,73,77), which may result in anomalous diffusion at intermediate length scales for these proteins.

Although it is clear that the deviation from normal diffusion behavior has to arise from the heterogeneous nature of the solution and interactions between the tracer particle and the obstacles, the nature of these interactions and the mechanism by which they cause anomalous diffusion need to be resolved. The possibility that the distribution of residence times observed in crowded media (Fig. 2) reflects the presence of inhomogeneities due to depletion interactions cannot be entirely ruled out. However, several pieces of evidence speak against this scenario. First, when aggregates are removed by ultracentrifugation, the anomalous behavior observed does not change. Second, if inhomogeneities present in our samples were due to depletion interactions, we would expect them to grow larger upon screening of the negative charges of the tracer proteins. But when adding NaCl in the solution, there are no observable changes until  $\sim 1.5$  M NaCl, when we start detecting signs of aggregation as a stable phenomenon. This suggests that for solutions with no added NaCl, aggregation is a relatively rare occurrence.

Third, in homogeneous streptavidin solutions where depletion interactions disappear, we still observe that the diffusion of fluorescent streptavidin is anomalous, to a degree comparable to that of its diffusion in small dextrans. In addition to these observations, the lack of visible temperature dependence for the anomalous behavior speaks against depletion interactions being the single cause for subdiffusion. In fact, it speaks against all possible models in which entropy effects cause the anomalous behavior, as entropy driven interactions will be sensitive to temperature changes.

Another potential cause for the anomalous diffusion is the polydispersity of the obstacles. Indeed, it may be noted that the polydispersity index (PI) of the dextrans used in our experiments roughly correlates with their molecular weight, as can be seen in Table 1, and so the observed dependence of  $\alpha$  on molecular weight could in fact be a dependence on PI. However, whereas the PI may play a role in determining the value of  $\alpha$ , the key variable is certainly the molecular weight. Indeed, when we mix two dextran samples of same concentration but unequal average polymer weights to obtain a sample of increased PI but lower average molecular weight as compared to the highest molecular weight sample, the anomalous diffusion exponent  $\alpha$  increases (data not shown). Also, diffusion is still anomalous when the solution is crowded with strictly monodisperse obstacles such as BSA or streptavidin.

We hypothesize that the subdiffusion process we observe may be separated into two different regimes, which correspond to two different anomalous diffusion mechanisms. These two different regimes are visible in Fig. 4 *a*, where the anomalous exponent  $\alpha$  depends strongly on obstacle concentration below the crossover volume fraction  $\phi_0$  whereas it is constant above  $\phi_0$ . The first regime corresponds to solutions containing globular proteins, low molecular weight dextrans, or high molecular weight dextrans at low concentration. The second regime corresponds to solutions containing high molecular weight dextrans at high concentrations. The crossover volume fraction  $\phi_0$  is found to be slightly above the chain overlap volume fraction  $\phi^*$  for all dextrans (cf. Fig. 4 *b*).

In the first regime, our samples may be compared to colloidal systems, picturing both the tracers and obstacles as spheres. These systems are similar in that in both cases the tracers and obstacles are globular, comparable in size, and interact mainly through excluded volume or hydrodynamic interactions. Also, both systems are glass-forming solutions. Single particle tracking experiments in colloidal systems showed that anomalous diffusion could be attributed unambiguously to caging effects (79,80). The diffusion behaves according to the prediction of the two-phase model, where diffusion is anomalous only at timescales where both rattling within a cage and hopping out of a cage significantly contribute to displacement. Observations in our systems are compatible with transient caging of the tracer proteins by an ensemble of random-coil polymer molecules or globular proteins. First, neither dextran molecules that can move by

means of reptation nor small fluorescein molecules are likely to be caged. Second, because larger polymers will move slower, they will tend to trap the tracer molecules for a longer time, causing the diffusion to be more anomalous. Third, compared to the case of globular proteins obstacles, anomalous diffusion is more pronounced in the case of random-coil polymer obstacles, because their more extended conformations increase the possibility of complex steric interactions and hence the probability of caging globular tracers. The smaller range of anomalous exponents we observe in this regime  $\alpha \approx 0.9-1$  compared to those reported in the mentioned colloidal systems  $\alpha \approx 0.1-1$  (81) could be attributed to the fact that our systems are farther away from the glass transition, which can be estimated using the Fox equation (82) to be above  $\phi_g = 0.4$  for dextrans in water at room temperature. Alternatively, one could argue that, in this low concentration regime, transient inhomogeneities due to depletion interactions are the cause of the anomalous behavior we observe because they could act as traps for the tracer proteins. The tracers may associate with and dissociate from these inhomogeneities while diffusing through the detection volume, which may result in an anomalous diffusion behavior similar to that predicted by caging models, or by models where tracers are allowed to bind to obstacles (66).

In the second regime, which occurs well above the chain overlap volume fraction  $\phi^*$ , that is, at a volume fraction where the polymer chains are entangled, we observe a constant value of the anomalous exponent  $\alpha_1 = 0.74 \pm 0.02$ . This value is reminiscent of the exponent  $\alpha = 3/4$  measured for the diffusion of beads in cross-linked polymer networks when the tracer diameter is larger than the network mesh size in agarose gels (68) and in actin networks (69). The same behavior ( $\alpha = 3/4$ ) has been observed for the diffusion of lipid granules in the cell cytoplasm (83), and recently for the diffusion of dextran in the cytoplasm of HeLa cells (27). In the case of the cross-linked networks, this result has been explained by a strong coupling between the diffusing beads and the thermal motions of the actin filaments, because the lateral mean-square displacement of the monomers of polymer filaments scales as  $t^{3/4}$  at short times (69). In our system at high dextran concentration, the polymer chains form an entangled, but not cross-linked, network. The center-of-mass diffusion of the polymer is slow compared to the thermal fluctuations of the monomers such that we can expect the coupling between the tracer proteins and the segments of the chains to become the predominant relaxation mechanism for the tracers, resulting in a subdiffusion characterized by  $\alpha = 3/4$ , which is what we observe. Once the polymer chains are well entangled, the average mesh size of the network does not depend on the polymer molecular weight (84), so that the characteristics of the motion of tracer particles should not depend on it either. This is in agreement with our observations: well above  $\phi^*$ , neither the apparent diffusion coefficient nor the anomalous exponent  $\alpha$  depend on the molecular weight of the dextrans.

## CONCLUSION

This study is the first report of unequivocal observations of anomalous diffusion of proteins in solutions crowded by mobile obstacles. Our results suggest that the failure of models of diffusion in random-coil polymer solutions to predict experimental observation, which becomes apparent at high concentrations, is due at least in part to the fact that none of these models allow for anomalous diffusion. Not only in random-coil polymer solutions, but also in cells, experimental measurements of protein diffusion, and models of processes that depend on diffusion should be done considering the possibility of anomalous diffusion. The cytoplasm may be pictured as a cytoskeleton filament network with a characteristic mesh size  $\xi \approx 20\text{--}30$  nm (37,38) filled with an aqueous phase containing a very high concentration of proteins, up to 400 g/l (85,86). Because this network mesh size is too large to produce anomalous diffusion for typical-sized proteins, we expect that the slight anomalous diffusion observed in the cytoplasm (28,29) may be due to the cage rearrangement effect or to binding interactions. Indeed, it was shown that anomalous diffusion of dextrans in cell did not disappear after depolymerization of the microtubule network (27). The fact that diffusion should generally be expected to be anomalous in the cytoplasm, even if the effect is small, is significant because it means that diffusion coefficients measured at larger scales will lead to an underestimation of the mobility of the proteins at molecular scales. In addition, even a slightly anomalous behavior might influence the outcome of such processes as pattern formation, whose stability has sometimes been linked to subdiffusion of the reactants (87). Also, our study of diffusion of proteins at high random-coil polymer concentration reproduces conditions found in living systems: in bacterial films (88), in the periplasmic peptidoglycan network of Gram-negative bacteria, in the hyaluronic acid coat enveloping some eukaryotic cells (89), and in the chromatin in places where DNA is not wrapped around structural proteins. Indeed, the anomalous behavior observed in cell nuclei for EGFP (29) is consistent with a motion coupled with the thermal fluctuations of filaments ( $\alpha$  approaches 3/4). Although the cellular environment is more complex than our simplified model systems, understanding diffusion in these systems will facilitate the use of probe diffusion to meaningfully characterize the cellular environment at the scale of biomolecules.

We thank Dr. Sudipta Maiti for graciously providing the MEMFCS algorithm and Kanchan Garai for support with using the software.

This work was funded by the Natural Sciences and Engineering Research Council (NSERC) of Canada. D.B. is the recipient of a CGS-M NSERC scholarship and C.F. is supported through the Canada Research Chairs Program.

## REFERENCES

1. Pederson, T. 2000. Diffusional protein transport within the nucleus: a message in the medium. *Nat. Cell Biol.* 2:E73–E74.

2. Cluzel, P., M. Surette, and S. Leibler. 2000. An ultrasensitive bacterial motor revealed by monitoring signaling proteins in single cells. *Science*. 287:1652–1655.
3. Macnab, R. 2000. Action at a distance: bacterial flagellar assembly. *Science*. 290:2086–2087.
4. Guthold, M., X. Zhu, C. Rivetti, G. Yang, N. Thomson, S. Kasas, H. Hansma, B. Smith, P. Hansma, and C. Bustamante. 1999. Direct observation of one-dimensional diffusion and transcription by Escheria coli RNA polymerase. *Biophys. J.* 77:2284–2294.
5. Berry, H. 2002. Monte Carlo simulations of enzyme reactions in two dimensions: fractal kinetics and spatial segregation. *Biophys. J.* 83:1891–1901.
6. Crick, F. 1970. Diffusion in embryogenesis. *Nature*. 225:420–422.
7. Valdez-Taubas, J., and H. Pelham. 2003. Slow diffusion of proteins in the yeast plasma membrane allows polarity to be maintained by endocytic cycling. *Curr. Biol.* 13:1636–1640.
8. Masaro, L., and X. X. Zhu. 1999. Physical models of diffusion for polymer solutions, gels and solids. *Prog. Polym. Sci.* 24:731–775.
9. Hall, D., and A. P. Minton. 2003. Macromolecular crowding: qualitative and semiquantitative successes, quantitative challenges. *Biochim. Biophys. Acta*. 1649:127–139.
10. Lavalette, D., C. Tetreau, M. Tourbez, and Y. Blouquit. 1999. Microscopic viscosity and rotational diffusion of proteins in a macromolecular environment. *Biophys. J.* 76:2744–2751.
11. Scott, R. A., and N. A. Peppas. 1999. Highly crosslinked, PEG-containing copolymers for sustained solute delivery. *Biomaterials*. 20:1371–1380.
12. Whang, K., T. K. Goldstick, and K. E. Healy. 2000. A biodegradable polymer scaffold for delivery of osteotropic factors. *Biomaterials*. 21:2545–2551.
13. Zimmerman, S., and A. Minton. 1993. Macromolecular crowding: biochemical, biophysical, and physiological consequences. *Annu. Rev. Biophys. Biomol. Struct.* 22:27–65.
14. Asakura, S., and F. Oosawa. 1958. Interaction between particles suspended in solutions of macromolecules. *J. Polym. Sci.* 33:183–192.
15. Minton, A. P. 2001. The influence of macromolecular crowding and macromolecular confinement on biochemical reactions in physiological media. *J. Biol. Chem.* 276:10577–10580.
16. Minton, A. P. 1993. Macromolecular crowding and molecular recognition. *J. Mol. Recognit.* 6:211–214.
17. Rivas, G., J. A. Fernandez, and A. P. Minton. 2001. Direct observation of the enhancement of noncooperative protein self-assembly by macromolecular crowding: indefinite linear self-association of bacterial cell division protein FtsZ. *Proc. Natl. Acad. Sci. USA*. 98:3150–3155.
18. Sasahara, K., P. McPhie, and A. P. Minton. 2003. Effect of dextran on protein stability and conformation attributed to macromolecular crowding. *J. Mol. Biol.* 326:1227–1237.
19. Amsden, B. 2002. Modeling solute diffusion in aqueous polymer solutions. *Polym.* 43:1623–1630.
20. Gorenflo, R., F. Mainardi, D. Moretti, G. Pagnini, and P. Paradisi. 2002. Discrete random walk models for space-time fractional diffusion. *Chem. Phys.* 284:521–541.
21. Bouchaud, J., and A. Georges. 1990. Anomalous diffusion in disordered media: statistical mechanisms, models, and physical applications. *Phys. Rep.* 195:127–193.
22. Bunde, A., and S. Havlin. 1991. Percolation II. In *Fractals and Disordered Systems*, 2nd Ed. Springer-Verlag, Berlin, Germany. 96–149.
23. Schaefer, D. W. 1984. A unified model for the structure of polymers in semidilute solution. *Polym.* 25:387–394.
24. Almeida, P., and W. Vaz. 1995. Lateral diffusion in membranes. In *Handbook of Biological Physics*. R. Lipowsky and E. Sackmann, editors. Elsevier, New York, NY. 305–357.
25. Saxton, M. 1994. Anomalous diffusion due to obstacles: a Monte Carlo study. *Biophys. J.* 66:394–401.

26. Kues, T., R. Peters, and U. Kubitscheck. 2001. Visualization and tracking of single protein molecules in the cell nucleus. *Biophys. J.* 80:2954–2967.
27. Weiss, M., M. Elsner, F. Kartberg, and T. Nilsson. 2004. Anomalous subdiffusion is a measure for cytoplasmic crowding in living cells. *Biophys. J.* 87:3518–3524.
28. Brown, E. B., E. S. Wu, W. Zipfel, and W. W. Webb. 1999. Measurement of molecular diffusion in solution by multiphoton fluorescence photobleaching recovery. *Biophys. J.* 77:2837–2849.
29. Wachsmuth, M., W. Waldeck, and J. Langowski. 2000. Anomalous diffusion of fluorescent probes inside living cell nuclei investigated by spatially-resolved fluorescence correlation spectroscopy. *J. Mol. Biol.* 298:677–689.
30. Feder, T. J., I. Brust-Mascher, J. P. Slattery, B. Baird, and W. W. Webb. 1996. Constrained diffusion or immobile fraction on cell surfaces: a new interpretation. *Biophys. J.* 70:2767–2773.
31. Jacobson, K., A. Ishihara, and R. Inman. 1987. Lateral diffusion of proteins in membranes. *Annu. Rev. Physiol.* 49:163–175.
32. Haupts, U., S. Maiti, P. Schwillle, and W. W. Webb. 1998. Dynamics of fluorescence fluctuations in green fluorescent protein observed by fluorescence correlation spectroscopy. *Proc. Natl. Acad. Sci. USA.* 95:13573–13578.
33. Swaminathan, R., C. Hoang, and A. Verkman. 1997. Photobleaching recovery and anisotropy decay of green fluorescent protein GFP-S65T in solution and cells: cytoplasmic viscosity probed by green fluorescent protein translational and rotational diffusion. *Biophys. J.* 72:1900–1907.
34. Gennerich, A., and D. Schild. 2000. Fluorescence correlation spectroscopy in small cytosolic compartments depends critically on the diffusion model used. *Biophys. J.* 79:3294–3306.
35. Fradin, C., A. Abu-Arish, R. Granek, and M. Elbaum. 2003. Fluorescence correlation spectroscopy close to a fluctuating membrane. *Biophys. J.* 84:2005–2020.
36. Mastro, A. M., M. A. Babich, W. D. Taylor, and A. D. Keith. 1984. Diffusion of a small molecule in the cytoplasm of mammalian cells. *Proc. Natl. Acad. Sci. USA.* 81:3414–3418.
37. Luby-Phelps, K. 1994. Physical properties of the cytoplasm. *Curr. Opin. Cell Biol.* 6:3–9.
38. Luby-Phelps, K., D. Taylor, and F. Lanni. 1986. Probing the structure of the cytoplasm. *J. Cell Biol.* 102:2015–2022.
39. Lukacs, G., P. Haggie, O. Seksek, D. Lechardeur, N. Freedman, and A. Verkman. 2000. Size-dependent DNA mobility in cytoplasm and nucleus. *J. Biol. Chem.* 275:1625–1629.
40. Seksek, O., J. Biwersi, and A. Verkman. 1997. Translational diffusion of macromolecule-sized solutes in cytoplasm and nucleus. *J. Cell Biol.* 138:131–142.
41. Verkman, A. 2002. Solute and macromolecule diffusion in cellular aqueous compartments. *Trends Biochem. Sci.* 27:27–33.
42. Dayel, M., E. Hom, and A. Verkman. 1999. Diffusion of green fluorescent protein in the aqueous-phase lumen of endoplasmic reticulum. *Biophys. J.* 76:2843–2851.
43. Wojcieszyn, J. W., R. A. Schlegel, E. S. Wu, and K. A. Jacobson. 1981. Diffusion of injected macromolecules within the cytoplasm of living cells. *Proc. Natl. Acad. Sci. USA.* 78:4407–4410.
44. Elowitz, M., M. Surette, P. Wolf, J. Stock, and S. Leibler. 1999. Protein mobility in the cytoplasm of *Escherichia coli*. *J. Bacteriol.* 181:197–203.
45. Fundueanu, G., C. Nastruzzi, A. Carpov, J. Desbrieres, and M. Rinaudo. 1999. Physico-chemical characterization of Ca-alginate micro-particles produced with different methods. *Biomaterials.* 20:1427–1435.
46. Brandrup, J., and E. H. Immergut. 1999. *Polymer Handbook*. Wiley, New York, NY.
47. Sivasankar, S., S. Subramaniam, and D. Leckband. 1998. Direct molecular level measurements of the electrostatic properties of a protein surface. *Proc. Natl. Acad. Sci. USA.* 95:12961–12966.
48. Goh, Y. Y., V. Freceer, B. Ho, and J. L. Ding. 2002. Rational design of green fluorescent protein mutants as biosensor for bacterial endotoxin. *Protein Eng.* 15:493–502.
49. Magde, D., E. Elson, and W. W. Webb. 1972. Thermodynamic fluctuations in a reacting system—measurement by fluorescence correlation spectroscopy. *Phys. Rev. Lett.* 29:705–708.
50. Thompson, N. L. 1991. Fluorescence correlation spectroscopy. In *Topics in Fluorescence Spectroscopy*. J. Lakowicz, editor. Plenum Press, New York, NY. 338–378.
51. Schwillle, P. 2001. Fluorescence correlation spectroscopy and its potential for intracellular applications. *Cell Biochem. Biophys.* 34:383–408.
52. Webb, W. 2001. Fluorescence correlation spectroscopy: inception, biophysical experimentations, and prospectus. *Appl. Opt.* 40:3969–3983.
53. Periasamy, N., and A. S. Verkman. 1998. Analysis of fluorophore diffusion by continuous distributions of diffusion coefficients: application to photobleaching measurements of multicomponent and anomalous diffusion. *Biophys. J.* 75:557–567.
54. Schwillle, P., J. Koriach, and W. W. Webb. 1999. Fluorescence correlation spectroscopy with single-molecule sensitivity on cell and model membranes. *Cytometry.* 36:176–182.
55. Widengren, J., U. Mets, and R. Rigler. 1995. Fluorescence correlation spectroscopy of triplet states in solution: a theoretical and experimental study. *J. Phys. Chem.* 99:13368–13379.
56. Metzler, R., and J. Klafter. 2000. The random walk's guide to anomalous diffusion: a fractional dynamics approach. *Phys. Rep.* 339:1–77.
57. Sengupta, P., K. Garai, J. Balaji, N. Periasamy, and S. Maiti. 2003. Measuring size distribution in highly heterogeneous systems with fluorescence correlation spectroscopy. *Biophys. J.* 84:1977–1984.
58. Módos, K., R. Galántai, I. Bárdos-Nagy, M. Wachsmuth, K. Tóth, J. Fidy, and J. Langowski. 2004. Maximum-entropy decomposition of fluorescence correlation spectroscopy data: application to liposome-human serum albumin association. *Eur. Biophys. J.* 33:59–67.
59. Skilling, J., and R. K. Bryan. 1984. Maximum entropy image reconstruction: general algorithm. *Mon. Not. R. Astron. Soc.* 211: 111–124.
60. Saffarian, S., and E. L. Elson. 2003. Statistical analysis of fluorescence correlation spectroscopy: the standard deviation and bias. *Biophys. J.* 84:2030–2042.
61. Sengupta, P., K. Garai, B. Sahoo, Y. Shi, D. J. E. Callaway, and S. Maiti. 2003. The amyloid peptide (A1–40) is thermodynamically soluble at physiological concentrations. *Biochemistry.* 42:10506–10513.
62. Nagle, J. 1992. Long tail kinetics in biophysics? *Biophys. J.* 63:366–370.
63. Phillips, R. J., and F. T. Kosar. 1995. Measurement of protein diffusion in dextran solutions by holographic interferometry. *AChE J.* 41:701–711.
64. Petit, J.-M., X. X. Zhu, and P. M. Macdonald. 1996. Solute probe diffusion in aqueous solutions of poly(vinyl alcohol) as studied by pulsed-gradient spin-echo NMR spectroscopy. *Macromolecules.* 29: 70–76.
65. Phillies, G. D. J. 1987. Dynamics of polymers in concentrated solutions: the universal scaling equation derived. *Macromolecules.* 20:558–564.
66. Saxton, M. 1996. Anomalous diffusion due to binding: a Monte Carlo study. *Biophys. J.* 70:1250–1262.
67. Netz, P. A., and T. Dorfmueller. 1995. Computer-simulation studies of anomalous diffusion in gels: structural-properties and probe-size dependence. *J. Chem. Phys.* 103:9074–9082.
68. Fatin-Rouge, N., K. Starchev, and J. Buffle. 2004. Size effects on diffusion processes within agarose gels. *Biophys. J.* 86:2710–2719.

69. Amblard, F., A. C. Maggs, B. Yurke, A. N. Pargellis, and S. Leibler. 1996. Subdiffusion and anomalous local viscoelasticity in actin networks. *Phys. Rev. Lett.* 77:4470–4473.
70. Wong, I. Y., M. L. Gardel, D. R. Reichman, E. R. Weeks, M. T. Valentine, A. R. Bausch, and D. A. Weitz. 2004. Anomalous diffusion probes microstructure dynamics of entangled F-actin networks. *Phys. Rev. Lett.* 92:178101.
71. Basu, S., C. W. Wolgemuth, and P. J. Campagnola. 2004. Measurement of normal and anomalous diffusion of dyes within protein structures fabricated via multiphoton excited cross-linking. *Biomacromolecules.* 5:2347–2357.
72. Dwyer, J. D., and V. A. Bloomfield. 1993. Brownian dynamics simulations of probe and self-diffusion in concentrated protein and DNA solutions. *Biophys. J.* 65:1810–1816.
73. Chirico, G., M. Placidi, and S. Cannistraro. 1999. Fractional Stokes-Einstein relationship in biological colloids: role of mixed stick-slip boundary conditions. *J. Phys. Chem. B.* 103:1746–1751.
74. De Smedt, S. C., A. Lauwers, J. Demeester, Y. Engelborghs, G. D. Mey, and M. Du. 1994. Structural information on hyaluronic acid solutions as studied by probe diffusion experiments. *Macromolecules.* 27:141–146.
75. Dauty, E., and A. S. Verkman. 2004. Molecular crowding reduces to a similar extent the diffusion of small solutes and macromolecules: measurement by fluorescence correlation spectroscopy. *J. Mol. Recognit.* 17:441–447.
76. Furukawa, R., J. L. Arauz-Lara, and B. R. Ware. 1991. Self-diffusion and probe diffusion in dilute and semidilute aqueous solutions of dextran. *Macromolecules.* 24:599–605.
77. Busch, N. A., T. Kim, and V. A. Bloomfield. 2000. Tracer diffusion of proteins in DNA solutions. 2. Green fluorescent protein in crowded DNA solutions. *Macromolecules.* 33:5932–5937.
78. Masuda, A., K. Ushida, and T. Okamoto. 2005. New fluorescence correlation spectroscopy enabling direct observation of spatiotemporal dependence of diffusion constants as an evidence of anomalous transport in extracellular matrices. *Biophys. J.* 88:3584–3591.
79. Weeks, E. R., and D. A. Weitz. 2002. Properties of cage rearrangements observed near the colloidal glass transition. *Phys. Rev. Lett.* 89:095704.
80. Kegel, W. K., and A. van Blaaderen. 2000. Direct observation of dynamical heterogeneities in colloidal hard-sphere suspensions. *Science.* 287:290–293.
81. Weeks, E. R., and D. A. Weitz. 2002. Subdiffusion and the cage effect studied near the colloidal glass transition. *Chem. Phys.* 284: 361–367.
82. Rauch, J., and W. Kohler. 2002. Diffusion and thermal diffusion of semidilute to concentrated solutions of polystyrene in toluene in the vicinity of the glass transition. *Phys. Rev. Lett.* 88:185901–185904.
83. Caspi, A., R. Granek, and M. Elbaum. 2002. Diffusion and directed motion in cellular transport. *Phys. Rev. E Stat. Nonlin. Soft Matter Phys.* 66:011916.
84. Schaefer, D. 1984. A unified model for the structure of polymers in semidilute solution. *Polym.* 25:387–394.
85. Fulton, A. B. 1982. How crowded is the cytoplasm? *Cell.* 30: 345–347.
86. Zimmerman, S. B., and S. O. Trach. 1991. Estimation of macromolecule concentrations and excluded volume effects for the cytoplasm of *Escherichia coli*. *J. Mol. Biol.* 222:599–620.
87. Weiss, M. 2003. Stabilizing Turing patterns with subdiffusion in systems with low particle numbers. *Phys. Rev. E Stat. Nonlin. Soft Matter Phys.* 68:036213.
88. Shirtliff, M. E., J. T. Mader, and A. K. Camper. 2002. Molecular interactions in biofilms. *Chem. Biol.* 9:859–871.
89. Zaidel-Bar, R., M. Cohen, L. Addadi, and B. Geiger. 2004. Hierarchical assembly of cell-matrix adhesion complexes. *Biochem. Soc. Trans.* 32:416–420.

***4.2 Diffusion Power Laws in Polymer Solutions and Gels Observed Using Variable Length Scale Fluorescence Correlation Spectroscopy***

Banks, D. S., R. Peters, and C. Fradin. 2007. Diffusion Power Laws in Polymer Solutions and Gels Observed Using Variable Length Scale Fluorescence Correlation Spectroscopy. *Biophys. J.* (to be submitted).

#### TITLE

Diffusion Power Laws in Polymer Solutions and Gels Observed Using Variable Length Scale Fluorescence Correlation Spectroscopy

#### RUNNING TITLE

Diffusion Power Laws Observed Using VLS-FCS

#### AUTHORS

Daniel S. Banks\*, Robert Peters\* and Cecile Fradin\*<sup>†</sup>

\*Department of Physics and Astronomy and <sup>†</sup>Department of Biochemistry and Biomedical Sciences, McMaster University, Hamilton, Ontario, Canada.

#### ABSTRACT

Variable Length Scale Fluorescence Correlation Spectroscopy (VLS-FCS) is a recently developed modification to conventional FCS that is used to study length-scale dependence of diffusion. Whereas previous studies varied the radius of the observation volume by a factor of 2 or 3, we demonstrate that the range of the observation length scale used in VLS-FCS can be extended to an order of magnitude, 0.2 – 1.5  $\mu\text{m}$ , which allows one to obtain the anomalous exponent  $\alpha$  by directly observing the diffusion power law. We applied this method to the study of systems where anomalous diffusion has been reported. For the diffusion of polymer beads in 1.4% agarose gels, the value of  $\alpha$  obtained from individual FCS measurements increases from 0.82 to 0.97 as the observation volume is increased, and the diffusion power law yields a corresponding value of  $\alpha = 0.92$ . This result is important because it demonstrates agreement between the complementary methods and directly verifies the length-scale dependence of diffusion in this system. For protein diffusion in dextran solutions where conventional FCS measurements show similar anomalous behavior, the diffusion power law shows no observable length-scale dependence over this range. Yet, the individual FCS measurements show that the two-component model, which is independent of length-scale, is insufficient to account for the observations. Observations similar to the protein-dextran system are reproduced in the bead-agarose system by reducing the concentration of the agarose to 0.5%. Therefore, VLS-FCS is an important tool for the study of anomalous diffusion in systems that are accessible to FCS.

#### KEYWORDS

fluorescence correlation spectroscopy, anomalous diffusion, polymer solutions, dextran, agarose gels, diffusion law.

#### INTRODUCTION

Experimental characterization of diffusion of tracers *in vivo* and in complex *in vitro* systems is commonly performed to probe the microenvironment of the tracers. These systems include polymer solutions and gels (1-6), colloidal suspensions (7, 8), and various cellular systems (9-18). There are several studies of diffusion in *in vitro* systems

conducted to shed light on corresponding phenomena *in vivo*. For example, the characterization of thermal fluctuations of microtubules *in vitro* has been shown to correspond to motions of beads *in vivo* (19), diffusion in two-component lipid membranes has been compared to diffusion in biolipids with rafts (20), and systems such as *f*-actin networks (5) and DNA solutions (6, 21) have been compared to cytoplasmic or nucleoplasmic environments. The study of diffusion is also used to characterize other cellular phenomenon. For example, diffusion coefficients are interpreted to deduce the size and oligomeric state of membrane proteins and domains (22), characterization of the diffusion of tracers particles in a cell has been used to determine the viscous and elastic shear moduli (16), to infer that the intradendritic network of microtubules may be oriented parallel to the dendrite (17), to demonstrate that diffusion coefficients in bacterial cytoplasmic networks are explained by crowding effects alone (23), to distinguish between isolated microdomains and meshworks in membrane organization (24), and recently to infer that the effect of macromolecular crowding on diffusion requires reevaluation of diffusion-limited intracellular kinetics (14). In fact, anomalous diffusion of transcription factors which are expressed close to their targets may explain how some transcription factors may find their binding sites faster than is predicted based on simple diffusion models (14).

Non-Brownian models of diffusion are often required to fit the data obtained in complex systems. In particular, many of these studies have used the anomalous diffusion model, which predicts length-scale dependence in the diffusion coefficient, to explain results obtained by experimental methods that have a fixed length-scale such as Fluorescence Correlation Spectroscopy (FCS) and Fluorescence Recovery After Photobleaching (3, 4, 9-13, 16). A length scale dependence in the diffusion rate of tracers in a system complicates the interpretation of the diffusion coefficient and must be taken into account when modeling diffusion as a probe of the local environment. This is of great interest to the study of cellular systems where the ability of proteins to react with targets is limited by diffusion (25). In some systems, Single Particle Tracking (SPT) can be used to verify the length-scale dependence of diffusive processes, but fast diffusive processes such the motion of proteins in the cytoplasm are difficult to access with SPT (7, 8, 14). Recently a variation of FCS has been developed independently by two groups to measure the length scale dependence in systems accessible to conventional FCS (24, 26, 27). In conventional FCS, diffusion coefficients are determined at a fixed observation length-scale, whereas in Variable Length Scale Fluorescence Correlation Spectroscopy (VLS-FCS) the length-scale dependence of diffusion coefficients is determined by performing FCS measurements for different sizes of the observation volume.

Previous studies using VLS-FCS have focused on detecting various forms of non-Brownian length-scale dependence in the diffusion. One group showed a small drop (10-20%) in the diffusion coefficient of a dye, Alexa 488, in aqueous solutions of hyaluronan as the size of the observation volume increased (26), and subsequently, that the diffusion coefficient in the same system reached a minimum after which it rose again slightly as the observation volume increased (28). These results were then compared to the results

obtained at different length-scales from photochemical bimolecular reaction and pulsed field gradient NMR to obtain a model of the non-Brownian behavior of the diffusion over a wider range of length scales (29), concluding that the dip in the diffusion coefficient may be due to translational motion and reorganization of the mesh structure.

In another study, VLS-FCS was applied to the diffusion of lipids in monophasic Giant Unilamellar Vesicles and in the plasma membranes of live cells (27). This study emphasized the importance of the diffusion law, that is, the dependence of the characteristic diffusion time,  $\tau_D$ , on the square of the radius of the observation volume,  $w_0^2$ . In these systems,  $\tau_D \propto w_0^2$  where  $\tau_D$  may have a non-zero intercept. According to simulations, diffusion among isolated microdomains results in a positive  $\tau_D$ -intercept, and diffusion hindered by a meshwork results in a negative  $\tau_D$ -intercept (24). Further, this method was applied to study diffusion in the plasma membrane of COS-7 cells by measuring the diffusion law of multiple tracers including lipids, transmembrane proteins, and anchored proteins and showed that both lipid-dependent microdomains and cytoskeleton-mediated meshwork contribute to the compartmentalization of the membrane (30).

In conventional FCS, an excitation laser fills the back aperture of the objective to obtain a diffraction-limited excitation volume. Fluorescence emitted in the excitation volume is collected and the fluctuations in the fluorescence signal are analyzed to determine the correlation decay over time. The correlation decay is modeled to characterize phenomena contributing to the fluorescence fluctuations in the signal such as diffusion, concentration, photophysics, and interactions (31). In VLS-FCS, the width of the beam illuminating the back aperture of the objective is incrementally reduced which effectively sacrifices the full resolving power of the objective to create wider excitation volumes. The resulting parameters are then analyzed as a function of the observation length-scale. To optimize the fluorescence signal and range of accessible length scales, a confocal pinhole should be selected for each observation volume size.

Other alternative approaches varying the size of the detection volume have been reported. It has been shown recently that for cases where fluorophores are restricted to 2-D diffusion inside a horizontal membrane, the observation length-scale can also be changed by performing a z-scan while collecting the correlation data at each z-position (32). Due to the 3-D Gaussian geometry of the confocal observation volume, moving the center of the observation volume slightly above or below the membrane increases the observation area. Even small changes in the observation volume may be achieved merely by changing the size of the confocal pinhole or optical fiber aperture used to collect the fluorescence (33) and are useful for observing the length-scale dependence of correlation data to distinguish between correlations due to diffusion and photophysical effects such as triplet state decay and fluorescent protein blinking. For simple diffusion where the diffusion coefficient is constant, the diffusion time scales linearly with the square of the radius of the detection volume. Therefore an increase in the detection radius will shift the diffusion component of the correlation data while correlations due to photophysical

effects will remain constant (or vary to a lesser degree if the photophysics is altered by a resulting change in the excitation intensity).

In a previous study, we used conventional FCS to study diffusion of proteins in aqueous buffer crowded by large molecular weight dextrans and showed that the data was compatible with an anomalous diffusion model (3). While conventional FCS may determine the existence of non-Brownian behavior, it cannot verify the prediction of the anomalous diffusion model that the diffusion coefficient is actually length-scale dependent. Confirmation of this prediction will distinguish between competing models which predict otherwise.

For Brownian motion, the mean-square displacement of a tracer particle scales linearly,

$$\langle r^2(t) \rangle = 2nDt. \quad (1)$$

whereas for anomalous diffusion it scales as a power law in time:

$$\langle r^2(t) \rangle \propto t^\alpha, \quad \alpha \neq 1 \quad (2)$$

$D$  is the diffusion coefficient, which is time independent,  $n$  is the number of dimensions of the diffusion and  $\alpha$  is referred to as the anomalous exponent.

Anomalous diffusion or other non-Brownian behavior may arise in complex media where Fick's law does not apply. As a simple example of such non-Brownian behavior, anomalous diffusion may appear as a cross-over between diffusion regimes in systems where hindrance to diffusion occurs at a characteristic length scale,  $\xi$ , due to structure in the media. Both well below and well above  $\xi$ , the diffusion is normal. Above  $\xi$ , the diffusion will be slower and may be modeled as if the structured media were replaced with an isotropic media of higher viscosity. But at a length scale similar to  $\xi$  there will be cross-over effects and anomalous diffusion may be observed (34). While living cells are much more complicated systems, a plausible biological interpretation of anomalous diffusion has been proposed recently where a wide cross-over regime is due to a broad hierarchy of binding sites (35).

Conventional FCS obtains  $\alpha$  as a fit parameter of the correlation data taken at a fixed observation length-scale. In this study, we demonstrate that the range of observation length scales used in VLS-FCS can be extended over an order of magnitude, 0.2 – 1.5  $\mu\text{m}$ , which allows one to obtain  $\alpha$  by directly observing the diffusion power law. This complementary method is based on the scaling of Eq. 1. If the diffusion is anomalous, since  $w_0$  is the observation length scale, and  $\tau_D$  is the corresponding observation time-scale, then we will have:

$$w_0^2 \propto \tau_D^\alpha, \quad (3)$$

Since VLS-FCS allows one to measure  $\tau_D$  as a function of  $w_0$ , then  $\alpha$  may be determined directly through this diffusion power law. Secondly, VLS-FCS also allows one to measure  $\alpha$  at multiple length-scales as a fit parameter to the correlation data in the same manner that conventional FCS does at a single length-scale. For the purpose of clarity in this study, we adopt the following convention: We refer to the value of  $\alpha$  obtained via Eq. 3, as the diffusion power law, denoted  $\alpha_{DL}$ , and the value of  $\alpha$  obtained as fit parameters to the correlation data (see Eq. 4 and 5 in Materials and Methods) as the anomaly parameter, denoted  $\alpha_p$ .

We apply this method to *in vitro* systems that are comparable to crowded cellular conditions, namely, proteins in dextran solutions and polymer beads in agarose gels. In both of these systems, diffusion has been previously reported to be anomalous using conventional FCS (3, 4). In this manner, we are able to test the prediction of length-scale dependent diffusion of these previous studies while demonstrating the usefulness of the VLS-FCS method.

## MATERIALS AND METHODS

### *Samples and Preparation*

Our tracers, including streptavidin labeled with Alexa Fluor 488, Fluorescein Isothiocyanate, or Oregon Green (Invitrogen, Carlsbad, CA), Enhanced Green Fluorescent Protein (EGFP, BioVision Research Products, Mountain View, CA), or labeled polystyrene beads (40nm Orange “FluoSpheres,” Invitrogen) were dissolved in phosphate buffered saline (PBS, pH 7.4) at low concentrations suitable for FCS (typically 1-10nM). As obstacles, dextrans (Sigma-Aldrich, St. Louis, MO) having a peak molecular weight of 276kDa were dissolved at 200g/l as described previously (3). All molecules were used without further purification.

For measurements with beads alone without agarose, the solution was prepared at 1nM beads and sonicated for 20 minutes to reduce aggregation. For samples with agarose, the agarose (Biotechnology Grade, BioShop, Burlington, ON, Canada) was added to PBS and heated to 90°C until dissolved to produce 1.4% or 0.5% agarose by weight. The dissolved agarose was then moved to a 60°C bath along with a 10 $\mu$ l concentrated sample of beads. After several minutes, approximately 500 $\mu$ l of the dissolved gel was transferred to the concentrated bead sample using pre-heated micropipette tips to prevent local cooling of the gel, vortexed, returned to the 60°C bath and sonicated for 20 minutes. A 96-well plate with a glass bottom (Whatman, Clifton, NJ) was pre-heated to 60°C in an oven. After sonication, 300 $\mu$ l of the agarose gel with beads was transferred to fill a well, again using pre-heated micropipette tips and the plate was covered with clear plastic wrap to prevent evaporation before the plate was returned to the 60°C oven for 10 minutes. Finally, the oven was allowed to cool to room temperature over the course of an hour after which the sample was finally transferred to the microscope and observed.

*VLS-FCS Apparatus*

The home-built FCS setup used for this work has been described previously (3). To adjust our setup to perform VLS-FCS, a continuously variable metallic neutral density filter and a calibrated iris diaphragm (both from Thorlabs, Newton, NJ) were added to the 488nm excitation beam path to control the power and width of the beam reaching the objective lens. The size of the observation volume was increased by incremental reduction of the iris diameter concentric to the optical axis and by selecting confocal pinholes with incrementally higher diameters. The pinholes (Thorlabs and Edmund Optics, Barrington, NJ) used had diameters of 50, 75, 100, 150, 200, and 300  $\mu\text{m}$ , corresponding to iris diameters of 12, 4, 2.5, 1.25, 0.9 and 0.5 mm respectively, resulting in observation volume radii evenly spaced on a logarithmic scale from about 200 nm to 1.5  $\mu\text{m}$ . This range of observation length-scales is at least twice as broad as that reported in other studies (24, 29) for a single experiment.

While the use of a variable focus lens as a beam expander would have preserved the Gaussian profile of the excitation beam, cutting the beam with an iris allowed us to reduce the size of the beam further. The loss of the Gaussian profile is not observably significant since Eq. 4 with  $\alpha_p = 1$  fits well the correlation data produced by freely diffusing fluorophores, for example, Alexa Fluor 488, Fluorescein or beads in PBS buffer, even at the largest observation volume which should correspond to the maximum distortion from a Gaussian profile. In any case, since all the measurements in this study are relative to the diffusion of the calibration dye, the value of the diffusion power law,  $\alpha_{DL}$ , will not depend on any systematic errors produced by a non-Gaussian profile.

The laser excitation power at the objective was held constant at either 20  $\mu\text{W}$  when fluorescein was used for calibration or 50  $\mu\text{W}$  when more photostable fluorophores such as beads were used in the experiments, in which case Alexa Fluor 488 - C5 Maleimide (Invitrogen) was used for the calibration. If the probability to photobleach a fluorophore during a passage through the observation volume,  $P$ , is approximately proportional to the number of photons absorbed, then  $P$  is approximately proportional to  $\Phi \tau_D$ , where  $\Phi$  is the average photon flux and  $\tau_D$  is the characteristic time a fluorophore spends in the observation volume. If the excitation power is constant, the photon flux,  $\Phi$ , scales as the inverse square of the observation volume radius,  $\Phi \propto w_0^{-2}$ . If the diffusion time of the fluorophore scales as the square of the observation volume radius,  $\tau_D \propto w_0^2$ , then the net change in probability to photobleach is zero between observation volumes if the excitation power is constant, since  $P \propto \Phi \tau_D$  does not depend on  $w_0$ . Thus, in order to keep the laser power at the objective constant, the variable neutral density filter was adjusted for each observation volume. This filter was placed at the exit of the beam from the laser where the beam is the smallest in order to reduce distortion in the beam front due to the filter's spatial gradient of transmission.

The disadvantage of using a constant excitation power is that at the large observation volume, the collected fluorescence per molecule is greatly reduced and the fluorescence per molecule is expected to scale as  $w_0^{-2}$  as a first-order approximation which would severely limit the accessible range of observation sizes. However, for the dyes used, the fluorescence per molecule scales as  $w_0^{-1.8}$ , whereas for the beads it scales as  $w_0^{-1.3}$ . These scaling behaviors result in greater fluorescence per molecule at larger observation volumes than a first-order approximation predicts. The difference in the scaling between the dyes and beads may be due to strong quenching effects for the beads which are labeled with large numbers of dye molecules.

### Data Analysis

The autocorrelation functions were analyzed using an expression modified to account for the possibility of anomalous diffusion, as described previously (3). When the propagator of the diffusion is anomalous, the autocorrelation function for a typical fluorescent species is expected to be (36):

$$G(t) = \frac{1/N}{\left(1 + \left(\frac{t}{\tau_D}\right)^{\alpha_p}\right) \left(1 + \frac{1}{S^2} \left(\frac{t}{\tau_D}\right)^{\alpha_p}\right)^{1/2}} \left(1 + \frac{T}{1-T} e^{-t/\tau_T}\right) \quad (4)$$

$S$  is the aspect ratio, height to width, of the ellipsoidal detection volume.  $N$  is the average number of fluorophores and  $\tau_D$  their characteristic residence time in this volume. The second term in Eq. 4 accounts for the existence of a non-fluorescent triplet state (37):  $\tau_T$  is the relaxation time of the triplet state, and  $T$  is the average fraction of fluorophores found in the triplet state. While Eq. 4 is not exact for all cases of anomalous diffusion, it has been shown to be a very good approximation of the more complex solution of a large class of anomalous diffusion equations (9). As explained below, a third term identical to the triplet state term was multiplied to Eq. 4 in order to account for the more complex photophysics which was observed for labeled streptavidin:

$$G(t) = \frac{1/N}{\left(1 + \left(\frac{t}{\tau_D}\right)^{\alpha_p}\right) \left(1 + \frac{1}{S^2} \left(\frac{t}{\tau_D}\right)^{\alpha_p}\right)^{1/2}} \prod_{i=1}^2 \left(1 + \frac{T_i}{1-T_i} e^{-t/\tau_{T,i}}\right) \quad (5)$$

In Eq.5, the additional photophysics is modeled as a second independent non-fluorescent state, and the  $\tau_{T,i}$ 's are the corresponding relaxation times of the non-fluorescent states and the  $T_i$ 's are the average fractions of fluorophores populating these states.

Autocorrelation data was typically recorded for 1-3 min and the measurements were performed typically 10 times each. The fit parameters obtained from each set of correlation data were averaged together and the error estimated from the standard deviations. In the case of measurements obtained with beads, the FCS data well above the diffusion time often contained erratic structure that may be attributed to residual aggregations and poor statistics in that time range. In order to obtain reliable fits to such data, it is advantageous to weight the more reliable data below and around the diffusion time favorably in the fitting process. Such weighting of the data does not change the average values of  $\alpha_p$ , or  $\tau_D$ , but does result in a significant increase in the number of data sets with stable fits. In our case, we weighted the data proportionally to the amplitude of correlation. Finally, the results from repeated experiments were averaged together.

The resulting values for  $\tau_D$  and  $w_0$  were compared to determine the scaling relationship of the anomalous diffusion power law (Eq. 3), and for comparison with previous studies  $\tau_D$  was also analyzed as a function of  $w_0^2$  according to a non-Brownian linear diffusion law (24, 27):

$$\tau_D = \frac{1}{2nD} w_0^2 + \tau_0, \quad (6)$$

### Stick and Diffuse Model

One of the simplest models of hindered diffusion that is expected to result in anomalous diffusion is a model where tracers bind transiently to immobile particles. Such models have been studied via simulations, but recently, an analytical solution to the correlation function for a specific case has been published as the “stick and diffuse” model (38). The stick and diffuse model was proposed to explain the FCS correlation data corresponding to the motion of synaptic vesicles in hippocampal neurons. This model assumes that the tracer particle sticks to a fixed obstacle for a characteristic bound time,  $\tau_b$ , and then diffuses in an unbound state for a characteristic time,  $\tau_u$ . If the binding and unbinding are a Poisson processes, then for 2-D diffusion (38),

$$\frac{G(t)}{G(0)} = \frac{\tau_b e^{-t/\tau_b}}{\tau_u + \tau_b} + \frac{\tau_u}{\tau_u + \tau_b} \frac{e^{-t/\tau_u}}{1 + t/\tau_D} + \frac{1}{\tau_u + \tau_b} \sum_{n=1}^{\infty} \frac{1}{(n-1)!} \int_0^t \frac{e^{-(t-s)/\tau_b - s/\tau_u}}{1 + s/\tau_D} \left( 2n + \frac{s}{\tau_b} + \frac{t-s}{\tau_u} \right) \left( \frac{s(t-s)}{\tau_u \tau_b} \right)^{n-1} ds \quad (7)$$

where  $\tau_D$  is the characteristic diffusion time that corresponds to free diffusion given by  $\tau_D = w_0^2/4D$ , where  $D$  is the diffusion coefficient. The stick and diffuse model may be extended in a straight-forward manner for the case of 3-D diffusion in a confocal observation volume, thus:

$$\begin{aligned}
 \frac{G(t)}{G(0)} &= \frac{\tau_b e^{-t/\tau_b}}{\tau_u + \tau_b} + \frac{\tau_u}{\tau_u + \tau_b} \frac{e^{-t/\tau_u}}{\left(1 + \frac{t}{\tau_D}\right) \left(1 + \left(\frac{1}{S}\right)^2 \frac{t}{\tau_D}\right)^2} + \\
 &\frac{1}{\tau_u + \tau_b} \sum_{n=1}^{\infty} \frac{1}{(n-1)n!} \int_0^t \frac{e^{-(t-s)/\tau_b - s/\tau_u}}{\left(1 + \frac{s}{\tau_D}\right) \left(1 + \left(\frac{1}{S}\right)^2 \frac{s}{\tau_D}\right)^2} \left(2n + \frac{s}{\tau_b} + \frac{t-s}{\tau_u}\right) \left(\frac{s(t-s)}{\tau_u \tau_b}\right)^{n-1} ds
 \end{aligned} \tag{8}$$

By reversing the order of the sum and the integral, Eq. 8 can be converted into another form which can be evaluated more efficiently using Maple 10 software (Waterloo Maple, Waterloo, ON, Canada):

$$\begin{aligned}
 \frac{G(t)}{G(0)} &= \frac{\tau_b e^{-t/\tau_b}}{\tau_u + \tau_b} + \frac{\tau_u}{\tau_u + \tau_b} \frac{e^{-t/\tau_u}}{\left(1 + \frac{t}{\tau_D}\right) \left(1 + \left(\frac{1}{S}\right)^2 \frac{t}{\tau_D}\right)^2} + \\
 &\frac{1}{\tau_u + \tau_b} \int_0^t \frac{e^{-(t-s)/\tau_b - s/\tau_u}}{\left(1 + \frac{s}{\tau_D}\right) \left(1 + \left(\frac{1}{S}\right)^2 \frac{s}{\tau_D}\right)^2} \left(2I_0 \left(2 \left(\frac{s(t-s)}{\tau_u \tau_b}\right)^{\frac{1}{2}}\right) + \frac{\left(\frac{s}{\tau_b} + \frac{t-s}{\tau_u}\right)}{\left(\frac{s(t-s)}{\tau_u \tau_b}\right)^{\frac{1}{2}}} I_1 \left(2 \left(\frac{s(t-s)}{\tau_u \tau_b}\right)^{\frac{1}{2}}\right)\right) ds
 \end{aligned} \tag{9}$$

where  $I_n(x)$  denotes the modified Bessel function of the first kind.

Because the stick and diffuse model yields an analytical correlation function, the correlation function's behavior as a function of observation length-scale may be used to predict the qualitative results of a VLS-FCS experiment on a sample that exhibits such stick and diffuse motion. That is, in this model varying  $\tau_D$  is equivalent to varying the size of the observation volume, since  $\tau_D$  depends only on  $w_0^2$  and the diffusion coefficient of the unbound state. When the diffusion time is much larger than the characteristic bound and unbound times ( $\tau_D \gg \tau_b, \tau_u$ ), Eq. 9 is approximately equal to Eq. 4 with  $\alpha_p = 1$ . Thus, the diffusion at large volumes is effectively normal. When  $\tau_D$  is comparable to  $\tau_b$  and  $\tau_u$ , the correlation function is approximately equivalent to Eq. 4 with  $\alpha_p < 1$  in some cases, corresponding to the anomalous diffusion model.

The stick and diffuse model describes a case where the probability for tracers to bind is spatially homogeneous. However, for systems where the obstacles or meshwork is fixed,

such as in our agarose gel samples, tracer interaction with the meshwork is spatially inhomogeneous. But the stick and diffuse model may be modified to qualitatively describe a system of fixed obstacles. If we consider fixed binding sites on a cubic lattice of length  $l$ , where  $w_0^3 < l^3$  and where no binding sites are present, the characteristic time of the unbound state,  $\tau_u$ , is effectively infinite. For  $w_0^3 \approx l^3$ , the system is perturbed by the presence of binding sites in the observation volume and  $\tau_u$  decreases. For  $w_0^3 \gg l^3$ ,  $\tau_u$  approaches a constant value,  $\tau_{u,\infty}$ . One may recover the qualitative behavior of this system by supposing that  $\tau_u$  converges to its limit value at a rate which scales as the number of binding sites in the observation volume, that is,  $(\tau_u - \tau_{u,\infty}) \propto w_0^{-3}$ , or  $(\tau_u - \tau_{u,\infty}) \propto \tau_D^{-3/2}$ . Therefore we model the approximate qualitative behavior of the stick and diffuse correlation data by substituting into Eq. 9 the expression:

$$\tau_u = \tau_{u,\infty} + k \tau_D^{-3/2}. \quad (10)$$

In this case,  $k$  is an arbitrary constant set equal to  $\tau_{u,\infty}^{3/2}$  so that the crossover in diffusion behavior from small observation volume regime to the large observation volume regime is expected to occur where  $\tau_D \approx \tau_{u,\infty}$ .

## RESULTS

To demonstrate that the diffusion power law observed by VLS-FCS yields  $\alpha_{DL} = 1$  when the diffusion is known to be Brownian, we applied VLS-FCS to streptavidin labeled with Alexa Fluor 488 diffusing in PBS. At small volumes close to the diffraction limit, there appears to be only two correlations, one attributed to the triplet state decay and one attributed to diffusion. However, as the detection volume is increased, the failure of Eq. 4 is evident (see Figure 1). Applying equation 5 to the data shows that there is a third term with a fast correlation decay time which varies from 40  $\mu$ s to 1.8 ms as the detection volume increases. This change is not great enough to be a diffusive term which depends on the excitation volume radius and therefore it is rather attributed to intensity-dependent photophysics as its characteristic time is observed to change when changing only the excitation intensity. The inset shows its characteristic time as a function of excitation intensity where  $w_0$  is fixed at 350 nm. This term has a small amplitude which is typically less than 10% of the correlation. This extra correlation also appeared for streptavidin labeled with fluorescein and Oregon-Green. The ubiquity of this correlation suggests that it is due to the properties of the protein rather than solely of the various dyes, such as proximity of tryptophan residues to the binding site of the dye which may result in quenching effects. Indeed, this extra term does not appear for these dyes when they are observed alone rather than conjugated to streptavidin. This extra correlation is not due to photobleaching because photobleaching of streptavidin-Alexa488 is instead observed at laser powers over 100  $\mu$ W at  $w_0 = 200$  nm as a reduction in the apparent diffusion time. Indeed, we observe Alexa488 by itself to be quite photostable, for example absorbing 600  $\mu$ W at  $w_0 = 470$  nm without photobleaching whereas fluorescein exhibits bleaching even at 100  $\mu$ W under the same conditions. We noted that the amplitude of the extra

correlation was smallest for streptavidin labeled with Oregon-Green, and therefore we used the streptavidin labeled with Oregon-Green in subsequent experiments using Eq. 5.

For streptavidin diffusing in PBS we measured  $\alpha_p$ ,  $\tau_D$ , and  $w_0$ , at each observation volume. Both means of determining  $\alpha$  show normal diffusion behavior, i.e.,  $\alpha_p = \alpha_{DL} = 1$ . Figure 2 shows the anomalous exponent measured by each method. This expected result is consistent with a constant diffusion coefficient for streptavidin in PBS over the range of detection volume sizes used and confirms that we correctly control the experiment for the effects of the photophysics and have sufficiently suppressed photobleaching.

For the Streptavidin-Oregon Green diffusing in 276kDa dextran solution at 200g/l, however, the two methods give different results. When adding the extra photophysical correlation in the fit to the data at the small volumes, the resulting anomalous exponent is approximately 0.85, but the error is rather large as a result of fitting overlapping correlations. As the detection volume is increased, the anomalous exponent rises to 1 (see Figure 2), which suggests that the anomaly of the diffusion is only observable at smaller length scales. But on the other hand, the diffusion power law for this sample shows that the diffusion coefficient is not measurably length scale dependent over this range of length-scales ( $\alpha_{DL} = 1$ ). In the discussion we suggest that these apparently contradictory results are compatible with a crossover interpretation.

Since the diffusion power law does not show a length scale dependence for the diffusion of Streptavidin in a crowded dextran solution, in order to demonstrate that this negative result is significant, it is instructive to show a positive result as well, that is, to observe a system with VLS-FCS where the diffusion power law is different than 1. Therefore we used the VLS-FCS method on another system which has been reported to show anomalous diffusion via both FCS and Single Particle Tracking (1, 4), namely, polystyrene beads in Agarose gels. These beads show anomalous diffusion in the form of a crossover between two behaviors when the size of the bead is comparable to the mesh size of the gel. In this system, there are no complications due to photophysics, as photophysical effects are effectively eliminated by the large number of dye molecules per bead. Thus, the only significant correlation is due to the diffusion (see Figure 1). To test the VLS-FCS measurements on this system, the diffusion of 40nm beads in PBS solution was first characterized. At each length scale, we measured  $\alpha_p = 1$ , and the corresponding diffusion power law returned  $\alpha_{DL} = 1$  as well (see Figure 3).

But for the diffusion of these beads in 1.4% Agarose gels, the results of VLS-FCS are much different as shown in Figure 3. The anomalous exponent measured at small volumes is low ( $\alpha_p = 0.82$ ) and rises up to 1 at larger length-scales. The diffusion power law yields  $\alpha_{DL} = 0.92$ , which is approximately the average of the exponents measured at each length-scale. Thus, both methods of determining alpha are consistent, and this result is an experimental confirmation of the anomalous length-scale dependence of the

diffusion predicted by fixed length-scale FCS measurements (4). This length scale dependence corresponds to a 35% drop in the apparent diffusion coefficient,  $D$ , over an order of magnitude of observation volume radius. To illustrate the significance of this 35% difference, we note that under conditions of normal diffusion of globular tracers in isotropic media, the diffusion coefficient scales as the cube-root of the molecular weight, and if  $D$  is underestimated to be 65% of its real value there is an apparent increase in molecular weight by a factor of 3.6.

Since the relative size of the mesh to the tracer is an important parameter that determines the value of the anomalous exponent (4), increasing the mesh size by reducing the agarose concentration should cause the diffusion to return to normal. Indeed, at 0.5% agarose, the length-scale dependence of the diffusion is no longer detectable from the diffusion power law, while the individual measurements indicate a smaller degree of deviation from Brownian motion at the smallest observation length scales (see Figure 3).

## DISCUSSION

We compared conventional FCS determination of anomalous diffusion with VLS-FCS diffusion power laws for two systems where the length scale dependence was predicted by FCS. Here we discuss the interpretation of these results as a cross-over effect, and address the observed intensity-dependent photophysics as well as the application of the VLS-FCS diffusion power law to cellular measurements.

We report a system, namely, streptavidin in dextran solution, which appears to be anomalous at a fixed diffraction-limited length scale, but varying the observation length-scale does not reveal a length-scale dependent diffusion coefficient. This observation is in contrast to previous studies which reported systems that appear to exhibit normal diffusion at each length-scale while a non-Brownian length-scale dependence is observed by VLS-FCS (24, 26-29). In those previous studies,  $\alpha_p = 1$  was attributed either to the fact that the change in the apparent diffusion coefficient at the observation length-scale was too small to deform the autocorrelation function for Alexa Fluor 488 in hyaluronan solutions (29), or that the relevant trap energies for fluorescent lipids diffusing in the cell plasma membrane did not vary over a wide range of time and space (24). Another contrast is revealed in the result of analysis with Eq. 5. For all of the samples used in this study,  $\tau_D$  was also analyzed as a function of  $w_0^2$  according to a linear diffusion law for comparison with previous studies (24, 27) where non-Brownian behavior is indicated by a non-zero value for  $\tau_0$ . In our case  $\tau_0$  was always found to be zero within the estimated error, indicating that in some cases using Eq. 6 to determine  $\tau_0$  may not be as sensitive as considering the diffusion power law to determine non-Brownian behavior. These contrasts are evidence that we observe a different type of non-Brownian behavior than was observed in those studies, and they emphasize that in VLS-FCS, both methods of evaluating  $\alpha$  ought to be compared because they yield complementary information.

The results of the VLS-FCS measurements with beads in 1.4% Agarose gels demonstrate agreement between two complementary methods for the study of anomalous diffusion and directly verifies the length-scale dependence of the diffusion in that case. The interpretation of our data as a cross-over effect is suggested first of all by the rise of  $\alpha_p$  from 0.85 to 0.97 for beads in 1.4% agarose gels as the observation length-scale is increased. If we consider the diffusion of beads to be best modeled by a two-state system composed of trapping in the network and diffusion between traps, then the diffusion cross-over occurs at or just above the characteristic length-scale of the network. In 1.5% Agarose gels, the mesh-size is predicted to be approximately 77 nm (4) which is an order of magnitude less than the average detection volume used in this study, and is comparable to the diameter of the beads used. Therefore even at the diffraction-limited observation volumes we are detecting the long length-scale end of the cross-over where each bead may become trapped multiple times during a passage through the observation volume. At larger detection volumes, the cross-over effect is no longer observable, that is, the effect of trapping may be absorbed into an effective diffusion coefficient as if the agarose gel were replaced by an isotropic medium with high viscosity (7, 34, 35, 39).

Secondly, the interpretation of our data as a cross-over effect is also suggested in the case of 0.5% agarose and of the streptavidin-dextran system. In both those cases, the diffusion power law showed no length-scale dependence in the diffusion coefficient ( $\alpha_{DL} = 1$ ), but there is a broadening of the correlation decay data at small observation length-scales as indicated by  $\alpha_p < 1$ . We showed previously that such a broadening can be produced by a large distribution of characteristic diffusion times through the observation volume (3). For the samples observed in this paper, that broadening disappears as the observation length-scale is increased as evidenced by  $\alpha_p = 1$ . Further, an alternative model to analyze a broad correlation decay is the two-component model where that the tracer particles are divided into two sub-species having different diffusion coefficients,  $D_1$  and  $D_2$ , where the diffusion of each subspecies obeys Eq. 2 independently. In this case the correlation is broad because it is the sum of two correlations corresponding to the two fractions. If the two subspecies correspond to bound and unbound fractions where no exchange of particles between the two subspecies is allowed, then the correlation should remain the sum of two correlations regardless of the observation length scale. Thus the two-component model cannot account for the observation of  $\alpha_p$  approaching 1 as the observation length scale is increased unless there is exchange between the subspecies at a characteristic time, or at a distribution of characteristic times, that will create a crossover effect. But in that case, the interpretation of the two-component model is equivalent to the cross-over interpretation of the anomalous diffusion model. These considerations suggest a cross-over interpretation for the anomalous diffusion observed for streptavidin in dextran solution and for beads in 0.5% agarose, namely, that the smallest observation length-scale is just small enough to detect the upper length-scale edge of the cross-over effect.

The independence of the observed diffusion coefficient of the beads in 0.5% agarose gels with the length-scale used agrees with a recent study of diffusion at a solution-gel

interface that concludes that anomalous diffusion occurs in agarose gels only for solutes with sizes close to the gel mesh size and for small observation length-scales (40). For the 0.5% agarose gel, the gel mesh size is much increased compared to the 40nm bead diameter, making the diffusion less restricted and narrowing the length-scale range over which a cross-over could be observed. These results emphasize the importance of the relative length-scales of the observation volume, the tracer, and the obstacle mesh when measuring a cross-over effect. The crossover interpretation suggests that if it were possible to fix the mesh and tracer sizes while extending the range of accessible length scales of observation below the diffraction limit to match the mesh size, then perhaps the anomalous exponent observed by FCS might be a consistent low value over an order of magnitude of  $w_0$  and a corresponding VLS-FCS diffusion power law might be observed. Alternatively, we may hypothesize that the same effect might be achieved by significantly increasing the size of the both tracer and the mesh size of the gel, while keeping the range of observation length scales the same. However, such samples would be suitable for measurement with Single Particle Tracking and not with FCS.

As described in the Materials and Methods, a modified stick and diffuse model can be used to demonstrate the cross-over behavior that aids in illustrating qualitatively the interpretation of the experimental results of this paper. Eq. 9 was evaluated numerically using Eq. 10 and fixing the values of  $S$ ,  $\tau_b$ , and  $\tau_{u,\infty}$ , and for a range of values for  $w_0^2$ . For each value of  $w_0^2$ , the correlation data was fit to the anomalous diffusion model (Eq. 4) with  $S$  fixed to the same value. The resulting fit parameters for  $\tau_D$  and  $\alpha$  are shown as in Figure 4. First, the diffusion laws corresponding to this modified stick and diffuse model for fixed obstacles for three values of  $\tau_{u,\infty}$  are shown in Fig. 4a. There are two regimes of Brownian motion, where  $w_0^2 \propto \tau_D$ . These regimes correspond to free diffusion at small scales and at the large scales, the diffusion is slower but still described by  $w_0^2 \propto \tau_D$ . In the middle region, the diffusion power law is non-Brownian with average values of  $\alpha_{DL} = 0.82, 0.75, \text{ and } 0.67$ . Fig. 4b shows the corresponding anomaly parameter where  $\alpha_p = 1$  for small and large volumes, as expected, and  $\alpha_p$  deviates from 1 at most to 0.86 around  $w_0^2 = 0.20$  for  $\tau_{u,\infty} = 0.25$ .

The numerical results from the modified stick and diffusion model suggest two points of qualitative behavior that are relevant to the observations in this study: In a cross-over regime, the diffusion power law  $\alpha_{DL}$  and the anomaly parameter  $\alpha_p$  will not necessarily agree in magnitude, nor will their minimum values necessarily occur at the same length scale. Therefore it is not surprising that for streptavidin in dextran solutions, the diffusion law shows normal diffusion while the anomaly parameter observed depends on the length-scale of the observation. Rather, it suggests that we observe only the upper edge of the cross-over regime. Similarly, in the case of beads in agarose gels where the two behaviors are free diffusion and hindered diffusion due to trapping in the agarose network, the VLS-FCS data suggests that we observe more of the cross-over regime than for the streptavidin system since the diffusion power law is less than 1, but the anomaly parameter values demonstrate that we still only observe its upper edge.

The cross-over interpretation of the modified stick and diffuse model described here results from binding with only one characteristic time. In highly complex environments such as a cell's cytoplasm, a typical tracer is likely to experience many types of interactions and characteristic length scales with greatly varied results in restricting its diffusion. It is reasonable to expect that the composite result of many length-scales and binding times will significantly extend crossover regime further than would be the case if there was only one phenomenon restricting diffusion. Indeed, this expectation is consistent with Monte Carlo simulations that led to a recent proposal that diffusion with a hierarchy of binding sites is a model for anomalous diffusion in cellular environments (35).

One of the important implications of this research for diffusion-based experimental observations is that the length-scale dependence occurs at (and presumably below) the diffraction limit and tends to go away at larger length-scales. Therefore in cellular environments that are comparable to polymer solutions or gels due to macromolecular crowding, the experimentalist must be alert to the possibility that diffusion coefficients measured at over areas significantly larger than the diffraction limit are likely to underestimate the rate of diffusion at smaller scales, and measurements near the diffraction limit may depend significantly on the length-scale used.

The VLS-FCS method reveals that additional photophysics played a role in the interpretation of the diffusion data of Streptavidin in dextran solutions since fitting an additional correlation term resulted in slightly higher  $\alpha_p$  than without the extra term. It is known that an extra correlation appears for streptavidin labeled with various red-absorbing dyes at the biotin binding site. This extra correlation has characteristic times of about 4 – 10  $\mu\text{s}$  and a large amplitude which adds 15 - 60% to the maximum amplitude of correlation (41). In that study, this extra correlation was attributed to quenching by tryptophan residues located at neighboring binding sites, and it was further demonstrated that the addition of unlabeled biotin eliminated the extra correlation, and this effect was attributed to the inhibition of tryptophan by the binding of the biotin. For the streptavidin used in this study, it is possible that the extra correlation term which we observe may be due to similar quenching effects, but we observed that the addition of biotin had no observable effect in our case (data not shown). The observed differences may be due to the differences in absorption maximum, in the location of the Alexa Fluor 488 dye, and in the multiple labeling of the dye, as each protein is labeled with 3 or 4 dye molecules. Thus, VLS-FCS provides complementary data in addition to the diffusion power law such as the existence of unexpected photophysics which may affect the interpretation of the data. In our case, the diffusion of streptavidin in dextran is still shown to be anomalous by VLS-FCS, although not to the same degree as predicted by conventional FCS. No significant photophysical effects were observed for the bead samples, a fact attributed to the large number of dye molecules per bead.

The application of VLS-FCS to the study of living biological systems has already been demonstrated in the study of the diffusion of a lipid and a transmembrane protein in COS-7 cells (24). Extending the range of length-scales used in VLS-FCS as we have done and applying this extended measurement range in living systems would be quite useful. In biological systems, the frequency of observations of strong anomalous diffusion of macromolecules in crowded cytoplasmic-like environments (typically with values of  $\alpha \approx 0.75$ ) indicates that this phenomenon must be understood well in order to model such systems effectively (9, 12, 14, 19). Thus, even where the anomaly of the diffusion is due to a cross-over effect, if the cross-over effect occurs over a broad length scale including the scale of interest, the anomaly cannot be ignored when modeling the system. However, there are significant challenges to overcome before reliable diffusion power laws could be measured by VLS-FCS in living cells. The limiting factors include technical aspects of calibration at each observation volume and the loss of brightness or photostability of fluorophores at larger observation volumes.

## CONCLUSION

In this study, we demonstrate that the range of observation length scales used in VLS-FCS can be extended over an order of magnitude, 0.2 – 1.5  $\mu\text{m}$ , which allows one to obtain  $\alpha$  by directly observing the diffusion power law. The results of the VLS-FCS measurements with beads in 1.4% agarose gels are important because it demonstrates agreement between the complementary methods and directly verifies the length-scale dependence of the diffusion. The interpretation of the anomaly of the diffusion as a cross-over effect is suggested for both the bead-agarose and the protein-dextran systems, although for the protein-diffusion system the diffusion power law is Brownian over this range. Even in this case, however, the two-component model, which is independent of length-scale, is insufficient to account for all of the observations. Observations similar to the protein-dextran system are reproduced in the bead-agarose system by reducing the concentration of the agarose. Further, we show that VLS-FCS is also useful to provide complementary data in addition to the diffusion power law such as the existence of unexpected photophysics which may affect the interpretation of the data. Therefore, VLS-FCS is an important tool for the study of anomalous diffusion in systems that are accessible to FCS.

## ACKNOWLEDGMENTS

This work was funded by the Natural Sciences and Engineering Research Council of Canada. DB is the recipient of a CGS-D NSERC scholarship and CF is supported through the Canada Research Chairs Program.

REFERENCES

1. Valentine, M. T., P. D. Kaplan, D. Thota, J. C. Crocker, T. Gisler, R. K. Prud'homme, M. Beck, and D. A. Weitz. 2001. Investigating the microenvironments of inhomogeneous soft materials with multiple particle tracking. *Phys. Rev. E* 64:061506-061509.
2. Wong, I. Y., M. L. Gardel, D. R. Reichman, E. R. Weeks, M. T. Valentine, A. R. Bausch, and D. A. Weitz. 2004. Anomalous Diffusion Probes Microstructure Dynamics of Entangled F-Actin Networks. *Phys. Rev. Lett.* 92:178101-178104.
3. Banks, D. S., and C. Fradin. 2005. Anomalous Diffusion of Proteins Due to Molecular Crowding. *Biophys. J.* 89:2960-2971.
4. Fatin-Rouge, N., K. Starchev, and J. Buffle. 2004. Size Effects on Diffusion Processes within Agarose Gels. *Biophys. J.* 86:2710-2719.
5. Amblard, F., A. C. Maggs, B. Yurke, A. N. Pargellis, and S. Leibler. 1996. Subdiffusion and anomalous local viscoelasticity in actin networks. *Phys. Rev. Lett.* 77:4470-4473.
6. Busch, N. A., T. Kim, and V. A. Bloomfield, editors. 2000. Tracer Diffusion of Proteins in DNA Solutions. 2. Green Fluorescent Protein in Crowded DNA Solutions.
7. Weeks, E. R., and D. A. Weitz. 2002. Properties of Cage Rearrangements Observed near the Colloidal Glass Transition. *Phys. Rev. Lett.* 89:095704-095704.
8. Weeks, E. R., and D. A. Weitz. 2002. Subdiffusion and the cage effect studied near the colloidal glass transition. *Chem. Phys.* 284:361-367.
9. Weiss, M., M. Elsner, F. Kartberg, and T. Nilsson. 2004. Anomalous Subdiffusion Is a Measure for Cytoplasmic Crowding in Living Cells. *Biophys. J.* 87:3518-3524.
10. Weiss, M., H. Hashimoto, and T. Nilsson. 2003. Anomalous Protein Diffusion in Living Cells as Seen by Fluorescence Correlation Spectroscopy. *Biophys. J.* 84:4043-4052.
11. Brown, E. B., E. S. Wu, W. Zipfel, and W. W. Webb. 1999. Measurement of Molecular Diffusion in Solution by Multiphoton Fluorescence Photobleaching Recovery. *Biophys. J.* 77:2837-2849.
12. Wachsmuth, M., W. Waldeck, and J. Langowski. 2000. Anomalous diffusion of fluorescent probes inside living cell nuclei investigated by spatially-resolved fluorescence correlation spectroscopy. *J. Mol. Biol.* 298:677-689.
13. Feder, T., I. Brust-Mascher, J. Slattery, B. Baird, and W. Webb. 1996. Constrained diffusion or immobile fraction on cell surfaces: a new interpretation. *Biophys. J.* 70:2767-2773.
14. Golding, I., and E. C. Cox. 2006. Physical Nature of Bacterial Cytoplasm. *Phys. Rev. Lett.* 96:098102.
15. Platani, M., I. Goldberg, A. I. Lamond, and J. R. Swedlow. 2002. Cajal Body dynamics and association with chromatin are ATP-dependent. *J. Cell Biol.* 157:502-508.

16. Guigas, G., C. Kalla, and M. Weiss. 2007. Probing the Nanoscale Viscoelasticity of Intracellular Fluids in Living Cells. *Biophys. J.* 93:316-323.
17. Gennerich, A., and D. Schild. 2002. Anisotropic Diffusion in Mitral Cell Dendrites Revealed by Fluorescence Correlation Spectroscopy. *Biophys. J.* 83:510-522.
18. Luby-Phelps, K., D. Taylor, and F. Lanni. 1986. Probing the structure of cytoplasm. *J. Cell Biol.* 102:2015-2022.
19. Caspi, A., R. Granek, and M. Elbaum. 2002. Diffusion and directed motion in cellular transport. *Physical Review E (Statistical, Nonlinear, and Soft Matter Physics)* 66:011916.
20. Hac, A. E., H. M. Seeger, M. Fidorra, and T. Heimburg. 2005. Diffusion in Two-Component Lipid Membranes--A Fluorescence Correlation Spectroscopy and Monte Carlo Simulation Study. *Biophys. J.* 88:317-333.
21. Dwyer, J. D., and V. A. Bloomfield. 1993. Brownian Dynamics Simulations of Probe and Self-Diffusion in Concentrated Protein and DNA Solutions. *Biophys. J.* 65:1810-1816.
22. Guigas, G., and M. Weiss. 2006. Size-Dependent Diffusion of Membrane Inclusions. *Biophys. J.* 91:2393-2398.
23. Konopka, M. C., I. A. Shkel, S. Cayley, M. T. Record, and J. C. Weisshaar. 2006. Crowding and Confinement Effects on Protein Diffusion In Vivo. *J. Bacteriol.* 188:6115-6123.
24. Wawrzynieck, L., H. Rigneault, D. Marguet, and P.-F. Lenne. 2005. Fluorescence Correlation Spectroscopy Diffusion Laws to Probe the Submicron Cell Membrane Organization. *Biophys. J.* 89:4029-4042.
25. Berry, H. 2002. Monte Carlo Simulations of Enzyme Reactions in Two Dimensions: Fractal Kinetics and Spatial Segregation. *Biophys. J.* 83:1891-1901.
26. Masuda, A., K. Ushida, and T. Okamoto. 2005. New Fluorescence Correlation Spectroscopy Enabling Direct Observation of Spatiotemporal Dependence of Diffusion Constants as an Evidence of Anomalous Transport in Extracellular Matrices. *Biophys. J.* 88:3584-3591.
27. Wawrzynieck, L., P.-F. Lenne, D. Marguet, and H. Rigneault. 2004. Fluorescence correlation spectroscopy to determine diffusion laws: application to live cell membranes. In *Biophotonics Micro- and Nano-Imaging*. D. Anselmetti, editor. SPIE. 92-102.
28. Masuda, A., K. Ushida, and T. Okamoto. 2005. Direct observation of spatiotemporal dependence of anomalous diffusion in inhomogeneous fluid by sampling-volume-controlled fluorescence correlation spectroscopy. *Physical Review E (Statistical, Nonlinear, and Soft Matter Physics)* 72:060101.
29. Masuda, A., K. Ushida, and T. Okamoto. 2006. New fluorescence correlation spectroscopy (FCS) suitable for the observation of anomalous diffusion in polymer solution: Time and space dependences of diffusion coefficients. *Journal of Photochemistry & Photobiology, A: Chemistry* 183:304-308.
30. Lenne, P.-F., L. Wawrzynieck, F. Conchonaud, O. Wurtz, A. Boned, X.-J. Guo, H. Rigneault, H.-T. He, and D. Marguet. 2006. Dynamic Molecular Confinement

- in the Plasma Membrane by Microdomains and the Cytoskeleton Meshwork. *The EMBO Journal* 25:3245-3256.
31. Magde, D., E. Elson, and W. W. Webb. 1972. Thermodynamic Fluctuations in a Reacting System—Measurement by Fluorescence Correlation Spectroscopy. *Phys. Rev. Lett.* 29:705-708.
  32. Humpolickova, J., E. Gielen, A. Benda, V. Fagulova, J. Vercammen, M. vandeVen, M. Hof, M. Ameloot, and Y. Engelborghs. 2006. Probing Diffusion Laws within Cellular Membranes by Z-Scan Fluorescence Correlation Spectroscopy. *Biophys. J.* 91:L23-25.
  33. Haupts, U., S. Maiti, P. Schwille, and W. W. Webb. 1998. Dynamics of fluorescence fluctuations in green fluorescent protein observed by fluorescence correlation spectroscopy. *PNAS* 95:13573-13578.
  34. Almeida, P. F. F., and W. L. C. Vaz. 1995. Structure and Dynamics of Membranes. In *Handbook of Biological Physics*. R. Lipowsky, and E. Sackmann, editors.
  35. Saxton, M. J. 2007. A Biological Interpretation of Transient Anomalous Subdiffusion. I. Qualitative Model. *Biophys. J.* 92:1178-1191.
  36. Schwille, P., J. Korfach, and W. W. Webb. 1999. Fluorescence correlation spectroscopy with single-molecule sensitivity on cell and model membranes. *Cytometry* 36:176-182.
  37. Widengren, J., U. Mets, and R. Rigler. 1995. Fluorescence Correlation Spectroscopy of Triplet States in Solution: A Theoretical and Experimental Study. *Journal of Physical Chemistry* 99:13368-13379.
  38. Yeung, C., M. Shtrahman, and X.-l. Wu. 2007. Stick-and-Diffuse and Caged Diffusion: A Comparison of Two Models of Synaptic Vesicle Dynamics. *Biophys. J.* 92:2271-2280.
  39. Saxton, M. 1996. Anomalous diffusion due to binding: a Monte Carlo study. *Biophys. J.* 70:1250-1262.
  40. Labille, J., N. Fatin-Rouge, and J. Buffle. 2007. Local and Average Diffusion of Nanosolutes in Agarose Gel: The Effect of the Gel/Solution Interface Structure. *Langmuir* 23:2083-2090.
  41. Buschmann, V., K. D. Weston, and M. Sauer. 2003. Spectroscopic Study and Evaluation of Red-Absorbing Fluorescent Dyes. *Bioconjugate Chem.* 14:195-204.

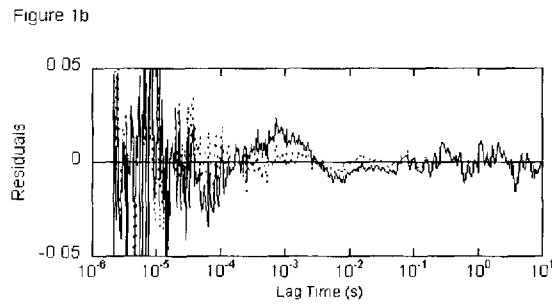
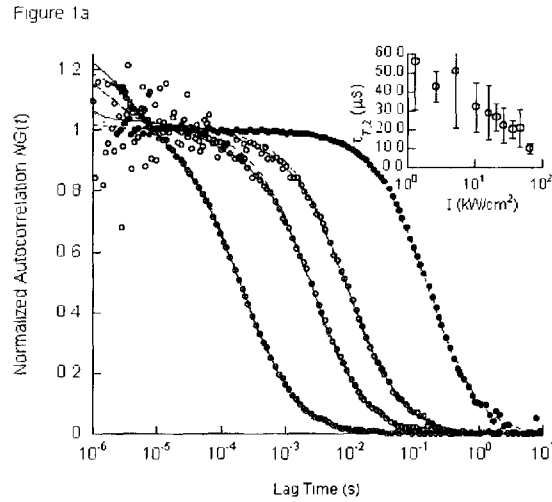


Figure 1. Normalized autocorrelation data for tracers diffusing in PBS buffer fit for normal diffusion (i.e.  $\alpha_p = 1$ ) with Eq. 4 (*dotted lines*) and 5 (*solid lines*): streptavidin-Alexa488 at  $w_0 = 200$  nm, 740 nm and  $1.5 \mu\text{m}$  from left to right (*empty circles*), and for 40 nm Orange beads at  $w_0 = 1.5 \mu\text{m}$  (*solid circles*). The correlation data for polymer beads shows only a correlation due to diffusion. The inset shows the characteristic time for the additional correlation decay versus the excitation laser power at  $w_0 = 350$  nm. (b) Residuals of the fits of the autocorrelation data in panel a for the case of streptavidin-Alexa488 at  $w_0 = 740$  nm for normal diffusion with Eq. 4 (*solid line*) and Eq. 5 (*dotted line*) which corrects for the additional correlation which decays from about  $10 \mu\text{s}$  to  $1$  ms (*dotted line*).

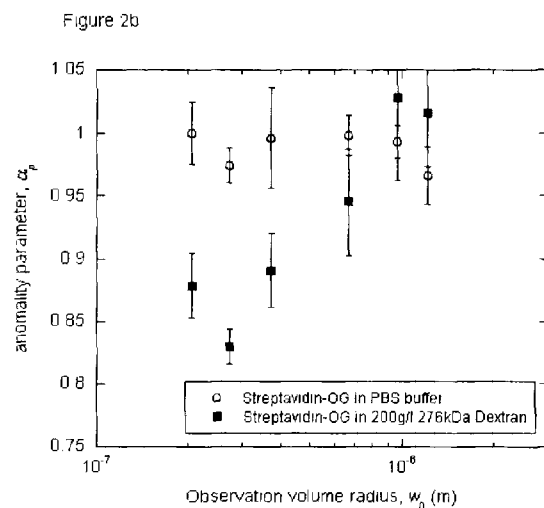
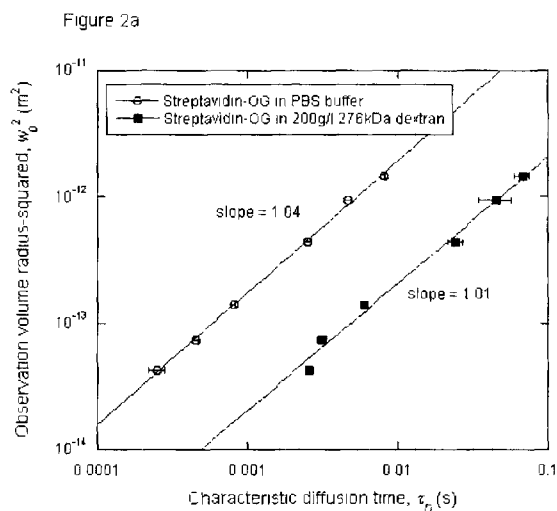


Figure 2. Diffusion laws for Streptavidin-OregonGreen in PBS buffer (*circles*) and with 200 g/l 276 kDa dextran (*squares*). The slope gives the value of the anomalous exponent for the diffusion power law,  $\alpha_{DL}$ . (b) The values of  $\alpha_p$ , the anomaly parameter determined by direct fit of the correlation data at each observation volume.

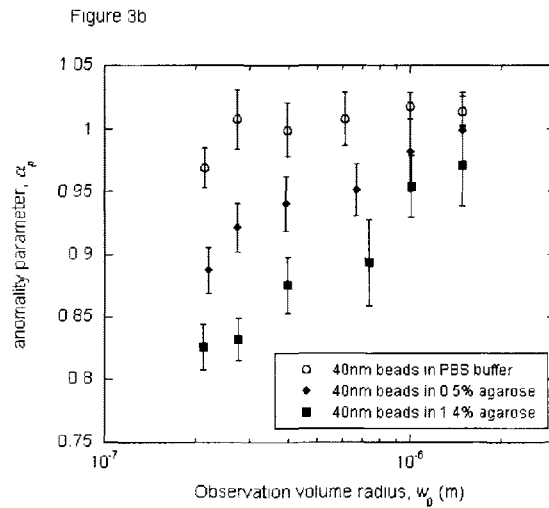
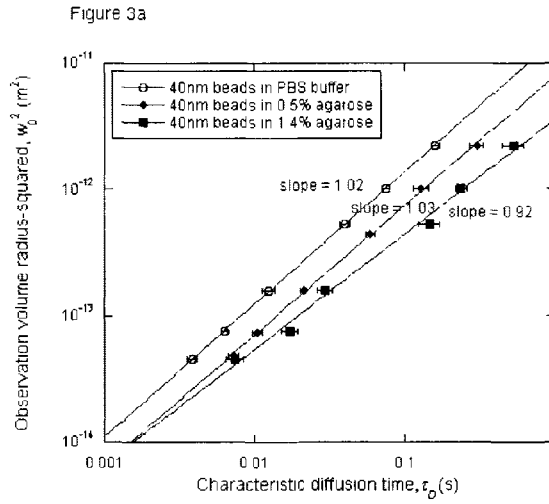


Figure 3. Diffusion laws for 40 nm Orange beads in PBS buffer (*circles*) and with 0.5% agarose (*diamonds*) and 1.5% agarose (*squares*). The slope gives the value of the anomalous exponent for the diffusion power law,  $\alpha_{DL}$ . (b) The values of  $\alpha_p$ , the anomaly parameter determined by direct fit of the correlation data at each observation volume.

Figure 4a

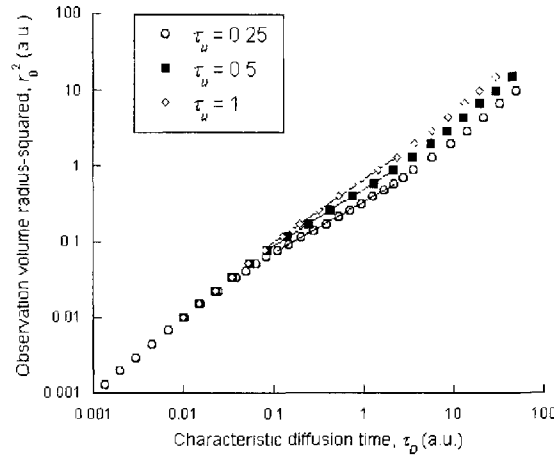


Figure 4b

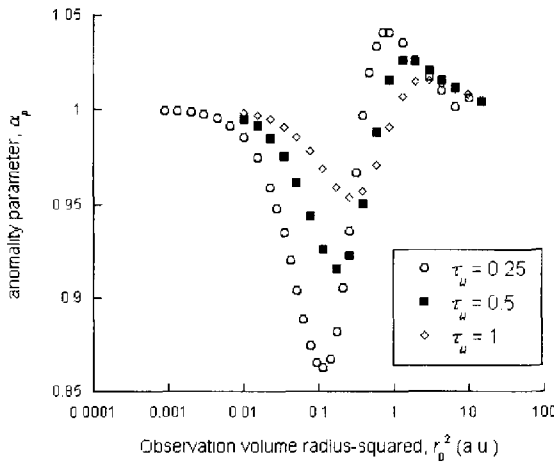
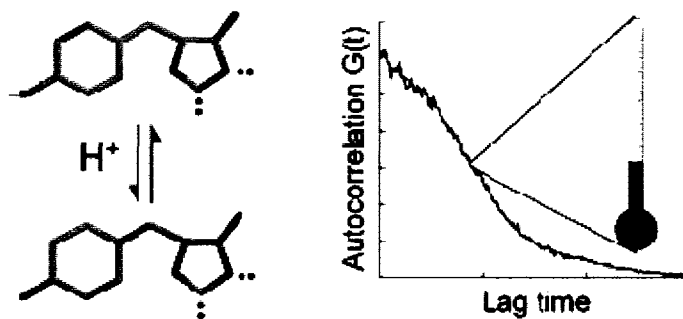


Figure 4. Cross-over diffusion power laws calculated using the modified stick and diffuse model for fixed obstacles for  $\tau_{u,\infty} = 0.25$  (*circles*),  $\tau_{u,\infty} = 0.5$  (*squares*), and  $\tau_{u,\infty} = 0.1$  (*diamonds*). While the slope is 1 for small and large  $\tau_D$ , in the middle regions, the diffusion power law,  $\alpha_{DL}$ , is non-Brownian with average values of 0.82, 0.75, and 0.67 respectively. (b) The anomalous exponents corresponding to the values of  $\tau_{u,\infty}$  used in (a). For small and large volumes  $\alpha_p = 1$ , and  $\alpha_p$  deviates from 1 at most to 0.86 around  $w_0^2 = 0.20$  for  $\tau_{u,\infty} = 0.25$ .

### 4.3 *A Molecular Thermometer Based on Fluorescent Protein Blinking*

Wong, F. H. C., D. S. Banks, A. Abu-Arish, and C. Fradin. 2007. A Molecular Thermometer Based on Fluorescent Protein Blinking. *J. Am. Chem. Soc.* 129:10302-10303.

#### 4.3.1 Table of Contents Graphic



#### 4.3.2 Abstract

With the present trend toward a miniaturization of chemical systems comes the need for a precise characterization of physicochemical parameters in very small fluid volumes. We describe here an original approach for small-scale temperature measurements based on the detection of fluorescent protein blinking. We observed that the characteristic time associated with the reversible protonation reaction responsible for the blinking of the enhanced green fluorescent protein is strongly temperature dependent at low pH. The blinking characteristic time can easily be detected by fluorescence correlation spectroscopy, and therefore provides the means for noninvasive, spatially resolved, absolute temperature measurements. We applied this approach to the quantification of laser-heating effects in thin liquid samples. As expected, we observed a linear dependence between the temperature increase at the laser focus and both the laser power and the sample extinction coefficient. In addition, we were able to measure the laser induced temperature increase at the glass/liquid interface, a value difficult to predict and hard to access experimentally, demonstrating the usefulness of our approach to study surface effects in microfluidic chips. The use of GFP derivatives as genetically encoded molecular thermometers should have direct applications for both microfluidics and single-cell calorimetry.

### 4.3.3 *JACS* Article

## A Molecular Thermometer Based on Fluorescent Protein Blinking

Felix H. C. Wong, Daniel S. Banks, Asmahan Abu-Arish, and Cécile Fradin\*

Department of Physics and Astronomy, McMaster University, 1280 Main Street West, Hamilton, Ontario, Canada L8S 4M1, and Department of Biochemistry and Biomedical Science, McMaster University, 1200 Main Street West, Hamilton, Ontario, Canada, L8N 3Z5

Received March 6, 2007; E-mail: fradin@physics.mcmaster.ca

With the current trend toward a miniaturization of chemical systems comes the need for precise physical measurements that will lead to an exact depiction of microfluidic environments. Traditionally, spatially resolved temperature measurements in fluids have been achieved using diffraction-limited optics to image dyes such as rhodamine B whose fluorescence quantum yield depends on temperature.<sup>1</sup> This method has been applied to observe temperature gradients in microfluidic channels<sup>2,3</sup> and in biological systems.<sup>4</sup> However it does not permit quantitative measurements because local dye concentration and background fluorescence also affect fluorescence intensity. To resolve this issue, methods based on the comparison between emission at different wavelengths<sup>5</sup> or on fluorescence lifetime measurements<sup>6</sup> have been proposed. Here, we propose another approach relying on the detection of the blinking of fluorescent proteins using fluorescence correlation spectroscopy (FCS). To demonstrate the usefulness of this method, we have applied it to the measurement of laser induced heating in thin liquid samples.

Many fluorescent proteins have the capacity to alternate between states with distinct fluorescence properties. In the case of the enhanced green fluorescent protein (EGFP), protonation of the Tyrosine-66 hydroxyl group on the chromophore brings the molecule from a deprotonated state, which is fluorescent upon 488 nm excitation, to a protonated state, which is mostly nonfluorescent under the same conditions. This characteristic has been exploited to design variants of the protein that can be used as genetically encoded molecular pH indicators.<sup>7</sup> The fluctuations in the fluorescence signal due to this reversible protonation reaction are referred to as blinking. The associated submillisecond relaxation time, which can be measured using FCS, is as expected very pH-sensitive.<sup>8</sup> We show here that this blinking also strongly depends on temperature, a property that makes GFP derivatives attractive candidates for use as molecular thermometers.

The temperature dependence of the relaxation time associated with the blinking of the EGFP is shown in Figure 1. To measure this dependence, protein samples were prepared by diluting purified recombinant EGFP (BioVision) to nanomolar concentrations in CP buffer (10 mM citric acid, 100 mM potassium phosphate) at different pH. The solution was then placed in a small chamber (thickness  $\approx 100 \mu\text{m}$ , volume  $\approx 10 \mu\text{L}$ ) made of two microscope cover slips spaced by Parafilm and sealed with wax. Blinking relaxation times were obtained using a home-built FCS instrument already described elsewhere.<sup>9</sup> EGFP fluorescence was excited with the 488 nm line of an argon laser, keeping the excitation power at the sample below  $80 \mu\text{W}$ . The temperature of the liquid was adjusted by controlling the temperature of both the stage and the water objective used for these experiments with two separate Peltier elements (Linkam Scientific Instruments). The resulting autocorrelation functions (each corresponding to a 60–180 s measurement) showed two separate decays, one due to the diffusion of the proteins

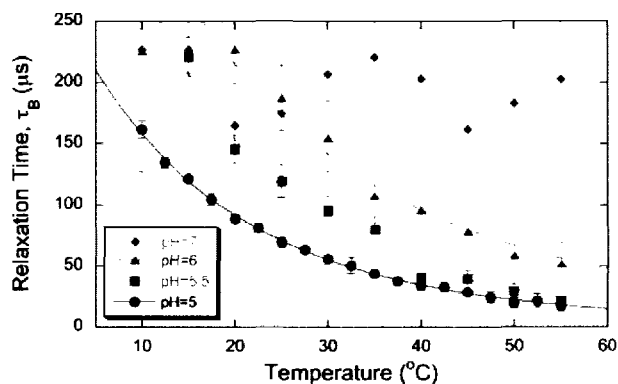


**Figure 1.** Calibration curves showing the temperature dependence of the relaxation time associated with EGFP blinking for different pH values. Data sets obtained for  $\text{pH} \leq 6$  have been fitted using eq 1.

in the observation volume ( $\sim 0.5 \text{ ms}$ ) and the other due to their blinking ( $\sim 0.1 \text{ ms}$ ). They were analyzed for lag times above  $10 \mu\text{s}$  using a model taking into account both processes. Two parameters characterizing the blinking process are extracted from this analysis: the relaxation time associated with protonation,  $\tau_B$ , and a coefficient,  $B$ , which in the absence of noise represents the average fraction of fluorophores found in the nonfluorescent protonated state.<sup>8</sup>

Simple protonation and deprotonation reactions should follow Arrhenius' law, in which case we expect at low pH ( $\text{pH} \leq 6$ )

$$1/\tau_B = 10^{-\text{pH}} A_p \exp(-E_p/RT) + A_d \exp(-E_d/RT) \quad (1)$$

$$B/(1 - B) = 10^{-\text{pH}} (A_p/A_d) \exp(-(E_p - E_d)/RT) \quad (2)$$

Using these relations to fit our data, we found that the values of the activation energies,  $E_p$  and  $E_d$ , and the frequency factors,  $A_p$  and  $A_d$  were constant within error at very low pH ( $\text{pH} \leq 5.5$ ) as expected for an external protonation reaction. These values ( $E_p = 9.2 \pm 0.3 \text{ kcal/mol}$  and  $E_d = 10.3 \pm 0.5 \text{ kcal/mol}$  for  $\text{pH} = 5$ ) are smaller than those measured using pH jump experiments,<sup>10</sup> but consistent with previous FCS measurements.<sup>8</sup>

Our measurements show that the relaxation time  $\tau_B$  is very sensitive to temperature changes at low pH. In contrast, the values obtained for  $\tau_B$  are not affected by fluorophore concentration, motion, or photobleaching, by the level of background fluorescence, by the excitation power, or by the size and shape of the detection volume. The relaxation time is therefore a useful parameter to exploit for temperature measurements. It does however depend on buffer composition (including viscosity) and pH,<sup>8</sup> so a new calibration curve must be obtained for each new buffer condition. The precision obtained on the value of  $\tau_B$  increases at low pH because the nonfluorescent protonated form of the protein becomes

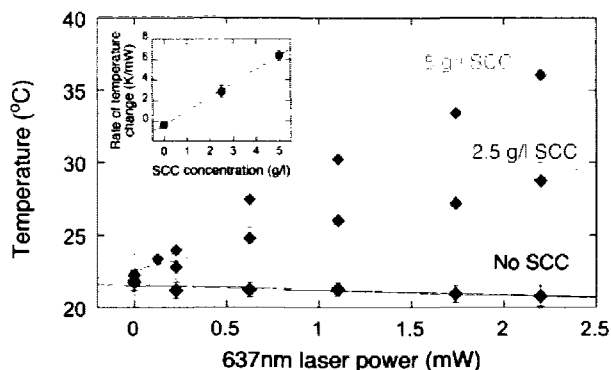


**Figure 2.** Increase in temperature at the focus of a 637 nm laser beam for solutions containing different concentrations of SCC. Lines represent linear fit of the data.

predominant, which increases the relative amplitude of the blinking term in the autocorrelation function.

As a first application of this molecular thermometer, we characterized the heating caused by a focused laser beam passing through a thin absorbing liquid sample, a situation often encountered in single cell or single molecule manipulation by optical tweezers. For this experiment, we used a commercial FCS instrument (Insight Cell, Evotec Technologies), which allowed combining two laser beams through the same optical fiber. We used the 637 nm radiation of a continuous-wave laser diode to produce a temperature increase in solutions of sodium copper chlorophyllin (SCC), a derivative of chlorophyll with a high extinction coefficient in the near-infrared. A second beam, the 488 nm line of an Ar Laser, was used to excite EGFP fluorescence. The power of that second laser was kept very low,  $P \approx 80 \mu\text{W}$  at the sample. The studied samples were prepared by dissolving SCC (Sigma) in CP buffer (pH = 5) supplemented with 100 g/L BSA and EGFP. The solutions were placed in  $\sim 100 \mu\text{m}$  thick chambers as described above. A calibration curve was acquired for each different SCC concentration. The temperature at the focus of the 637 nm laser line was inferred from the measured relaxation time of EGFP at that same position (10–20 s measurements).

The measured temperature increase is shown in Figure 2 in the case where the 637 nm laser was focused far from the glass cover slip. We expect a temperature change  $\Delta T \approx \epsilon P/K$ , where  $P$  is the incident laser power and  $\epsilon$  and  $K$  are the extinction coefficient and thermal conductivity of the solution, respectively. Indeed, our results show that the increase in temperature at the laser focus is directly proportional to the power of the 637 nm radiation, and that it is also directly proportional to SCC concentration, with no detectable increase in the absence of SCC. In addition, our measurements show that the increase in temperature due to laser heating is reduced as the laser focus is brought closer to the glass surface of the sample chamber (Figure 3). This is because the light absorption in the glass is negligible compared to that in the liquid, and because the cover slip, which is in direct contact with the water objective, acts as a heat sink. Far from the glass surface, a model taking into account light absorption and heat dissipation accurately predicts the temperature increase we measured.<sup>11</sup> However this simple model fails close to the surface, due to the difficulty of accurately taking boundary conditions into account. Our method on the other hand allows an accurate temperature measurement at the cover slip. The blinking properties of EGFP are not modified in the proximity of the glass surface, as proved by the fact that in the absence of laser heating the same temperature is correctly recovered in the bulk and at the surface of the sample (Figure 3). This has interesting

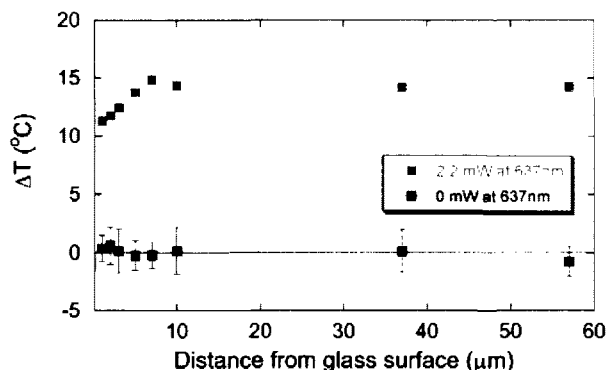


**Figure 3.** Temperature change at the laser focus in a 5 g/l SCC solution as a function of the distance between the laser focus and the glass cover slip, in the presence and in the absence of the 637 nm laser radiation. Solid lines are theoretical predictions from ref 11 ( $\epsilon = 35 \text{ cm}^{-1}$ ,  $K = 5.86 \text{ W}\cdot\text{K}^{-1}\cdot\text{cm}^{-1}$ ).

implications for the exact monitoring of temperature at the surface of microfluidic channels containing tethered active biomolecules.

Using fluorescent protein blinking as detected by FCS to measure temperature presents multiple advantages. It provides absolute temperature measurements, independent of experimental conditions when using typical FCS conditions (excitation intensity below  $200 \mu\text{W}$ , fluorophore concentration below 100 nM). It can be used to characterize steep temperature gradients, such as those expected in microfluidic and microcapillary flows. It can be used at a liquid/solid interface as long as the blinking properties of the proteins are not modified by presence of the solid surface. It is noninvasive providing an air objective is used instead of a water objective. The blinking properties of EGFP, however, remain sensitive to pH and buffer composition,<sup>8</sup> and therefore one limitation of the method is that a specific calibration curve should be obtained for each buffer condition. Finally, we note that this method has the potential to be applied directly in biological samples using genetically encoded fluorescent protein fusions. Using appropriate variants of the protein with an observable temperature dependence at pH = 7.4 should lead to precise temperature determination under normal physiological condition.

**Acknowledgment.** This work was supported by the Canadian Institute for Photonic Innovations (CIPI) and by the Natural Sciences and Engineering Research Council of Canada (NSERC) in particular through its Canada Research Chair program.

**Supporting Information Available:** Details on data fitting, thermodynamic parameters obtained at different pH, and reproducibility of the calibration curves. This material is available free of charge via the Internet at <http://pubs.acs.org>.

## References

- (1) Karstens, T.; Kobs, K. *J. Phys. Chem.* **1980**, *84*, 1871.
- (2) Erickson, D.; Sinton, D.; Li, D. *Lab. Chip* **2003**, *3*, 141.
- (3) Ross, D.; Gaitan, M.; Locascio, L. E. *Anal. Chem.* **2001**, *73*, 4117.
- (4) Kato, H.; Nishizaka, T.; Iga, T.; Kinoshita, K., Jr.; Ishiwata, S. *Proc. Natl. Acad. Sci. U.S.A.* **1999**, *96*, 9602.
- (5) Sakakibara, J.; Adrian, R. J. *Exp. Fluids* **1999**, *26*, 7.
- (6) Jeon, S.; Turner, J.; Granick, S. *J. Am. Chem. Soc.* **2003**, *125*, 9908.
- (7) Miesenbock, G.; De Angelis, D. A.; Rothman, J. E. *Nature* **1998**, *394*, 192.
- (8) Haupts, U.; Maiti, S.; Schwille, P.; Webb, W. W. *Proc. Natl. Acad. Sci. U.S.A.* **1998**, *95*, 13573.
- (9) Banks, D. S.; Fradin, C. *Biophys. J.* **2005**, *89*, 2960.
- (10) Saxena, A. M.; Udgaonkar, J. B.; Krishnamoorthy, G. *Protein Sci.* **2005**, *14*, 1787.
- (11) Peterman, E. J. G.; Gittes, F.; Schmidt, C. F. *Biophys. J.* **2003**, *84*, 1308.

JA0715905

#### **4.3.4 Supplementary Data**

**SUPPORTING INFORMATION:**

**A- Analysis of the autocorrelation functions**

Examples of normalized autocorrelation curves obtained for EGFP at pH=5 for different temperatures are shown in Fig. I.

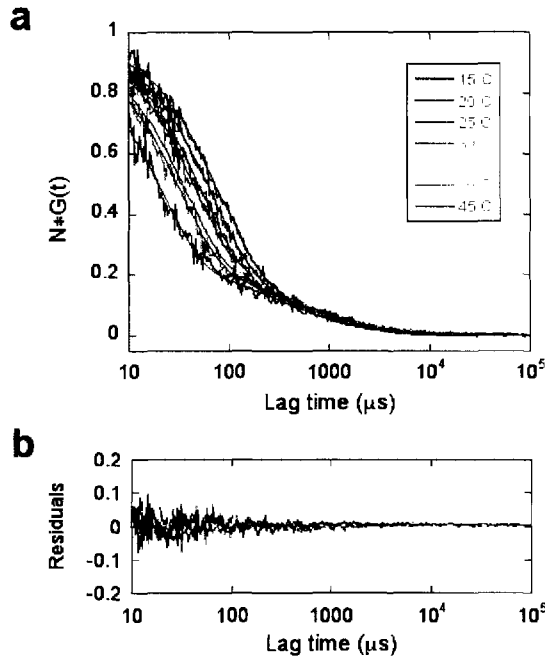


**Figure. I. (a)** Autocorrelation data obtained for EGFP in CP buffer (pH = 5) at different temperatures. Each curve corresponds to a 60s measurement. Correlation functions have been normalized to allow a better comparison between the different curves. Thin black lines are fit of the data using Eq. (A1). **(b)** Residuals corresponding to the fit of the curves shown in (a).

Autocorrelation functions were analyzed using a model taking into account both the diffusion and the blinking of the protein<sup>1</sup>:

$$G(t) = \frac{1/N}{\left(1 + t/\tau_d\right) \sqrt{1 + t/S^2\tau_d}} \left(1 + \frac{B \exp(-t/\tau_B)}{1 - B}\right). \quad (A1)$$

In Eq. (A1), S is the aspect ratio of the detection volume; N and  $\tau_d$  are the average number of fluorophores and average residence time of the fluorophores in the detection volume, respectively; B and  $\tau_B$  are the fraction of EGFP in the dark state and average relaxation time associated with the blinking process, respectively. For each temperature, a minimum of five measurements were taken and analyzed, from which average values and standard deviations for each parameter were calculated.

## B- Comparison between characteristic diffusion time and blinking relaxation time

When the protein is diffusing its average residence time in the detection volume,  $\tau_D$ , is roughly one order of magnitude larger than its blinking relaxation time,  $\tau_B$  (Fig. II). This permits the independent determination of these two parameters when analyzing autocorrelation functions since the two corresponding decays are well separated. This separation will be maintained in the case of a flow (velocity  $v$ ) as long as the particle residence time in the detection volume,  $\tau = w_0/v$  (where  $w_0 \sim 0.5 \mu\text{m}$  is the half-width of the detection volume), remains larger than  $\tau_B$ , i.e. as long as  $v < w_0/\tau_B \sim 5000 \mu\text{m/s}$ .

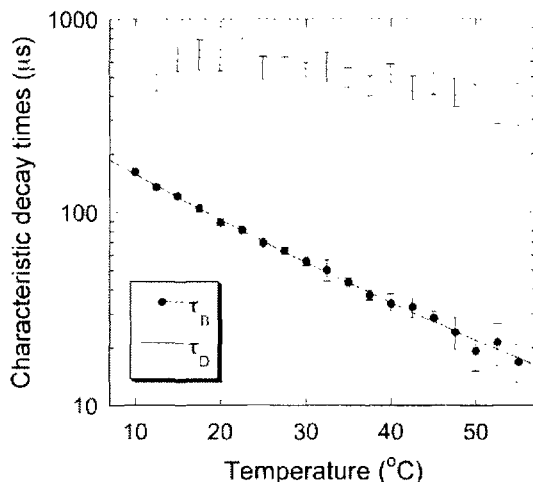
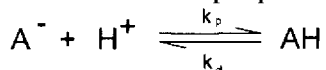


**Figure II.** Comparison between the two characteristic decay times (blinking relaxation time  $\tau_B$  and average residence time  $\tau_D$ ) observed in autocorrelation functions recorded for freely diffusing EGFP (pH=5). The solid lines correspond to the expected temperature dependence of these two parameters (as discussed in the text).

When the protein is diffusing, the residence time  $\tau_D$  should be proportional to  $\eta/T$ , where  $T$  is the absolute temperature and  $\eta$  is the buffer viscosity. The viscosity of aqueous solutions steeply decreases with increasing temperatures, so that we would expect  $\tau_D$  to vary by a factor of 3 in the studied temperature range (solid grey line in Fig. II). In fact, measurement of  $\tau_D$  has recently been proposed as a possible way to measure temperature<sup>2</sup>. However, probably due to photobleaching at low temperatures when  $\tau_D$  is large, only a 2-fold variation in  $\tau_D$  is observed, to be compared to the 10-fold variation in  $\tau_B$  in the same temperature range. Measurement of the relaxation time therefore offers a greater dynamic range for temperature measurements.

## C- Derivation of equations (1) and (2)

Consider the simple protonation process:



If the protonation and deprotonation rates,  $k_p$  and  $k_d$ , follow Arrhenius law we can write:

$$k_p = A_p e^{-E_p/RT}, \quad (C1)$$

$$k_d = A_d e^{-E_d/RT}. \quad (C2)$$

R is the gas constant;  $E_p$  and  $E_d$  are the activation energies corresponding to protonation and deprotonation, respectively;  $A_p$  and  $A_d$  are the so-called frequency factors.

The equilibrium constant associated with the reaction is:

$$K = \frac{[AH]_{eq}}{[A^-]_{eq}[H^+]_{eq}} = \frac{k_p}{k_d} = \frac{A_p}{A_d} e^{-(E_p - E_d)/RT}. \quad (C3)$$

Its dependence on temperature obeys van't Hoff equation:

$$\frac{d(\ln K)}{d(1/T)} = -\frac{\Delta H}{R}, \quad (C4)$$

where the enthalpy change associated with the reaction,  $\Delta H$ , is linked to the activation energies:  $\Delta H = E_p - E_d$ .

If we assume that the protonated form of the protein is totally non-fluorescent under the conditions of the experiment, then the factor B that appears in the expression of the autocorrelation function (Eq. A1) corresponds to the average fraction of protonated proteins, so  $B = [AH]_{eq} / ([A^-]_{eq} + [AH]_{eq})$ . Thus according to Eq. C3:

$$\frac{[AH]_{eq}}{[A^-]_{eq}} = \frac{B}{1-B} = 10^{-pH} \left( \frac{A_p}{A_d} \right) e^{-(E_p - E_d)/RT}. \quad (C5)$$

For small concentration variations away from equilibrium we will have  $[AH] = [AH]_{eq} + \delta$ ,  $[A^-] = [A^-]_{eq} - \delta$  and  $[H^+] = [H^+]_{eq} - \delta'$ , where  $|\delta'| < |\delta|$ , since the buffer could correct for variations in proton concentration faster than the reaction involving the proteins. Thus the rate of formation of [AH]:

$$\frac{d[AH]}{dt} = -k_d[AH] + k_p[H^+][A^-], \quad (C6)$$

can be rewritten:

$$\frac{d\delta}{dt} = -[k_d + k_p[H^+]_{eq}] \delta + k_p[A^-] \delta' \quad (C7)$$

where second order terms in  $\delta$  and  $\delta'$  have been neglected.

In the limit case where  $\delta = \delta'$  (meaning that at the time scale of the considered fluctuations the buffer has no influence on the relaxation process) the relaxation time associated with the fluctuation is:

$$\tau = \frac{1}{k_d + k_p([H^+]_{eq} + [A^-]_{eq})}. \quad (C8)$$

The other limit case arises when the relaxation in proton concentration happens much faster due to buffer than due to reactions involving the proteins, in which case we can consider that  $\delta' = 0$ , leading to a relaxation time:

$$\tau = \frac{1}{k_d + k_p[H^+]_{eq}} \quad (C9)$$

In either case, when  $[A^-]_{eq} \ll [H^+]_{eq}$ , which in the condition of our calibration experiments (protein concentration in the nM range) is true for  $pH \leq 6$ , the relaxation time should be given by Eq. C9.

If the EGFP blinking process is due to a simple protonation/deprotonation equilibrium we thus expect that the relaxation time of the blinking process,  $\tau_B$ , which is measured by FCS will obey (by combining Eqs. C1 and C2 with Eq. C9):

$$1/\tau_B = 10^{-pH} A_p e^{-E_p/RT} + A_d e^{-E_d/RT}. \quad (C10)$$

## D- Thermodynamic parameters

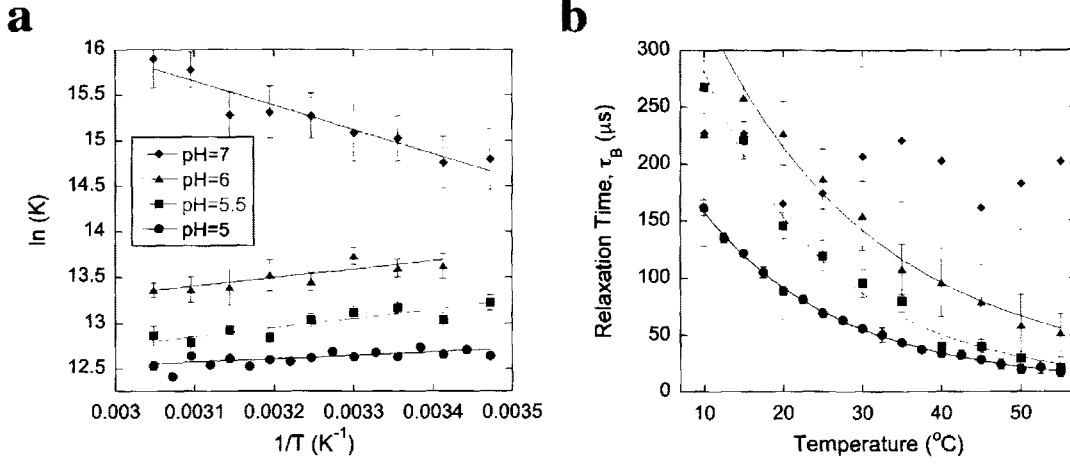


**Figure III.** (a) Temperature dependence of the equilibrium constant associated with EGFP blinking for different pHs. Each data set was fit using Eq. C3. (b) Temperature dependence of the relaxation time associated with EGFP blinking for different pHs. Data for  $pH \leq 6$  was fit using Eq. C10.

The equilibrium constant  $K=B/[(1-B)10^{pH}]$  and the relaxation time associated with the blinking process,  $\tau_B$ , are shown in Fig. III as a function of temperature for different pHs. To extract thermodynamics parameters at a given pH, we first obtained the ratio of the frequency factors,  $(A_p/A_d)$ , and the enthalpy change associated with the reaction,  $\Delta H=E_p-E_d$ , by using Eq. C3 to fit the equilibrium constant data. We then fixed the values of these parameters when using Eq. C10 to fit the relaxation time data for  $pH \leq 6$ . Resulting values of the activation energies and frequency factors are shown in Table I. These values represent average values obtained for several calibration curves measured at each pH, and the errors indicated are standard deviations.

pH	pH = 5.0	pH = 5.5	pH = 6.0	pH = 7.0
$A_p$ (/s/M)	$(7.1 \pm 4.2) \times 10^{15}$	$(5.4 \pm 6.5) \times 10^{15}$	$(2.7 \pm 2.2) \times 10^{14}$	
$A_d$ (/s)	$(1.4 \pm 1.1) \times 10^{10}$	$(31 \pm 43) \times 10^{10}$	$(1.5 \pm 1.9) \times 10^9$	
$E_p$ (kcal/mol)	$9.2 \pm 0.3$	$9.0 \pm 1.1$	$6.7 \pm 0.5$	
$E_d$ (kcal/mol)	$10.3 \pm 0.5$	$10.4 \pm 1.9$	$7.2 \pm 1.3$	
$\Delta H$ (kcal/mol)	$-1.1 \pm 0.1$	$-1.4 \pm 0.8$	$-0.6 \pm 1.8$	$5.3 \pm 1.4$

**Table I:** Average values measured for the thermodynamics parameters corresponding to EGFP protonation and deprotonation. Errors in this table are standard deviations between different measurements such as the one presented in Fig. III.

For a simple protonation reaction, we expect the enthalpy change  $\Delta H$  to be independent of pH. However, whereas the enthalpy changes we measured at  $pH \leq 6$  were all slightly negative, and in agreement with previous FCS measurements (where it was found that  $\Delta H = -2.7$  kcal/mol at  $pH = 6.5$ )<sup>1</sup>, the enthalpy change observed at  $pH = 7$  was clearly positive. This raises the question of whether the blinking observed at that pH has the same cause as at lower pH. The values of the activation energies obtained here ( $E_p \sim 9$  kcal/mol,

$E_d \sim 10 \text{ kcal/mol}$ ) are at odd with values obtained in a different study using pH jump experiments ( $E_p \sim 0.3 \text{ kcal/mol}$ ,  $E_d \sim 14.8 \text{ kcal/mol}$ )<sup>3</sup>. Contrarily to FCS experiments, pH jump experiments involve large deviations from equilibrium (in that case from pH=8 to pH=5). Thus the relaxation processes observed in either case might be different. It was suggested in Ref. 3 that the relaxation process observed in pH jump experiments might involve protons coming from the bulk solution, while the relaxation process observed by FCS might involve protons coming from the inside of the protein. Taken together, these observations show that the observed blinking cannot be reduced to a simple protonation reaction, at least not at all pHs.

### E- Dependence of the relaxation time on excitation power and EGFP concentration

We verified that the dependence of the measured relaxation time on excitation power was minimal in the range useful for FCS measurements,  $P \leq 200 \mu\text{W}$  (Fig. IV). Well above that range however, a slow decrease of the measured relaxation time with increasing laser power is observed, either due to photobleaching or to the emergence of a triplet state term not accounted for in the fitting of the autocorrelation functions.

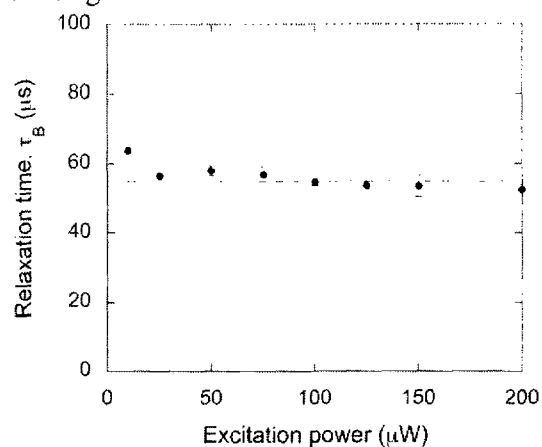


**Figure IV.** Relaxation time associated with EGFP blinking measured by FCS as a function of excitation power (pH=5,  $T=25^\circ\text{C}$ ).

Accordingly, when thermodynamic parameters are calculated from calibration curves recorded at different laser powers in the range habitually used for FCS measurements, they are found to be in very good agreement (Table II).

Laser power	20 $\mu\text{W}$	50 $\mu\text{W}$	200 $\mu\text{W}$	500 $\mu\text{W}$
$A_p$ (/s/M)	$(7.1 \pm 4.2) \times 10^{15}$	$(6.0 \pm 2.0) \times 10^{15}$	$(7.2 \pm 0.9) \times 10^{15}$	$(5.3 \pm 0.8) \times 10^{15}$
$A_d$ (/s)	$(1.4 \pm 1.1) \times 10^{10}$	$(2.5 \pm 1.1) \times 10^{10}$	$(9.0 \pm 1.5) \times 10^{10}$	$(10 \pm 4) \times 10^{10}$
$E_p$ (kcal/mol)	$9.2 \pm 0.3$	$9.1 \pm 0.2$	$9.1 \pm 0.1$	$8.7 \pm 0.2$
$E_d$ (kcal/mol)	$10.3 \pm 0.4$	$10.6 \pm 0.3$	$10.0 \pm 0.1$	$10.0 \pm 0.3$
$\Delta H$ (kcal/mol)	$-1.1 \pm 0.1$	$-1.5 \pm 0.1$	$-0.9 \pm 0.1$	$1.2 \pm 0.1$

**Table II.** Thermodynamic parameters extracted from the fit of calibration curves obtained at pH=5 for different laser powers. Errors in this table are the standard error values obtained from the fit of each separate calibration curves (using the software Kaleidagraph).

Similarly, EGFP concentration had no influence on the measured blinking relaxation times and on the values of the thermodynamic parameters obtained from the resulting calibration curves for  $\text{pH} \leq 6$  and in the concentration range useful for FCS measurements,  $c \leq 100 \text{ nM}$ . According to Eq. C8, a dependence on EGFP concentration is to be expected at higher pH ( $\text{pH} \geq 7$ ).

In summary, in the range of conditions useful for FCS experiments ( $P < 200 \mu\text{W}$  and  $c < 100 \text{ nM}$ ) and for the range of pH useful for the proposed temperature measurements ( $\text{pH} \leq 6$ ), the measured blinking relaxation time does not depend on excitation power nor on EGFP concentration.

#### F- Comparison between calibration curves obtained in different conditions

We investigated the robustness of the temperature calibration curve obtained in CP buffer at  $\text{pH} = 5$  for two specific situations: first when adding large quantities of SCC to the solution, and second in the case when the EGFP is part of a fusion protein. In the first case, a sample was prepared by dissolving 100g/l BSA and 5g/l SCC into CP buffer at  $\text{pH} = 7$  and subsequently adjusting the pH of the buffer to 5. The addition of BSA in the sample further enhanced the solubility of SCC at this low pH. EGFP was added at a  $\sim 100 \text{ nM}$  concentration. The calibration curve obtained from this sample is shown in Fig. IV. It shows a systematically faster relaxation time associated with EGFP blinking than in the absence of SCC. On the other hand, when the calibration was repeated using an EGFP-Bax fusion (CP buffer,  $\text{pH} = 5$ ), the calibration curve was very similar to that obtained for EGFP (Fig. V). This confirms that blinking characteristics are sensitive to buffer condition (which means that a different calibration curve needs to be obtained for each different buffer solution used). It also shows that fusing EGFP to another protein does not affect its capacity to act as a thermometer.

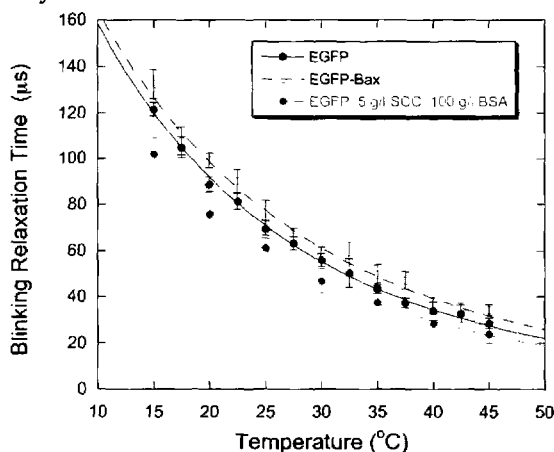


**Figure V.** Temperature dependence of the relaxation time associated with the blinking of the EGFP chromophore for three different samples: EGFP, EGFP fused with Bax, and EGFP in presence of 5g/l SCC and 100g/l BSA. All samples were prepared in CP buffer at  $\text{pH} = 5$ .

### G- Comparison between calibration curves obtained with different objectives

To avoid any influence of the microscope on the temperature of the system, the use of an air objective instead of a water objective is necessary, because a water objective can act as a strong heat sink. The absence of physical contact between an air objective and the sample also allows achieving higher temperature in the sample without risking damaging the objective. Traditionally, however, FCS measurements have been done with water objectives, because they can have higher numerical apertures and allow working closer to the diffraction limit. To verify that the same precision on the temperature measurement could be obtained with an air objective than with a higher NA water objective, we obtained two different calibration curves for the same  $\sim 100\text{nM}$  EGFP sample (CP buffer,  $\text{pH}=5$ ), using first a water immersion objective (Nikon Plan Apo, 60x, NA 1.2) and second an air objective (Nikon Plan Apo, 60x, NA 0.95). The two calibration curves (shown in Fig. VI) are identical within error, and the standard deviation of the data obtained with the air objective is not larger than that obtained with the water objective. This is despite the fact that for the water objective the  $1/e^2$  radius of the detection volume was  $0.325\mu\text{m}$  (as opposed to  $0.193\mu\text{m}$  for the water objective) and the light energy flux at the focus was  $6.2\text{kW}/\text{cm}^2$  (as opposed to  $10.3\text{kW}/\text{cm}^2$  for the water objective).

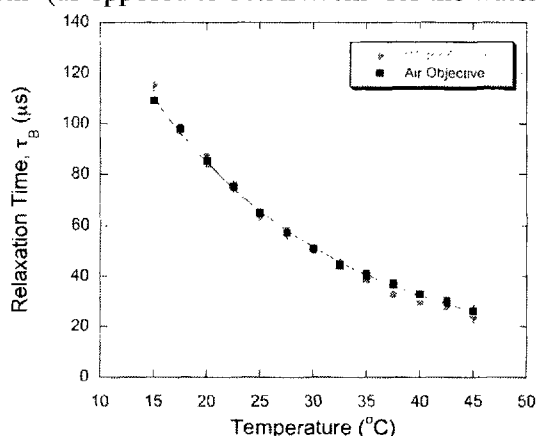


**Figure VI.** Temperature dependence of the relaxation time associated with EGFP blinking as measured with a water immersion objective and with an air objective.

#### References:

- (1) Haupts, U.; Maiti, S.; Schwille, P.; Webb, W. W. *Proc Natl Acad Sci U S A* **1998**, *95*, 13573.
- (2) Ito, S.; Sugiyama, T.; Toitani, N.; Katayama, G.; Miyasaka, H. *J Phys Chem B* **2007**, *111*, 2365.
- (3) Saxena, A. M.; Udgaonkar, J. B.; Krishnamoorthy, G. *Protein Sci* **2005**, *14*, 1787.